In the IOCCG Report Series:

1. *Minimum Requirements for an Operational Ocean-Colour Sensor for the Open Ocean (1998)*
2. *Status and Plans for Satellite Ocean-Colour Missions: Considerations for Complementary Missions (1999)*
3. *Remote Sensing of Ocean Colour in Coastal, and Other Optically-Complex, Waters (2000)*
4. *Guide to the Creation and Use of Ocean-Colour, Level-3, Binned Data Products (2004)*
5. *Remote Sensing of Inherent Optical Properties: Fundamentals, Tests of Algorithms, and Applications (2006)*
6. *Ocean-Colour Data Merging (2007)*
7. *Why Ocean Colour? The Societal Benefits of Ocean-Colour Technology (2008)*
8. *Remote Sensing in Fisheries and Aquaculture (2009)*
9. *Partition of the Ocean into Ecological Provinces: Role of Ocean-Colour Radiometry (2009)*
10. *Atmospheric Correction for Remotely-Sensed Ocean-Colour Products (2010)*
11. *Bio-Optical Sensors on Argo Floats (2011)*
12. *Ocean-Colour Observations from a Geostationary Orbit (2012)*
13. *Mission Requirements for Future Ocean-Colour Sensors (2012)*
14. *In-flight Calibration of Satellite Ocean-Colour Sensors (2013)*
15. *Phytoplankton Functional Types from Space (2014)*
16. *Ocean Colour Remote Sensing in Polar Seas (this volume)*

The printing of this report was sponsored and carried out by the National Oceanic and Atmospheric Administration (NOAA), USA, which is gratefully acknowledged.

Reports and Monographs of the International Ocean Colour Coordinating Group

An Affiliated Program of the Scientific Committee on Oceanic Research (SCOR)
An Associated Member of the Committee on Earth Observation Satellites (CEOS)

IOCCG Report Number 16, 2015

Ocean Colour Remote Sensing in Polar Seas

Editors:
Marcel Babin, Kevin Arrigo, Simon Bélanger and Marie-Hélène Forget

Report of an IOCCG working group on Ocean Colour Remote Sensing in Polar Seas, chaired by Marcel Babin, Kevin Arrigo and Simon Bélanger, and based on contributions from (in alphabetical order):

Kevin Arrigo	Stanford University, USA
Marcel Babin	Takuvik Joint International Laboratory, Université Laval & CNRS
Simon Bélanger	Université du Québec à Rimouski, Canada
Josefino Comiso	NASA Goddard Space Flight Center, USA
Marie-Hélène Forget	Takuvik Joint International Laboratory, Université Laval & CNRS
Robert Frouin	Scripps Institution of Oceanography, USA
Clémence Goyens	Université du Québec à Rimouski, Canada
Victoria Hill	Old Dominion University, USA
Toru Hirawake	Hokkaido University, Japan
Atsushi Matsuoka	University of Laval, Canada
B. Greg Mitchell	Scripps Institution of Oceanography, USA
Don Perovich	ERDC-CRREL, New Hampshire, USA
Rick A. Reynolds	Scripps Institution of Oceanography, USA
Knut Stamnes	Stevens Institute of Technology, USA
Menghua Wang	NOAA/NESDIS/STAR, USA

Series Editor: Venetia Stuart

Correct citation for this publication:

IOCCG (2015). Ocean Colour Remote Sensing in Polar Seas. Babin, M., Arrigo, K., Bélanger, S. and Forget, M-H. (eds.), IOCCG Report Series, No. 16, International Ocean Colour Coordinating Group, Dartmouth, Canada.

The International Ocean Colour Coordinating Group (IOCCG) is an international group of experts in the field of satellite ocean colour, acting as a liaison and communication channel between users, managers and agencies in the ocean colour arena.

The IOCCG is sponsored by Centre National d'Etudes Spatiales (CNES, France), Canadian Space Agency (CSA), Commonwealth Scientific and Industrial Research Organisation (CSIRO, Australia), Department of Fisheries and Oceans (Bedford Institute of Oceanography, Canada), European Space Agency (ESA), European Organisation for the Exploitation of Meteorological Satellites (EUMETSAT), Helmholtz Center Geesthacht (Germany), National Institute for Space Research (INPE, Brazil), Indian Space Research Organisation (ISRO), Japan Aerospace Exploration Agency (JAXA), Joint Research Centre (JRC, EC), Korea Institute of Ocean Science and Technology (KIOST), National Aeronautics and Space Administration (NASA, USA), National Centre for Earth Observation (NCEO, UK), National Oceanic and Atmospheric Administration (NOAA, USA), Scientific Committee on Oceanic Research (SCOR), and Second Institute of Oceanography (SIO), China.

http: //www.ioccg.org

Published by the International Ocean Colour Coordinating Group,
P.O. Box 1006, Dartmouth, Nova Scotia, B2Y 4A2, Canada.

ISSN: 1098-6030
ISBN: 978-1-896246-51-2

Printed by the National Oceanic and Atmospheric Administration (NOAA), USA

Contents

Chapter 1

General Introduction

Marcel Babin and Marie-Hélène Forget

1.1 Background

Ocean colour remote sensing has often been used to study polar seas, especially in the Southern Ocean where the optical properties of the upper ocean are not as complex as they are in the Arctic Ocean (Comiso et al. 1990, 1993; Sullivan et al. 1993; Arrigo et al. 1998; Stramski et al. 1999; Arrigo et al. 2008b). The analysis of SeaWiFS time series shows that primary production in the Southern Ocean has changed little over the 1997 — 2006 period (Arrigo et al. 2008b), which is consistent with relatively stable pan-Antarctic sea-ice conditions. In contrast, spectacular impacts of climate change have been observed recently in the Arctic Ocean, including the receding of the summer ice cover by nearly 40% over the last 3 decades (Stroeve et al. 2007; Comiso et al. 2008; Stroeve et al. 2012). It is predicted that the summer ice cover will disappear almost completely by the end of the current century (Serreze et al. 2007; Holland et al. 2008) and perhaps much earlier (Wang and Overland 2012). As a consequence of perennial ice receding, the pan-Arctic primary production, as well as the photooxidation of coloured dissolved organic matter, appear to be increasing (Bélanger et al. 2006; Pabi et al. 2008; Arrigo et al. 2008a; Bélanger et al. 2013b). The annual maximum phytoplankton biomass is now reached earlier in several Arctic seas (Kahru et al. 2010). As the extent of the seasonal ice zone increases (i.e., the difference between the annual maximum and minimum extent), ice-edge blooms may play an increasing role (Perrette et al. 2011). The occurrence of autumn phytoplankton blooms is increasing (Ardyna et al. 2014). Finally, changes in the properties of marine snow and sea ice may favour phytoplankton blooms taking place under the ice-pack (Arrigo et al. 2012).

The ongoing changes within the context of accelerating climate change calls for a vastly improved understanding of the polar ecosystems based on an intensive observation program. *In situ* observations from ships are, however, inherently sparse in space and time, especially in the harsh and inaccessible Arctic Ocean. Ocean colour remote sensing is certainly one of the most appropriate tools to extensively monitor marine ecosystems, as it provides recurrent pan-Arctic and pan-Antarctic observations at relatively low cost.

The use of ocean colour remote sensing in Polar Regions is, however, impeded by a number of difficulties and intrinsic limitations including:

- **The persistence of clouds and fog**: High latitude areas are characterised by heavy cloud cover. Furthermore, as soon as sea ice melts and open waters come into direct contact with the atmosphere, fog develops near the sea surface. These features limit the use of ocean colour data. At high latitudes, multiple overpasses by Low Earth Orbit (LEO) satellites over the same region on the same day may overcome this problem to some extent. Perrette et al. (2011) attempted to monitor ice-edge blooms in the Arctic Ocean, following to some extent the criteria used by Arrigo et al. (1998) in the Southern Ocean. Over the assumed 20-day duration of ice-edge conditions for any given pixel, only 50% of the pixels had at least 3 observations. This reflects the difficulty to monitor changes in the Arctic Ocean over short time scales, because of the impact of clouds and fog.

- **The prevailing low solar elevations**: At high latitudes, the Sun zenith angle is often larger than the maximum for which atmospheric correction algorithms have been developed, based on plane-parallel radiative transfer calculations (generally 70°). Consequently, at high latitudes, a large fraction of the ocean surface is undocumented for a large part of the year even though primary production may be non-negligible. Whether or not this is a major problem must be determined, and the quality of standard atmospheric corrections for Sun zenith angles larger than 70° must be assessed.
- **The impact of ice on remotely-sensed reflectance**: Based on radiative transfer simulations, Bélanger et al. (2007) and Wang and Shi (2009) examined the effects of the sea ice adjacency and of sub-pixel ice contamination on retrieved seawater reflectance and Level-2 ocean products. They found significant impacts over the first several kilometers from the ice-edge and for concentrations of sub-pixel ice floes beyond a few percent. The extent of the problem, i.e., whether it compromises the use of ocean colour in typical polar conditions, is unknown.
- **The optical complexity of seawater, especially over the Arctic shelves**: Because of the important freshwater inputs, the Arctic continental shelves, which occupy 50% of the area, are characterized by high concentrations of CDOM (Matsuoka et al. 2007; Bélanger et al. 2008; Matsuoka et al. 2011, 2012, 2013). In addition, as a consequence of photoacclimation to low irradiances, phytoplankton cells often exhibit high intracellular pigment concentrations resulting in particularly low chlorophyll-specific absorption coefficients due to pronounced pigment packaging (Cota et al. 2003; Wang et al. 2005a; Matsuoka et al. 2012). Because of these optical peculiarities, standard ocean colour algorithms do not work well in the Arctic Ocean (Cota et al. 2004; Matsuoka et al. 2007).
- **The deep chlorophyll maximum (DCM)**: A DCM is often observed both in the Southern Ocean and Arctic Ocean. In the Arctic Ocean, the freeze-thaw cycle of sea ice, and the large export of freshwater to the ocean by large Arctic rivers, create pronounced haline stratification within the surface layer. In post-bloom conditions, a deep chlorophyll-maximum is associated with that vertical stratification. Contrary to the DCM generally observed at lower latitudes (Cullen 1982), the Arctic DCM is exposed to higher photosynthetically available radiation (PAR) and often corresponds to a maximum in particulate carbon and primary production (e.g., Martin et al. 2010). The statistical relationships between surface chlorophyll and chlorophyll concentration at depth developed for lower latitudes (Morel and Berthon 1989) are likely not valid for the polar seas (Martin et al.

2010). Ignoring the vertical structure of the chlorophyll profile in the Arctic Ocean may lead to significant errors when estimating areal primary production (Pabi et al. 2008; Hill and Zimmerman 2010; Ardyna et al. 2013).

- **Under-ice phytoplankton blooms**: Arrigo et al. (2012) recently documented massive phytoplankton blooms under the ice pack during spring, which cannot be observed using ocean colour data. The impact of these under-ice blooms on pan-Arctic estimates of seasonal and annual primary production, derived using ocean-colour data, must be assessed.
- **The peculiar phytoplankton photosynthetic parameters**: The low irradiance and low seawater temperatures prevailing in polar seas are associated with unique bio-optical and photosynthetic parameters reflecting extreme environments (e.g., Rey 1991; Palmer et al. 2011; Huot et al. 2013; Babin et al. 2015) and must be accounted for in primary production models. Only a few authors (e.g., Arrigo et al. 2008b; Bélanger et al. 2013b) have tried to do so.

This report sheds light on the impact of the peculiar conditions found in polar regions on ocean colour products. Chapter 2 highlights the specific sun, cloud and ice conditions found in polar environments. The complexity of remote sensing of ocean colour from the surface to the top-of-atmosphere is addressed in Chapter 3. A large dataset of *in situ* observations of optical properties in polar seas was put together to test the current ocean colour algorithms through sensitivity analyses in Chapter 4. An intercomparison between various primary production models for polar regions is presented in Chapter 5, and the impact of the DCM on primary production estimates is investigated using a sensitivity analysis. Finally, recommendations are made and new approaches and concepts for studying polar regions using ocean colour remote sensing are proposed.

Chapter 2

The Polar Environment: Sun, Clouds, and Ice

Josefino Comiso, Don Perovich and Knut Stamnes

2.1 Introduction

The polar regions are places of extremes. There are months when the regions are enveloped in unending darkness, and months when they are in continuous daylight. During the daylight months the sun is low on the horizon and often obscured by clouds. In the dark winter months temperatures are brutally cold, and high winds and blowing snow are common. Even in summer, temperatures seldom rise above 0°C. The cold winter temperatures cause the ocean to freeze, forming sea ice. This sea ice cover acts as a barrier limiting the transfer of heat, moisture, and momentum between the atmosphere and the ocean. It also greatly complicates the optical signature of the surface. Taken together, these factors make the polar regions a highly challenging environment for optical remote sensing of the ocean.

The sea ice cover of the polar oceans extends over a vast area (millions of square kilometers), but it is only a thin veneer of less than a few meters thick. Sea ice exhibits tremendous spatial and temporal variability. Ice thickness can range from zero (open water) to several meters thick over a short distance. For much of the year sea ice is covered by snow giving a fairly uniform white appearance to the surface. During the melt season, Arctic sea ice cover becomes a mix of open water, bare ice, and ponded ice. Thin ice appears dark gray, melt ponds are shades of blue, and thick snow covered ice is bright white.

Figure 2.1 shows the extent of sea ice in March and September 2012 for the Arctic and Antarctic. March is the month of maximum ice extent in the Arctic and minimum extent in the Antarctic, while September is the opposite. Examining data from 1979 to 2013, in winter the Arctic sea ice fills the entire basin and extends down into the peripheral seas and Hudson Bay covering an average maximum of 15.5 million km^2. By the end of summer the ice extent falls to an average of about 6.4 million km^2 and covers only part of the central Arctic. In the Antarctic, the maximum sea ice extent in September shows an annulus around the continent covering an average maximum of 19.0 million km^2. By the end of summer (in March) the ice extent averages only about 2.9 million km^2, with the largest amount of ice found near the Palmer Peninsula.

There are strong contrasts between the Arctic and Antarctic. First there is the striking difference in geography; the Arctic is an ocean surrounded by land and the Antarctic is land surrounded by ocean. This fundamental geographical difference impacts many of the

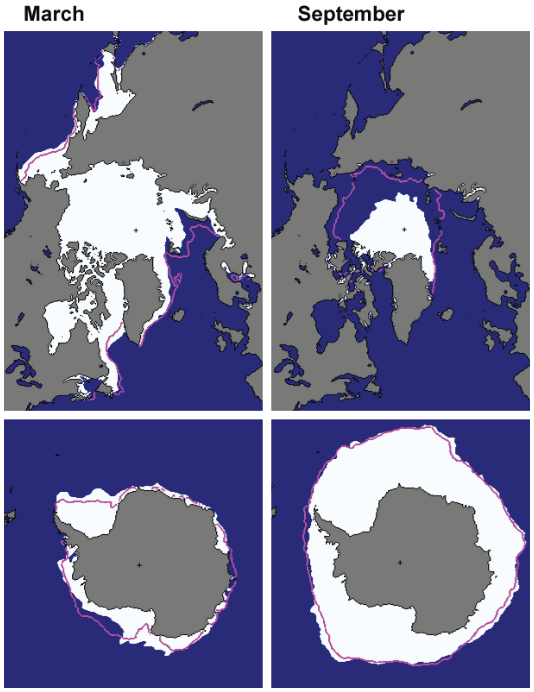

Figure 2.1 Extent of sea ice in the Arctic and Antarctic in March and September 2012 (the months of maximum and minimum sea ice extents).

properties of the Arctic and Antarctic ice cover. For example, in the closed basin of the Arctic, the ocean heat flux is smaller than in the open ocean Antarctic, and the ice thickness is greater. The surrounding land masses limit the maximum area covered by ice in the winter Arctic, while the temperature of the ocean is the primary constraint in the Antarctic. Arctic sea ice receives little snowfall, in contrast to the Antarctic where there is so much snow that, in some places, the ice surface is flooded with sea water. The sea water infiltrates the snow and freezes forming snow–ice. During summer, melt ponds are common in the Arctic, but are rare in the Antarctic. According to Andreas and Ackley (1982), this may be caused by lower relative humidity and stronger winds in the region, causing enhanced turbulent heat losses. Such conditions make it less likely for surface melting to occur since air temperature would rarely rise much above 0°C (Tucker et al. 1992).

There are the many difficulties that must be surmounted to effectively conduct optical remote sensing in polar oceans. In this chapter we address the environmental conditions of sun, clouds, and ice conditions in the polar ocean and examine the impact of low sun angles, cloudy skies, and highly variable surface conditions. We follow the spectral distribution of solar radiation from the top of the atmosphere to the top of the water column. Section 2.2 discusses solar elevation in the polar regions and spectral absorption due to ozone, water, pure ice, and chlorophyll. Cloud optical properties and the seasonality of the arctic cloud cover are discussed in Section 2.3. In Section 2.4 sea ice optical properties, the seasonal evolution of sea ice, and the spectral albedo of sea ice are presented. In addition, remote sensing techniques used to determine sea ice extent, ice type, and ice thickness are explored and the seasonal and interannual variability in the ice cover are presented. Finally, in Section 2.5 the radiative transfer equation is applied to model upward and downward spectral irradiances at the top of the atmosphere, just above the ocean surface, and just below the ocean surface.

2.2 Sun

2.2.1 Solar elevation in polar regions

North of the Arctic Circle (66.56°N) the Sun is above (boreal summer) or below (boreal winter) the horizon for 24 hours at least once per year. Similarly, south of the Antarctic Circle (66.56°S) the Sun is above (austral summer) or below (austral winter) the horizon for 24 hours at least once per year. Thus, the polar regions are characterized by a sparsity of sunlight in winter, and an abundance of sunlight in summer. During summer, the solar elevation is low implying that the proportion of diffuse (scattered) light is larger than at latitudes closer to the equator. For much of the year ice is predominant, both in the air (ice clouds, diamond dust, and snow) and on the surface, resulting from the lack of sunlight in winter and the low solar elevations during summer. Ice and snow scatter, transmit, and absorb solar and thermal infrared energy differently from liquid water. As a consequence, the annual average radiative energy input is negative at high latitudes; more energy is radiated to space than is received from the Sun. The cold temperatures lead to extremely dry atmospheric conditions that strongly impact the surface and near-surface radiative cooling in the 16 – 33 micron wavelength region of the thermal infrared part of the spectrum. Also, when sunlight is scarce or absent, very strong, persistent surface temperature inversions develop that influence atmospheric processes, cloud formation, evolution, and dissipation. It is generally believed that boundary layer stratus clouds lead to cooling (the albedo effect dominates over the infrared cloud greenhouse effect) whereas the opposite situation seems to prevail for high clouds (cirrus). Finally, the cloud–radiation feedback is further complicated by the presence of high-albedo snow–ice surfaces, and the scarcity of sunshine through the long winter. This circumstance leads to reversal of the feedback for low clouds (warming rather than cooling) except for about one month, around summer solstice, when the sun is higher and the albedo is lower than during the rest of the year. As discussed by Stamnes et al. (1999) it is important to keep in mind that the ice-albedo and the cloud-radiation feedbacks seem to be inextricably linked to one another so that studying one in isolation from the other may lead to misleading conclusions.

2.2.2 Spectral incidence, UV, and PAR

In this section we will examine the incident spectral solar irradiance from the top of the atmosphere to the water column. The solar spectrum consists of shortwave radiation including ultraviolet (UV) radiation (290 nm $< \lambda <$ 400 nm), photosynthetically active radiation (PAR) or visible light (400 nm $< \lambda <$ 700 nm), and near-infrared (near-IR) radiation (700 nm $< \lambda <$ 3,500 nm), where λ is the wavelength of light. The spectrum emitted by the Earth, also called the terrestrial radiation, consists of longwave, thermal infrared radiation with wavelengths from about 3,500 nm to 20,000 nm.

There is little overlap between the shortwave spectrum of the Sun and the long wave spectrum of the Earth. The dominant shortwave interaction is in the UV spectral range below 300 nm where sunlight is absorbed by ozone in the middle atmosphere and never reaches the surface. Hence ozone provides an effective shield against UV radiation from the Sun. The most harmful UV radiation reaching the Earth's surface lies in the spectral range between 280 nm and 320 nm, referred to as UV-B, while UV-A radiation at wavelengths between 320 and 400 nm is little affected by ozone (see ozone cross section in Figure 2.2a).

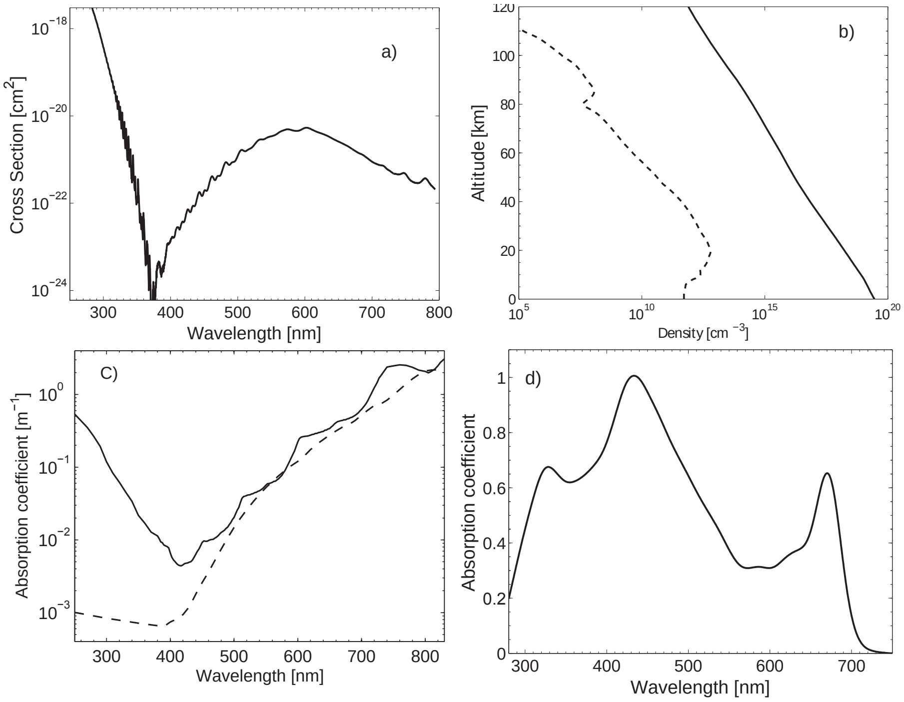

Figure 2.2 a) Absorption cross section of ozone at 261 K (Voigt et al. 2001). b) Number density of atmospheric ozone (dashed line) and total air number density (solid line). c) Absorption spectrum for pure ice (dashed line), (Grenfell and Perovich 1981; Perovich and Govoni 1991; Ackermann et al. 2006; using data from `http://www.atmos.washington.edu/ice_optical_constants/`, Warren and Brandt 2008), and for pure water (solid line — Smith and Baker 1981; Pope and Fry 1997; Sogandares and Fry 1997). d) Chlorophyll-specific absorption spectrum of some natural seawater normalized at 440 nm (Credit: Figure prepared by B. Hamre).

Figure 2.2b shows the number density of air, which decreases exponentially with height according to the barometric law, as well as the number density of ozone, which does not obey the barometric law because it is created and destroyed by photochemical reactions. The bulk air density determines light scattering by atmospheric molecules, while absorption is due to a variety of trace gases of which ozone and water vapor are the most important ones. For light penetration into water and ice the absorption coefficients, shown in Figure 2.2c, are needed (the optical properties of ice including scattering by ice inclusions are discussed in

Section 2.4.1). Finally, in addition to scattering and absorption by water molecules, water impurities have a large impact on light penetration. In open ocean water, the scattering and absorption properties of these impurities are often parameterized in terms of the chlorophyll concentration; the chlorophyll-specific absorption coefficient is shown in Figure 2.2d.

2.3 Clouds

Clouds have a strong nonlinear influence on the surface energy budget in the Arctic (Tsay et al. 1989; Curry and Ebert 1992; Schweiger and Key 1994; Walsh and Chapman 1998; Intrieri et al. 2002; Sandvik et al. 2007) including the timing of the onset of snowmelt (Zhang et al. 1997). The relatively thin boundary layer clouds that are prolific in spring through fall in the Arctic transmit sunlight (shortwave) and absorb thermal radiation (longwave) (Lawson et al. 2001; Intrieri et al. 2002; Zuidema et al. 2004; Lawson and Zuidema 2009). The greenhouse effect produced by this thin cloud cover accelerates melting and increases the amount of open water, which absorbs more incoming sunlight than ice surfaces, setting up a positive feedback process that leads to more melting and warming near the surface (Perovich et al. 2008; Bennartz et al. 2013).

Clouds have also been observed to play a major role in sea ice loss (Kay and Gettelman 2009), but identifying the reason is a challenge because the sea ice decline over the last 30 years can be attributed to an energy surplus of just 1 W m^{-2} (Kwok and Untersteiner 2011). Mixed-phase clouds (MPCs), consisting of super-cooled liquid droplets and ice crystals, have been found to cover large areas in the Arctic (Shupe 2011). MPCs tend to consist of stratiform layers of super-cooled liquid water from which ice crystals form and precipitate (Curry et al. 1997; Rangno and Hobbs 2001; Shupe et al. 2006; Verlinde et al. 2007; de Boer et al. 2009; Sikand et al. 2010; Lawson et al. 2011). Even though a mixture of super-cooled droplets and ice is microphysically unstable because ice will grow at the expense of liquid water (Morrison et al. 2012), MPCs can be very persistent and often last for several days. The solar radiation field in a cloudy atmosphere is strongly influenced by scattering and absorption by cloud particles as well as by the albedo of the underlying surface.

2.3.1 Cloud optical properties

Correct treatment of the interaction of radiation with liquid water, ice, and mixed-phase clouds is important for the proper performance of climate models as well as for proper interpretation of remote sensing observations of clouds. For warm clouds consisting of spherical liquid water droplets, one may use Lorentz-Mie theory (applicable to light scattering by a dielectric sphere) to compute scattering and absorption coefficients as well as the scattering phase function for a specified size distribution of water droplets, and the known refractive index of water. Such computations require a significant amount of computing time, but fast parameterizations are available in terms of mean particle size (e.g., Hu and Stamnes 1993) which are suitable for estimating irradiances and cloud radiative forcing defined as the difference between the net irradiance in the presence of, and without, clouds.

For ice particles one must also take into account the shape of the particles, which makes the computational effort much more challenging. Thus, to quantify the radiative properties of ice clouds, in addition to the cloud particle size distribution, horizontal extent, and vertical structure, one also needs information about ice particle shape and composition (inclusions). Several investigators have attempted to parameterize the optical properties of ice clouds suitable for use in climate models (Heymsfield and Platt 1984; Sassen et al. 1995; Fu 1996; Mitchell et al. 1996a,b; Fu et al. 1998; Key et al. 2002). Despite differences in detail, existing parameterizations of ice particles in climate models have been found to yield satisfactory results for given size and shape distributions of particles (Edwards et al. 2007). To investigate the importance of particle shape, Kahnert et al. (2008) used four different non-spherical particle models to compute ice cloud optical properties and to simulate irradiances and cloud radiative forcing. They found that differences in cloud radiative forcing, downward irradiance at the surface, and absorbed irradiance in the atmosphere resulting from the use of the four different ice cloud particle models were comparable to differences in these quantities resulting from changing the surface albedo from 0.4 to 0.8, or by varying the ice water content by a factor of 2. Thus, use of a suitable non-spherical ice cloud particle model appears to be important for a realistic assessment of the radiative impact of ice clouds.

2.3.2 Cloud cover seasonality

One of the basic cloud parameters that can be derived from satellite data is the cloud fraction, which is defined as the fraction of the time that there is cloud in a certain area over a specified period. Cloud fraction is important because it provides information about the persistence and horizontal distribution of clouds that control the availability of solar energy and hence the physical and biological property and productivity of the surface. Studies of cloud fraction have been carried out using NOAA/AVHRR data (e.g., Yamonouchi et al. 1987; Schweiger and Key 1994; Wang and Key 2005). Some problems associated with the use of AVHRR data for cloud studies have been cited by Simpson and Keller (1995) and Comiso (2010). These problems include the lack of an adequate number of channels required for cloud detection, noise contamination in the 3.7 μm channel data at low temperatures, and for the polar regions, the similarity of the signatures of clouds and snow covered regions.

The ability to characterize clouds improved considerably with advent of MODIS which has 36 channels, a few of which are suitable for cloud detection. Data from MODIS (and similar sensors like ENVISAT/MERIS) currently provide the most comprehensive data on cloud cover. Using MODIS data in 2007, month-to-month changes in the Arctic cloud cover fraction over sea ice and ice free oceans for the period from April to September are illustrated in Figure 2.3. This is the period when sea ice is retreating, and the Arctic region has ample sunlight and is most productive. The areas with the least cloud cover (blue) are usually located in the sea ice covered Arctic basin but the location of such areas shifts from one month to another. The ice free (open) regions near the ice edge in the Pacific and Atlantic Oceans are shown to have the highest cloud fraction (reds and oranges) with values as high as 100%. The high cloud fraction indicates a very persistent cloud cover in the open ocean even with the use of the MODIS data

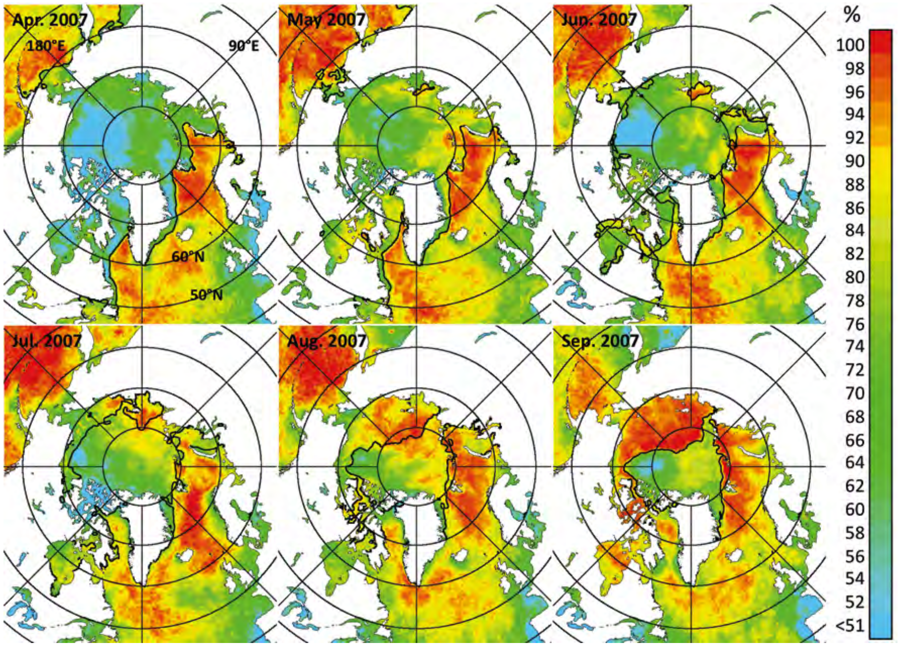

Figure 2.3 Colour-coded monthly cloud fraction in the Arctic in April to September, 2007. The sea-ice extent is also presented (solid black lines).

set that is regarded as "probably clear" compared to that classified as "confident clear". These two data sets provide very similar values over sea ice but the "probably clear" version provides significantly less and more realistic cloud cover data over ice free regions. The high cloud fraction areas in April are confined near the ice edges while medium or lower cloud fractions are observed in sea ice covered areas in the Arctic Basin, Hudson Bay and Baffin Bay, as well as the coastal areas in Europe. In May there are more clouds in the Arctic Basin and in the peripheral seas than the previous month, but not always. The retreat of sea ice in July and August is accompanied by higher cloud fractions in the Arctic Basin, especially in August when high cloud fractions are apparent even in sea ice covered areas. In September, clouds over sea ice start to recede but among the highest cloud fraction are ice free areas in the Arctic Basin. It is apparent that clouds are important factors affecting the productivity of the region. It also affects the ability to obtain consistent spatial coverage from satellite ocean colour data that are used to estimate primary productivity. The data presented is just for 2007 but similar characteristics of the cloud cover were inferred from 2010 data.

The spatial distribution of clouds in the Antarctic is quite different from that of the Arctic mainly because of the large difference in the geographical location of land areas as mentioned earlier. Monthly cloud fractions in the region during the retreat of the sea ice cover from October to March 2007 are presented in Figure 2.4, where it can be seen that the seasonality is also heavily influenced by the distribution of the sea ice cover. The cloud fraction is again high in open ocean areas, but in sea ice covered regions the fractions are relatively higher than those in the Arctic. Cloud cover over sea ice increased progressively from October to

December when ice starts breaking up and retreating rapidly, with little change from January to February, when a large fraction of the ice cover has melted. It becomes less cloudy in March as the surface becomes colder and the atmosphere more dry. During the entire six month period, the ice free ocean south of 50°S is persistently cloud covered (88% – 98% cloud cover). Again, this has to be taken into consideration in the estimate of primary productivity.

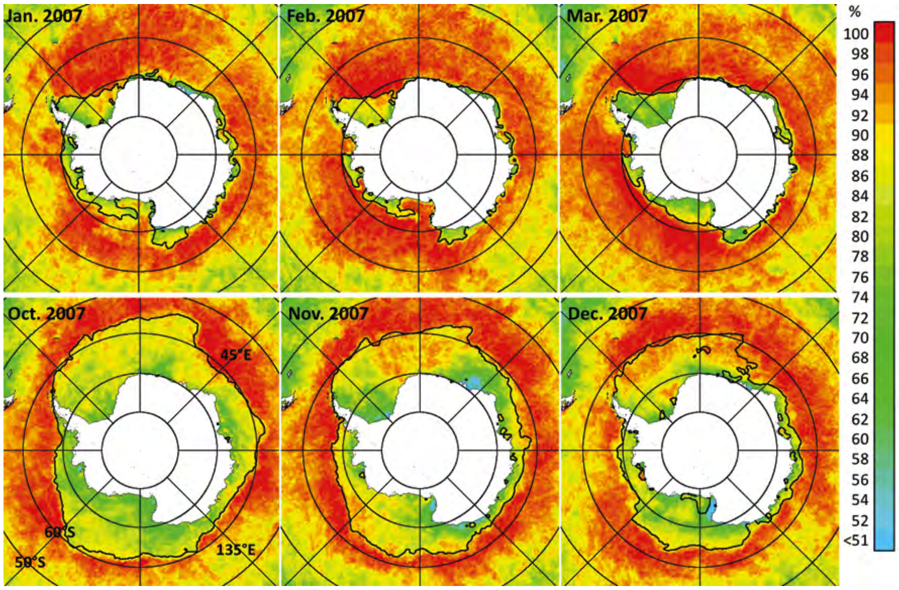

Figure 2.4 Colour-coded monthly cloud fraction in the Antarctic in January to March and October to December, 2007. The sea-ice extent is also presented (solid black lines).

The MODIS cloud data provide spatially detailed information about the global cloud cover at a good temporal resolution. The cloud masking technique used to generate the standard cloud product is usually effective, but there is room for improving the accuracy of the current data set, especially in the ice free ocean regions. Through studies of concurrent A-Train observations from MODIS, CALIPSO and CloudSat, it has been shown that there are cases when the current technique is not able to identify some cloud types, especially optically thin and low clouds (Chan and Comiso 2013). The same study also shows that sometimes, areas with significant aerosol are misidentified as cloud covered areas. Improvements in the technique are thus desirable for optimal accuracy. One promising technique is a Neural Network based algorithm that makes use of CALIPSO and CloudSat data as the training data sets (Chan and Comiso, unpublished data). The technique has been shown to be effective in identifying clouds that are usually missed by the current standard technique. Another promising technique is the dynamic threshold method based on comprehensive radiative transfer simulations, which was shown by Chen et al. (2014) to be superior to the MODIS cloud mask in terms of accuracy over snow covered areas. Interannual variability and trend studies also need a longer time series than is currently available from MODIS. Improvements in the technique used for AVHRR data using enhanced MODIS data as the baseline during the period of overlapping coverage (2002 – present), would add more than three decades of satellite data that could be used for meaningful assessments of the interannual variability and trends in polar cloud cover.

2.4 Ice

2.4.1 Optical properties of the ice cover

Sea ice is a complex material consisting of an ice matrix with inclusions of liquid brine and air bubbles (Weeks and Ackley 1982). At cold temperatures, solid salts form in the brine inclusions. There may also be ice biota, sediments, and black carbon in the ice, or on the surface of the ice. This complex physical structure results in complex optical properties.

Light reflection from sea ice is governed by both scattering and absorption. The spectral shape of reflected and transmitted light is determined by absorption. Figure 2.2 shows that the absorption of pure, bubble free ice has a strong wavelength dependence, with absorption coefficients ranging by more than 5 orders of magnitude (Grenfell and Perovich 1981; Perovich and Govoni 1991; Ackermann et al. 2006; Warren and Brandt 2008). E-folding lengths are more than one kilometer in the blue portion of the spectrum and only a few meters in the red.

As sea ice forms, most salt is rejected from the growing ice matrix. However, some brine and air are trapped forming brine pockets and air bubbles. The large number of brine inclusions and air bubbles makes sea ice a highly scattering medium at visible and near infrared wavelengths. Because the scatterers are much larger than the wavelength, diffraction and interference can be neglected (Bohren and Huffman 1983; Grenfell 1983). Also the index of refraction of ice is a weak function of wavelength over the spectral region of interest. Thus scattering coefficients and phase functions of sea ice are often assumed to be constant with wavelength (Grenfell 1983; Light et al. 2003). Changes in the magnitude in sea ice albedo and transmittance are due to differences in scattering, with more scattering resulting in larger albedo and smaller transmittance.

2.4.2 Ice types and evolution

During initial growth, sea ice cover can form rapidly over open water (Figure 2.5a). First, the new ice consists of randomly oriented small ice grains called frazil ice that accumulate at the surface to form grease ice. This solidifies to form a thin layer of ice called nilas* (Figure 2.5b), which in turn becomes young ice as the ice thickens to about 15 to 30 cm (Figure 2.5c). Under quiescent growth conditions the ice growth shifts to a more orderly columnar form. In the presence of wind and waves, pancake ice (Figure 2.5d) can form. Under cold conditions ($< -20^\circ$C) this entire process can occur in only a few days. Frost flowers often form on the ice surface during the initial growth phase (Perovich and Richter-Menge 1994). As the ice thickens, it is able to support a snow cover and becomes first year ice, which is the most dominant sea ice cover.

There are large changes in spectral albedo during ice formation as illustrated in Figure 2.6 (Allison et al. 1993). The open water albedo is small (about 0.07) and shows little spectral

---

*Nilas: a thin, continuous elastic sheet of sea ice up to 0.1 m thick.

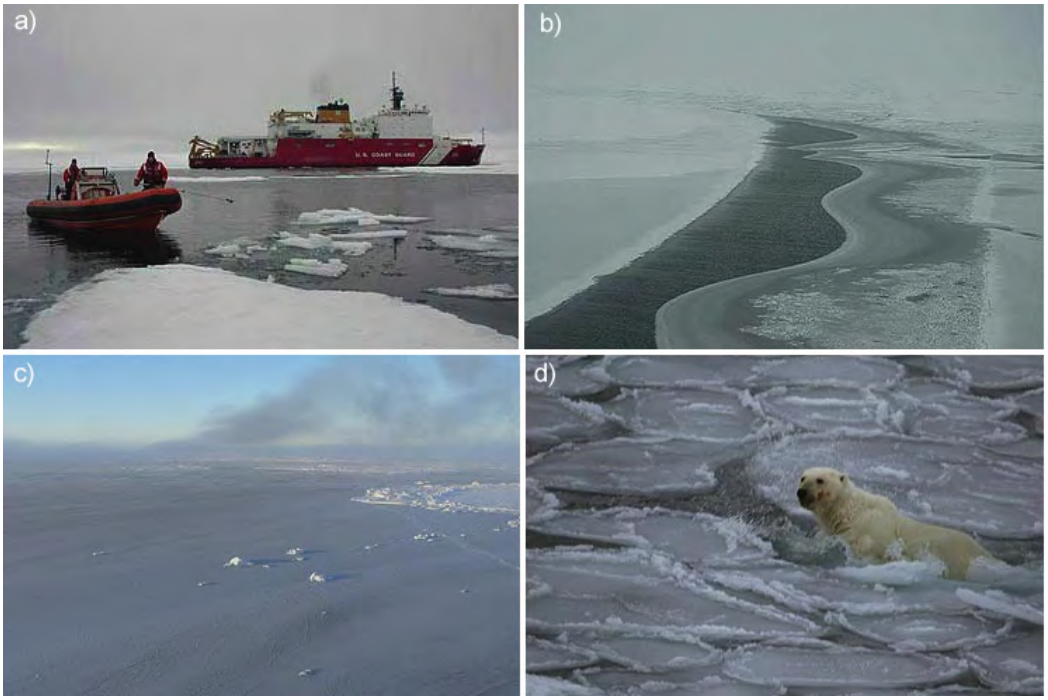

Figure 2.5 Photographs taken in the Arctic showing the initial growth of sea ice for (a) open water; (b) frazil ice and nilas; (c) young ice, and (d) pancake ice (Credit: D. Perovich).

variability because it is governed primarily by Fresnel reflection by the air-water interface. As the ice grows thicker, the albedo increases at all wavelengths, with the largest increases between 450 and 600 nm. The increase is due to enhanced multiple scattering in the thicker ice. More scattering results in longer pathlengths and an increased contribution from the spectral dependence of absorption. There is a large increase in albedo when an optically thick snow layer is present (red curve).

Even after the initial growth phase there are still large spatial and temporal variations in sea ice surface conditions, reflectance, and albedo. Figure 2.7 shows ice surface conditions in early spring and mid-summer. In spring, the surface is a mix of snow-covered ice and open water. The contrast in albedo is extreme at visible wavelengths from 0.98 for snow to less than 0.10 for water. In mid-summer there is much more variability in surface conditions and in albedo. In addition to bare ice and open water, there is a wide variety of melt ponds. As Figure 2.7 shows, ponds range from dark (item 7) to turquoise (item 6), to light blue (item 5). Ponds are areas where melt waters collects on top of the ice, reaching depths of a few centimeters to 0.5 m (Perovich et al. 2002; Polashenski et al. 2012). The differences in pond appearance are due to the properties of the underlying ice. Dark ponds typically have thinner ice, while lighter ponds have thicker ice with more scatterers. In many cases, pond albedos decrease during the melt season as the underlying ice thins.

Spectral albedos for different sea ice conditions are plotted in Figure 2.8. The highest albedos are for sea ice covered by cold, dry snow. Due to the large number of air-ice interfaces,

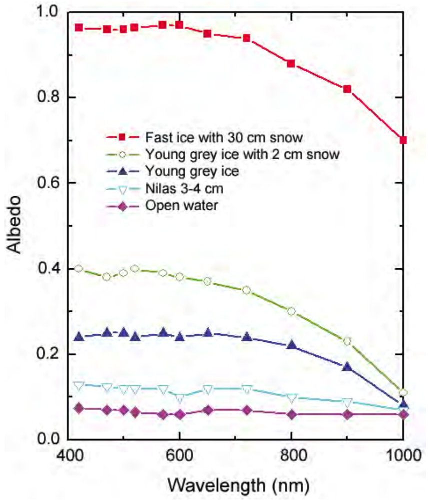

Figure 2.6 Spectral albedos of young growing Antarctic sea ice (after Allison et al. 1993).

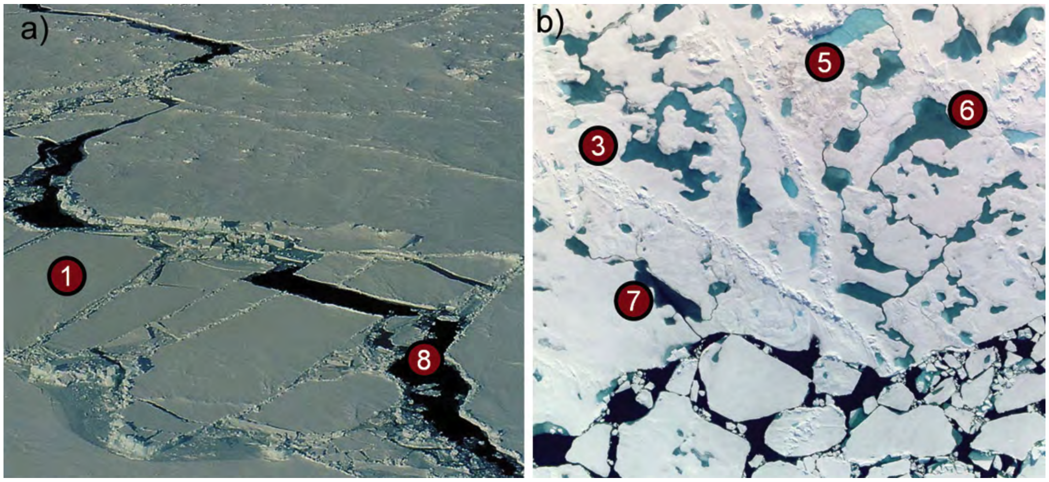

Figure 2.7 Photographs showing different ice surface conditions in spring (a), and mid-summer (b). Sites shown are 1) cold snow covered ice, 3) melting multi-year bare ice, 5) light blue melt pond, 6) medium blue melt pond, 7) dark melt pond, and 8) an open lead (Credit: D. Perovich).

snow is highly scattering, resulting in a large albedo. As the snow melts, scattering decreases and the albedo drops. Bare ice albedos are less than for snow, but still large (greater than 0.7) in the visible (Grenfell and Maykut 1977; Perovich et al. 2002). This is due to the presence of a surface scattering layer composed of deteriorated ice. This layer is usually a few centimeters thick. The albedo of bare melting multi-year ice is slightly greater than first year ice due to a thicker surface scattering layer and more scattering in the upper portion of the ice (Light et al. 2008). There are large differences in melt pond albedos in the visible, as discussed earlier. The light blue pond (item 5) in Figure 2.7 has a larger albedo than the other ponds, with a peak value at 470 nm (blue colour). Because of absorption in the pond water, near infrared pond albedos are small and the same as open water (less than 0.1).

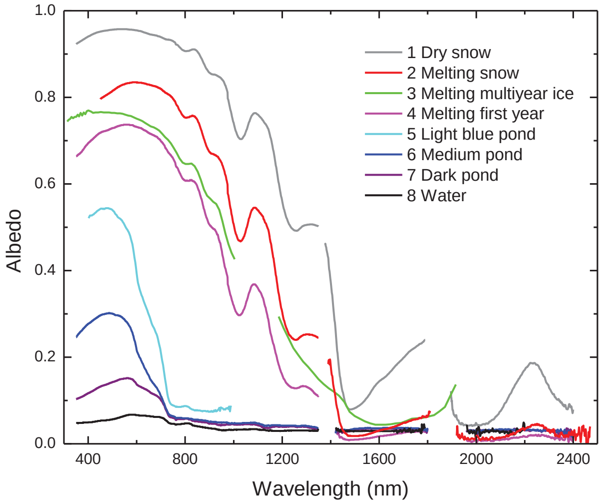

Figure 2.8 Spectral albedos of different sea ice surface conditions in spring and mid-summer. Results for 1) cold snow covered ice, 2) melting snow on sea ice, 3) melting multi-year bare ice, 4) melting first year bare ice, 5) light blue melt pond, 6) medium blue melt pond, 7) dark melt pond, and 8) an open lead. Measurements were made in the Arctic.

2.4.3 Snow on ice

Snow is highly scattering and its presence greatly increases the albedo of sea ice (Warren 1982). Figure 2.9 shows albedo as a function of snow depth for selected wavelengths in the visible and near-infrared (Perovich 2007). The results are from an experiment where new snow fell on a black base that had an albedo of about 0.15. The snow was a mix of dendrites and rounded grains roughly 1 mm in size and the density was 160 kg m^{-3}. There is a rapid asymptotic increase in albedo with snow depth at all wavelengths. Depending on wavelength, the snow cover was optically thick between depths of 8 to 12 cm.

Snow is pervasive over both the Arctic and Antarctic sea ice for much of the year (Massom et al. 2001; Sturm et al. 2002). Observations show that from fall to summer melt, over 90% of the ice cover has an optically thick snow layer. This snow cover determines the albedo and reflectance of the surface. A key issue for Arctic sea ice is how will the ongoing shift from perennial to seasonal ice impact the snow cover. With sea ice forming later in the fall, less snow may be accumulating on seasonal ice than on perennial ice. This is a topic of current research.

2.4.4 Remote sensing of sea ice

The large scale characteristics of the global sea ice cover were not known until the advent of satellite passive microwave sensors. The robust capabilities (day/night observing, almost all weather conditions) and the large contrast of the emissivity of sea ice and that of ice free water

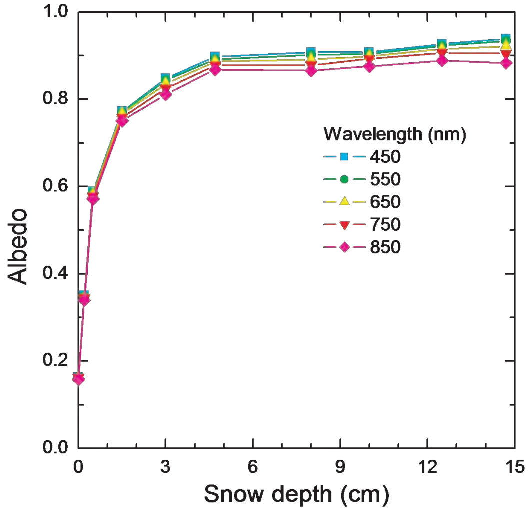

Figure 2.9 Impact of snow depth on albedo measured at five wavelengths. The snow fell on a black base. Measurements were made on mid-latitude snow (after Perovich, 2007).

surfaces made these sensors ideal for monitoring the sea ice cover. Continuous and consistent coverage of global sea ice cover started with the launch of Nimbus-7 Scanning Multichannel Microwave Radiometer (SMMR) which provided good data from November 1978 up to August 1987 (Gloersen et al. 1992). Nimbus-7 also carried the first ocean colour sensor called Coastal Zone Color Scanner (CZCS). The time series was continued by an operational satellite called DMSP/Special Scanning Microwave Imager (SSM/I) which has been providing continuous data from July 1987 up to the present. In the meantime, more capable systems, like the Advanced Microwave Scanning Radiometer (AMSR-E), which was launched on board Aqua of the Earth Observing System (EOS), became available. AMSR-E provided higher resolution and more accurate brightness temperature data than SMMR or SSM/I from June 2002 to October 2011 and has since been succeeded by AMSR-2 which was launched on board the JAXA/GCOM-W satellite in May 2012.

Because of relatively coarse resolution (i.e., 10 – 30 km), passive microwave data have some limitations in mesoscale studies of the sea ice cover. Although the fraction of open water within each data element (pixel) can be estimated from passive microwave data, the character of the ice cover changes significantly from the ice edge into the consolidated ice pack. The character also changes with the occurrences of strong storm, polar lows and tides, and the formation of polynyas[†] and the Odden[‡]. Some important features of the ice cover like ridges, leads, meltponds and polynyas, which have dimensions of a few meters to several meters, are difficult to study with current passive microwave systems. Several high-resolution systems are available but the coverage is not global and is usually sparse and temporally discontinuous in part because of limitations in the acquisition of highly dense data. The

---

[†] Polynya: an area of open water surrounded by ice, in a location where sea ice would be expected.

[‡] Odden: a tongue of sea ice that sometimes forms during winter. It is located east of the main boundary of the sea ice cover east of Greenland between 72 and 74° N.

preferred system for mesoscale studies has been the Synthetic Aperture Radar (SAR) which provides day/night and all weather coverage at a resolution of about 30 m. The first satellite system was the SAR on board SeaSat which was launched in July 1978, and although the satellite lasted only for 3 months, it provided insights into the great potential of the sensor for sea ice studies. Similar systems have been launched by ESA, JAXA and Canada since the 1990s and in the last decade, the technology has advanced to allow the imaging of the Earth's surface at a resolution of 1m, as with the German System called Terra-SAR-X. Despite the high resolution, the interpretation of SAR data has not always been easy or reliable because of so many surface types. Concurrent measurements with visible and infrared systems have been used for optimum interpretation. Data from several visible systems are available, but the coverage is again sparse and, in addition, the scenes that are cloud free are difficult to find. The visible sensors that have been used most frequently are Landsat which has 7 channels and a resolution of 30 m (15m for the panchromatic) and SPOT which has even better resolution and more flexibility in the acquisition but less polar coverage. Landsat data has been available since 1972 while SPOT data started to become available in the 1980s. Cloud free data from these sensors have provided the most striking information about the distribution and spatial surface characteristics of the sea ice cover. Some studies can take advantage of MODIS 250 m resolution data in the visible which has been providing continuous global coverage since 2000.

2.4.5 Variability and trends in sea ice

2.4.5.1 Sea ice concentration, ice extent, and ice area

With more than three decades of continuous passive microwave observations of the polar regions, it has become possible to make accurate assessments of the daily, seasonal and interannual variations in the sea ice cover. The basic parameter that is derived from passive microwave data is sea ice concentration, which is the percentage of the area within the field-of-view of the satellite sensor that is covered by sea ice. Several algorithms have been developed to estimate sea ice concentration and the most recent ones have been shown to provide very similar results (Comiso and Parkinson 2008; Parkinson and Comiso 2008) using AMSR-E data. The results presented in this report make use of the Bootstrap algorithm as described by Comiso and Nishio (2008). Daily ice concentration maps have been generated from passive microwave data and used to generate monthly and yearly ice concentration maps that are used to study large-scale changes in the ice cover. To illustrate how the sea ice cover has been changing on a seasonal basis, trend analysis was done on each data element of the maps using the time series ice concentration data from November 1978 to the 2012 and the results are presented in Figure 2.10a, b, c and d. The trend maps show large spatial variations in the trends in each of the four seasons with the most significant trends occurring near the ice edges. The trends are mainly negative, indicating a general retreat of the ice cover during the 34 year period with some slightly positive values in some areas, like the Bering Sea. In the winter, declines in ice cover are largest and most apparent in the Barents Sea area while in the summer, the declines are mainly concentrated in the Beaufort/Chukchi seas area.

The parameters that are usually used for quantitative studies of the sea ice cover are:

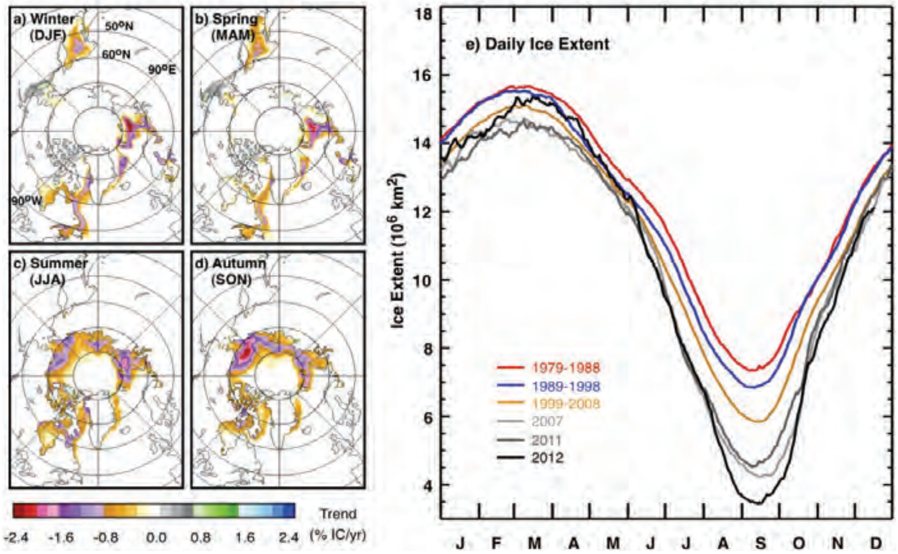

Figure 2.10 Trends in ice concentration in (a) winter, (b) spring, (c) summer and (d) autumn in the Northern Hemisphere. (e) Daily averages of ice extents from January to December during the decades 1979 – 1988 (red), 1989 – 1998 (blue), and 1999 – 2008 (gold), and for each year in 2007, 2011 and 2012.

sea ice extent, which has been defined as the integral sum of ice covered areas with ice concentration of more than 15%, and sea ice area which is simply the area actually covered by sea ice estimated by taking the integral sum of the product of the area of each data element and the ice concentration estimated within the area. Ice extent thus provides information about how extensive the ice cover is and how far into the lower latitudes it may develop during each time period. Ice area provides the means to estimate the volume of the ice cover, if the average thickness of the ice is known.

The sea ice cover is the most seasonal parameter on the surface of the Earth (second only to the snow cover). In the Arctic, the seasonality of the sea ice extent for different decades is illustrated in Figure 2.10e. During the first two decades of satellite data (e.g., 1979 – 1988 and 1989 – 1998), the seasonality was basically stable with the annual cycle in the ice extent changing from about 7.3×10^6 km^2 in the summer to about 15.6×10^6 km^2 in the winter. The ice extent was apparently about half a million km^2 lower during the summer in the second decade when compared with the first, but there was very little change in the winter. During the third decade (1999 – 2008), the extent was lower than the previous decade by about a million km^2 in the summer and by about half a million km^2 during the winter. The average, shown in gold, includes that of 2007 (gray line) which was reported to be abnormally low in the summer (Comiso et al. 2008; Cavalieri and Parkinson 2012; Stroeve et al. 2012). Figure 2.10e also shows plots of single year data during the years when the three lowest summer minima occurred (i.e., 2007, 2011, and 2012). It is apparent that the ice extent during these 3 years was considerably lower than that of the decadal averages, with 2012 values (bold black line) even considerably lower than the 2007 values.

To evaluate the interannual changes in the ice cover quantitatively, plots of monthly anomalies of sea ice extent in the two hemispheres are presented in Figure 2.11. The monthly anomalies are derived by subtracting climatological averages (using the November 1978 to 2012 monthly data) from each month to identify monthly averages that are abnormal, and to assess trends in the ice cover. In the Northern Hemisphere, the time series shows an enhanced value in 1996 for ice extent and ice area (not shown) reflecting the abnormally high ice cover in summer of that year. This was followed by a steady decline and large interannual variability after the anomalously low summer ice cover in 2007. The large variability is caused mainly by persistently low values at the end of summer while the winter values tend to be similar to those of pre-2007 level. Trend analysis using linear regression indicates that the sea ice extent has been declining at the rate of $-480,000\pm$ 21,000 km^2 (or -3.8%) per decade. For comparison, the trend in ice area (not shown) is $-527,000\pm$ 20,000 km^2 (or -4.5%) per decade. The errors indicated are statistical error of the slopes of the trend line and do not reflect systematic errors that may be associated with other factors like differences in instrument calibration, resolution and incident angle between SMMR and SSM/I. The September 2012 anomaly stands out as being the most negative during the satellite era, suggesting continuation of the acceleration in the decline of the Arctic sea ice cover (Comiso et al. 2008; Parkinson and Comiso 2013). The difference in the trends in ice area compared to ice extent is, in part, due to the trend in ice concentration, which has been declining (not shown) at about -1% per decade.

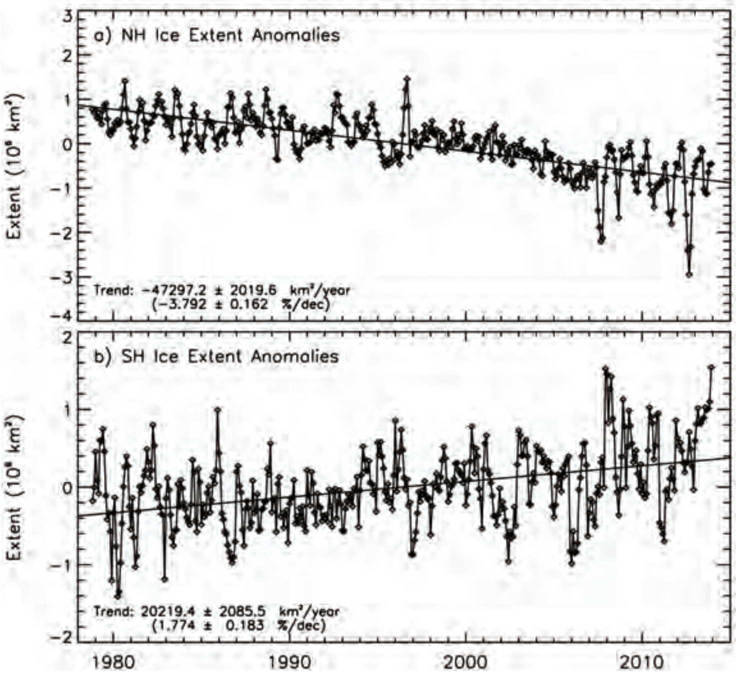

Figure 2.11 Monthly ice extent anomalies in (a) Norther Hemisphere (NH) and (b) Southern Hemisphere (SH). Linear regressions are presented and the trend results (km^2 per year and percentage per decade) are provided.

A surprising asymmetry in the trends of the Arctic and the Antarctic sea ice cover has been reported (Cavalieri et al. 1997; Comiso and Nishio 2008), and it is apparent that such trend differences continue to the present. Seasonal trend maps for the Antarctic, similar to those shown for the Arctic, are presented in Figure 2.12a, b, c and d. It is apparent that the seasonal trends are predominantly more positive than those in the Arctic. In the Antarctic, the trend maps for each season also show the characteristic alternating advance and decline of sea ice along the ice edges around the continent that has been referred to as the Antarctic Circumpolar Wave by White and Peterson (1996). It is apparent that trends are strongly negative in the Bellingshausen/Amundsen Seas while they are strongly positive in the Ross Sea and other regions. This situation makes the interpretation of the trends in terms of climate change difficult, especially since the overall positive trend is caused by the larger extent of the Ross Sea ice cover than that of the Bellingshausen/Amundsen Sea. The positive trend in the extent of the Ross Sea ice cover has been observed to be mainly due to increased ice production at the coastal polynya regions (Martin et al. 2007; Comiso et al. 2011). It has been postulated through modelling studies that the ozone hole has caused a deepening of the lows in the Western Antarctic region causing stronger winds off the Ross Sea ice shelf and, therefore, more extensive coastal polynya regions and higher sea ice production (Turner et al. 2009).

In the Antarctic, the sea ice cover is even more seasonal than in the Arctic with the ice extent changing from 3×10^6 km^2 in the summer to almost 19×10^6 km^2 in the winter. The plots of decadal sea ice cover, as depicted in Figure 2.12e, show a relatively stable Antarctic sea ice cover with the averages for the three decades almost on top of each other all year round. However, it is evident that during the 1999 to 2008 decade, the extents are slightly higher than those of the previous years.

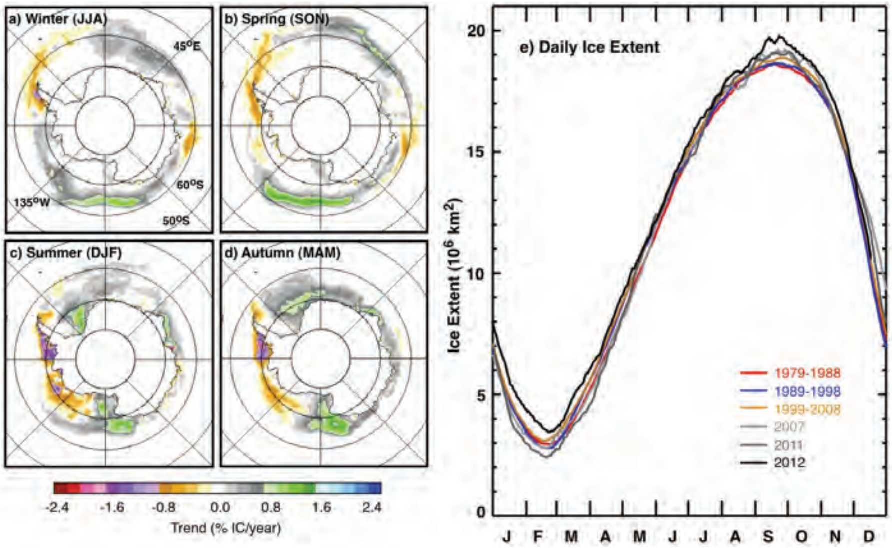

Figure 2.12 Trends in ice concentration in (a) winter, (b) spring, (c) summer and (d) autumn in the Southern Hemisphere. (e) Daily averages of ice extent from January to December during the decades: 1979 – 1988 (red), 1989 – 1998 (blue), 1999 – 2008 (gold), and for each year in 2007, 2011 and 2012.

The corresponding plot of monthly ice extent anomalies and trends in the Antarctic is presented in Figure 2.11b. Monthly ice extent displays large interannual fluctuations with a similar number of positive and negative anomalies, and a high positive value in 2008. Despite strong negative trends in the ice cover in the Bellingshausen/Amundsen Seas, as reported previously (Jacobs and Comiso 1993; Comiso et al. 2011), the overall trend is positive (Comiso et al. 2011; Parkinson and Cavalieri 2012). The overall trend in ice extent is estimated to be 174,720 km^2/decade (or 1.5 ± 0.2%/decade) while that of area (not shown) is 207,841 km^2/decade (or 2.2 ± 0.1% per decade). The error indicated is the statistical error of the slope of the trend line as indicated earlier for the Arctic. Again, the difference in the trends for ice area and ice extent is, in part, caused by the observed positive trend (0.7%/decade) in ice concentration (not shown).

2.4.5.2 Multi-year ice and age of the ice

The ice that survives the summer has been referred to as perennial ice. The ice cover during the summer minimum consists mainly of perennial ice, but because temperatures are already below freezing in parts of the ice pack during the period, there may be some contamination of new and young ice. However, the summer minimum and the perennial ice provide the same variabilities and trends, as discussed by Comiso (2002). The ice cover summer minimum has thus been used to characterize the perennial ice cover. The ice that survives at least two-summer seasons has been referred to as multi-year ice by WMO and others. This is the ice type that is retrieved from passive microwave data since it is almost free of brine and hence has the characteristic signature of fresh ice that is different from that of the saline seasonal or first year ice (Vant et al. 1978). The microwave signature of multi-year ice has also been observed to be different from that of second year ice by Tooma et al. (1975) and indirectly by Comiso (2006).

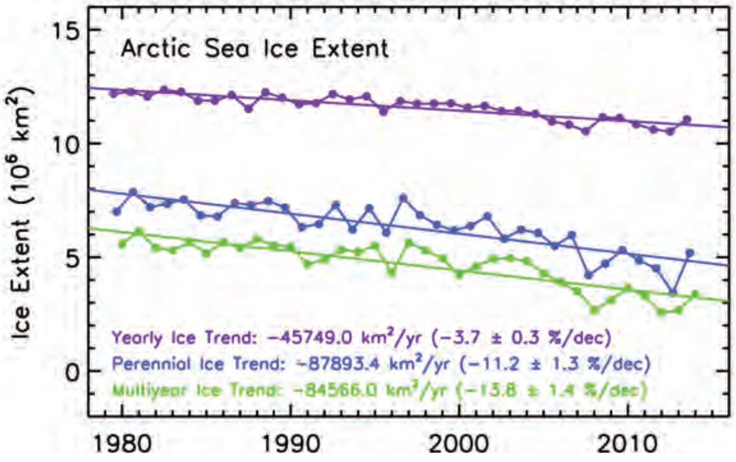

Figure 2.13 Plots of ice extents of yearly average (purple), perennial ice (blue) and multi-year ice (green) in the Arctic from 1980 to 2013.

Time series of the extent of the summer ice minimum (representing perennial ice) and multi-year ice (as derived from passive microwave using winter data) are presented in Figure 2.13. For comparison, the yearly averages (January to December) of the extent of the Arctic ice cover are also presented. The interannual variability for the perennial and multi-year ice are shown to be coherent with each other, but that of the annual averages is significantly different. This indicates that the seasonal ice has a different interannual variability than the thicker perennial and multi-year ice cover. The overall trends are also different with the trends in extent being −3.7, −11.2, and −13.8% per decade for the yearly averages of annual ice, perennial ice and multi-year ice, respectively. This data has been updated to 2013 to show a slight recovery in 2013 from the record low in 2012. Again, the slight negative trend in the annual ice cover suggests a positive trend in the seasonal ice cover because of the much more negative trend in the thicker perennial and multi-year ice cover. The trend is mostly negative for multi-year ice indicating that the thickest component of the ice cover is the type that is declining the most. This is consistent with the observed changes in the average age of the Arctic ice cover as inferred from ice drift data by Maslanik et al. (2007) and Maslanik et al. (2011). Note that multi-year ice shows more modest recovery in 2013 and less interannual variability than perennial ice.

2.4.6 Ice thickness

Much of the past information about the basin-wide distribution and changes in the thickness of the Arctic sea ice cover has come from measurements of the ice draft by submarine upward looking sonars (Wadhams 2006). The ice draft data is converted to ice thickness assuming that the density of the ice and the thickness of the snow cover are known. Because of sparse coverage over different regions of the ice cover during different time periods, the submarine sonar data are usually difficult to interpret, especially because the sea ice cover is dynamic. Some robust data sets, however, were collected in parts of the Arctic region in the 1990s and, when compared with data during the 1958 to 1977 period, the results show significant changes in thickness as reported by Rothrock et al. (1999). In this study, the thickness in the Eurasian Basin was observed to have declined by about −1.7 m during the two periods while a decline of −0.9 m was observed in the Canadian Basin. The general decline of sea ice thickness was also reported by Wadhams and Davis (2000) in the Lincoln Sea, Fram Strait and Greenland Sea region. The results are consistent with the general decline in the thick component of the sea ice cover as reported in the previous section.

Recent studies include the use of satellite measurements of the thickness of the freeboard of the ice to infer ice thickness, assuming that the density of the ice and the thickness of the snow cover are known. A study using ESA’s ERS and Envisat radar altimeter data indicates high interannual variability in ice thickness for the region south of 81°N during the period from 1993 to 2001, but no significant trends in the thickness were observed (Laxon et al. 2003). However, for the period from 2002 and 2008, a decrease of 0.25 m was observed in the Beaufort/Chukchi seas region (Giles et al. 2008) following the dramatic decline in the perennial ice cover in 2007 (Comiso et al. 2008). Studies using ICEsat lidar altimeter data from 2003 to 2008 also show thinning of about 0.6 m over areas south of 86°N covered by multi-year ice in spring (Laxon et al. 2003; Kwok et al. 2009).

2.5 Modelled Radiation Field

The purpose of this section is to illustrate how the radiation field can be computed given the inherent optical properties discussed above of the atmosphere. The lower boundary is open ocean, bare sea ice, or sea ice covered with snow or melt ponds. Although this system is three-dimensional due to fractional cloud cover and a heterogeneous lower boundary as illustrated in Fig. 2.7, it is useful to start with a one-dimensional model and combine results with and without cloud cover, melt ponds and snow cover to mimic the behavior of the real system.

Thus, for simplicity we may think of the atmosphere and underlying ocean (or sea ice with or without snow cover and melt ponds) as two vertically stratified, plane parallel, adjacent slabs with different refractive indices. To compute the radiation field in this coupled system in response to solar illumination as well as thermal emission, we must solve the radiative transfer equation (RTE):

$$\begin{aligned}\mu\frac{dI(\tau,\mu,\phi)}{d\tau} &= I(\tau,\mu,\phi) - S^*(\tau,\mu,\phi) - [1-\varpi(\tau)]B(T(\tau)) \\ &- \frac{\varpi(\tau)}{4\pi}\int_0^{2\pi} p(\tau,\mu',\phi';\mu,\phi)I(\tau,\mu',\phi')d\mu'. \end{aligned} \tag{2.1}$$

Here $I(\tau,\mu,\phi)$ is the diffuse radiance distribution, τ is the optical depth, μ is the cosine of the polar angle θ, ϕ is the azimuth angle, $p(\tau,\mu',\phi';\mu,\phi)$ is the scattering phase function, $B(T(\tau))$ is the Planck function, and T is the temperature. The differential vertical optical depth is $d\tau(z) = -[\alpha(\tau)+\sigma(\tau)]dz$, where $\alpha(\tau)$ is the absorption coefficient, $\sigma(\tau)$ is the scattering coefficient, and the minus sign indicates that τ increases in the downward direction, whereas z increases in the upward direction. $\varpi(\tau) = \sigma(\tau)/[\alpha(\tau)+\sigma(\tau)]$ is the single-scattering albedo, and $S^*(\tau,\mu,\phi)$ is the source term due to attenuated solar radiation.

The integro-differential RTE (Equation 2.1) can be solved using a variety of methods. For example, the discrete-ordinate method, which converts Equation 2.1 into a system of coupled ordinary differential equations, can be used to compute radiances at any desired optical depth, polar, and azimuth angle. It works as follows: (i) the upper slab (atmosphere) and the lower slab (ocean or sea ice) are separated by an interface at which the refractive index changes abruptly; (ii) each slab is divided into a sufficiently large number of homogenous horizontal layers to adequately resolve the vertical variation in the inherent optical properties (IOPs); (iii) the reflection law, Snell's law, and Fresnel's equations are applied at the atmosphere-ocean (or sea ice) interface; (iv) discrete-ordinate solutions to the RTE are computed separately for each layer in the two slabs; (v) finally, boundary conditions at the top of the atmosphere (TOA) and the bottom of the water are applied, in addition to continuity conditions at layer interfaces in each of the two slabs.

Figure 2.14 (left) shows the simulated upward irradiance at the TOA, just above the ocean surface, and just below the ocean surface. The areas below all curves have been coloured by a

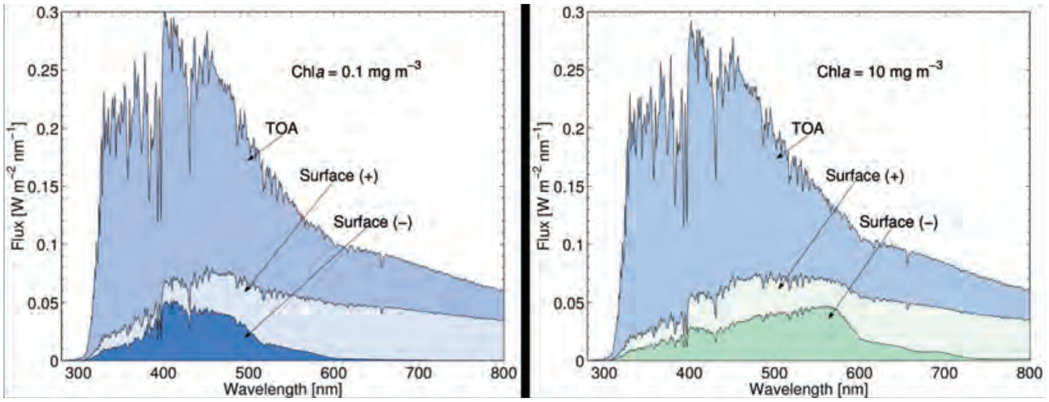

Figure 2.14 Left: Simulated upward irradiance at TOA (upper curve filled with blue colour), just above the ocean surface (middle curve filled with light blue colour), and just below the ocean surface (lower curve filled with dark blue colour). Right: Same as left panel, except that the chlorophyll concentration has been changed by a factor of 100 (After Hamre et al. 2013).

RGB translation of the spectra weighted by the three human eye colour response functions. Note the blue colour of the TOA irradiance, the light blue colour of the just above (Surface (+)) irradiance, and the dark blue colour of the just below (Surface (-)) irradiance. Figure 2.14 (right) shows results similar to those in the left panel, but for a 100-fold increase in the chlorophyll concentration. Note the significant change in sub-surface colour with increasing chlorophyll concentration, while at the same time there is only a slight change in colour at the TOA, showing that the TOA spectra are dominated by light from atmospheric scattering.

2.6 Summary

As solar radiation penetrates from the top of the atmosphere to the surface of the ice and ocean, its spectral distribution is impacted by sun angle, clouds, and ice conditions. This chapter examined the impact of these factors on downwelling and upwelling spectral irradiance. Solar radiation in the polar regions is characterized by a sparsity of sunlight in winter and an abundance of sunlight in summer. Ozone plays an essential role in providing a shield against UV exposure. Bulk air density plays a key role in light scattering by molecules. Clouds have a large impact on the surface energy budget and near-surface warming. Unusually high cloud fractions are observed from satellite data in ice free regions near the ice edge limiting the accuracy of assessing the primary productivity of these regions.

The optical characteristics of sea ice are shown to vary considerably during growth stages from nilas, to young grey ice without snow cover to young ice with 2 cm snow cover and fast ice with very thick snow cover. The albedo is high and relatively stable for sea ice cover with dry snow thicker than 6 cm. The values can change dramatically during the spring and summer depending on the liquid state of the snow cover and the depth and size of melt ponds.

The variabilities and trends of the sea ice cover in both hemispheres, as revealed by satellite passive microwave observations from November 1978 to December 2012, are presented. Large interannual and seasonal fluctuations are observed but the trends are asymmetric for the two hemispheres. In the Arctic, the extent of the sea ice cover has been declining at 3.8% per decade but the ice that survives the summer (perennial ice) has been declining at a higher rate of 11% per decade. The ice that survives two summer melts (multi-year ice), which is the mainstay of the Arctic ice cover, is declining even faster at 14% per decade. On the other hand, the extent of the Antarctic sea ice cover has been increasing at around 1.8% per decade. The positive trend is mainly due to large increases in ice extent in the Ross Sea, which more than offsets the decline in extent in the Bellingshausen and Amundsen Seas. Ice production has been observed to be increasing at the coastal polynyas (which are known as ice production factories) along the Ross ice shelf, and appears to be the primary reason for the increase. Studies of ice drifts around the Antarctic appears to support this phenomenon.

Sea ice data, as derived from passive microwave brightness temperature, allow for accurate identification of the ice edge even during cloudy conditions. This is important for studies of ocean colour remote sensing because it makes it possible to assess the rate of melt water production at the ice margin. Such information is required for accurate interpretation of the ocean colour distribution at the ice margin, which is expected to be influenced by the relatively stable melt water. It also allows for accurately identifying ocean colour data that is free from contamination of sea ice. Furthermore, the data can be used to keep some bona fide ocean colour data that are normally rejected because of improper evaluation of the location of sea ice. The improper masking of ocean colour data near the marginal ice zone can lead to inaccurate estimates of primary productivity in the Arctic.

Radiative transfer modelling provides a means to simulate total, diffuse and direct radiance and irradiance spectra in an atmosphere-snow-ice-ocean system. The distribution of spectral radiance and irradiance is impacted by changes in the ocean chlorophyll concentration and CDOM absorption, and the TOA radiance is influenced by atmospheric aerosol loading and water constituents.

Chapter 3

From Surface to Top-of-Atmosphere

Simon Bélanger, Robert Frouin, Menghua Wang, Clémence Goyens and Knut Stamnes

3.1 Introduction

The scope of this Chapter is to review in more detail the limitations of the current algorithms implemented to assess the colour of the ocean from space with respect to the particularities of polar regions. We define this part of the ocean colour processing chain as "atmospheric correction" (AC), i.e., the processing steps that aim at extracting the normalized water-leaving radiance from the top-of-atmosphere (TOA) signal, which is largely dominated by the contribution of the atmosphere between the sea surface and the satellite. In particular, we will address polar-related issues such as sea ice, low sun elevation and cloud cover.

The ultimate objective of ocean colour remote sensing is to provide accurate information about the seawater constituents at synoptic scales. This goal can only be reached if the normalized water-leaving radiance (IOCCG 2010), nL_w, can be estimated with high accuracy. Typically, the accuracy required for nL_w at the blue bands must be <5% (Hooker et al. 1992). The particular environmental setting of polar regions (Chapter 2) makes these objectives extremely challenging. The purpose of this chapter is to expose a number of problems that are potentially more important in polar regions, relative to other oceans. It is noted that in this report we use the normalized water reflectance (also referred to as normalized water-leaving reflectance), $\rho_{wN} = \frac{\pi nL_w}{F_0}$, and remote sensing reflectance, $R_{rs} = \frac{nL_w}{F_0}$, where F_0 is the extraterrestrial solar irradiance. Normalized water (or ice) reflectance is equal to the water reflectance (ρ_w) divided by the total transmittance (direct + diffuse) of the atmosphere between the sun and the surface. That is, $\rho_{wN} = \frac{\rho_w}{t(\theta_s)}$ where $t(\theta_s)$ is the atmospheric total transmittance, commonly defined as the atmospheric diffuse transmittance at solar-zenith angle of θ_s (Yang and Gordon 1997; IOCCG 2010).

First, the presence of sea ice in polar regions creates an optical environment characterized by extreme contrasts between bright and dark targets. Historical observations from CZCS showed that very high contrasts in the presence of sea ice can result in frequent electronic overshoot of the detectors, deteriorating the quality of the radiometric measurements at the TOA (Comiso et al. 1990). The new generation of sensors, with improved response and dynamic range, reduce the sensor saturation problem. Nevertheless, sea ice remains a problem for ocean colour retrieval through two physical phenomena: the adjacency effect and sub-pixel contamination, outlined in Section 3.2.

The prevalence of low solar elevation is another challenging problem for ocean colour remote sensing at high latitudes (Section 3.3). Low sun elevation makes the contribution of the atmosphere to the TOA signal received by the sensors more important than at high sun elevation. In this situation, small errors in atmospheric corrections can lead to relatively large errors when estimating nL_w. Standard AC schemes rely on look-up-tables (LUTs) generated using radiative transfer codes that assume a plane-parallel atmosphere (PPA) rather than the actual spherical-shell atmosphere (SSA) (Gordon and Wang 1994; IOCCG 2010; Ahmad et al. 2010). Although the problem was identified and discussed long ago (Ding and Gordon 1994; Wang 2003), the extent at which this assumption can degrade nL_w at solar zenith angles >70°, which is frequent at high latitude, still needs to be assessed quantitatively and checked with actual observations.

Polar Regions are also known for their persistent cloud cover (see Figures 2.3 and 2.4), especially during the late open water season when sea ice extent is minimal. Clouds can seriously reduce the amount of valid ocean colour pixels in some regions. The extent of the problem is still poorly quantified and needs more attention. In addition, clouds and ice cover can be treated together as "bright pixels" and masked out by ocean colour algorithm processing (e.g., SeaWiFS). However, one may be interested in distinguishing clouds from sea ice for several reasons, e.g., thin clouds may allow a significant amount of light to reach the sea surface, which can be harvested by phytoplankton for photosynthesis. Section 3.4 presents methods to mask clouds in current ocean colour algorithms, as well as the importance of cloud frequency for ocean colour data availability.

The atmospheric composition at the South Pole, in terms of aerosols, differs substantially from the aerosol composition at the North Pole, since the South Pole is relatively isolated from continental and anthropogenic aerosols relative to the North Pole. For example, anthropogenic emissions of sulphate aerosols and black carbon from industrial cities of Northern Europe and Russia may be transported and trapped in the Arctic air mass during the polar nights of the northern hemisphere. These aerosols may significantly contribute to light scattering and absorption in the Arctic atmosphere during springtime, when the Sun rises above the horizon and creates the so-called Arctic Haze. Section 3.5.1 will review our knowledge of the polar aerosols and their implication for atmospheric correction of ocean colour images.

Another important difference between the poles from the atmospheric correction perspective is the supply of particulate inorganic matter from land to sea by rivers, and coastal erosion in the Arctic coastal zones. These turbid waters are known to cause problems in AC algorithms, although schemes do exist to minimize their effect on the water radiance retrievals. Section 3.5.2 will discuss the potential zones and months where turbidity may affect the data quality in the Arctic.

Approaches to detect contaminated pixels in ocean colour data are presented in Section 3.6, in presence of sea ice (Section 3.6.1) and cloud and fog (Section 3.6.2). Examples of the applications of these detection methods are shown and illustrated with MODIS-Aqua and SeaWiFS images. The last section (Section 3.7) includes a discussion about atmospheric correction schemes dealing with adjacency contamination in the presence of sea-ice and examples are given where ocean colour properties are derived in the presence of thin clouds and under certain conditions.

Each potential problem presented above will be introduced with a literature review and illustrated with concrete examples. Methods and approaches to address these issues are presented and potential solutions discussed. In addition, new products relevant for the monitoring of high latitude marine ecosystems, such as sea ice optical properties potentially derived from ocean colour sensor information, are presented.

3.2 Issues Related to Sea Ice

Evidence of ocean colour product contamination by sea ice was first reported by Gregg and Casey (2004) in their effort to validate SeaWiFS chlorophyll data. Later, Bélanger et al. (2007) described how sea ice can introduce errors in the retrieval of chlorophyll-a and inherent optical properties (IOPs) from ocean radiance measurements. There are two ways that sea ice can contaminate ocean colour retrievals of water-leaving radiance: adjacency effects (Section 3.2.1) and sub-pixel contaminations (Section 3.2.2).

3.2.1 Adjacency contamination

Sea ice, often overlaid by snow, reflects up to 90% of the incident energy in the visible portion of the spectrum. A fraction of the photons backscattered by snow and sea ice ends up being scattered above open water pixels by air molecules and aerosols as they travel upward from the surface of the ocean up to the TOA. This process, known as the adjacency effect (Tanré et al. 1979, 1981), is defined as the change in pixel radiance caused by the atmospheric scattering of radiance that originates outside of the sensor instantaneous-field-of-view (IFOV).

Formally, in the presence of adjacency effects, the reflectance at the top-of-atmosphere (ρ_{TOA}) can be expressed according to Equation 3.1 (Tanré et al. 1979, 1981; Santer and Schmechtig 2000):

$$\rho_{TOA} = t_g(\theta_s, \theta_v)[\rho_{path} + \rho_w^* + \rho_{env}] \tag{3.1}$$

where $t_g(\theta_s, \theta_v)$ is the total gas transmittance in both downward and upward direction, ρ_{path} is the atmospheric path reflectance, and ρ_w^* and ρ_{env} are surface reflectance terms for the water pixel in the presence of the adjacency effect and its environment, respectively, defined as:

$$\rho_w^* \approx \rho_w t^{dir}(\theta_v) \tag{3.2}$$

and

$$\rho_{env} \approx \langle\rho\rangle t^{dif}(\theta_v) \tag{3.3}$$

where t^{dir} is the direct atmospheric transmittance and t^{dif} the diffuse transmittance in the upward direction (θ_v), $\langle\rho\rangle$ is a spatial average of each pixel reflectance over the whole surface and ρ_w is the water reflectance (in absence of adjacency effect). In Equations 3.2 and 3.3, the effect of photons diffusively reflected by the water body and backscattered by the atmosphere toward the surface is neglected. In the absence of adjacency effects and sun glint, Equation 3.1 reduces to:

$$\rho_{TOA} = t_g(\theta_s, \theta_v)[\rho_{path} + t(\theta_v)\rho_w] \tag{3.4}$$

where $t(\theta_v)$ is the atmospheric total transmittance in the upward direction (again known as atmospheric diffuse transmittance; for details see Appendix C in IOCCG, 2010). In the presence of a non-uniform surface, however, $\langle\rho\rangle$ is a function of the atmospheric conditions and the mean surface reflectance, which is given by:

$$\langle\rho\rangle = F\rho_w + (1 - F)\rho_{ice} \tag{3.5}$$

where ρ_{ice} is the ice reflectance and F is an environmental function that represents the probability of a photon coming from space toward the target and scattered by the atmosphere to reach the surface within the IFOV. F depends on the distance between the targeted and the adjacent pixel and the atmospheric scattering properties. F is equal to unity when the ice is far enough from the target and approaches 0 when the distance between targeted and the adjacent pixel tends towards 0. Spectrally speaking, F is a function of the molecular and aerosol scattering and its spectral dependency can be expressed as:

$$F \approx 1/(a_0\lambda^{-1} + a_1\lambda^{-4}), \tag{3.6}$$

where a_0 and a_1 are scale parameters for aerosols and molecular scattering respectively, which varies as a function of sun-viewing geometry, aerosol concentration and composition and altitude. In other words, the adjacency effect for a white surface such as snow will be small in the NIR and increases exponentially towards short wavelengths approximately following a spectral dependency of $\sim \lambda^{-4}$. This results from the fact that atmospheric scattering is dominated by air molecules (Rayleigh scattering), which exhibits a λ^{-4} spectral dependency, and because sea ice albedo shows moderate spectral variations in the visible which drops in the near infrared (NIR) wavebands (750 to 900 nm) (Chapter 2). Potentially, it can contaminate ocean colour retrievals as far as 20 km from the ice edge (for details see Bélanger et al. 2007).

3.2.2 Sub-pixel contamination

When sea ice melts and degrades during summer, its spectral reflectance decreases progressively (See Figure 2.8 and Perovich et al. 2007) and relatively small ice floes can detach from the landfast, icebergs or the ice pack and drift in the open ocean. These pieces of ice can escape the cloud and ice detection flag, which is based on a threshold in the NIR wavebands (see Wang and Shi 2009), and be erroneously assigned by the AC algorithms as an increase in aerosols. Physically, however, the phenomenon can be compared to the effect of sea foam or whitecaps (ρ_{wc}; Frouin et al. 1996). In such a case, Equation 3.4 can be expanded to include all surface and atmospheric contributions for a given ocean pixel:

$$\rho_{TOA} = t_g(\theta_s, \theta_v)[\rho_R + \rho_a + \rho_{Ra} + t(\theta_v)[\sigma_{wc}\rho_{wc} - \sigma_{ice}\rho_{ice} + (1 - \sigma_{wc} - \sigma_{ice})\rho_w]] \qquad (3.7)$$

where ρ_R and ρ_a are the reflectance due to air molecules and aerosols alone, respectively, ρ_{Ra} represents the multiple scattering interaction between molecules and aerosols; σ_{ice} is the fractional sea ice coverage within the pixel (dimensionless, from 0 to 1); and σ_{wc} is the fractional coverage of whitecaps within the pixel (dimensionless, from 0 to 1). Note that the latter is always a small fraction in coarse pixel resolution (e.g., 1.1-km), even at large wind speed.

Depending on the reflectance of sea ice in the NIR, σ_{ice} may reach as much as 25% without being detected by the cloud and ice detection flag (e.g., thin grey ice; Bélanger et al. 2007). For example, an ice floe covered by melting snow with a ρ_{ice} value of 45% at 865 nm can cover up to 6% of the surface area of a pixel before being flagged as sea ice (assuming a Rayleigh-corrected reflectance threshold of 2.7% for cloud and ice detection at 865 nm as in SeaWiFS). In terms of surface area, this represents a piece of sea ice as large as 6 600 m^2 (~80 × 80 m) in a 1.1-km pixel resolution.

3.2.3 Illustrative examples

In this section we will illustrate how ocean colour data can be contaminated by ice using several examples from SeaWiFS and MODIS-aqua data. Two different AC schemes were used to estimate the water-leaving radiance: the NASA standard AC approach (Gordon and Wang 1994; Stumpf et al. 2003) for both SeaWiFS and MODIS, and an alternative scheme proposed by Wang and Shi (2007) for MODIS that uses wavebands from the shortwave infrared domain (SWIR, 1000 – 3000 nm). For a detailed description of those AC schemes, refer to the original publications or IOCCG Report number 10 (IOCCG 2010).

Briefly, the NASA standard AC algorithm, hereafter refer to as STD-AC, relies on the black pixel assumption, which assumes that all incoming radiation in the NIR (750 to 900 nm) is absorbed. Thus after removing the molecular scattering (Rayleigh) contribution to the TOA signal in the NIR, the remaining signal is assumed to come from the aerosols, which vary significantly in time and space. This approach was first proposed by Gordon and Wang (1994) and implemented successfully in the SeaWiFS processing chain in 1997. The method fails to retrieve the water-leaving radiance in the short wavebands as soon as the black pixel assumption is violated, which often occurs when there is particle backscattering, for example in turbid coastal waters or above intense phytoplankton blooms (Ruddick et al. 2000; Siegel et al. 2000). A few years later, the NASA implemented an iterative scheme to retrieve the inherent optical properties in the red bands and extrapolate these to the NIR spectral domain to assess the water reflectance in the NIR (Stumpf et al. 2003; Bailey et al. 2010). This scheme is triggered when the chlorophyll concentration, estimated from the first guess of normalized water reflectance is above 0.7 mg m^{-3}.

The second method, hereafter refer to as NIR-SWIR, proposed by Wang and Shi (2007) is designed to deal with very turbid waters where STD-AC is expected to fail. It is based on the assumption that the water is black in the SWIR wavebands. Those bands are only available on MODIS and were originally optimized for land applications. According to Wang and Shi (2009), the NIR-SWIR scheme can improve ice detection.

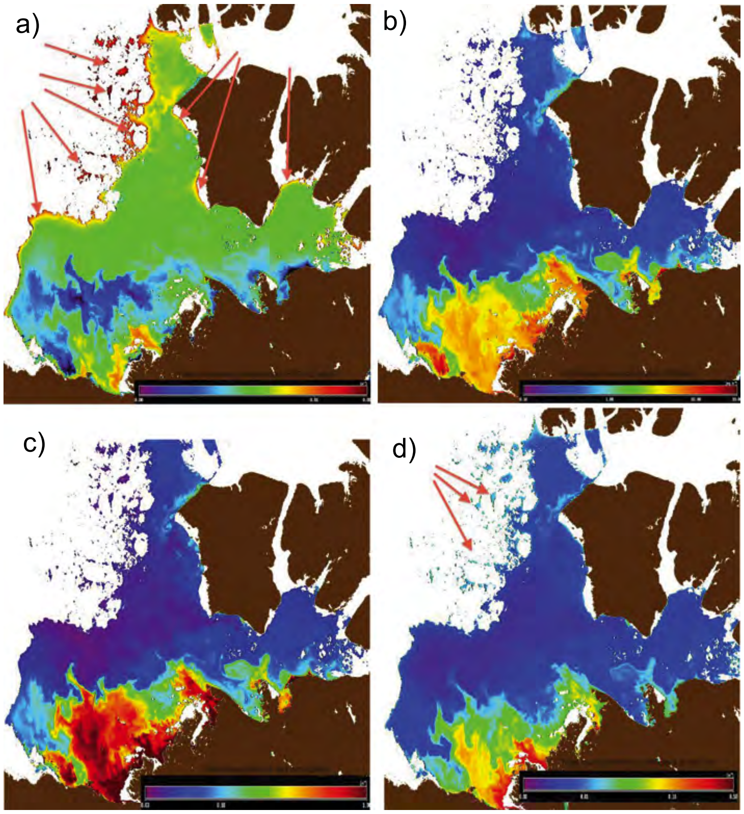

Figure 3.1 SeaWiFS standard retrievals of a) normalized water leaving reflectance at 443 nm, b) chlorophyll-a concentration from OC4v6, and total c) absorption and d) backscattering coefficients at 443 nm from a quasi-analytical algorithm (QAA). Arrows indicate evidence of contamination (very high values for nL_w and b_b).

Level 1A data were obtained from the NASA Ocean Biological Processing Group and processed to Level 2 using SeaDAS 6.1. The STD and NIR-SWIR AC algorithms were applied to SeaWiFS and MODIS-Aqua data, respectively. Look-up-tables for Rayleigh and aerosol reflectance (N=80 aerosol models) for both SeaWiFS and MODIS-Aqua are those calculated by Ahmad et al. (2010).

The first example is a cloud free image of the eastern Beaufort Sea captured by SeaWiFS in June 1998 (Figure 3.1). It shows the spectacular turbid plume of the Mackenzie River, the fourth-largest Arctic river, flowing into highly stratified and oligotrophic waters of the Canada Basin. Offshore in the Basin, the ice pack shows numerous leads and ice-free areas. In these waters, the retrieved normalized water-leaving reflectance in the blue (443 nm; 3.1a) reaches very high values, most likely resulting from adjacency effects.

Retrieval of chlorophyll-a concentration (Chla), however, does not seem to be affected by adjacency effects since it uses spectral band ratios, which minimize the problem (Figure 3.1b).

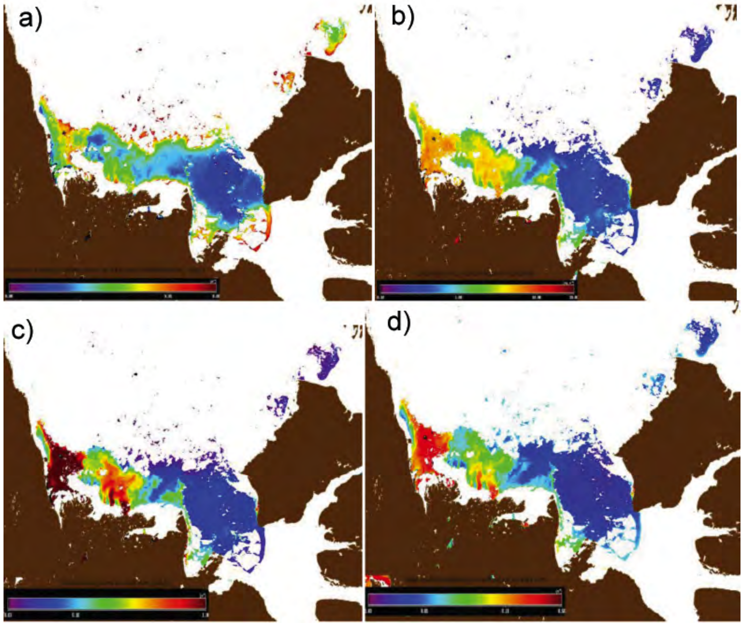

Figure 3.2 MODIS-Aqua retrievals, after application of NIR-SWIR AC algorithm (Wang and Shi 2007), of a) remote sensing reflectance at 443 nm, b) chlorophyll-a concentration from OC4v6, and total c) absorption and d) backscattering coefficients at 443 nm from a quasi-analytical algorithm (QAA).

This holds true when the actual Chla is low, as demonstrated by Bélanger et al. (2007) (see their Figure 5), but not when Chla is > 0.5 mg m^{-3}. In contrast, IOP retrievals using semi- or quasi-analytical approaches are more sensitive to the adjacency effect as illustrated in Figure 3.1d for the total backscattering coefficient (b_b) retrieved by QAA (Lee et al. 2002). Note that the impact of the adjacency effect depends on the initial water constituents and their concentrations. At low Chla, the adjacency effect largely impacts estimates of b_b as apposed to total absorption (a_t).

Figure 3.2 shows the same problem using MODIS-Aqua data from 29 June, 2003 in the same region. At that time, the sea ice cover was closer to the coast and adjacency contamination could be found north of the Mackenzie river plume, in the marginal ice zone. The true-colour image (not shown) indicates that the river plume was spreading below the sea ice cover. The effect of sea ice is less evident in the plume although lower Chla and total absorption coefficient (Figures 3.2b and c) were found nearby sea ice. In contrast, Figure 3.2d shows that the b_b retrieval in the turbid plume is less affected by the adjacency effect (opposite to the case study described in Figure 3.1) since higher Chla is encountered. But further offshore, where Chla is lower, adjacency effects render large errors on b_b retrievals (Figure 3.2d).

Wang and Shi (2009) found evidence of sub-pixel contamination by sea ice in MODIS-Aqua data. Results of Wang and Shi (2009) are re-plotted in Figure 3.3. Regions with sub-pixel contamination by sea ice are circled in panels a, b, and c, showing low nL_w values at 412 nm and high Chla. The effect of adjacency contamination (Figure 3.1 and 3.2) is thus opposite to sub-pixel contamination (Figure 3.3).

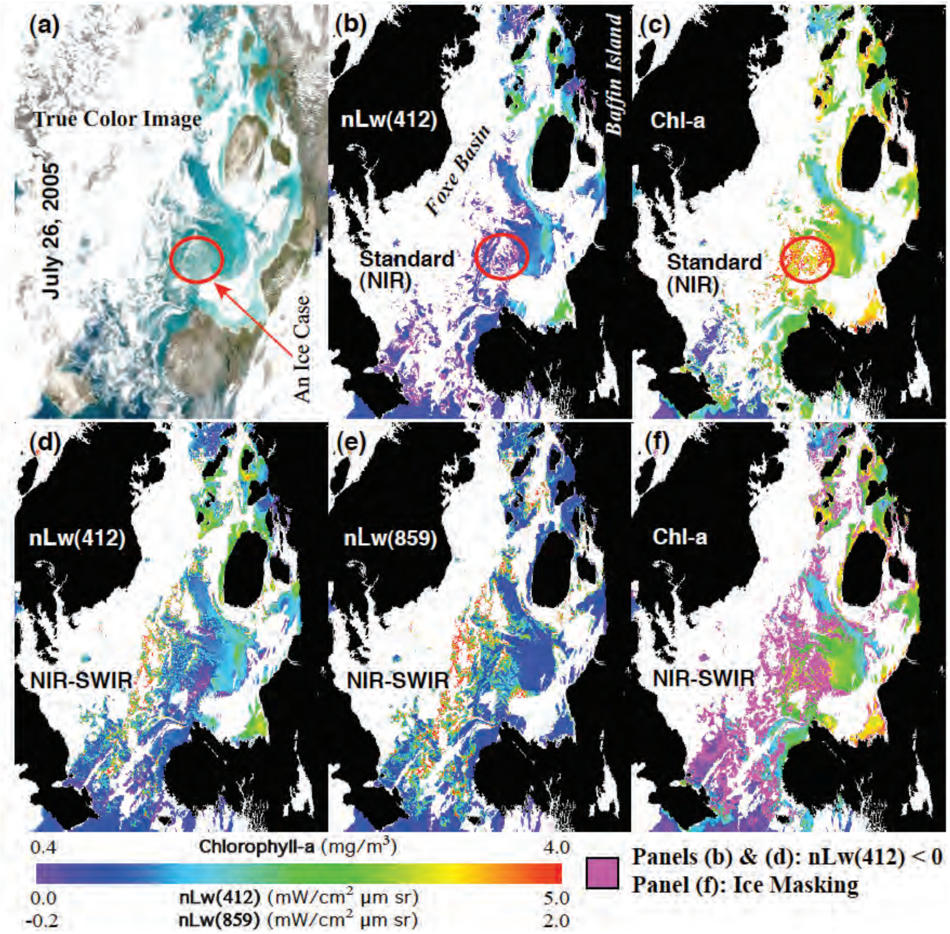

Figure 3.3 An example of mixed ice-water scenario from MODIS-Aqua measurements on 26 July 2005 in the Foxe Basin around the Baffin Island, Canada for (a) true colour image, (b) $nL_w(412)$ image using the standard (NIR) AC algorithm, (c) Chla image using the standard (NIR) algorithm, (d) $nL_w(412)$ image using the NIR-SWIR AC algorithm, (e) $nL_w(859)$ image using the NIR-SWIR AC algorithm, and (f) Chla image using the NIR-SWIR AC algorithm with sea ice masking in pink (pixels masked in pink in panels (b) and (d) are for cases with $nL_w(412) < 0$). Redrawn from Wang and Shi (2009) and reprinted with permission from IEEE.

3.3 Issues Related to Low Sun Elevation

The sun elevation at a latitude of 70°, at the satellite overpass (i.e., noon ± 1 hour), is below 20° (or sun zenith angle > 70°) for nearly six months per year. At a latitude of 80° (e.g., Svalbard) low sun elevation prevails for almost eight months per year, limiting the window for good ocean colour observations to a few summer months. Background information about the problem of low solar elevation, from a radiative transfer point of view, is provided below because the LUTs used in ocean colour processing are generated using PPA models that assume a flat Earth, which may present a problem when the Sun is just above the horizon.

3.3.1 Theoretical background: Plane parallel versus spherical-shell atmosphere

For low sun elevations, the curvature of the atmosphere must be taken into account. In a curved atmosphere the radiance is found by solving a radiative transfer equation appropriate for spherical-shell geometry, which contains three angle derivative terms that are absent in a plane parallel (or slab) geometry (Sobolev 1975; Lenoble 1985; Dahlback and Stamnes 1991; Thomas and Stamnes 1999; Spurr et al. 2007). In a spherically symmetric atmosphere only one of these derivative terms is needed, while in spherical-shell geometry all three terms must be considered, as discussed by Thomas and Stamnes (1999). It has been shown that, in a stratified atmosphere, accurate results may be obtained for solar zenith angles less than 90° by ignoring all three angle derivatives, but using spherical geometry to compute the direct beam attenuation (Dahlback and Stamnes 1991; Slusser et al. 1996).

Ding and Gordon (1994) investigated the influence of the Earth's curvature on atmospheric correction using Monte Carlo simulations of the radiance exiting the top of a spherical-shell atmosphere. They concluded that the error in the water-leaving radiance is negligible for solar zenith angles less than about 70°. They also suggested that for solar zenith angles larger than 70°, the error in atmospheric correction can be reduced by computing the Rayleigh scattering component in spherical-shell geometry, and that the resulting error can be predicted reasonably well from computations done with a PPA radiative transfer code, in agreement with the findings of previous investigators that the ratio between the singly-scattered radiance and the total radiance is approximately the same for plane parallel and spherical geometry (Adams and Kattawar 1978; Kattawar and Adams 1978). Wang (2003) further showed Earth's curvature effects on satellite data using real SeaWiFS measurements.

To illustrate the effects of curvature on the radiation field, we show results computed by a coupled atmosphere-ocean discrete ordinate radiative transfer model (Jin and Stamnes 1994; Yan and Stamnes 2003) with a pseudo-spherical treatment of the solar beam in a curved atmosphere (Dahlback and Stamnes 1991; Spurr et al. 2007). The importance of taking curvature into account is illustrated in Figure 3.4 where (a) shows results for pseudo-spherical geometry at the TOA, (b) shows the corresponding results just above the water surface, (c) shows the error incurred by using the PPA at the TOA, and (d) the corresponding error just above the water surface. Computations were done for the nine MODIS ocean colour wavelengths. Denoting the radiance in upward (+) and downward (-) directions by $L^{\pm}(\tau, \mu, \phi)$, where τ is the optical depth, μ is the cosine of the polar angle and ϕ the azimuthal angle, we define the TOA radiance plotted in Figure 3.4 as:

$$L_{TOA}(\mu, \phi) = L^{+}(\tau = 0, \mu, \phi) \tag{3.8}$$

while the radiance emerging from the sea, i.e., the water-leaving radiance, $L_w(\tau_a^-, \mu, \phi) = L^{+}(\tau = \tau_a^-, \mu, \phi)$, computed as follows:

$$L_w(\tau_a^-, \mu, \phi) = L_{ocn}(\tau = \tau_a^-, \mu, \phi) - L_{black-ocn}(\tau = \tau_a^-, \mu, \phi) \tag{3.9}$$

where $L_{ocn}(\tau_a^-, \mu, \phi)$ is computed for a non-black ocean, and $L_{black-ocn}(\tau_a^-, \mu, \phi)$ is computed for a totally absorbing (black) ocean and τ_a^- is the optical depth from the TOA to just above the water surface.

The deviation in radiance between the pseudo-spherical approximation (PSA) and the plane-parallel approximation (PPA) at the TOA is plotted in Figure 3.4c as the percentage difference: $100 \times (L_{TOA}^{PSA} - L_{TOA}^{PPA})/L_{TOA}^{PSA}$. The use of plane parallel geometry is sufficient for solar zenith angles smaller than about 75°, where the % difference in L_{TOA} at 412 and 443 nm is ~1%, whereas it is <1% at longer wavelengths (Figure 3.4). At SZA=80°, the errors on L_{TOA} are larger than 2% in the shortwave wavelengths (<600 nm). At SZA=87°, the relative difference between PSA and PPA reaches as much as 30%. Note that the pseudo-spherical treatment is expected to be adequate for solar zenith and viewing angles approaching 90° (Spurr et al. 2007). The difference between PSA and PPA lies in the diffuse radiation field. For large SZAs the diffusion will be larger in the PSA (Earth's curvature accounted for) than in the PPA at all levels in the atmosphere and depths in the ocean. This explains why the relative difference between PPA and PSA results increase with SZA.

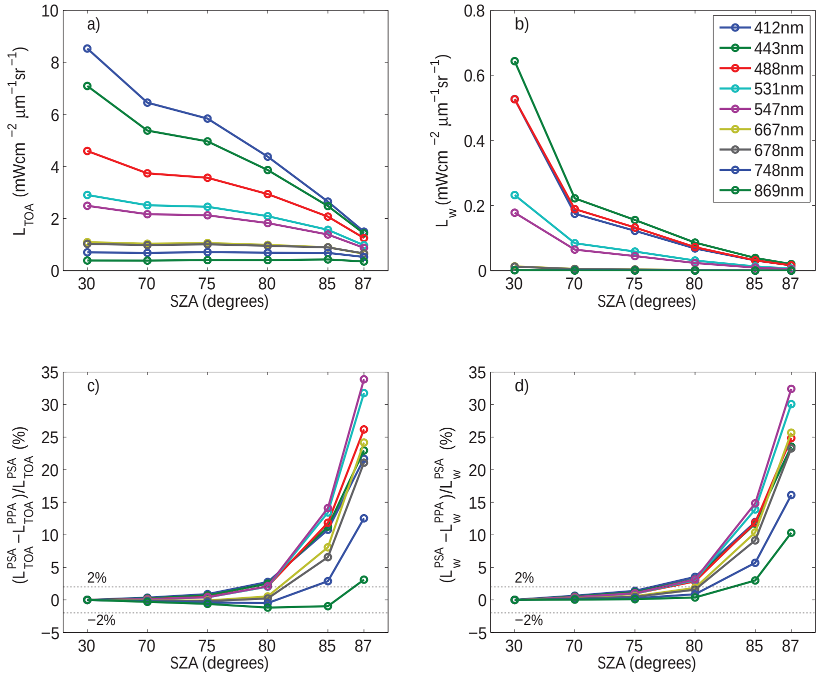

Figure 3.4 a) Top-of-the-atmosphere radiance (L_{TOA}) and c) relative difference incurred by using plane-parallel geometry (PPA) for several values of solar zenith angle (SZA) between 30° and 87°. b) Same as for a) but for the water-leaving radiance and d) relative difference incurred on L_w by using PPA. Dashed lines on c) and d) are the relative error boundary of -2 and +2% , respectively. Viewing geometry: ϕ = 120°; $\tau_a(865)$ = 0.05. Fraction of small vs. large aerosol particles was set to 0.5. Water-leaving radiance was generated using the following bio-optical properties: Chla =0.1 mg m^{-3}, coloured detrital absorption coefficient at 443 nm = 0.05 m^{-1}, particulate backscattering coefficient at 443 nm = 0.001 m^{-1}.

The amount of energy emerging from the sea when the SZA is 70° is about three times smaller than that calculated for the SZA of 30° (Figure 3.4b). The errors incurred by the PPA on L_w are slightly larger than that on L_{TOA} (Figure 3.4c vs 3.4d). This is probably due to the fact that PPA underestimates the contribution of diffuse skylight that can penetrate in the water column.

To quantify the contribution of the radiance emerging from the sea to the TOA, we computed the TOA radiance for a (non-black) ocean, $L_{ocn}(\tau = 0, \mu, \phi)$, repeated the computation for a black (totally absorbing) ocean, $L_{black-ocn}(\tau = 0, \mu, \phi)$, and then computed the difference:

$$L_{w,TOA} = L_{ocn}(\tau = 0, \mu, \phi) - L_{black-ocn}(\tau = 0, \mu, \phi), \tag{3.10}$$

where $L_{w,TOA}$ is the radiance emerging from the ocean that reaches the TOA after being attenuated along the pathlength from the ocean to the TOA. This quantity is shown in Figure 3.5a for PSA. Next we estimated the contribution of $L_{w,TOA}$ to the total TOA as $\%L_{w,TOA} = 100 \times L_{w,TOA}/L_{ocn}(\tau = 0, \mu, \phi)$ for PSA. The $\%\,L_{w,TOA}$ for PSA is shown in Figure 3.5b.

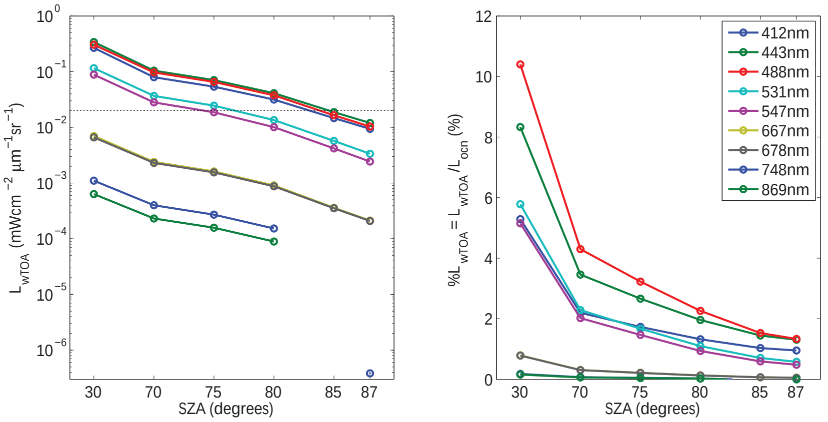

Figure 3.5 Radiance emerging from the sea that reaches the TOA, as defined by Equation 3.10, for several values of the solar zenith angle from 30° to 87°, and b) the percentage contribution of water signature to the TOA. The dashed line in a) is the accepted atmospheric correction algorithm uncertainty.

Beyond the effects of the Earth's curvature on the calculation of the LUTs used in the atmospheric correction schemes, there is a physical limitation resulting from the small amount of energy penetrating the ocean when the sun is just above the horizon. First, the amount of radiance exiting the ocean becomes extremely small at high SZA (Figures 3.4b, 3.5a). Secondly, the contribution of the ocean to the TOA radiance decreases as SZA increases (Figure 3.5b). In the green band, for example, $\%L_{w,TOA}$ drops below 2% when SZA is >75° while it reaches 5% for a SZA = 30°.

In fact, the contribution of the ocean to the TOA signal is <0.1 mW cm^{-2} sr^{-1} μm^{-1} for SZA >75° (Figure 3.5a), which is close to the detection limit of the sensor. The typical noise level at 443 nm for MODIS aqua is 5×10^{-3} mW cm^{-2} sr^{-1} μm^{-1} and the accuracy of the atmospheric correction is ~0.03 mW cm^{-2} sr^{-1} μm^{-1}. Hence, the accuracy of the AC relative to the contribution of the ocean to the TOA radiance would be >30% for SZA > 75° (i.e., 0.1 ± 0.03 mW cm^{-2} sr^{-1} μm^{-1}). Thus even a small error in the AC will have a dramatic impact on the L_w retrieval when SZA is larger than 75°.

3.3.2 Illustration of the problem

LEO satellites with a wide swath (i.e., ~2000 km) can observe high latitudes several times per day at a time interval of ~75 minutes. Under clear sky conditions near the solar solstice, for example, the North Water polynya, located in northern Baffin Bay (75 to 78°N latitude), can be seen by MODIS as much as seven times on the same day. Therefore, a time series of seven acquisition of the same location can be constructed to assess the reliability of ocean colour retrievals for solar zenith angles varying from ~52° to 75°. These settings offer the opportunity to further examine the current sensitivity of ocean colour product retrievals to a gradient of SZA. Assuming that the ocean is spatially homogenous and that diurnal changes in ocean optical properties are negligible, one can expect that satellite-derived nL_w and Chla will remain relatively constant over the range of SZAs explored during a given day.

Table 3.1 presents the detailed sun-viewing geometry and the atmospheric parameters retrieved, namely the aerosol optical thickness (τ_a) and its spectral dependency (Ångström exponent, α), for MODIS-Aqua and SeaWiFS acquisitions at three locations in the North Water Polynya (NOW) on 29 June 2004 (Figure 3.6). Note that for these cases, Ångström exponents are meaningless with such low aerosol optical thickness values, since the radiance due to aerosols is negligible in absolute terms. Huge errors in α are thus expected for such cases.

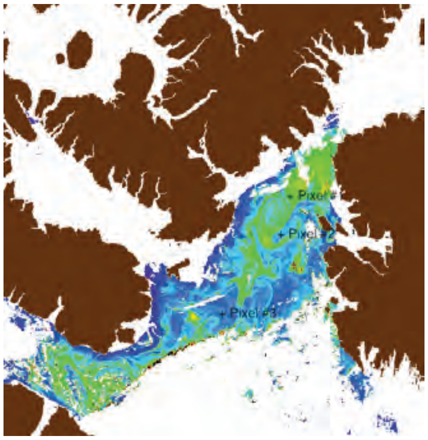

Figure 3.6 Localisation of the selected pixel to assess the impact of low sun elevation on SeaWiFS and MODIS−Aqua L2 products. The colour-coded image is the chlorophyll-a concentration retrieved by MODIS-Aqua at 16h55 UTC, 29 June 2004.

The pixel's locations were carefully chosen to cover three Chl-a concentrations from 0.45 to ~2 mg m^{-3}, and to keep sea ice typically ~>15 km away from the chosen locations (Figure 3.6). Sky conditions during that day were particularly good for most acquisitions. Despite good and stable atmospheric conditions, cloud contamination could not be always avoided as confirmed by a careful visual inspection of each scene (not shown).

Table 3.1 Time and geometry of data acquisition on 29 June 2004 for MODIS-Aqua and SeaWiFS, for three locations in the NOW polynya. Averaged values of a 3 × 3 pixel window is taken (at the nominal spatial resolution of the sensor, i.e., 1 or 1.1-km)

Sensor	Time UTC	SZA	θ_v	$\delta\phi$	$\tau_a(865)$	α	Chl
Pixel 1	**74°W 55’, 77°N 30’**						
MODIS-A	10:25	69.1	23.5	73.3	0.027	0.57	1.76
MODIS-A	12:00	63.8	37.0	72.5	0.013	1.54	1.88
MODIS-A	13:40	59.0	33.9	71.7	0.011	1.52	2.03
MODIS-A	15:15	55.5	12.4	68.7	0.045	1.06	2.03
MODIS-A	16:55	54.1	27.3	−113.3	0.010	2.02	2.44
SeaWiFS	18:04	54.7	46.6	110.2	0.016	0.82	1.99
SeaWiFS	19:43	57.6	22.2	160.3	0.008	1.82	2.35
SeaWiFS	21:21	62.7	33	−137.1	0.010	1.67	2.23
SeaWiFS	23:00	67.4	41.4	−126.7	0.046	0.47	2.63
SeaWiFS	00:39 (+1D)	72.4	36.9	−130.7	0.005	2.14	3.21
Pixel 2	**74°W 30’, 77°N**						
MODIS-A	12:00	63.7	40.3	73.5	0.015	1.38	0.65
MODIS-A	13:40	58.7	37.1	72.6	0.012	1.46	0.66
MODIS-A	15:15	55.0	15.5	71.5	0.016	1.00	0.68
MODIS-A	16:55	53.6	26.2	−114.4	0.011	1.80	0.67
SeaWiFS	18:04	54.3	45.7	110.8	0.009	1.56	0.58
MODIS-A	18:30	54.8	57.5	−117	0.015	1.57	0.61
SeaWiFS	19:43	57.4	21.7	169.2	0.004	1.84	0.63
SeaWiFS	21:21	62.1	35.9	−133.1	0.005	1.62	0.68
SeaWiFS	23:00	67.5	44.0	−124.6	0.002	0.36	0.98
SeaWiFS	00:39 (+1D)	72.6	39.4	−127.9	0.012	0.83	0.99
Pixel 3	**76°W, 75°N 45’**						
MODIS-A	8:45	75.0	4.8	−106.5	0.010	−0.15	0.62
MODIS-A	10:25	69.8	34.3	73.3	0.013	0.10	0.49
MODIS-A	12:00	63.9	47.3	73.8	0.016	1.14	0.52
MODIS-A	13:40	58.3	45.2	73.2	0.024	0.97	0.52
MODIS-A	15:15	54.2	25.5	70.8	0.024	1.16	0.47
MODIS-A	16:55	52.4	18.6	-112.7	0.020	1.69	0.54
SeaWiFS	18:04	53.0	45.6	110.8	0.017	1.28	0.46
MODIS−A	18:30	53.5	55.9	−118	0.029	1.47	0.48
SeaWiFS	19:43	56.3	22.0	−178.4	0.004	2.05	0.46
SeaWiFS	21:21	61.4	41.3	-127.7	0.007	1.65	0.52
SeaWiFS	23:00	67.3	50.2	-120.7	0.007	1.86	0.57
SeaWiFS	00:39 (+1D)	72.9	46.4	-122.0	0.002	2.13	0.76

Figure 3.7 presents the nL_w retrievals of MODIS-Aqua and SeaWiFS for the northern most location in a phytoplankton-rich area of the NOW polynya. SeaWiFS nL_w spectra retrieved vary significantly between the first and fifth acquisition (Figure 3.7a). A general decrease in

nL_w was observed along the increasing values of cos(SZA)$^{-1}$, which was more pronounced at shorter wavelengths (factor of 2 at 443 nm; Figure 3.7c). MODIS-Aqua also showed significant differences in nL_w between the first and the last acquisition (Figure 3.7b), but the differences were much smaller than those for SeaWiFS (~20% at 443 nm). Surprisingly, the relationship between nL_w and cos(SZA)$^{-1}$ showed an opposite trend with increasing normalized water-leaving radiance with the SZA (Figure 3.7d). Note, however, that the variations in R_{rs} may also reflect an actual increase in phytoplankton biomass during daytime from 10:25 UTC (1.76 mg m^{-3}) to 00:39 (+ 1 day) (3.22 mg m^{-3}) (Table 3.1) due to phytoplankton growth or/and advection.

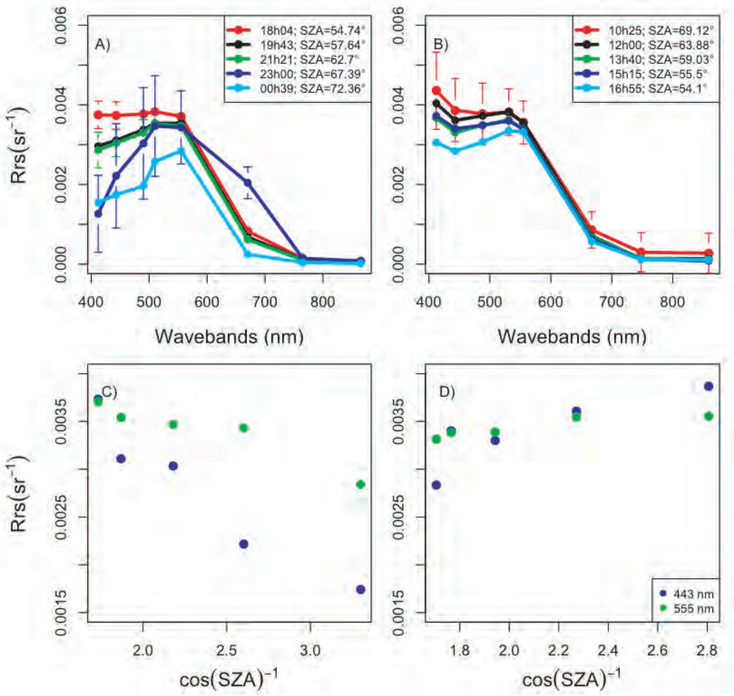

Figure 3.7 Spectral remote sensing reflectance retrieved by (a) SeaWiFS and (b) MODIS-Aqua at 77°N 30' and 74°W 55' in the North Water polynya, northern Baffin Bay, on June 24 2004. Variation in remote sensing reflectance at 443 and 555 nm as a function of the sun zenith angle (SZA) for both (c) SeaWiFS and (d) MODIS.

The same general trends were observed at the two locations 50 and 120 km south of the first one (Figure 3.6). However, in the clearest water located at 75°N 45' (Pixel 3 in Table 3.1), a markedly stable nL_w was observed for both sensors (not shown), even though the SZA was approaching 75°. This is above the 70° limit currently used in the L3 binning algorithm. Nevertheless, because there is a spectral dependency in the nL_w differences among the acquisitions, the Chla retrieval is not constant throughout the day, but the variations were relatively small (coefficient of variation of 16%). The MODIS-Aqua Chla retrieval for the acquisition with SZA = 75° was 0.62 mg m^{-3} compared to 0.49 ± 0.03 mg m^{-3} for the six acquisitions obtained the same day. For SeaWiFS, the Chla retrieval for the acquisition with SZA = 72.9° was 0.76 mg m^{-3} compared to 0.52 ± 0.05 mg m^{-3} for the four acquisitions obtained the same day. These results indicate that the 70° threshold for SZA used for the binning of SeaWiFS data may be appropriate or even too high, while it may be pushed beyond 70° for MODIS-Aqua.

Note that for all cases, AC returns very low aerosol optical thickness, with values as low as 0.005 and even lower for SeaWiFS (Table 3.1). These values are likely too low since the atmosphere of the Arctic is known to have a non-negligible amount of aerosols (τ_a(500)= 0.05; Tomasi et al. 2012). This may indicate that the Rayleigh correction applied to the TOA radiance is slightly too high. On the contrary, if the effect of the Earth's curvature was accounted for in the LUTs computation, it would tend to increase the Rayleigh contribution. This is because the Rayleigh contribution to the TOA reflectance is higher in a spherical-shell RT model relative to a plane-parallel model. Therefore, we cannot rule out a possible bias in the absolute calibration of the NIR bands of both sensors.

3.3.3 Implication of the SZA threshold on ocean colour availability

As mentioned above, it might be possible to obtain reliable estimates of nL_w from MODIS-Aqua even at SZA larger than 70°, which is the current limit used in the standard L3 processing. Changing the threshold to a higher value will affect the number of potential observations in autumn, and in the northern hemisphere relative to the southern hemisphere. Here we examine the implications of using a higher threshold for SZA for the Arctic ocean. From the beginning of May to end of July, SZA is suitable for ocean colour observations in almost the entire Arctic Ocean (i.e., for latitudes from 66.68°N to 85°N; ~13 million km^2). Note that prior to May, the SZA is not the main factor reducing ocean colour data availability. Winter and early-spring sea ice contamination affects the usability of ocean colour images in polar seas, while low sun elevation is a factor later in the season when open water is maximum. The impact of increasing the threshold used for L3 generation from 70 to 74° was examined in terms of data coverage for the Arctic Ocean (Figure 3.8). From mid-August to mid-September the amount of data available increases significantly. For example, the current threshold limits observations to <71.87°N latitude on September 15, while a threshold of 75° would permit observations up to 77°N, increasing the total observable area by a factor ~2.5 (3.1 vs 7.6 Mkm^2).

3.4 Issues Related to Clouds

3.4.1 Cloud impact in terms of ocean colour data availability

The Arctic and Southern Oceans are located in the region of the sub-polar low pressure systems, between the polar easterlies and mid-latitude westerlies, where air rises, spreads out, and travels towards the poles. Associated with these semi-permanent low-pressure systems are heavy cloud cover and substantial precipitation in all seasons. According to the climatology (Warren et al. 1988; Rossow and Schiffer 1991), cloud cover is on average 85-90% at 60°S and about 80% at 60°N during spring, summer, and fall. It decreases with increasing latitude to 75% at 80°S, remains about the same between 60 and 80°N during summer, and decreases to 60%

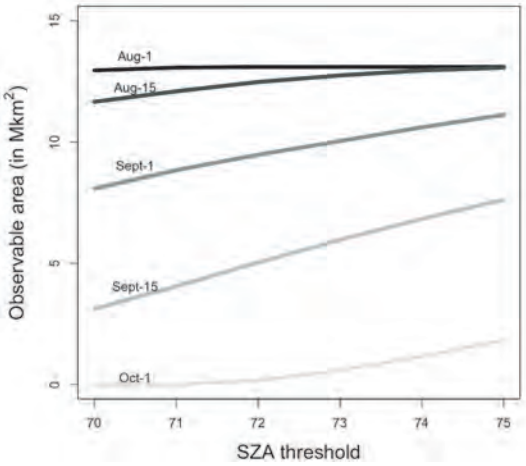

Figure 3.8 Implication of SZA threshold on ocean colour data coverage over the Arctic Ocean. The area is calculated as the area of ocean surface lying between 66.68°N and the latitude at which the SZA is equal to the threshold for a given date.

and 70% at 80°N during spring and fall, respectively. The dominant cloud types are stratiform (stratus, altostratus, and nimbostratus), including a significant amount of cirrus.

Similar to cloud cover, fog also tends to limit ocean colour data availability in polar regions. Indeed, fog, resulting from the condensation of the relatively warm water to cold air above, occurs when sea ice melts and open waters come in direct contact with the atmosphere. For this reason, fog tends to be more frequent in the summer months (Hanesiak and Wang 2005), further reducing ocean colour data availability throughout the year. Since fog presents similar spectral properties as low stratiform clouds, ocean colour data processing does not distinguish between fog and clouds. Therefore, in the next few sections, the impact of clouds on ocean colour data availability also includes that of fog.

Cloud cover is a major problem for satellite ocean-colour remote sensing. In the state-of-the-art atmospheric correction algorithms (e.g., Gordon 1997; IOCCG 2010), the presence of cloud cover prevents the use of ocean colour data, and strict cloud filters are applied to avoid any cloud contamination in the derived products. The impact of clouds is illustrated in Figure 3.9 which shows the percentage of valid combined SeaWiFS and MODIS-Aqua pixels processed into Chla by the NASA OBPG standard algorithm, as a function of latitude, for 15 January and 15 July, 2006. The percentage of valid pixels decreases from 42% at 30°S to 0 at 80°S on 15 January 2006, and from 37% at 30°S to 0 at 55°S on 15 July 2006. This decrease in the percentage of valid pixels is essentially due to cloudiness. Chlorophyll concentration is only retrieved over a small fraction (<10%) of the Southern Ocean on 15 January 2006. During winter, low solar elevation also limits the satellite data processing, explaining the lack of information at latitudes south of 55°S on 15 July 2006.

If ocean coverage is strongly limited by cloudiness on a daily time scale, even weekly products show no information in many areas. This considerably limits the utility of satellite observations, since information every 3 – 5 days is necessary to resolve seasonal biological

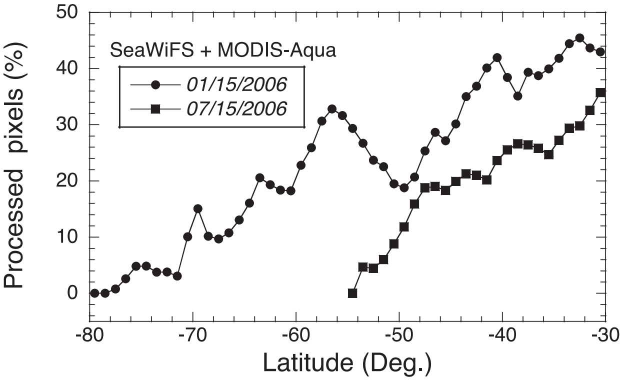

Figure 3.9 Percentage of combined SeaWiFS and MODIS-Aqua valid pixels in Chla imagery as a function of latitude in the Southern Hemisphere, on 15 January and 15 July, 2006. Uniform [0.05, 0.05] degree latitude/longitude boxes in rectangular grid were used to generate the percentage statistics.

phenomena such as phytoplankton blooms (e.g., IOCCG 1999). As an example, Figure 3.10 displays 8-day composite maps of SeaWiFS-derived Chla in the (ice-free) Beaufort and Chukchi Seas for five different periods in summer 2003. During this time, 16% (4 – 11 July) to 56% (28 July – 4 August) of the open ocean pixels were missing, and the monthly variability is not easily inferred in some regions. Figure 3.11 further indicates that during June to October 2003, the percentage of the Beaufort and Chukchi Seas observed in 8-day composites is about 30% in June, peaks to 90% in July, decreases to 50-60% in August and 30% in September and becomes nil in mid-October.

An important issue associated with cloud cover is the number and distribution of retrievals used in generating composite images. Due to ocean biological and physical variability (e.g., phytoplankton growth rates, wind forcing events), the number of observations may not represent adequately weekly or monthly variability in derived ocean-colour products. Perrette et al. (2011) illustrated this limitation in the context of an ice-edge bloom monitoring in the Baffin Bay (see their Figure 3d).

Figure 3.12a displays a composite of chlorophyll-a concentration retrievals for the Arctic Ocean from all available MERIS observations during July 2010, and Figure 3.12b gives the corresponding number of retrievals in the composite for each pixel in the image. In these results, the standard MEGS atmospheric correction algorithm was used to estimate chlorophyll-a concentration. Some regions were observed more than 30 times during a single month due to several overpasses per day at high latitude. The northern part of the Baffin Bay is particularly well documented, with up to 150 observations (see also Section 3.2.2). Many parts of the ocean (45% of total area) are, however, observed less than 30 times, and often the observations are not spaced regularly in time, but concentrated during a few days. A single observation was used to generate the monthly values in 10% of the total area, and 7% of the total area has only 10 observations.

In summary, persistent cloudiness is a serious drawback in the study of high-latitude marine ecosystems. Satellite ocean-colour products provide either no data, or inadequate

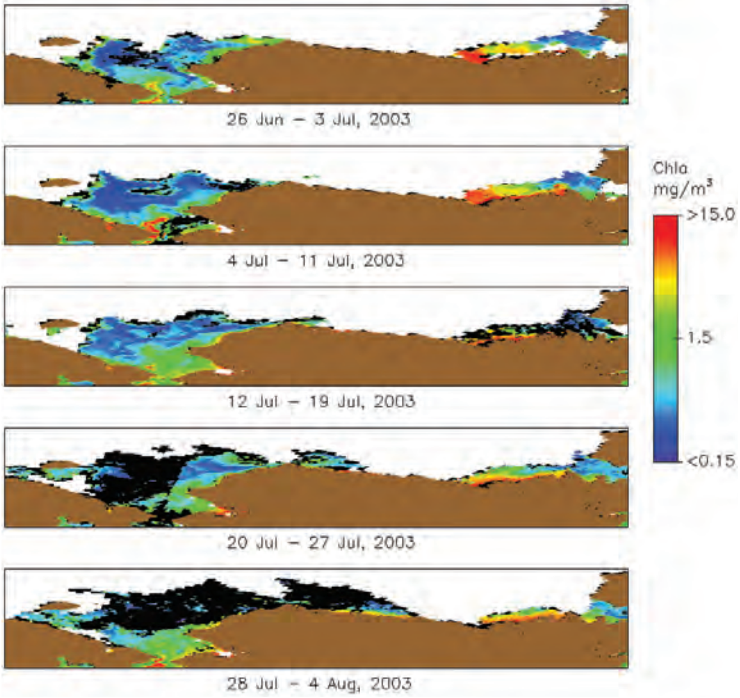

Figure 3.10 8-day Level 3 composites of SeaWiFS-derived Chla in the Chukchi and Beaufort Seas from 26 June to 4 August, 2003. During each week, 18%, 16%, 23%, 45%, and 56% of the open ocean pixels are missing, respectively.

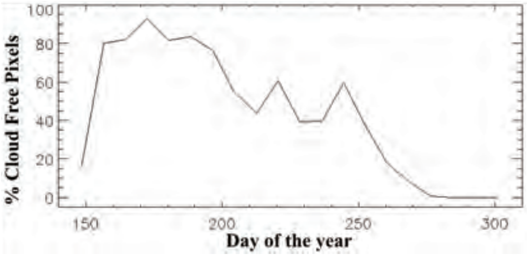

Figure 3.11 Percentage of the Chukchi and Beaufort Seas (ice-free area) for which Chla was retrieved by the standard SeaWiFS processing in 8-day composites from June to October 2003.

sampling in many areas, even in weekly or monthly composites. Improved products in terms of spatial and temporal coverage are necessary to determine the characteristics of Arctic and Antarctic phytoplankton blooms, which develop over relatively short time scales, and to estimate phytoplankton primary production and quantify its annual to inter-annual variability. Multiple polar orbiters increase the daily ocean coverage, but not sufficiently. Addressing the cloudiness issue satisfactorily would contribute to a better understanding and forecasting of air-sea exchanges of carbon dioxide and taxonomic change within phytoplankton communities associated with sea-ice extent and environmental change.

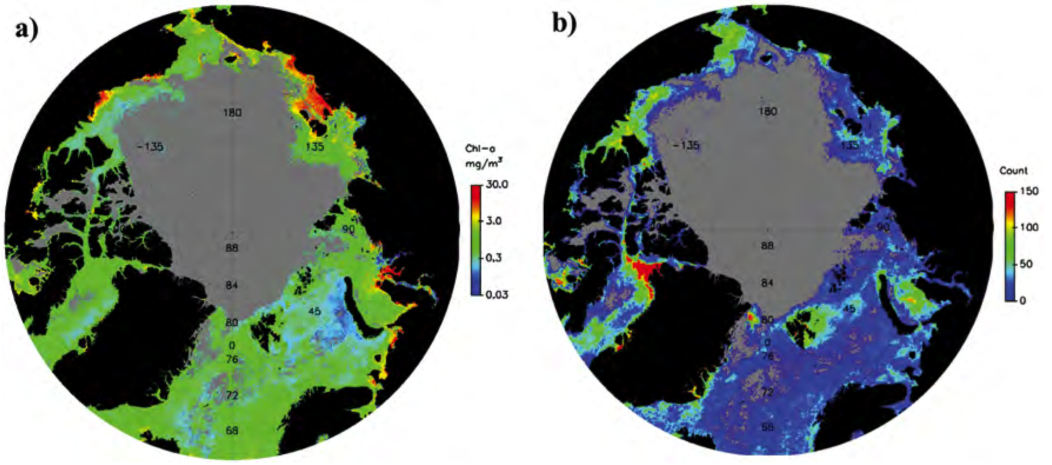

Figure 3.12 a) July 2010 chlorophyll concentration derived from MERIS observations of the Arctic Ocean (MEGS algorithm). b) Number of observations used in composites. 10% of the total area has a single observation, and 7% of the total has only 10 observations.

3.5 Other Issues

3.5.1 Polar aerosols

Atmospheric aerosols are known to play an important role in changing the radiation budget of the surface-atmosphere system, inducing both direct and indirect radiative effects (Quinn et al. 2007). There has been a growing interest in polar aerosols as a result of the importance of the decline in mean annual albedo in the northern latitudes (Tomasi et al. 2012 and reference therein). Following the International Polar Year 2007 – 2009, Tomasi et al. (2012) analyzed time series of derived aerosol optical depth (τ_a) and Ångström's exponent α from a number of Arctic and Antarctic stations to determine the long-term variations of these two parameters.

Several distinctions can be made between Arctic and Antarctic aerosols. While Antarctic troposphere is virtually free of both natural and anthropogenic sources of aerosols, the Arctic troposphere can host multiple sources of aerosols. In the Arctic, a phenomena commonly known as Arctic Haze is observed every year in late spring and early summer (Quinn et al. 2007 and reference therein). Arctic Haze is of anthropogenic origin due to emissions, in particular sulfate aerosols (SO_2), from Europe and the former Soviet Union that are transported to, and trapped in, the Arctic air mass during the winter and early spring (Quinn et al. 2007). The weakness of aerosol removal processes in winter and spring, i.e., photochemical processes and wet deposition, and the strong temperature inversion, are among the factors explaining the accumulation of the aerosols in the troposphere. Peaks of Arctic Haze occur between April to June with values for τ_a at 500 nm > 0.1 and reaching 0.2 (Tomasi et al. 2012). The altitude of Arctic Haze is typically near the surface in spring but can reach higher altitudes at the end of the haze season in June (Quinn et al. 2007).

Northern latitudes are also characterized by episodic emissions of smoke particles from boreal forest fires and by volcanic particles in the stratosphere. For example, Smirnov et al.

(2011) reported values for τ_a at 500 nm > 0.5 in the Beaufort Sea, which resulted from the aerosol transported northward from the Alaskan forest fires. Time series of τ_a at various arctic AERONET coastal sites showed evidence of a relatively high load of stratospheric aerosols after major volcanic eruptions such as Pinatubo, Kasatochi and Sarychev that occurred in 1992, 2008 and 2009, respectively (Tomasi et al. 2012).

Beyond these episodic emission events, the Arctic aerosols background concentration is lower than the global τ_a at 870 nm average of 0.1 (Ahmad et al. 2010). Tomasi et al. (2012) reported that 90% of the τ_a at 500 nm measurements fall between 0.02 to 0.08, with a mode around 0.045. In the Southern Ocean, τ_a rarely reaches values above 0.08, except in a period following major volcanic eruption such as Pinatubo.

The composition of the aerosol determines its optical properties, which are of prime importance for atmospheric correction schemes. In general, atmospheric aerosols in polar regions are small in size yielding efficient back-scatters (Quinn et al. 2002). At Barrow, Alaska, the small fraction is mainly composed of mineral dust and sulfate aerosols while sea salt dominates the coarse fraction. In contrast, the predominant fraction of the coastal aerosols sampled in the Southern Ocean is composed of sea salt, with percentages appreciably greater than 50% and lower fractions of sulphates and mineral dust. As a result, the Arctic aerosols are slightly more absorbing than the Antarctic ones. On average, the single scattering albedo in the visible wavelengths varies around 0.95 and 0.97 for the Arctic and Antarctic aerosols, respectively (Tomasi et al. 2012 and reference therein). Spectrally speaking, the single scattering albedo tends to decrease in the NIR bands. The typical Ångström exponent is around 1 and 1.5 for the Arctic and Antarctic aerosols, respectively (Tomasi et al. 2012).

In summary, these aerosol properties are not markedly different from the ones employed in the NASA standard data processing (Ahmad et al. 2010). They do not present spectral features in the visible and NIR that would invalidate the performance of the atmospheric correction in terms of water reflectance. Nevertheless, a detailed evaluation of the aerosol properties retrieved by ocean colour sensors at high latitude has never been performed. For example, several Arctic and Antarctic coastal sites are equipped with AERONET devices to monitor aerosol properties. The performance of the atmospheric correction retrieval of aerosol optical depth and Ångström exponent could be estimated. Such an evaluation could reveal important insights about the overall performance of the atmospheric correction and help to identify potential improvements.

3.5.2 Turbid waters

As outlined in the previous sections, ocean colour methods still need to be improved to provide accurate space-borne biogeochemical products over polar regions (see also Chapter 4). This is particularly true along the coastal zones where ice contribution affects the retrieved sensor-measured signal. But these coastal regions also present additional issues as they often encompass optically-complex waters, i.e., waters not dominated by phytoplankton and associated materials (also referred to as Case 2 waters, Morel and Prieur 1977). In the literature, most bio-optical models and Earth observation methods have been developed for phytoplankton dominated waters (referred to as Case 1 waters). Indeed, waters presenting anomalous scattering in the visible and near-infrared (Case-2S for sediment-dominated; Morel and Bélanger 2006) often require more complex atmospheric correction algorithms and enhanced Earth observation methods (IOCCG 2000, 2010).

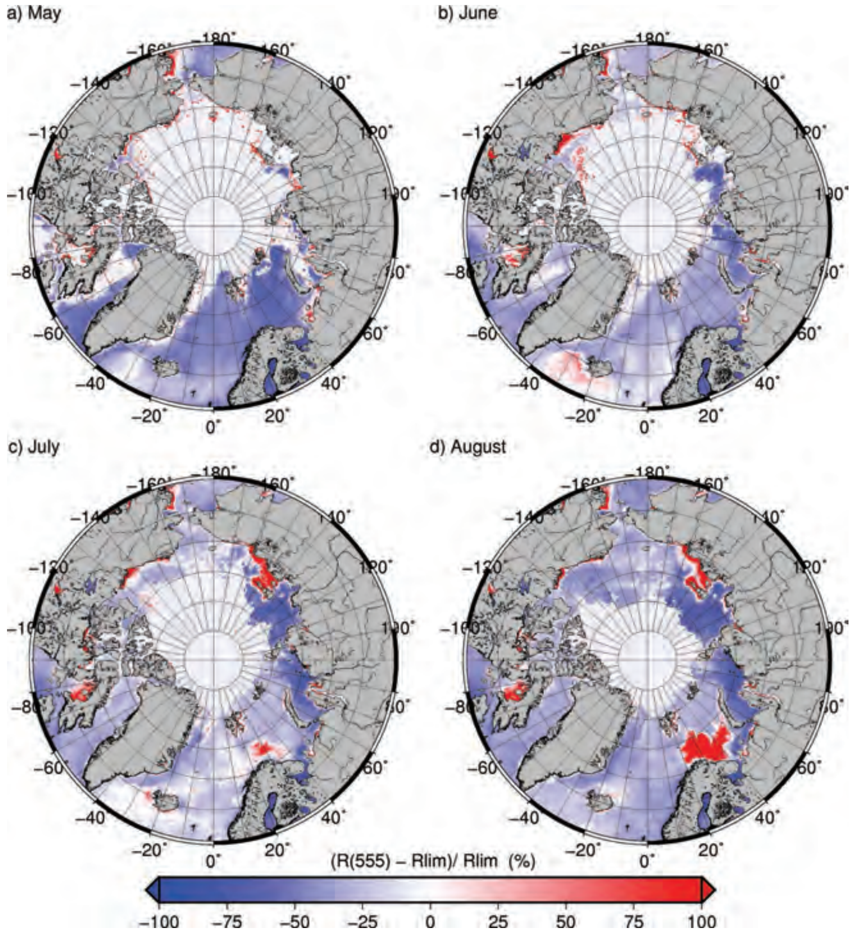

Figure 3.13 Visualization of the Case-2S waters in the Arctic by applying Lee and Hu (2006) criterion to MODIS-Aqua monthly climatology composite distributed by the NASA-OBPG. Results are shown as the percentage relative difference between the actual $R_{rs}(555)$ value and $R_{rs}(555)^{\mathrm{LIM}}$ (see text). Red pixels can be considered as Case-2S waters.

Figure 3.13 shows the presence of Case-2S waters in the Arctic Ocean from May to August based on the climatology of MODIS-Aqua data. Case-2S waters are identified here based on an inclusive Case-1 remote sensing criterion developed by Lee and Hu (2006). The criterion compares the actual $R_{rs}(555)$ with an expected $R_{rs}(555)$ value estimated according to a Case 1 bio-optical model (denoted as $R_{rs}(555)^{\mathrm{CASE1}}$) including a spectral reflectance ratio at 555 and 490 nm (Morel and Maritorena 2001). Hence, any pixel showing a $R_{rs}(555)$ value that deviates by more than 50% from the estimated $R_{rs}(555)^{\mathrm{CASE1}}$ is considered to present anomalous scattering in the visible. As suggested by Lee and Hu (2006), a 50% deviation is used since only a limited number of natural waters follow the quantitative relationships for Case-1 waters. $R_{rs}(555)^{\mathrm{LIM}}$

is therefore defined as 1.5 times $R_{rs}(555)^{\mathrm{CASE1}}$.

According to Figure 3.13, which shows the percentage relative difference between the actual $R_{rs}(555)$ value and $R_{rs}(555)^{\mathrm{LIM}}$, Case-2S waters are mostly encountered in Foxe Basin, along the coast of the Beaufort Sea, along the west-coast of Alaska in the Bering Sea and in the East Siberian Sea, from May to August. Most of these regions are indeed affected by river inputs as well as coastal erosion, resulting in a significant supply of organic matter from coastal land. Figure 3.13 also shows that the presence of Case-2S waters increases from May to August. Indeed, ice-melt and glacial run-off from nearby land also represents a large input in sediment loading. With the ongoing climate change, ice melt and polar precipitation are expected to increase, leading to increased coastal turbidity. In July and August a large patch of anomalous scattering in the visible is also noticeable in the Barents Sea. This patch of Case-2S waters results from coccolithophore blooms, known to occur in late summer in this region (e.g., Smyth et al. 2004).

As demonstrated earlier by Bélanger et al. (2007), in polar regions, turbid pixels are often erroneously identified as sea-ice contaminated pixels due to adjacency effects. Figure 3.13 confirms this plausible confusion between ice contamination and turbid coastal waters. Indeed, speckle patterns of anomalous scattering are observable in the Beaufort Sea, on the Mackenzie Shelf, and in the East Siberian Sea, mostly in May and June. These speckle patterns may result from ice-contamination due to the presence of floating ice sheets. Note, however, that at this time of the year an increase in particulate organic matter (POM) is also expected nearby ice-floes due to multi-year ice melting, but this should not increase $R_{rs}(555)$ due to the highly absorbing nature of POM (Bélanger et al. 2013a; their Figure 9b). Hence, in polar regions, Earth observation methods should consider the spectral properties of optically-complex waters, in addition to the multiple and divergent spectral impacts of sea-ice.

3.6 Detection of Contaminated Data

3.6.1 Detection of adjacency effect and sub-pixel contamination

Bélanger et al. (2007) proposed a simple method to identify pixels contaminated by the adjacency effect, based on examining the spectral shape of the water-leaving reflectance in the violet-blue wavebands, which are the most affected by adjacency effects. The normalized water reflectance band ratio between 412 and 443 [$R_{rs}(412)/R_{rs}(443)$] tends to increase with increasing adjacency effect with values typically above 1. In contrast, the remote sensing reflectance spectra in polar regions tend to present values of [$R_{rs}(412)/R_{rs}(443)$] below 1, because of a higher background in CDOM in those regions (Reynolds et al. 2001; Wang and Cota 2003). The $R_{rs}(412)/R_{rs}(443)$ threshold above which pixels are contaminated by adjacency effects can be adjusted as a function of the reflectance in the green following the relationship:

$$Threshold = C - 0.14\log_{10}\left(\pi * R_{rs}(555)\right), \qquad (3.11)$$

where C is an offset that requires tuning, depending on the region. A value of 0.64 for C was found acceptable for the Beaufort Sea (Bélanger et al. 2007). This threshold is sensitive to the

CDOM concentration, because of the use of the shortest wavebands, and is expected to vary from region to region.

Wang and Shi (2009) also proposed a method to detect ice and sub-pixel contamination when the NIR-SWIR scheme is used to process MODIS data. With this atmospheric correction scheme, cloud masking is made using the 1240-nm channel rather than the typical 865-nm channel (Wang and Shi 2006). While the NIR-based cloud masking can remove most sea ice contaminated pixels, the SWIR-based cloud masking skips several ice-contaminated pixels. This is because sea ice has a rather low reflectance in the SWIR compared with NIR bands (Figure 2.8). Consequently, Wang and Shi (2009) proposed a method to detect ice-contaminated pixels based on the excess of radiance in the NIR bands that resulted after the application of NIR-SWIR atmospheric correction algorithm. In theory, this method will not detect adjacency contamination because the process does not substantially affect NIR wavebands. For polar regions (latitude >55°), it was proposed that pixels with $nL_w(859) > 0.2$ mW cm^{-2} μm^{-1} sr^{-1} are masked (see Wang and Shi (2009) for details).

Examples of the application of these methods are shown in Figures 3.14 and 3.15 using MODIS-Aqua data. Note that the adjacency methods can be applied to any ocean colour sensor, while the ice detection method of Wang and Shi (2009) is suitable only when SWIR bands are used in the data processing. The adjacency flag proposed by Bélanger et al. (2007) performs very well in the Beaufort Sea (Figure 3.14a) as most pixels in the proximity of large sea ice patches are identified. For the same image, the Wang and Shi (2009) flag was raised over the Mackenzie River plume because of the water turbidity (Figure 3.14b), and was also raised in an area where an ice floe is detached from the landfast ice (see Figure 3.14d-e). A closer examination of the MODIS 250-m NIR band confirmed that pixels flagged in this area were affected by undetected small pieces of sea ice (Figure 3.14e). The contaminated pixels found in the ice floe showed slightly higher values of aerosol optical thickness (~0.05 versus 0.02 for the surrounding pixels), but the chlorophyll retrieval did not present evidence of severe contamination when compared to adjacent pixels (not shown). In terms of IOP retrievals, however, undetected sub-pixel contamination has a serious impact on data quality.

The Wang and Shi (2009) method may misinterpret ice-contaminated and turbid waters pixels (Figure 3.14b), because non-negligible $nL_w(\text{NIR})$ is generally found for the latter. At latitudes lower than 55°, Wang and Shi (2009) proposed a second spectral test to distinguish turbid and ice-contaminated pixels using a band ratio ($R_{rs}(555)/R_{rs}(412)$), but this approach failed when sub-pixel contamination produced an underestimation of the reflectance at 412 nm.

Sea ice contamination flagging was tested in two other sectors: in Baffin Bay (Arctic) and in the Ross Sea (Antarctica). A MODIS-Aqua image of Baffin Bay during the ice edge bloom observed in June 2007 was chosen (Figure 3.15a–d). Perrette et al. (2011) described this particular phytoplankton bloom using SeaWiFS imagery (their Figure 3). The use of the MODIS-Aqua 250-m channels was helpful to detect whether potential sub-pixel contamination by sea ice could explain the bloom. According to the sub-pixel contamination flag of Wang and Shi (2009), only a few pixels were affected by small pieces of sea ice (Figure 3.15d). Examination of the 250-nm channel did not show evidence of extensive contamination within the high

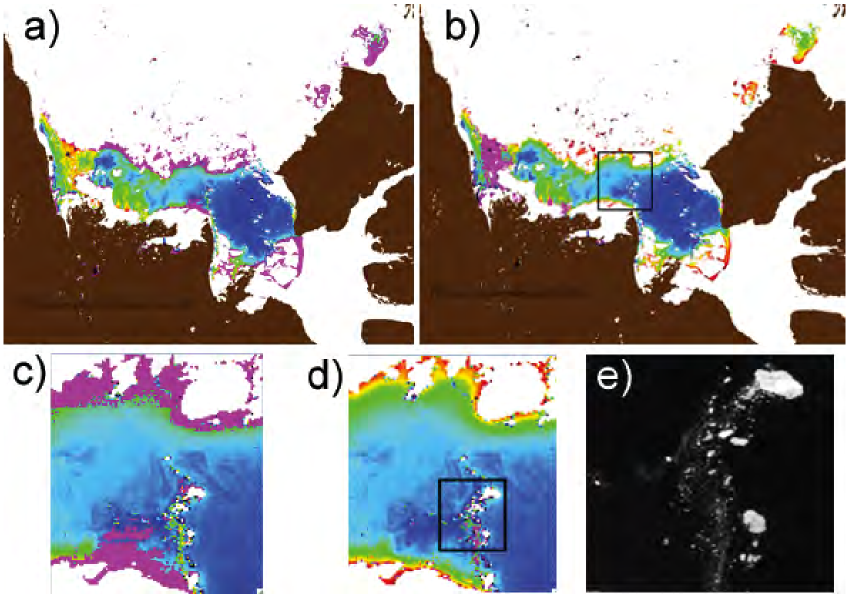

Figure 3.14 Examples of the application of ice-contamination flagging methods (pink) proposed by a) and c) Bélanger et al. (2007) for adjacency contamination (with $C = 0.7$ in Equation 3.11), and b) and d) Wang and Shi (2009) for ice and ice mixed pixels. The black square in panel b) is magnified in c) and d), and that in panel d) is magnified in panel e). Images a) – d) show $R_{rs}(443)$ while image e) shows the surface reflectance of the MODIS 865 nm channel (250-m resolution) which allows a better appreciation of the broken ice field.

chlorophyll patch detected by MODIS (not shown), suggesting that ice edge blooms are not an artifact of ocean colour algorithms.

In contrast, relatively low Chla was observed along the ice edge as a result of the adjacency effect (Figure 3.15b), which artificially increases the blue-to-green water reflectance ratio. The adjacency flag (Figure 3.15c), however, masked out a very large band, up to ~50 km from the ice edge, comprising the bloom itself. This result is incompatible with the simulations performed by Bélanger et al. (2007) which suggested that adjacency effect should not be important >20-km away from the ice edge. The thresholds determined by Bélanger et al. (2007) (Equation 3.11) for the Beaufort Sea are not adapted for optically-different water masses, since the $R_{rs}(412)/R_{rs}(443)$ ratio depends on the magnitude of CDOM absorption, which is much higher in the Beaufort Sea relative to other polar regions. CDOM absorption in the Ross Sea is much lower (Chapter 4), making the reflectance ratio at 412 and 443 nm higher than that of the Beaufort Sea. Consequently, all pixels in the Ross Sea were flagged (Figure 3.15g) with the method. These results indicate that a regional tuning of the adjacency flag threshold is necessary for application of this method at large scale.

In summary, sea ice contamination flagging is possible but the methods are not ready for implementation in the operational processing of ocean colour data. Future work should aim at generalizing the approaches, and exploring other strategies to avoid contamination of high-latitude ocean colour products.

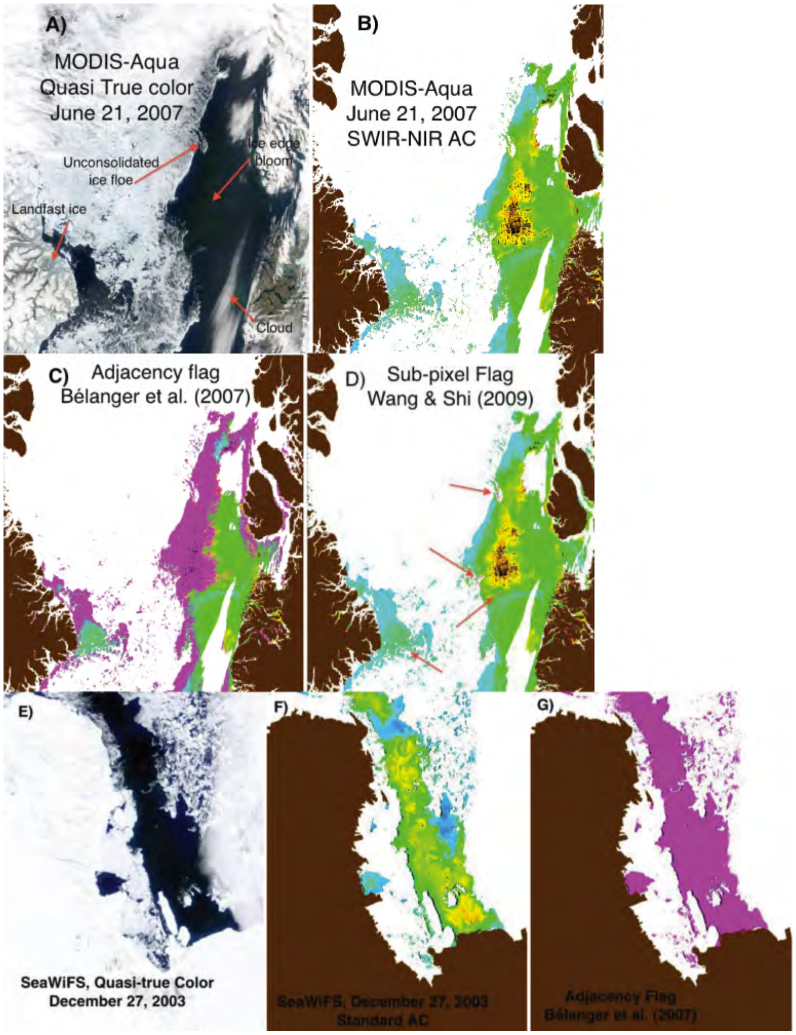

Figure 3.15 Sea ice contamination flagging of on an ice edge bloom in Baffin Bay (MODIS-Aqua scenes a–d) and (e) Ross Sea, Antarctica (SeaWiFS). a) MODIS-Aqua quasi true-colour image; b) Chla derived from OC3 algorithm; c) Bélanger et al. (2007) flag; d) Wang and Shi (2009) flag; e) SeaWiFS quasi true-colour image of the Ross Sea; f) Chla derived from OC4 algorithm; g) Bélanger et al. (2007) flag. Note that the Wang and Shi (2009) flag is not applicable on SeaWiFS as it requires SWIR bands.

3.6.2 Cloud detection in ocean colour algorithms

Ocean colour remote sensing is only possible over oceans with a clear atmosphere (cloud-free), requiring cloud-masking for standard ocean colour data processing (Ackerman et al. 1998). For SeaWiFS and MODIS, Rayleigh-corrected NIR reflectance threshold at 865 nm (869 nm for MODIS) is used to identify clear sky pixels for processing of ocean colour products (Robinson et al. 2003).

Specifically, the standard SeaWiFS/MODIS cloud-masking uses the NIR Rayleigh-corrected reflectance threshold ($\delta\rho^{(RC)}(\mathrm{NIR})$) computed as $\delta\rho^{(RC)}(\mathrm{NIR}) = \rho_{TOA}(\mathrm{NIR}) - \rho_R(\mathrm{NIR})$, where

ρ_{TOA}(NIR) and ρ_R(NIR) are the sensor-measured reflectance and the Rayleigh scattering reflectance from lookup tables, respectively (Gordon et al. 1988a; Wang 2002, 2005). Over open oceans, the NIR ocean radiance contribution is usually negligible (i.e., the black ocean assumption). Thus, the Rayleigh-corrected TOA reflectance results predominantly from aerosol reflectance contributions for clear atmosphere. A threshold value of 2.7% in $\delta\rho^{(RC)}$(NIR) is used for the cloud masking, which corresponds to an aerosol optical thickness of ~0.3 in the NIR for maritime aerosols (Wang and Shi 2006).

The SeaWiFS/MODIS cloud-masking scheme usually performs well over the global open oceans, because the ocean is usually black at the NIR band, and aerosols are generally dominated by maritime aerosols (Smirnov et al. 2002; Knobelspiesse et al. 2004; Wang et al. 2005b). SeaWiFS and MODIS have provided high quality ocean colour products over the global open oceans (McClain 2009), although significant errors in cloud-masking could have occurred in the coastal regions when using the NIR threshold scheme due to ocean contributions in the NIR spectral domain and aerosol reflectance from non-maritime aerosols (e.g., aerosols with small particle size from pollution, Wang and Shi 2006). Subsequently, cloud masking using the SWIR bands has significantly improved performance over coastal turbid waters (Wang and Shi 2006). Corresponding to the Rayleigh-corrected reflectance threshold of 2.7% at the NIR, the reflectance thresholds for the SWIR 1240, 1640, and 2130 nm bands are 2.35%, 2.15%, and 1.75%, respectively.

For sensors without SWIR bands (e.g., SeaWiFS), cloud detection has been improved by using the Rayleigh-corrected reflectance ratio value from two NIR bands in addition to the reflectance threshold at 865 nm. This is simply because clouds are generally spectrally flat and have lower NIR reflectance ratio values relative to ocean and aerosols (Wang and Shi 2006).

In polar regions, however, cloud detection over sea ice is challenging. The SeaWiFS/MODIS cloud-masking scheme may not distinguish clouds from sea ice, since both increase the NIR reflectance beyond the threshold. Note, however, that MODIS Cloud Products (MYD35) are obtained using a combination of several bands including visible, NIR and thermal IR bands. Moreover, the MODIS cloud mask algorithm uses several cloud detection tests allowing the estimation of a confidence level for clear-sky scenes. The MODIS cloud mask algorithm employs up to 14 MODIS spectral bands to maximize reliable cloud detection (Ackerman et al. 1998). Despite significant improvements (Frey et al. 2008), MODIS cloud detection is still negatively biased over sea ice (Liu et al. 2010). A comparison of the MODIS cloud mask product with the Cloud-Aerosol Lidar and Infrared Pathfinder (CALIPSO) indicated a better performance of the algorithm over open water in the Arctic (Liu et al. 2010).

3.7 New approaches for processing ocean colour data and new geophysical products

3.7.1 Advances towards solving the sea-ice and cloud contamination problem

Adjacency effects may be important when viewing the ocean in the presence of snow/ice (Section 3.2). They can be detected using the spectral shape of the retrieved water reflectance

(Section 3.6), or they may also be corrected. This can be accomplished by first applying the selected atmospheric correction scheme ignoring adjacency effects (i.e., assuming that the target is infinitely large). The retrieved water reflectance and aerosol properties can then be used to estimate the environment reflectance $<\rho>$ and the atmospheric functions T_a and t_d, therefore ρ_{env}. In the next step, ρ_{env} is subtracted from ρ_{TOA}/t_g, and the selected atmospheric correction scheme is applied again. This gives a second estimate of ρ_{wN}. After some iterations, a final ρ_{wN} is obtained, corrected for adjacency effects.

The advantage of correcting the ocean colour imagery for adjacency effects, as opposed to detecting its presence, is that the contaminated pixels are not discarded, i.e., spatial coverage of the water reflectance and derived products are not compromised. Computing the environment reflectance $<\rho>$ is, however, computer intensive, since it requires convolving the spatial ρ_w field with the atmospheric spread function over a distance of at least 10 km (the typical horizontal scale of the adjacency effect due to molecular scattering). Furthermore, the atmospheric spread function is critically dependent on the altitude (or scale height) of the aerosols, a parameter not routinely estimated from space. Nevertheless significant improvement in ρ_w retrieval is expected using a typical aerosol profile (e.g., from climatology or an atmospheric transport model). Note that this approach is also applicable to ocean pixels in the vicinity of clouds. Like snow/ice, clouds may scatter unwanted light in the instrument field-of-view. Correcting for this light may contribute to higher quality ocean colour products and larger spatial coverage, a desirable outcome in the Arctic Ocean which is strongly affected by cloud cover (see Section 3.4). In the absence of information about cloud altitude, the correction may assume, in first approximation, that clouds are located at the surface.

Another approach to correct for adjacency effects due to snow/ice and clouds is based on the observation that the perturbing signal from the atmosphere and surface, i.e., $\rho_{path} + \rho_{env}$ in Equation 3.1, varies smoothly with wavelength and can thus be approximated by a polynomial with a few terms. This is the principle of the POLYMER algorithm proposed by Steinmetz et al. (2011), originally developed to process MERIS imagery in glitter-affected areas. The algorithm fits $\rho_{path} + \rho_{env}$ by a polynomial with (1) a non-spectral term that accounts for any non-spectral scattering (clouds, coarse aerosol mode) or reflection (glitter, whitecaps, small ice surfaces), (2) a spectral term with a power law in λ^{-1} (fine aerosol mode), and (3) a spectral term with a power law in λ^{-4} (molecular scattering, adjacency effects from clouds and white surfaces). We recall here that the coupling between molecular scattering (spectral effect in λ^{-4}) and diffuse reflection by a white surface (no spectral effect) varies like $\lambda^{-4}\lambda^{0} = \lambda^{-4}$. No aerosol model is used, giving simplicity and robustness to the algorithm.

Figure 3.16 displays an example of processing in the Beaufort Sea, at the delta of the Mackenzie River. In the top left part of the image, open waters are surrounded by ice floes. The POLYMER processing (middle right, and bottom right) retrieves a consistent marine reflectance at 560 nm over ice-free areas in the middle of the ice pack. The standard MEGS processing, on the other hand, does not account for environment effects (middle left and bottom left), leading to an anomalous increase of water reflectance. This is explained by a too low spectral dependence of the atmospheric signal estimated from spectral bands in the near infrared. Indeed, in this part of the spectral domain, molecular scattering, and subsequently ice reflection from adjacent sea-ice is relatively ineffective.

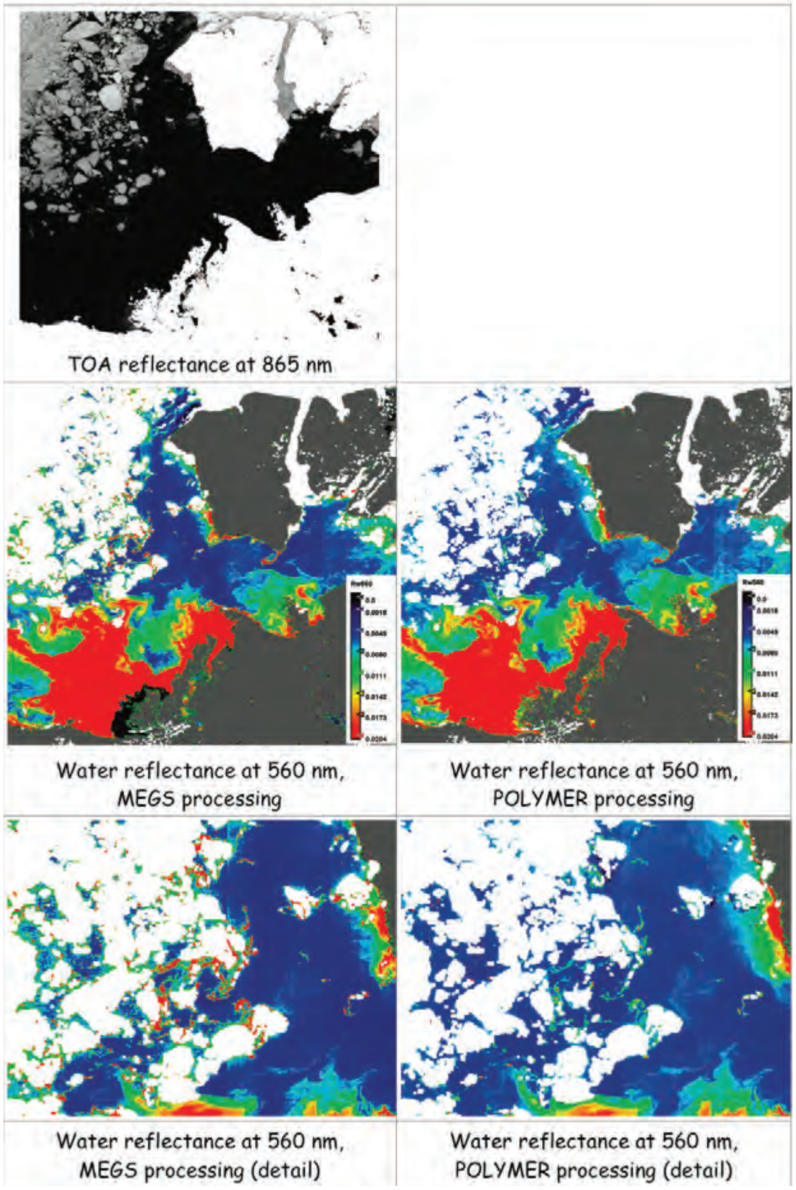

TOA reflectance at 865 nm

Water reflectance at 560 nm, MEGS processing

Water reflectance at 560 nm, POLYMER processing

Water reflectance at 560 nm, MEGS processing (detail)

Water reflectance at 560 nm, POLYMER processing (detail)

Figure 3.16 MERIS image of the Beaufort Sea (4 July 2008), showing that the marine reflectance at 560 nm derived by the POLYMER algorithm is consistent over ice-free areas in the middle of the ice pack, while the MEGS processing is affected by the ice environment, leading to an anomalous marine reflectance increase. (Courtesy of F. Steinmetz, HYGEOS.)

The POLYMER algorithm is also able to handle situations of thin clouds, which makes it especially useful to increase spatial coverage of ocean colour products. The polynomial approximation for the perturbing signal is still valid in such situations, and the effect of cloud transmittance on the water reflectance, not accounted for in the algorithm, is compensated by the effect of the backscattering coefficient for non-phytoplankton particles, one of the parameters used to minimize the difference between modelled and observed TOA reflectance (for algorithm details, see Steinmetz et al. 2011).

Figure 3.17 gives an example of results obtained with MERIS imagery of the Chukchi Sea in the presence of a large semi-transparent cloud. The POLYMER algorithm retrieves marine reflectance in all the thin cloud areas masked by the MEGS algorithm, and the marine reflectance features under the clouds exhibit continuity with those of the adjacent, cloud-free areas. Note that other atmospheric correction algorithms, which also use all available spectral bands for atmospheric correction, have the potential to deal effectively with thin clouds. In the statistical methodology of Gross-Colzy et al. (2007a,b) in particular, large aerosols with optical properties that resemble those of cloud droplets are considered. Therefore, cases of thin clouds are virtually represented in the principal component analysis of the TOA signal, leading to accurate mapping of the useful components to the marine reflectance (for algorithm details and examples of application in the presence of clouds, see Gross-Colzy et al. 2007a,b). Performance in cloudy conditions with this type of algorithms is expected to improve by specifically taking into account realistic cloud cases in the ensemble of simulated TOA reflectance.

3.7.2 Retrieval of sea ice optical properties using ocean colour data

Recent observations of phytoplankton blooms under sea ice (Mundy et al. 2009; Arrigo et al. 2012) has led to a growing interest for remote sensing of sea ice optical properties. In addition, coupled sea ice-atmosphere-ocean-biogeochemical numerical models have predicted significant primary production under sea ice in the future Arctic Ocean (Popova et al. 2010). Light transmission across sea-ice depends on its optical properties, the presence of snow cover and melt ponds etc. (see Chapter 2). The presence of melt ponds, for example, indicates major increase in light transmission through sea ice, significantly impacting the biological activity underneath. Optical sensors used in ocean colour remote sensing may be used, potentially, to derive some optical properties of sea ice.

Until recently, most of the sea ice optical observations have been made *in situ*. Even though *in situ* studies can provide details on sea ice physical and optical properties, they have some limitations. Collecting *in situ* sea ice data at high latitudes is both labor-intensive and time-consuming, and often confined to a relatively short time period. The lack of spatial coverage and long-term observations makes it impossible to study the impact of the sea ice on climate and ecosystems at a large scale. In contrast, satellite remote sensing can provide synoptic views of global land, ocean, and atmosphere. Even though a variety of satellite sensors can provide global sea ice information, such as passive microwave sea ice concentration from the Advanced Microwave Scanning Radiometer EOS (AMSR-E, Cavalieri and Comiso 2000; Comiso et al. 2003), MODIS sea ice extent data (Riggs et al. 1999, 2006), and ice sheet elevation data from the Ice, Cloud, and land Elevation Satellite (ICESat, Kwok et al. 2004; Schutz et al. 2005), no sea ice reflectance data have ever been retrieved for the global ocean in the visible and NIR bands with MODIS observations.

Shi and Wang (2012a,b) demonstrated that sea ice reflectance spectra at MODIS-Aqua visible and NIR wavelengths can be derived reasonably accurately in the Bohai Sea after carrying out

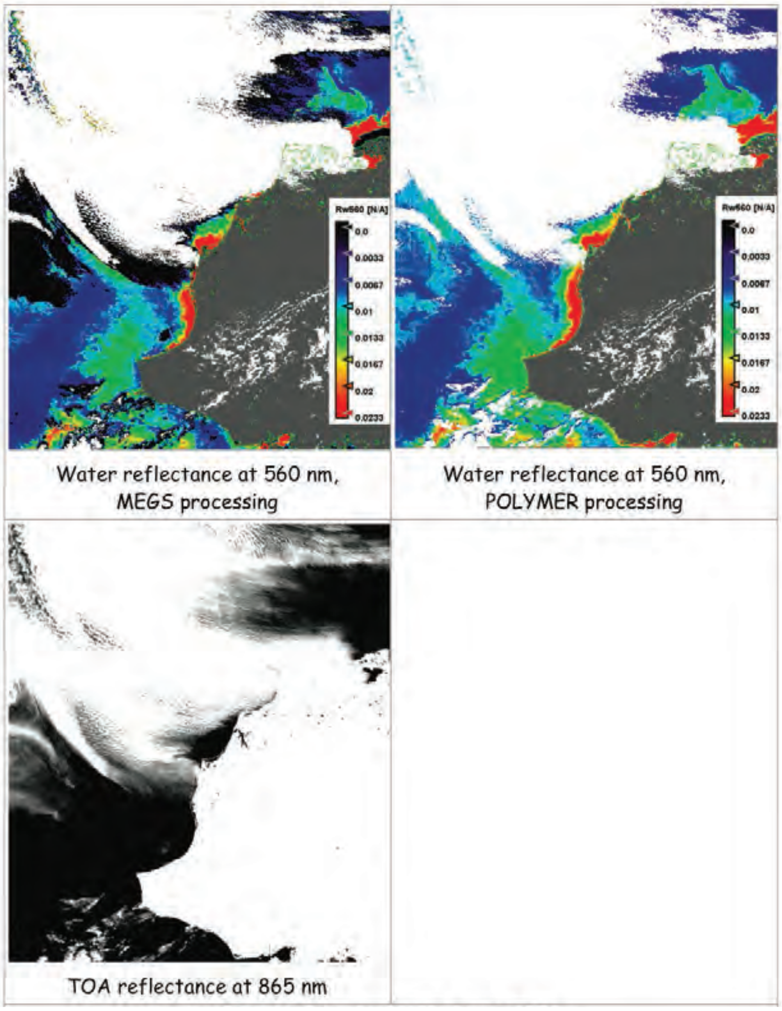

Water reflectance at 560 nm, MEGS processing

Water reflectance at 560 nm, POLYMER processing

TOA reflectance at 865 nm

Figure 3.17 MERIS image of the Chukchi Sea (21 August 2007) showing that water reflectance in the presence of a large semi-transparent cloud is retrieved in some cloudy areas by the POLYMER algorithm (top right), but not by the MEGS algorithm (top left). (Courtesy of F. Steinmetz, HYGEOS.)

atmospheric correction using the MODIS SWIR measurements at the 1640 and 2130 nm bands. *In situ* sea ice spectral albedo measurements in the polar regions show that the spectral albedo values drop sharply from the NIR to SWIR wavelengths for all types of sea ice (Heymsfield and Platt 1984; Perovich 1996). For the MODIS SWIR wavelengths at 1640 and 2130 nm, the sea ice reflectance values are small (normally less than ~0.05), compared with ice reflectance in the visible wavelengths (that can reach ~0.9) for both snow-covered and other types of ice in the polar regions (Perovich 1996). Thus, MODIS SWIR bands at 1640 and 2130 nm can be used for atmospheric correction for deriving sea ice optical properties (Shi and Wang 2012b).

A MODIS-Aqua-measured true colour image on 12 February 2010 in the Bohai Sea, on which sea ice coverage is clearly visible, has been corrected for atmospheric contribution using the MODIS-Aqua bands at 1640 and 2130 nm (Wang 2007). The reflectance values over both the ocean and sea ice (the green-yellow colour on Figure 3.18) are derived at different MODIS wavelengths. Figure 3.18 shows the normalized water-leaving reflectance maps of the entire Bohai Sea at 412, 443, 555, 645, 859 and 1240 nm. Significant contrast can be identified between the ocean water and sea ice coverage for all the wavelengths except 1240 nm. For the ocean water region, normalized water-leaving reflectance $\rho_{wN}(\lambda)$ spectrum is featured with peak values at ~0.15 for 555 and 645 nm bands (Figure 3.19). At 443 and 859 nm, however, $\rho_{wN}(\lambda)$ values are generally weak. At the SWIR 1240 nm band, the normalized water-leaving reflectance is close to zero. For the sea-ice-covered region, reflectance values are significantly enhanced for all the visible and NIR wavelengths. Peak reflectance values over the sea ice region occur at wavelengths of 555 and 645 nm. Sea ice reflectances at these two wavelengths reach over ~0.30 for a large part of the sea-ice covered area in the Bohai Sea.

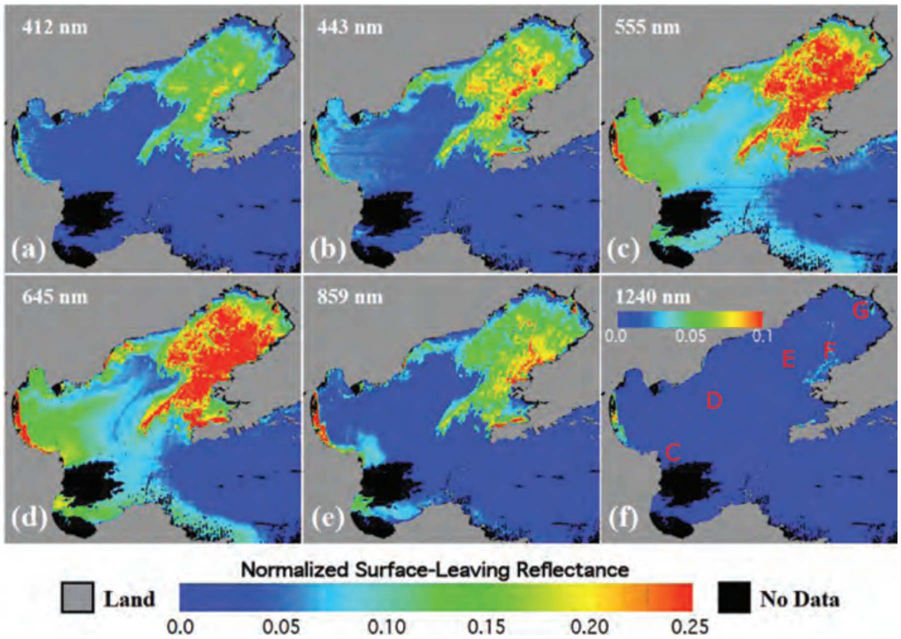

Figure 3.18 Normalized water-leaving reflectance at (a) 412 nm, (b) 443 nm, (c) 555 nm, (d) 645 nm, (e) 859 nm, and (f) 1240 nm derived from MODIS-Aqua measurements on 12 February 2010 using the SWIR atmospheric correction algorithm with the band set of 1640 and 2130 nm. Note that the colour scale for (f) is different from others and is indicated in the panel (from Shi and Wang 2012a).

Figure 3.19 further quantifies the normalized water-leaving reflectance values for different ocean surface types, i.e., coastal turbid waters, central Bohai Sea waters, dark and light ice, grey ice, and grey-white ice. However, it is noted that the properties of sea ice in the polar region are different from those in the Bohai Sea, e.g., the SWIR sea ice albedo in the Polar Region is still significant. Thus, it is still a challenge for deriving accurate sea ice optical property data from ocean colour satellite sensors in the Polar Regions.

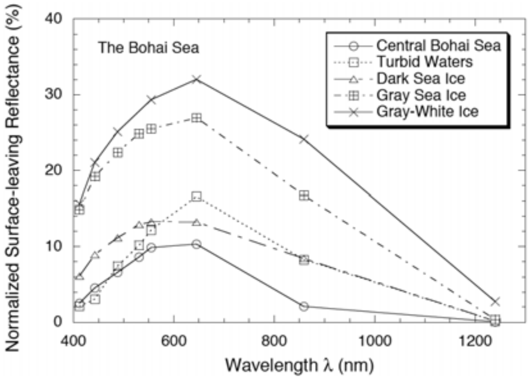

Figure 3.19 Comparison of the satellite-derived normalized water-leaving reflectance spectra on 12 February 2010 for coastal turbid waters at 38.21°N, 119.09°E (location C in Figure 3.18f), central Bohai Sea waters at 39.04°N, 119.62°E (location D in Figure 3.18f), grey ice at 39.89°N, 120.96°E (location E in Figure 3.18f), grey white ice at 40.10°N, 121.36°E (location F in Figure 3.18f), and dark ice at 40.71°N, 121.67°E (location G in Figure 3.18f) (from Shi and Wang 2012a).

3.8 Recommendations

Several conclusions and recommendations can be drawn from this review, the most important of which is the need to assess the overall accuracy of the normalized water-leaving radiance and atmospheric retrievals distributed by the space agencies. In this report, we have shown clear evidence of contamination of the signal by sea ice, but the extent of the problem and how it is reflected in higher level data products (e.g., Level 3) remains to be demonstrated.

- Considering the importance of marginal ice zones (MIZ) in terms of ocean biology and primary production in both poles (Comiso et al. 1990; Perrette et al. 2011), the problem of sea ice contamination needs more attention and new approaches to improve the data coverage and the data quality need to be developed, tested and validated. Data fusion between moderate (300 – 1000 m) and high resolution (10 – 30 m) satellite sensors in the MIZ may be possible with recent and future missions such as Landsat-8, VIIRS, Sentinel-2 and -3, and PACE.
- Low sun elevation strongly limits data coverage in late summer and autumn. Based on radiative transfer calculations and a limited dataset, it may be possible to extract ocean optical properties at solar zenith angles beyond the 70° threshold adopted by space agencies. Before extending the threshold, however, more work is needed to ensure the data quality is not being degraded for the benefit of data coverage.
- Multiple satellite overpasses at high latitudes provide several observations of the same location during clear sky days. These multiple observations offer opportunities to study the SZA problem as well as short-term oceanographic features (e.g., surface currents, phytoplankton growth rates, export production). It also brings into question the method used to aggregate multiple overpasses when producing Level 3 data (e.g., should all observations on a given day be averaged, or only those nearest to noontime?)
- Considering the prevalence of clouds at high latitudes, there may be some data gaps.

Gap filling methods are required when biogeochemical fluxes are estimated from ocean colour data (e.g., primary production, see Chapter 5). This problem needs to be examined in depth, and fusion with *in situ* autonomous systems may be explored in the near future.

- Aerosol retrievals in polar regions need to be examined to obtain new insights in the performance of atmospheric correction algorithms. Weekly and monthly values may be substantially biased.
- Turbid waters occupy a significant fraction of many coastal arctic regions. Although common to all coastal regions, this problem will need to be considered for long-term monitoring of polar ecosystems.

Chapter 4

Ocean Colour Algorithms and Bio-optical Relationships for Polar Seas

Rick A. Reynolds, Atsushi Matsuoka, Toru Hirawake, Simon Bélanger, and B. Greg Mitchell

4.1 Introduction

In this chapter, the performance of existing ocean colour algorithms for estimating the concentration of chlorophyll-a (Chla) in surface waters is assessed when applied to polar oceans and their marginal seas. The discussion is limited to relationships within or immediately above the sea surface, omitting additional challenges to satellite retrievals which arise from low sun angle, atmospheric conditions, and the presence of sea ice. We first examine application of standard empirical algorithms commonly employed for global use, which are based on relationships derived from large oceanic datasets in which polar regions are typically under-represented. We then explore differentiation in underlying bio-optical relationships for polar seas and discuss their potential influence on empirical algorithms. A simplified sensitivity analysis using semi-analytical modelling is used to show that differing bio-optical relationships can explain the observed deviations from empirical algorithms formulated for non-polar waters.

There have been reports in the literature for several years that the relationships between ocean colour and Chla in polar regions differ markedly from lower latitude waters. A multitude of studies (Mitchell and Holm-Hansen 1991; Mitchell 1992; Arrigo et al. 1998; Dierssen and Smith 2000; Hirawake et al. 2000; Reynolds et al. 2001; Korb et al. 2004; Garcia et al. 2005; Mitchell and Kahru 2009) have indicated that standard ocean colour algorithms perform poorly when applied to waters of the Southern Ocean. Similar observations have been noted in the Arctic Ocean and northern polar seas (Mitchell 1992; Sathyendranath et al. 2001; Cota et al. 2003; Wang and Cota 2003; Stramska et al. 2003; Cota et al. 2004; Matsuoka et al. 2007; Naik et al. 2010; Ben Mustapha et al. 2012). The differences are often explained by the adaptation or acclimation of polar phytoplankton to extreme environmental characteristics such as low solar radiation and cold temperature, or because of alterations in the relative abundances and characteristics of other optically-significant constituents resulting from particular geographical settings. These individual studies are based on limited data collected in specific regions, which hinders the extrapolation of the findings to widespread areas.

A further complication arises in that methods for measuring Chla have evolved over time, with different techniques employed by various studies. The fluorometric method, which estimates chlorophyll-a concentration from measurements of stimulated fluorescence by chlorophyll molecules extracted in solvent, has a long tradition in oceanography and has been employed extensively in past studies. It is a relatively simple and inexpensive measurement, but can be subject to inaccuracies caused by the concomitant fluorescence of other pigments present in solution. In modern times, these problems have been circumvented by the development of more advanced techniques such as High-Performance Liquid Chromatography (HPLC) which enable the separation and quantification of individual pigments with much greater accuracy, at the cost of higher analytical complexity and expense. The two measurements are generally highly-correlated, but may exhibit significant offsets relative to one another in some marine environments (Trees et al. 1986; Neveux et al. 1990). This confounds the interpretation of historical results for polar regions, in which the fluorometric method was predominantly used.

Ultimately, systematic deviations from the empirical models observed in polar waters imply differences in the underlying bio-optical relationships. The inherent optical properties (IOPs) of seawater, which are dependent solely on the medium and independent of the directional structure of the light field, strongly influence the magnitude and spectral shape of the light field emerging from the ocean. These quantities include the spectral absorption coefficient, $a(\lambda)$, and the volume scattering function, $\beta(\Psi, \lambda)$, with the latter describing the radiant intensity of light at wavelength λ scattered by a unit volume of water at an angle Ψ per unit irradiance of the incident light beam (see Mobley 1994 for a review of definitions and notation in hydrologic optics). Integration of the volume scattering function over the backward hemisphere yields the spectral backscattering coefficient, $b_b(\lambda)$, which is of fundamental importance to optical remote sensing. To a first approximation, the spectral remote-sensing reflectance, $R_{rs}(\lambda)$, is directly proportional to the backscattering coefficient and inversely proportional to the absorption coefficient through the relationship (Gordon et al. 1988b; IOCCG 2006):

$$R_{rs} \approx C(\lambda) \frac{b_b(\lambda)}{a(\lambda) + b_b(\lambda)}, \tag{4.1}$$

where C is a proportionality factor which merges several directional aspects of radiative transfer and the transfer of light across the sea surface.

The IOPs in turn are directly related to the concentrations and optical properties of water molecules, dissolved substances, and particles — thus providing an important linkage between remote-sensing reflectance and the concentration and relative proportions of seawater constituents. For a seawater suspension containing suspended particles and dissolved materials, both the absorption and backscattering coefficients of the suspension can be viewed as the cumulative sum of the partial contributions by each optically-significant constituent in the medium. For example, the total spectral absorption coefficient of the suspension can be described as:

$$a(\lambda) = a_w(\lambda) + a_g(\lambda) + a_p(\lambda), \tag{4.2}$$

where a_w represents the contribution to absorption by water molecules, a_g is the contribution by coloured dissolved organic material (CDOM, historically referred to as "gelbstoff"), and a_p symbolizes the contribution of suspended particles. Because of the primary importance of algal light absorption to photosynthesis and other biogeochemical processes, the particulate absorption coefficient is often further divided into separate contributions by phytoplankton (a_{ph}) and non-algal "detrital" particles (a_d); i.e., $a_p = a_{ph} + a_d$. Similarly, under the assumption that dissolved substances make a negligible contribution to scattering, the total backscattering coefficient can be partitioned into:

$$b_b(\lambda) = b_{bw}(\lambda) + b_{bp}(\lambda). \tag{4.3}$$

As the range of pure water optical properties is generally small within the ocean, they are often considered as constants. Variability in the absorption and backscattering coefficients of seawater, and consequently R_{rs}, is thus primarily related to changes in the dissolved and particulate matter pools.

A paucity of reliable and comprehensive optical and biogeochemical datasets from polar regions for evaluating such differences is a recurring theme throughout this chapter, and partially reflects the difficulty and cost in accessing and working in these remote regions. However, this same rationale provides the justification for developing a capability for remote sensing of these regions. Fortunately, interest spurred by the most recent International Polar Year (2007 – 2009), and continued observations of environmental changes in these regions, are resulting in an increasing number of studies focused on understanding optical and biogeochemical complexity in these regions.

4.2 Ocean Colour Algorithms in Polar Regions

4.2.1 Empirical models for chlorophyll-a

4.2.1.1 Band ratio algorithms

Chlorophyll-a, the primary photosynthetic pigment present in all phytoplankton, is often employed as a convenient indicator of plant biomass and serves as a basic input to most models of carbon fixation and primary production (see Chapter 5). Chlorophyll-a and co-varying accessory pigments typically have much stronger blue *in vivo* absorption compared to the green or red region of the spectrum, thus changes in the concentration of chlorophyll alter the spectrum (colour) of the light field emerging from the ocean. These changes can be quantified through the remote-sensing reflectance, $R_{rs}(\lambda)$. Over the past few decades, a number of algorithms have utilized changes in the blue-to-green ratio of nL_w or R_{rs} to estimate Chla from passive radiometric measurements obtained by sensors mounted on air- or spaceborne platforms (Gordon and Morel 1983; McClain 2009). Modern satellite missions continue to estimate Chla from such relationships.

One example of this approach is the ocean chlorophyll four-band algorithm (OC4, O'Reilly et al. 2000), which is routinely employed in the global analysis of ocean colour data. This algorithm employs the maximum band ratio (MBR) principle, in which the blue-to-green reflectance ratio is calculated as the maximum value of R_{rs} in three bands (443, 490, and 510 nm) divided by $R_{rs}(555)$. Utilizing an expanded version of the SeaWiFS Bio-optical Algorithm mini-workshop dataset (SeaBAM; O'Reilly et al. 1998), more than 2,800 coincident *in situ* measurements of spectral R_{rs} and surface Chla were used to parameterize a fourth-order polynomial expression which provided the best statistical fit to the observations. Modifications of this algorithm have been adapted for use by ocean colour sensors which measure different spectral bands, such as the OC4E algorithm for ESA MERIS and the three-band OC3M for the NASA MODIS series, and different versions of the algorithm have been released as more data for parameterization become available.

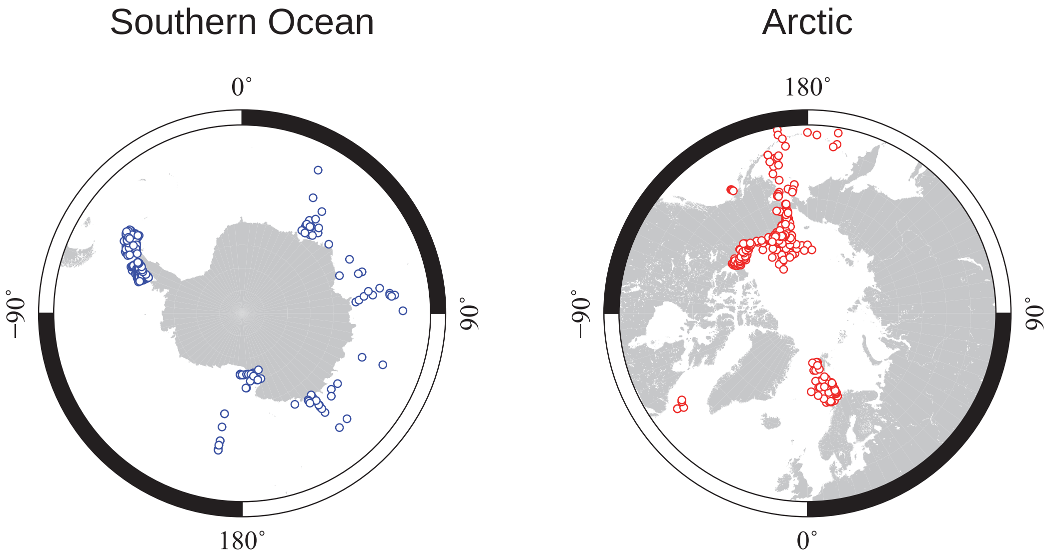

Figure 4.1 Geographic distribution of stations in the polar data set assembled by the IOCCG Polar Seas working group. A description of individual experiments is provided in Table 4.1.

An implicit requirement in such work is utilization of a globally-distributed dataset which represents a diversity of water types and trophic levels; in reality, however, polar regions are often considerably under-represented owing to a lack of measurements. In the formulation of the original OC4 algorithms, only a small fraction of the total number of observations was located in high latitude waters. More recently, a compendium of high-quality, bio-optical data for ocean colour research has been created and made publicly available by the NASA Ocean Biology Processing Group (Werdell and Bailey 2005). The NASA bio-Optical Marine Algorithm Dataset (NOMAD) includes 4,127 stations with coincident radiometric and phytoplankton pigment measurements, and has been used in the formulation of the current version of the OC4 algorithm (OC4v6). High-latitude (>55° S) observations in the southern hemisphere are reasonably well represented in this dataset ($N = 1175$), although the spatial distribution of these stations is heavily weighted towards the Antarctic Peninsula region and the Ross Sea. Measurements in high-latitude northern regions are much more sparse in NOMAD, representing less than 3% of the dataset and located primarily in the north polar Atlantic and Beaufort Sea.

For this report, we supplemented the NOMAD dataset with additional data collected from other field campaigns to polar regions (Table 4.1). A particular emphasis was placed on increasing the number of observations from the Arctic, which is considerably under-represented in NOMAD. An additional 321 stations were added to this polar dataset, mostly from recent projects in the western regions of the Arctic (Beaufort and Chukchi Seas). Sixty-three additional stations were also added to the NOMAD Southern Ocean dataset from Japanese expeditions in the Indian sector of the Southern Ocean (designated as UM in Table 4.1). Figure 4.1 illustrates the location of observations used in the subsequent analysis. We acknowledge that there are still many polar regions where measurements are lacking, particularly in the eastern portion of the Arctic encompassing the extensive Eurasian shelves.

Table 4.1 Polar data sets assembled by the IOCCG Polar Seas working group for use in analyses described in this chapter. *N* represents the number of stations, and the letters in the Chla column indicates the method(s) used for determination of chlorophyll-a (F for fluorometry and H for HPLC). The availability of the data in NOMAD is also indicated.

Experiment	General location	Years	*N*	Chla	In NOMAD	Reference or Investigator(s)
Arctic						
Oceania	N. Polar Atlantic	’98 – ’00	90	F	yes	Stramska et al. 2003
ORCA	Canadian Arctic and Labrador Sea	’97 – ’00	24	F	yes	Wang and Cota 2003
CASES	E. Beaufort Sea	’04	58	FH	no	Ben Mustapha et al. 2012
ICESCAPE	Chukchi and W. Beaufort Seas	’10 – ’11	51	FH	no	Arrigo et al. 2012
KH09-4	Bering & Chukchi Seas	’09	12	FH	no	Fujiwara et al. 2011
MALINA	E. Beaufort Sea	’09	37	FH	no	Antoine et al. 2013
MR	Bering & Chukchi Seas	’08 – ’09	64	FH	no	Fujiwara et al. 2014
OS	Bering & Chukchi Seas	’07 – ’08	56	FH	no	Fujiwara et al. 2011
SBI	Bering & Chukchi Seas	’02	43	FH	no	Hill and Cota 2005
S. Ocean						
AMLR	Antarctic Peninsula	’00 – ’07	117	FH	yes	Allison et al. 2010a
BWZ	Antarctic Peninsula	’04, ’06	21	H	yes	Hewes et al. 2008
I8SI9N	Indian S. Ocean	’07	6	FH	yes	N. Nelson
Palmer LTER	Antarctic Peninsula	’94 – ’99	1005	F	yes	Smith et al. 1995
ROAVERRS97	Ross Sea	’97	8	F	yes	Arrigo et al. 1998
SO JGOFS	Ross Sea, Pacific S. Ocean	’97 – ’98	40	FH	yes	Reynolds et al. 2001
UM	Indian S. Ocean	’04 – ’08	63	FH	no	Takao et al. 2012

Figure 4.2 compares performance of the OC4v6 algorithm with *in situ* measurements from this combined polar dataset. The first panel (Figure 4.2a) illustrates results when the observations are restricted to HPLC measurements of total chlorophyll-a concentration, TChla, which is defined as the summed contribution of the individual concentrations of mono- and divinyl chlorophyll-a, chlorophyllide-a, and allometric and epimeric forms of chlorophyll-a. The second panel (Figure 4.2b) depicts observations with more numerous measurements of fluorometrically-derived chlorophyll concentration (denoted FChla). Qualitatively, the trends

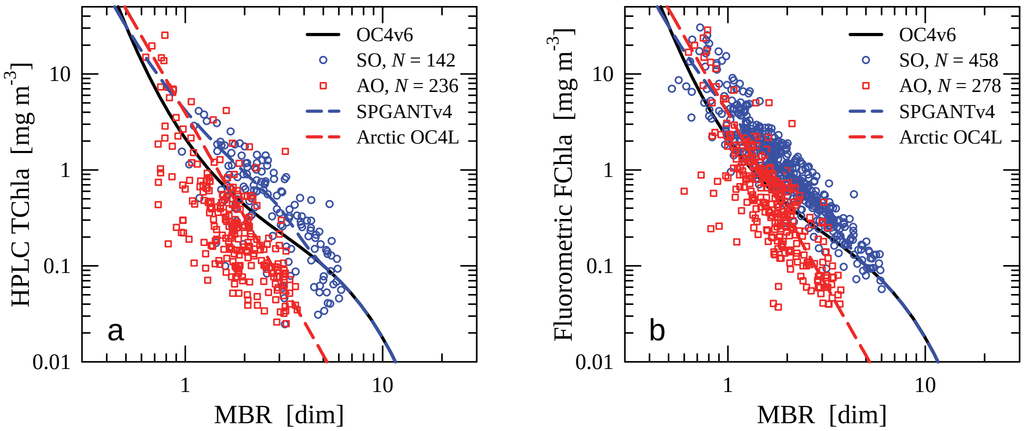

Figure 4.2 Relationships between near surface chlorophyll-a concentrations and the maximum band ratio (MBR) of remote-sensing reflectance measured *in situ*. (a) Observations for HPLC-measured TChla. Blue symbols represent locations in the Southern Ocean, red symbols depict measurements in the Arctic Ocean and surrounding seas. For comparison, the predicted relationships from the global OC4v6 algorithm (black solid line), the SPGANT regional algorithm for the Southern Ocean (blue dash), and the Arctic OC4L regional algorithm (red dash) are shown. (b) As in (a), but for fluorometrically-determined FChla.

are similar in both panels, and we limit our discussion primarily to results obtained with the HPLC method as they represent the current state-of-the-art in pigment analysis and are the recommended analytical method for use in ocean colour validation (Mueller et al. 2003; Hooker et al. 2005). We note, however, that although HPLC measurements are in principle more accurate than fluorometric determinations, as with any analytical technique they are also subject to uncertainties related to methodological differences, calibration procedures, and implementation by the analyst. The relationship between the two Chla estimates is presented in Figure 4.3 for cases when both measurements were present and reported.

Statistical measures comparing algorithm estimates of surface chlorophyll with measurements of HPLC TChla are provided in Table 4.2. The observations for the Southern Ocean confirm previous reports that global algorithms such as the OC4 generally underestimate Chla over much of the observed range of data (Chla > 0.1 mg m^{-3}). On average the OC4 algorithm under-predicts Chla by about twofold, with a value of 0.47 for the slope of the linear regression comparing observed and predicted values and a value of 0.61 for the median ratio (MdR) of $\mathrm{Chla}_{\mathrm{OC4}}$ to TChla. A bias of similar magnitude is also observed for FChla throughout this range (MdR = 0.51), suggesting that differences in pigment methodology are not the sole explanation. This bias is greatly reduced when measured Chla values are less than 0.1 mg m^{-3}, with the observations suggesting a small (10%), but generally consistent, overestimation of the HPLC values by OC4v6.

Figure 4.2 also depicts the behavior of a regional algorithm, designated SPGANT, developed specifically for use in the Southern Ocean (Mitchell and Kahru 2009; Kahru and Mitchell 2010). SPGANT is a MBR-based algorithm similar to OC4 but parameterized using a Southern Ocean

Table 4.2 Summary of statistical properties for the comparison of near surface chlorophyll-a concentrations computed using either the OC4v6 algorithm, the SPGANTv4 algorithm, or the Arctic OC4L algorithm with measurements of HPLC TChla (Figure 4.2).

Property	**Southern Ocean**		**Arctic**	
	OC4v6	SPGANTv4	OC4v6	OC4L
$N^{\dagger}$	142	142	236	236
r	0.65	0.67	0.67	0.67
Slope	0.47	1.02	0.53	1.07
MdR	0.61	1.04	2.45	1.99
MdAPD (%)	53.6	43.6	144.8	99.4
RMSD (mg m^{-3})	0.65	0.61	2.10	2.44

† N is the number of paired observations in the comparison. The value of r is the correlation coefficient between the predicted (P_i) and observed (O_i) values and slope indicates the geometric mean slope of a Model II linear regression. MdR is the median ratio of P_i to O_i, and MdAPD is the median value of the individual absolute percent differences calculated as $\text{APD}_i = 100|P_i\text{–}O_i|/O_i$. RMSD represents the root mean square deviation.

dataset of radiometry and a combination of fluorometric and HPLC chlorophyll determinations. SPGANT produces substantially higher estimates of Chla in the range 0.1 – 10 mg m^{-3} which reduces the average bias to <5% as compared to OC4. The algorithm employs a blended weighting scheme over the MBR range of 3 – 5 to force convergence with the OC4 algorithm at low values of Chla (Kahru and Mitchell 2010).

In contrast to the Southern Ocean, observations from the Arctic Ocean and surrounding seas suggest that Chla is overestimated by the OC4 algorithm for much of the dataset (Figure 4.2). For the entire Chla range the average value of this bias is nearly +150%, with the largest over-predictions (exceeding 1000%) occurring for Chla < 0.5 mg m^{-3}. For concentrations similar to those observed in phytoplankton bloom situations (> 3 mg $^{-3}$), however, Chla is generally underestimated by the global OC4 algorithm. Such behaviour is of particular importance to estimates of primary production.

These observations are consistent with those reported by Cota et al. (2004) using a dataset obtained from measurements in high-latitude northern waters. They proposed a modified, linear version of the OC4 (dubbed the Arctic OC4L) for regional application in the Arctic Ocean. Matsuoka et al. (2007) reported an improvement in performance using the Arctic OC4L as compared to the standard OC4 when compared to FChla measurements from the western Arctic, with the exception of strongly turbid stations exhibiting high values of reflectance. In the low Chla range, both Matsuoka et al. (2007) and Ben Mustapha et al. (2012) concluded that the bias observed in waters of the Arctic Ocean was due to higher background concentrations of CDOM relative to the open ocean. For the current dataset, the Arctic OC4L algorithm provides better estimates at the lower and higher range of chlorophyll concentration, and yields an overall reduction in bias and prediction error as compared to the standard OC4. This trend is also observed for the relationship with fluorometrically-derived Chla measurements, which were used in the original formulation of the algorithm. However, because of the large scatter observed in the Arctic dataset, the absolute prediction errors and the RMSD remain large. Such a degree of variability makes it difficult to establish standard empirical formulations that will provide robust predictions with acceptable error limits, at least on the scale of the entire Arctic region.

A portion of the scatter observed in Figure 4.2 is also associated with spatial differences in the behaviour of algorithm performance, where the presence of strong consistent biases in the relationship is associated with some regions. For example, in the Southern Ocean, OC4v6 generally under-predicts measured values of TChla by 30 – 50% in the Antarctic Peninsula region. In the Arctic, the general over-prediction of TChla observed over the continental shelves is particularly high in the eastern Beaufort Sea (usually exceeding 400%), illustrating the strong influence of the Mackenzie River on seawater optical properties in this region.

4.2.1.2 The issue of HPLC vs. fluorometric chlorophyll concentration

Most of the algorithms described above have been formulated utilizing pigment estimates obtained fluorometrically, or using some combination of fluorometric and HPLC-determined chlorophyll concentrations. As a result, predictions from these algorithms often improve when compared with FChla as opposed to HPLC TChla. However, such differences in the methodology employed for determination of Chla also confound the parameterization and interpretation of these algorithms. This is a particularly relevant issue for polar seas, which have only a limited number of observations in general and much of the older, historical data consists solely of fluorometric measurements.

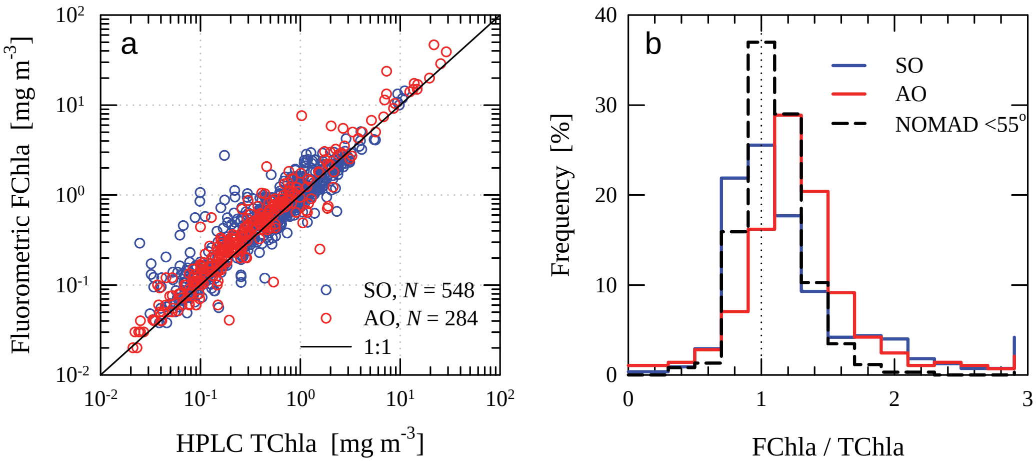

Figure 4.3 (a) Comparison of HPLC TChla and fluorometrically-derived FChla for the polar data set, (b) frequency distributions for the ratio of FChla to TChla. The distribution obtained from NOMAD with lower latitude samples (<55°) is also depicted for comparison.

Figure 4.3 illustrates the relationship between HPLC TChla and fluorometrically-derived FChla for observations in the present dataset, with statistical measures of the relationship provided in Table 4.3. For comparison, similar statistics are also reported for the relationship observed in lower latitude waters using the NOMAD dataset. Overall, the three datasets suggest a strong correlation between FChla and TChla ($r > 0.9$ in all cases) and show similar statistical trends. FChla values are generally higher than measurements of TChla made with HPLC by ~10 – 20%. The results of this comparison from the Arctic suggest a somewhat higher positive bias than that observed for the Southern Ocean or lower latitudes.

Table 4.3 Summary of statistical properties for the comparison of surface chlorophyll-a concentrations measured with both HPLC (TChla) and fluorometry (FChla) in the polar data set (Figure 4.3). Statistics are also reported for lower latitude data (<55°) from the NOMAD dataset for comparison.

	Southern Ocean	**Arctic**	**NOMAD** (<55°)
$N^{\dagger}$	548	284	603
r	0.95	0.94	0.97
Slope	1.12	1.41	1.20
MdR	1.08	1.24	1.07
MdAPD (%)	20.5	28.5	13.2
RMSD (mg m^{-3})	0.44	2.04	1.38

† In Table 4.3, statistical measures are calculated in a similar manner as described in Table 4.2, but with TChla treated as the observed variables, O_i, and FChla as the predicted variables, P_i.

Despite good relationships for the aggregated data from each region, for individual experiments or cruises the comparison can exhibit much greater discrepancies. An example of such bias is particularly evident in the results from the UM experiment in the Southern Ocean, in which fluorometric values of Chla are typically more than twofold higher than those determined from HPLC over the range spanned by concurrent measurements (0.02 – 1.1 mg m^{-3}). On these cruises, the solvent employed to extract pigment samples was N,N-dimethylformamide (DMF) for fluorometry as opposed to methanol extraction for HPLC, so methodological differences may also contribute to this larger difference.

Large systematic differences between HPLC and fluorometric Chla have been reported previously in both polar regions. Ben Mustapha et al. (2012) noted that in the southeastern Beaufort Sea, FChla values (extracted in 90% acetone) were often two times greater than TChla (extracted in 100% methanol) determined on the same samples. A similar bias, but of lesser magnitude, was reported for north polar Atlantic waters by Stramska et al. (2003). Within the Southern Ocean, similar discrepancies have also been reported in the Antarctic Polar Front Zone (APFZ) (but were not observed in the Ross Sea) (Reynolds et al. 2001) and the Antarctic Peninsula region (Marrari et al. 2006). Reynolds et al. (2001) noted that the HPLC-derived Chla values in the APFZ could not be easily reconciled with independent optical measurements, for example the use of HPLC determinations resulted in calculated Chla-specific absorption coefficients in the red absorption peak well above values observed and reported in numerous laboratory and field studies, suggesting a potential issue with HPLC values. In contrast, Marrari et al. (2006) stated that HPLC TChla provided a much better match to SeaWiFS-derived Chla using the standard OC4 algorithm, and attributed the discrepancy in FChla measurements to contamination of the fluorometric signal by the presence of chlorophyll-c in the samples.

At the present time, this is an outstanding question with no definitive answer. As observed in Figure 4.3 and reported elsewhere, there are situations in which the agreement is good, as well as occasions in which there is a significant bias. Although systematic errors arising from methodological issues cannot be ruled out for any given dataset, some discrepancies may also be related to the physiological state and species composition of the phytoplankton assemblage, and thus will be regionally- and time-dependent. It is probable that a portion of the overall scatter observed in Figure 4.2 is related to these discrepancies, but we note that regardless of the Chla method used, a similar general bias from the global OC4 algorithm is observed. This contradicts the general assertion of Marrari et al. (2006) that use of TChla leads to no deviation from the OC4 algorithm, and that the Southern Ocean as a whole is consistent with the lower latitude waters.

4.2.1.3 Intercomparison of algorithms when applied to ocean colour images

The choice of algorithm for chlorophyll retrieval can lead to substantial differences in the interpretation of ocean colour from polar regions. As surface Chla is a primary input to nearly all existing models of primary production (Chapter 5), the choice also strongly impacts estimates of ecosystem productivity and biogeochemical cycles. As an illustration, three satellite images obtained with the MODIS-Aqua sensor were selected from each polar region for intercomparison of derived surface concentrations of Chla computed using different algorithms (Figure 4.4). The analyzed scenes, described in Table 4.4, were chosen based on criteria related to minimal cloud coverage, the presence of strong gradients, and representativeness of particular conditions. These scenes are identical to those chosen for an intercomparison of primary production models in Chapter 5, in which surface Chla is a common input to most of the tested models.

Table 4.4 Ocean colour images from MODIS-Aqua selected for intercomparison of Chla algorithms (Figures 4.4 and 4.6). Selected data files represent Level 2 Local Area Coverage (LAC) files with a resolution of 1.1-km. Data courtesy of NASA Ocean Color Web (Feldman and McClain 2012).

	Region	Date	Filename
S. Ocean	W. Antarctic Peninsula	24 February 2003	A2003055183000.L2_LAC
	Ross Sea	10 December 2010	A2010344035000.L2_LAC
	Prydz Bay	2 January 2010	A2010002093000.L2_LAC
Arctic	Barents Sea	5 July 2004	A2004187082000.L2_LAC
	Chukchi Sea	22 August 2008	A2008235233000.L2_LAC
	Beaufort Sea	18 September 2007	A2007261212000.L2_LAC

Three chlorophyll algorithms were selected to obtain Chla estimates from each of the selected images; version 6 of the standard MODIS algorithm employed for global processing (OC3Mv6), regional empirical algorithms modified for available MODIS wavebands (SPGANT for the Southern Ocean, OC4L for the Arctic), and the globally-optimized version of the Garver-Siegel-Maritorena model (GSM; Maritorena et al. 2002). The GSM is a so-called semi-analytical inversion model (described in Section 4.2.3), which estimates Chla and additionally provides the spectral absorption and backscattering coefficients of selected seawater constituents.

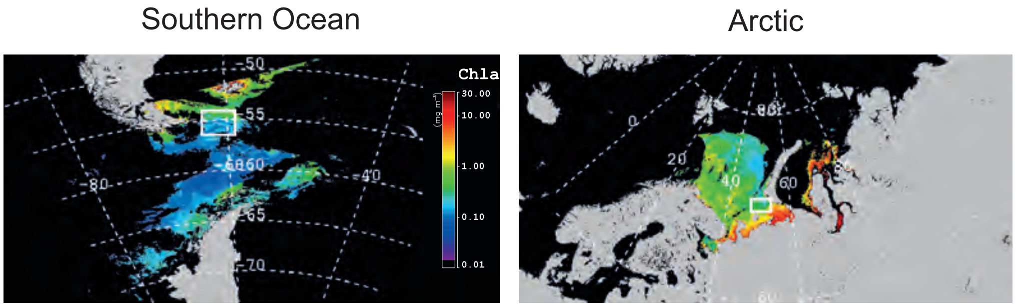

Western Antarctic Peninsula

Barents Sea

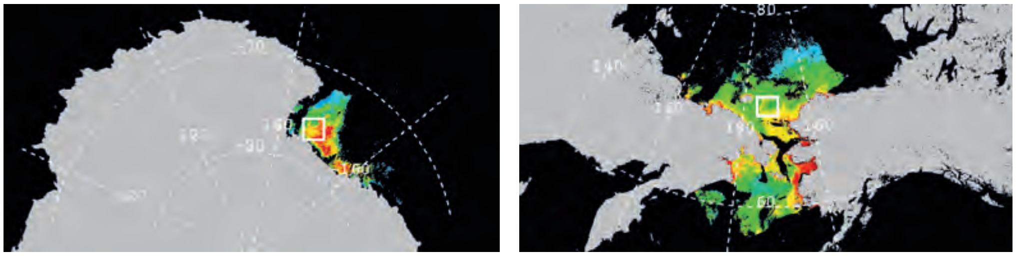

Ross Sea

Chukchi Sea

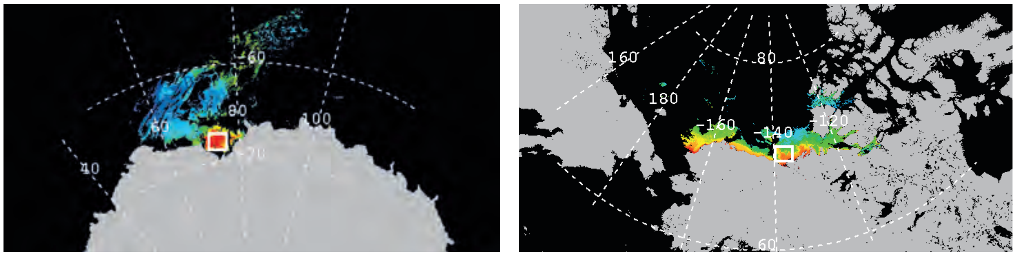

Prydz Bay

Beaufort Sea

Figure 4.4 Projections of MODIS-Aqua false-colour images used for intercomparison of Chla algorithms. Surface Chla is calculated using the global OC3Mv6 algorithm, and displayed according to the colour bar scale depicted in the top left panel. Grey pixels represent land, and black pixels indicate a lack of data owing to the presence of clouds, ice, or invalid measurements. The white boxes denote regions selected for the analysis shown in Figure 4.5 and Table 4.5. Additional scene information is provided in Table 4.4.

All processing was done using the SeaWiFS Data Analysis System (SeaDAS; Baith et al. 2001) v. 6.3 software. Figure 4.4 illustrates projected false-colour images of Chla derived from each of the scenes using the OC3M algorithm. Calculated values of Chla span the range from less than 0.05 to greater than 50 mg m^{-3}, and the presence of strong gradients and complex patterns in surface Chla concentration are evident in each of the regions.

To quantitatively relate the results obtained from the different algorithms, a small region of each scene was chosen for a comparative analysis of algorithm output (delineated by the white boxes in Figure 4.4). Figure 4.5 depicts histograms of the relative frequency distribution of chlorophyll-a concentration computed for each of the three algorithms within the identified region of each image. Statistical measures characterizing each distribution are provided in

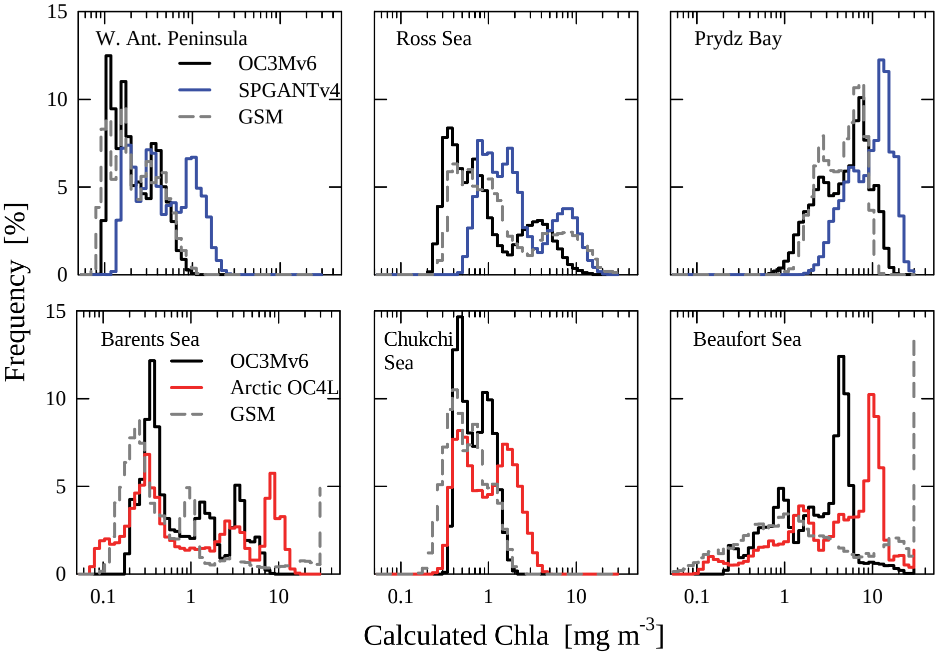

Figure 4.5 Frequency distributions of surface Chla computed from the selected sub-scenes shown in Figure 4.4 using different algorithms. The standard global MODIS algorithm (OC3Mv6), regional models for the Southern Ocean (SPGANTv4) and the Arctic (OC4L), and results from a semi-analytical model (GSM) are depicted.

Table 4.5. It should be noted that the purpose of this exercise is simply to demonstrate the differences in the derived Chla values that are obtained dependent upon the choice of algorithm; in the absence of ground truth measurements, we have no objective basis from which to state one algorithm as superior to another. However, several studies have confirmed that the use of regional algorithms in the polar regions generally improves the agreement with *in situ* measurements of Chla (e.g., Holm-Hansen et al. 2004; Matsuoka et al. 2007).

The distribution of Chla from OC3M in all scenes is multi-modal, and this behavior is also reproduced in the regional and GSM algorithms. The location and relative width of peaks within the distribution varies with algorithm. As expected from the results shown in Figure 4.2, use of the SPGANT regional algorithm within the Southern Ocean shifts the frequency distribution of Chla within each image towards higher concentrations than those observed with the global OC3M, resulting in a median concentration value computed from each of the Southern Ocean scenes 2 – 2.4 times greater. The greatest difference is observed in the Ross Sea example, in which the majority of observations are in the intermediate range of Chla (~0.5 – 5 mg m^{-3}) where the maximum differences in the algorithms occur. SPGANT also increases the range and standard deviation of the values in each distribution. The results of the GSM are generally comparable with those of OC3M for the West Antarctic Peninsula (lowest biomass) and Prydz Bay (highest biomass), but provides significantly higher Chla estimates for the Ross Sea.

Table 4.5 Statistical properties derived from the selected regions of the MODIS-Aqua images shown in Figure 4.4. For each sub-scene, surface Chla was computed using the standard global MODIS algorithm (OC3Mv6), a regional algorithm parameterized for the Southern Ocean (SPGANT) or for the Arctic (OC4L), and the GSM semi-analytical algorithm. *N* indicates the number of pixels, SD the standard deviation, and all statistical values represent Chla in units of mg m^{-3}.

S.Ocean	**W. Antarctic Peninsula**			**Ross Sea**			**Prydz Bay**		
Algorithm	OC3M	SPGANT	GSM	OC3M	SPGANT	GSM	OC3M	SPGANT	GSM
N total	43648	43648	43648	34918	34918	34918	29151	29151	29151
N invalid	534	534	650	0	0	0	2698	2698	2747
Minimum	0.00	0.00	0.05	0.21	0.46	0.21	0.60	1.50	0.09
Maximum	1.13	2.70	1.41	22.4	36.4	64.3	274.1	844.3	245.7
Mean	0.26	0.60	0.27	1.58	3.29	2.99	5.71	10.7	4.98
Median	0.20	0.41	0.20	0.70	1.72	1.02	5.18	10.3	4.75
Mode	0.11	0.18	0.11	0.34	0.77	0.39	2.26	4.80	2.66
SD	0.16	0.45	0.19	1.93	3.41	4.37	4.34	8.88	3.00
Arctic	**Barents Sea**			**Chukchi Sea**			**Beaufort Sea**		
Algorithm	OC3M	OC4L	GSM	OC3M	OC4L	GSM	OC3M	OC4L	GSM
N total	38577	38577	38577	36960	36960	36960	35334	35334	35334
N invalid	78	78	1198	28	28	28	6794	10248	7990
Minimum	0.18	0.07	0.01	0.18	0.07	0.12	0.21	0.09	0
Maximum	9.9	18.8	999.1	2.25	5.23	2.69	329.5	813.2	998.9
Mean	1.37	2.67	7.07	0.76	1.18	0.66	3.31	6.90	20.7
Median	0.53	0.62	0.36	0.68	0.95	0.54	2.69	4.88	1.63
Mode	0.36	0.31	0.20	0.41	0.42	0.43	0.85	0.13	0.17
SD	1.55	3.51	39.7	0.32	0.77	0.37	4.70	12.5	64.0

Within the Arctic, the use of the OC4L regional algorithm yields a wider range of computed Chla values (lower minima and higher maxima in observed concentrations) which leads to a greater standard deviation than provided by the standard OC3M algorithm. This is a consequence of the OC4L relationship crossing the OC3M algorithm at a Chla value of ~0.8 mg m^{-3} (Figure 4.2), with increasing divergence as Chla values depart from this value. The increased frequency of higher chlorophyll-a concentrations computed from OC4L leads to higher average concentrations computed from each subscene, despite an additional increase in the frequency of low Chla values (most evident in the Barents Sea). The GSM generally shifts the frequency distribution over much of the range to lower Chla than either of the empirical algorithms, but in the Barents and Beaufort Seas also increases the number of higher (> 2 mg m^{-3}) Chla values. A large number of computed concentrations from the GSM are, however, unrealistically high (>50 mg m^{-3}) and are generally associated with nearshore coastal regions where terrestrial influences on both the ocean and atmosphere are strongest (e.g., eastern Beaufort Sea), indicating that challenges remain in application of such algorithms for use in many regions of the Arctic.

Figure 4.6 illustrates the different Chla spatial distributions obtained for the three algorithms when applied to a single scene from each region; the Ross Sea in the Southern Ocean, and the Chukchi Sea in the Arctic.

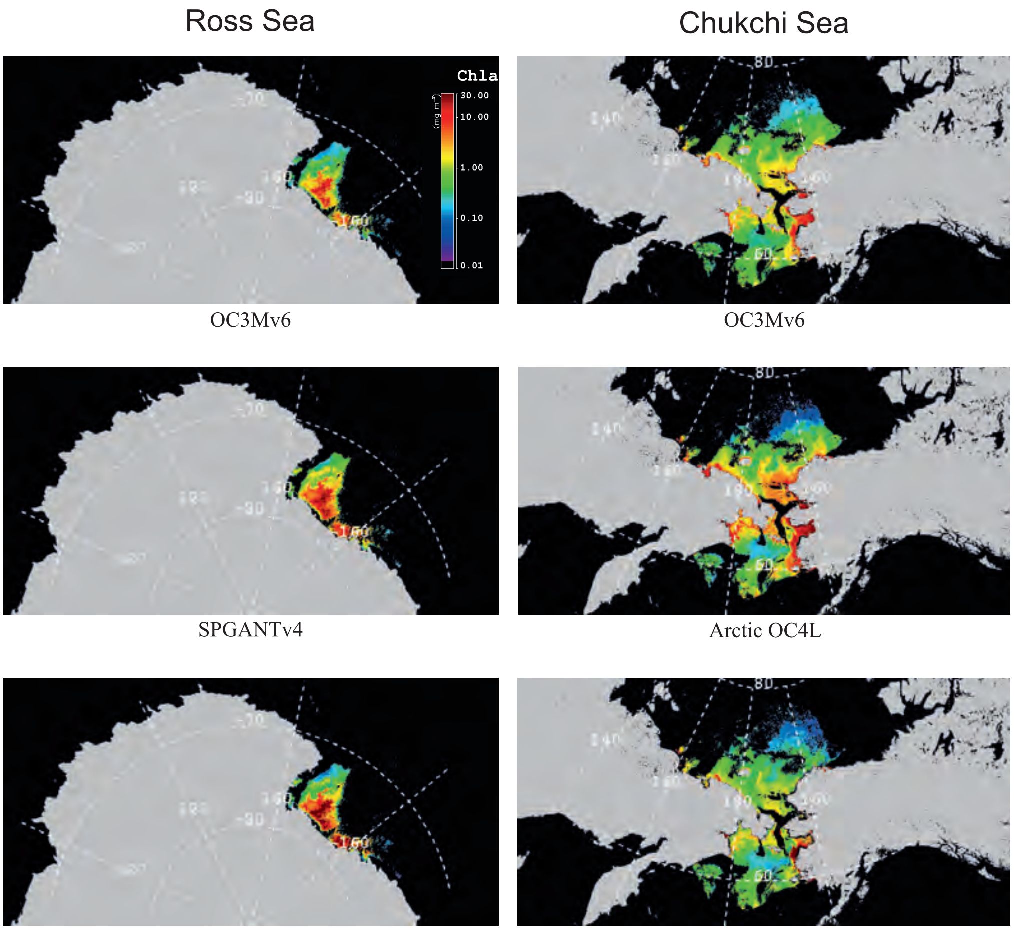

Ross Sea

Chukchi Sea

OC3Mv6

OC3Mv6

SPGANTv4

Arctic OC4L

GSM

GSM

Figure 4.6 Projections of MODIS-Aqua false-colour images for two scenes from Figure 4.4, the Ross Sea and the Chukchi Sea, in which surface Chla is computed with three different algorithms; the OC3Mv6 algorithm, a regional algorithm, and the GSM. The colour bar scale for all images is depicted in the top left panel.

4.2.2 Empirical models for carbon

Traditionally, chlorophyll-a concentration has been used as a convenient proxy for phytoplankton biomass in aquatic ecosystems, but in most models of primary production and biogeochemical cycling, carbon is the fundamental quantity of interest. Conversion of Chla to the concentration of phytoplankton carbon, C_{ph}, relies on assuming a value of the Chla:C_{ph} ratio, a quantity which is highly variable among and within species and can change widely based on ambient environmental conditions. Furthermore, phytoplankton represent only one component of the total particulate organic carbon concentration (POC) within the ocean, which additionally includes contributions from heterotrophic organisms and nonliving detrital particles originating from grazing and cell decay. It is this combined highly-dynamic carbon reservoir which contributes a large portion to the export flux of carbon from the surface waters to the ocean interior or benthos.

Algorithms for estimating POC from ocean colour have been proposed and utilized in both polar regions. The first large scale distribution of POC estimates from satellite measurements was produced by Stramski et al. (1999), who formulated a two-step empirical model relating POC in surface waters to $R_{rs}(555)$ utilizing measurements from the Ross Sea and the Antarctic Polar Front Zone (APFZ). Combining this model with SeaWiFS measurements of ocean colour, they estimated the net change in the upper ocean POC pool of the Southern Ocean over a seasonal cycle. This approach was recently updated and extended to a 10-year time series of SeaWiFS data by Allison et al. (2010a,b) to examine regional and interannual variability.

The development and application of POC algorithms for high-latitude northern waters has been explored to a lesser extent, and primarily in a regional context. Stramska and Stramski (2005) evaluated a variety of algorithms for estimating POC in the North Polar Atlantic, west of Spitzbergen and Norway, and demonstrated that robust estimates of POC were feasible in this region. Application of their algorithm revealed complex patterns of interannual variability in surface POC that varied spatially, which, when coupled with physical modelling suggested substantial changes in the flux of POC to the ocean interior (Stramska 2010). Using a similar approach, Forest et al. (2010) utilized remote sensing to estimate surface values and vertical fluxes of POC within the Amundsen Gulf region of the Beaufort Sea. It is interesting to note that their algorithm is remarkably similar to that derived by Stramska and Stramski (2005), suggesting that regional variability may not be large. From a three-year time series of satellite observations and sediment trap measurements, they were able to estimate interannual variability in POC export from the surface ocean, and suggest that changes in the timing and extent of the seasonal ice cover may influence coupling between the benthic community and overlying waters. More recently, Doxaran et al. (2012) have formulated a semi-analytical approach for satellite estimation of POC and suspended particle mass concentration which can improve estimates in more optically-complex regions such as the Mackenzie River delta.

As is the case with Chla algorithms, the extent of regional variability in POC algorithms is generally unknown. Working in the Ross Sea, Pabi and Arrigo (2006) demonstrated that the relationship between POC and R_{rs} was strongly influenced by the taxonomic composition of the phytoplankton assemblage. The slope of the POC vs. $R_{rs}(555)$ relationship was markedly lower for communities dominated by diatoms as compared to those in which the haptophyte *Phaeocystis antarctica* was the predominant taxon. Similarly, in high-latitude waters of the north polar Atlantic, Stramska et al. (2003) observed substantial differences in blue-to-green reflectance ratios for communities dominated either by diatoms or by dinoflagellates and/or prymnesiophytes, which contributed to the variability in R_{rs} vs. Chla relationship. These results suggest that both Chla and POC estimates can be improved by concomitant information on taxonomic or ecological types of waters under investigation. Retrieving such information from remote sensing was an active area of research investigated by the IOCCG Phytoplankton Functional Type Working Group (see IOCCG 2014).

Calcite, an inorganic form of particulate carbon, is produced by specific calcifying groups of phytoplankton such as coccolithophores, and its presence can lead to increased spectral reflectance of the ocean. Gordon et al. (2001) proposed an algorithm for deriving coccoliths from satellite imagery, and this has been utilized to examine global distribution of calcite and calcification rates (Balch et al. 2005, 2007). Recently, Balch et al. (2011) have presented evidence that large areas of the Southern Ocean may represent sites with high abundance of coccolithophorids and enhanced formation of inorganic particulate carbon.

4.2.3 Semi-analytical models

Semi-analytical models couple radiative transfer approximations with empirical formulations to derive the inherent optical properties of seawater from measurements of spectral reflectance. Because the IOPs are more directly associated with individual seawater constituents, they offer the potential to provide more robust estimates for products of biogeochemical interest, particularly for oceanic waters in which non-algal materials dominate optical behaviour and vary independently of Chla. These advantages are of direct relevance to many polar regions which exhibit considerable optical complexity throughout the year.

The Quasi-Analytical Algorithm (QAA) (Lee et al. 2002; Lee et al. 2007b) and Garver-Siegel-Maritorena (GSM) model (Garver and Siegel 1997; Maritorena et al. 2002) are two examples of such models commonly employed by the ocean colour community. Both algorithms invert measurements of spectral reflectance to estimate coefficients for absorption and backscattering of various constituents, and have been developed from simulations and measurements of lower latitude waters. As both non-algal particles and dissolved materials exhibit similar spectral shapes, and are therefore difficult to distinguish operationally, their contribution to absorption is typically combined into a single parameter (a_{dg}). Only recently have there been initial attempts to apply or evaluate portions of these algorithms in polar regions.

Hirawake et al. (2011) utilized the QAA model in the Southern Ocean to compute the spectrally-averaged absorption coefficient of phytoplankton just beneath the sea surface, $\bar{a}_{ph}$, from *in situ* measurements of remote-sensing reflectance. They reported reasonable agreement between the QAA-derived $\bar{a}_{ph}$, with small adjustments to some coefficients, with a limited number of *in situ* measurements using the filter pad technique. Similarly, Lee et al. (2011) compared QAA-derived absorption values with *in situ* measurements for a region northeast of the Drake Passage and concluded that model estimates of $a(\lambda)$, $a_{ph}(\lambda)$, and $a_{dg}(\lambda)$ in the blue spectral region were generally within 10 – 20% of independent absorption measurements; however, much larger errors were observed in some spectral regions and also dependent on the method used for measuring absorption.

Current use of semi-analytical models in the Arctic has also focused primarily on retrieval of the total absorption coefficient. Good agreement has been reported for comparisons of QAA model-derived $a(\lambda)$ with *in situ* measurements, particularly when some reparameterization is involved (e.g., Bélanger et al. 2007; Hirawake et al. 2012; Matsuoka 2008). However, two studies (Hirawake et al. 2012; Zheng et al. 2014) have noted that the globally-parameterized QAA markedly underestimates the phytoplankton absorption coefficient in Arctic regions, with unrealistic negative values a frequent output. The primary source of these errors has been attributed partly to the assumptions adopted by the model used to partition total absorption into contributions of individual constituents (Zheng et al. 2014).

The GSM model has also seen increasing use in Arctic applications. Wang and Cota (2003) compared GSM-derived estimates of absorption, backscattering and Chla with field measurements in the Chukchi and Beaufort Seas, and demonstrated high correlations between retrieved and measured values of Chla and particle backscattering. Poorer results were obtained for other constituents, including the absorption coefficient for coloured dissolved organic materials. Ben Mustapha et al. (2012) found that GSM performance for Chla estimation was better than OC4 or OC4L in the Beaufort Sea using the standard parameterization of the algorithm, and show that improvement can be achieved after optimization of the algorithm. Matsuoka et al. (2013) modified the GSM algorithm with specific parameterizations developed from data collected in Arctic waters to estimate the CDOM absorption coefficient in the Beaufort Sea. Subsequent evaluation of the tuned model with an independent dataset exhibited uncertainties of 35% and 50% for oceanic and coastal waters, respectively. This kind of approach can be used for yielding other geophysical products for polar seas.

Despite their inherent advantages, few rigorous assessments of any semi-analytical model have been reported for either polar region. This deficiency stems from the lack of sufficiently large and comprehensive polar datasets that combine contemporaneous measurements of reflectance with detailed information on the absorption and scattering by individual constituents; such datasets are essential for purposes of both assessment and parameterization. Furthermore, at present it is also difficult to exploit the full potential of these algorithms with the limited spectral range and resolution of bands available on current satellite-based sensors. Ben Mustapha et al. (2012) recently demonstrated that although use of the GSM improved Chla retrievals relative to global algorithms such as the OC4 in the Beaufort Sea, it was unable to outperform an empirical algorithm specifically parameterized from local data. The collection of appropriate datasets and subsequent refinements of semi-analytical algorithms is a major task required for present and future applications of ocean colour remote sensing in polar regions.

4.3 Inherent Optical Properties and Bio-optical Relationships in Polar Seas

The observation of large, systematic deviations from statistical models suggests that polar waters may exhibit unique bio-optical behaviour which differentiate them from lower latitude oceans. In this section we summarize current knowledge regarding the inherent optical properties of seawater within polar regions, and their relationship to dissolved or suspended materials within the water.

The optical properties of pure water have been studied theoretically and experimentally in some detail (e.g., Morel 1974; Pope and Fry 1997; Jonasz and Fournier 2007), and are generally treated as known constants in most bio-optical models. In clear waters, the molecular absorption and scattering of light by water can comprise a significant contribution to the IOPs and, in such cases, accurate values which account for environmental variations are important. One of the defining characteristics of polar seas are surface waters with temperatures near or below the freezing point of pure water. Additionally, the surface ocean in polar regions can undergo large rapid changes in salinity because of river input, precipitation, and the effects of ice formation and melting. It is therefore of interest to examine how temperature and salinity influence the intrinsic optical behaviour of water.

The measurements of Pope and Fry (1997) are generally considered to be the most reliable experimental measurements of the spectral absorption coefficient of pure water over the visible spectral range. Their data were obtained with samples at 22°C, and these values are used to represent the contribution of $a_w(\lambda)$ in the majority of modern bio-optical models. Studies have indicated that the temperature dependence of water absorption in the visible spectrum is generally small, with a linear rate of change of <0.001 m^{-1} $^\circ\text{C}^{-1}$ in most spectral bands (Trabjerg and Højerslev 1996; Pegau et al. 1997; Langford et al. 2001; Röttgers et al. 2014). The variation of absorption with salinity has also been shown to be linear, but the dependence is much smaller than that observed for temperature (Pegau et al. 1997; Röttgers et al. 2014) and for most practical applications can be considered negligible within the visible range.

The elastic scattering of light by water molecules arises from small scale random fluctuations in molecular density (hence refractive index), and thus, in contrast to absorption, exhibits a greater dependence on both temperature and salinity. Recent theoretical treatments (Zhang and Hu 2009) predict a minimum in pure water scattering near 22°C, with values increasing by 3 to 4% as temperatures approach the freezing point. Variability in the scattering coefficient is significantly larger with regards to changes in salinity over the range typically encountered in the marine environment. The widely-used experimental measurements of Morel (1974) indicate a +30% linear change in pure water molecular scattering as salinities increase to values typical of seawater (35 – 38 PSU), and these observations are consistent with predictions from fluctuation theory (Zhang et al. 2009).

It is interesting to note that all of the experimental studies examining changes in water optical properties have generally been restricted to temperatures greater than 15°C, and we are unaware of measurements at colder temperatures within the range relevant to polar seas. Although accurate determination of the water contribution is of particular importance in clear waters, or to certain applications such as the partitioning of total absorption or scattering into individual constituent contributions, it is the much larger variations in concentrations and optical properties of particle and dissolved substances which usually dominate the optical variability of seawater. In the following discussion we focus on these components of the seawater medium.

4.3.1 Absorption

The light absorption properties of particulate and dissolved materials affect transmission and reflectance of visible light in oceanic waters, and strongly influence the performance of ocean colour algorithms. Here we review absorption properties of polar seas from the literature, and examine the difference in those properties between waters of the Southern and Arctic Oceans. Based on these analyses, the unique regional implications for interpreting ocean colour in polar regions are discussed.

A comparison of optical properties between the Arctic and Southern Oceans with specific consideration of chlorophyll-dependent spectral attenuation and reflectance was first reported by Mitchell (1992), who evaluated ocean colour algorithms based on band ratios of water-leaving radiance, L_w, and the spectral diffuse attenuation coefficient of downwelling irradiance, K_d, relative to chlorophyll pigment concentrations. A comparison to other published work for lower latitudes indicated significant differentiation between the chlorophyll relationships for both L_w and K_d in the Arctic Ocean and Southern Ocean. The observations were consistent with lower absorption per unit chlorophyll, and were attributed to pigment packaging in larger cells (Morel and Bricaud 1981; Mitchell and Kiefer 1988). The offset of the Arctic data from the Barents Sea and Greenland Seas, and an analysis of the slope of the regression of spectral K_d vs. chlorophyll pigments, led to the hypothesis that the Arctic Ocean has more coloured dissolved organic matter (CDOM) absorption than observed in the Southern Ocean.

The following discussion relies heavily on results from two studies of absorption in polar regions. Matsuoka et al. (2011) recently published a detailed study of absorption and optical properties for the western Arctic Ocean, an area which includes strong shelf and terrestrial influence. An overview of absorption properties in the Southern Ocean near 170°W, from the Ross Sea to subpolar waters, was published by Reynolds et al. (2001). Although regionally-restricted, these studies are the most comprehensive to date and generally corroborate the results of other published measurements (Mitchell and Holm-Hansen 1991; Mitchell 1992; Arrigo et al. 1998; Wang and Cota 2003).

4.3.1.1 Absorption by dissolved material

Values of $a_g(440)$ reported by Matsuoka et al. (2011) varied widely in both coastal and offshore waters of the western Arctic Ocean ($0.018\ \text{m}^{-1} < a_g(440) < 1.08\ \text{m}^{-1}$). These values generally fall within the range observed in various coastal waters at lower latitudes (Kirk 1994; Vodacek et al. 1997; Babin et al. 2003), with higher values (up to $1.08\ \text{m}^{-1}$) observed near the mouth of the Mackenzie River. Values of the spectral slope of CDOM absorption, S_g, fell within a narrower range ($0.015\ \text{nm}^{-1}1 < S_g < 0.023\ \text{nm}^{-1}$; Matsuoka et al. 2011), and were similar to values in coastal waters around Europe (Babin et al. 2003).

In the Southern Ocean, reported values of $a_g(440)$ vary in a narrower range than those from Arctic Ocean coastal waters ($0.004 - 0.1\ \text{m}^{-1}$; Reynolds et al. 2001), however the values are similar to those obtained in Arctic Ocean offshore waters ($0.004\ \text{m}^{-1}$ to $0.5\ \text{m}^{-1}$; Matsuoka et al. 2011). While higher concentrations of CDOM can be transported from lower latitudes into the Arctic Ocean by oceanic currents (Matsuoka et al. 2011), the dominant source of CDOM in the Arctic region appears to be from riverine input, as hypothesized by Mitchell (1992). There is little such terrestrial input of CDOM in the Southern Ocean and transport across the Antarctic Polar Front is limited in the upper ocean, thus CDOM in the Southern Ocean is considered to be predominantly from marine sources (Reynolds et al. 2001). For both

Arctic and Antarctic offshore waters, a large fraction of the CDOM is of marine origin including phytoplankton exudation, excretion by grazers, and degradation or production by bacteria (e.g., Carlson and Ducklow 1996; Bussmann 1999; Kirchman et al. 2005, 2007).

4.3.1.2 Absorption by particles

Figure 4.7 depicts statistical relationships between $a_p(440)$ and Chla reported for the Arctic Ocean and Southern Ocean, and compares these with other published relationships (Bricaud et al. 1998; Reynolds et al. 2001; Matsuoka et al. 2011). The relationship for the Arctic Ocean is very similar to those at lower latitudes (Figure 4.7a); we hypothesize that this is caused in part by increased non-algal particle absorption, $a_d(440)$, in the Arctic Ocean which compensates for lower values of phytoplankton Chla-specific absorption, $a^*_{ph}(440)$, that is associated with larger cells, low light acclimation and pigment packaging effects. A similar observation was made by Naik et al. (2010) in the Bering Sea. In contrast, the relationship for the Southern Ocean indicates significantly lower $a_p(440)$ values per unit Chla, for Chla concentrations less than 1 mg m^{-3}, compared to the Arctic Ocean and lower latitudes.

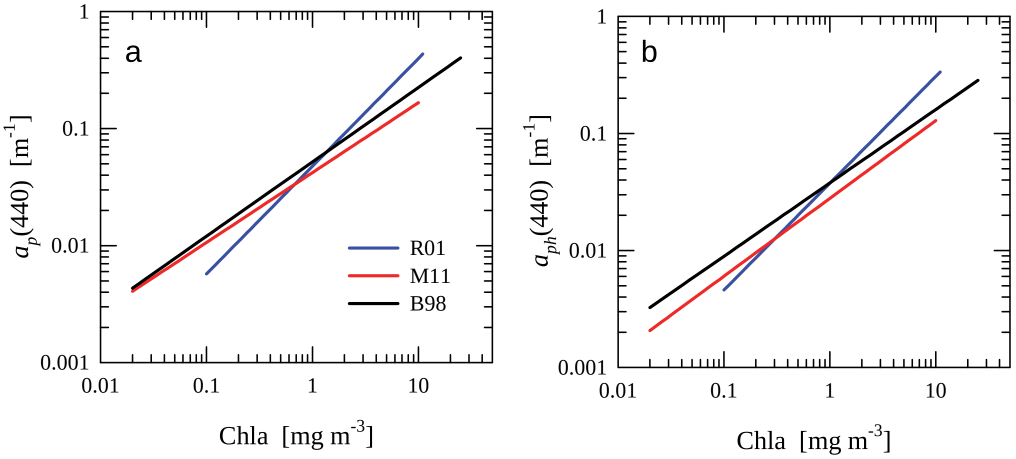

Figure 4.7 (a) Relationships between the particle absorption coefficient at 440 nm and Chla reported for the Southern Ocean (R01; Reynolds et al. 2001), the western Arctic (M11; Matsuoka et al. 2011), and for lower latitude oceanic waters (B98; Bricaud et al. 1998). (b) Similar to (a), but for the phytoplankton absorption coefficient.

The values for $a_{ph}(440)$, determined by subtracting the detrital component from total particulate absorption (i.e., $a_p(440) - a_d(440)$), are lower per unit Chla for both Arctic Ocean and Southern Ocean waters compared to those at lower latitudes when Chla is <1 mg m^{-3} (Figure 4.7b). It is worth noting that because results in Figure 4.7 were obtained by slightly different algorithms for conversion of absorbance on glass fiber filters into quantitative absorption coefficients, the true Chla-specific absorption may differ from the relationships in the literature. During a NASA Ocean Optics Protocol absorption workshop (Mitchell et al. 2000), a comparison of different methods using the exact same sample material indicated the Bricaud et al. (1998) method would produce values lower than the method of Mitchell (1990) that was used by Reynolds et al. (2001). In Figure 4.7, the black B98 regression line would be shifted left relative to the blue R01 line if the two datasets were to be reconciled into a consistent method, based on Mitchell (1990), and thus the differences between the lower latitude results of Bricaud et al. (1998) and the polar regions may be greater than that shown in Figure 4.7. The reduced absorption per unit Chla is likely caused by stronger pigment packaging effects (Morel and Bricaud 1981; Mitchell and Kiefer 1988) for both the Southern Ocean and Arctic Ocean due to the lack of pico-phytoplankton, for example coccoid cyanobacteria and *Prochlorococcus*, that are abundant at lower and mid-latitudes. Doolittle et al. (2008) report the farthest southward extension of phycoerythrin-containing coccoid cyanobacteria to be the Antarctic Polar Front at about 55°S in the Atlantic sector. In the Arctic Ocean, the prasinophyte *Micromonas pusilla* has been reported at a high relative abundance in low Chla waters (Throndsen and Kristiansen 1991; Balzano et al. 2012). This species is in the picoplankton size range (diameter of ~1 – 2 μm; Worden et al. 2009), and is thus expected to exhibit relatively low levels of pigment packaging. Also, the Arctic Ocean is more prone to shallow stratification resulting in higher light exposure and nutrient depletion within the surface layer, both of which will lead to less cellular pigmentation (Sosik and Mitchell 1991, 1995) and hence would also lower pigment packaging effects. This may explain in part why the Arctic Ocean has higher Chla–specific absorption than the Southern Ocean at low values for Chla.

In the Arctic Ocean, values of detrital absorption, $a_d(440)$, varied widely ($0.0016\ \mathrm{m}^{-1} < a_d(440) < 0.22\ \mathrm{m}^{-1}$; Matsuoka et al. 2011), falling within the range obtained in coastal waters around Europe (Babin et al. 2003). Values of the slope for non-algal particle absorption (S_d, nm^{-1}) also varied widely ($0.005\ \mathrm{nm}^{-1} < S_d < 0.017\ \mathrm{nm}^{-1}$), and were in the lower range of values published in the literature (Nelson and Guarda 1995; Babin et al. 2003). In the Southern Ocean, reported values of $a_d(440)$ vary within a narrower range than the Arctic Ocean (0.0001 – 0.038 m^{-1}; Arrigo et al. 1998; Reynolds et al. 2001), suggesting that $a_d(440)$ values in the Southern Ocean are lower than in the Arctic Ocean. Values of the spectral slope for detritus, S_d, fall within the range of the Arctic Ocean (0.011 – 0.017 nm^{-1}; Arrigo et al. 1998; Reynolds et al. 2001). Compared to the Southern Ocean, higher values of detrital absorption relative to phytoplankton or soluble absorption for the data compiled from the Arctic Ocean as part of this report (Figure 4.7), may in part be due to resuspension of bottom sediments from the shallow shelves, and also delivery of material from rivers. Recent observations by Bélanger et al. (2013b) in the Arctic Ocean also suggest that multi-year ice could release significant amounts of non-algal particles, which affect the optical properties of near-surface waters. These authors also showed that the particle enrichment in the near-surface layer impacted the absorption, vertical diffuse attenuation and reflectance of the incident solar radiation.

4.3.1.3 Partitioning of absorption among constituents

The contribution to absorption by coloured dissolved organic matter (CDOM, a_g) at 440 nm is, on average, significantly higher for the Arctic Ocean (66 ± 17%) compared to lower latitudes (41 ± 14%, Matsuoka et al. 2011), which is also observed in measurements contained within the polar dataset assembled by the IOCCG Polar Seas Working Group (62% in Figure 4.8). The strong contribution of CDOM is consistent with the fact that the Arctic Ocean receives the largest amount of freshwater relative to its volume (11% of global freshwater input whilst its volume is only 1% of the global ocean; Shiklomanov 1993). In contrast, terrigenous input of CDOM into the Southern Ocean is usually negligible and dissolved absorption originates from *in situ* oceanic processes. As a result, the contribution of CDOM to seawater absorption in the Southern Ocean is generally much weaker compared to the Arctic, and particulate absorption plays a more dominant role (Figure 4.8).

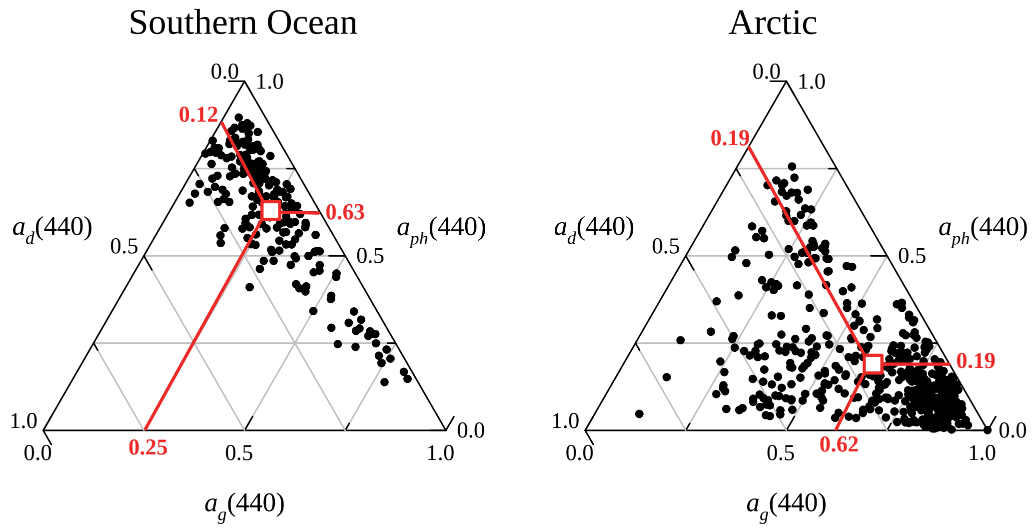

Figure 4.8 Ternary plots depicting the relative partitioning of the non-water absorption coefficient at 440 nm into contributions by phytoplankton (a_{ph}), non-algal particles (a_d), and coloured dissolved organic matter (a_g) for observations from the polar data set. The red square and solid lines represent the mean values for the contribution by each component.

For several applications, the ability to discriminate the relative contributions to absorption by differing constituents would be a useful capability. The decomposition of the total non-water absorption into phytoplankton and non-phytoplankton components remains a challenge (e.g., IOCCG 2000), although Matsuoka et al. (2011) reported a possible approach based on the strong and significant inverse relationship between the spectral slope of CDOM absorption, S_g, and the magnitude of $a_g(440)$ for the Arctic Ocean ($r^2 = 0.80$, $p < 0.0001$, $N = 408$). Although such an inverse relationship is not observed everywhere (see Babin et al. 2003), a clear trend was also previously reported across seasons along a transect from Delaware Bay to the Middle Atlantic Bight (Vodacek et al. 1997). A similar relationship for detrital absorption (S_d vs. $a_d(440)$) was not significant for the Arctic Ocean, and the magnitude of S_d is generally much smaller than S_g. However, when detrital and CDOM absorption coefficients are combined (i.e., $a_{dg}(\lambda) = a_d(\lambda) + a_g(\lambda)$), the slope, S_{dg}, does have a significant inverse relationship with a_{dg} (440) ($r^2 = 0.54$, $p < 0.0001$, $N = 370$) which is largely controlled by the strong inverse relation between S_g and $a_g(440)$. Thus, it may be possible to use this approach to separate phytoplankton absorption from a_{dg}, the sum of the non-algal absorption components

(Matsuoka et al. 2011).

It is extremely difficult to obtain independent information about phytoplankton absorption across the visible spectrum from ocean colour sensors with a limited number of spectral bands. Going from estimates of absorption at one spectral band (or a limited number of bands in the best case) to a spectral description of absorption therefore requires ancillary information. One approach is to utilize statistical analyses of *in situ* data. For example, Matsuoka et al. (2011) presented an analysis to derive multi-spectral absorption from absorption at 440 nm, which in principle can be obtained from remote sensing through the use of semi-analytical models. This approach is useful for describing $a_{ph}(\lambda)$ over the visible spectral domain using $a_{ph}(440)$ derived from ocean colour, and the statistical relationships defined by the *in situ* data.

4.3.1.4 Summary of absorption

A review of the literature and comparative analysis by the IOCCG Working Group on Polar Seas found that the Arctic Ocean and Southern Ocean have differentiation of the absorption properties that strongly influence ocean colour algorithms, and create challenges for retrieval of Chla. While some common patterns are observed, for example lower Chla–specific absorption of phytoplankton in both the Arctic Ocean and the Southern Ocean compared to lower latitudes, there are also considerable differences between the Arctic Ocean and the Southern Ocean, especially for CDOM and detrital absorption, where the Arctic Ocean exhibits much higher values of a_g and a_d than lower latitudes. Higher absorption of $a_g(440)$ may also play a role in heat storage in the surface waters that can also contribute to sea ice melting (Hill 2008; Matsuoka et al. 2011) since the values are high even when Chla values are low. Furthermore, there is strong variability within both the Southern Ocean and the Arctic Ocean. For example, in the Southern Ocean, blooms of *Phaeocystis* have higher Chla-specific absorption coefficients than diatoms for similar values of Chla. Also, higher CDOM absorption coefficients have been associated with large blooms of *Phaeocystis* in the Ross Sea (Reynolds et al. 2001) which does not seem to be the case for diatom blooms observed near the Antarctic Peninsula.

4.3.2 Backscattering by particles

Backscattered light exiting the ocean represents the primary source of the water-leaving radiance signal detected by sensors viewing the surface ocean, and is thus of critical importance to the interpretation of ocean colour. Although the magnitude of $b_b(\lambda)$ is generally low compared to $a(\lambda)$, variations in $b_b(\lambda)$ and its spectral variability also directly influence the behaviour of R_{rs} band-ratio algorithms. Scattering of light within the ocean results from interactions of light with localized fluctuations in density arising from the random motion of water molecules, turbulence and mixing, the presence of dissolved ions and gas bubbles, and suspended particulate matter. The molecular backscattering properties of pure water thus represent the minimal baseline scattering conditions; however, in most environments it is the contribution of particles to backscattering and the variability associated with this component that drives changes in ocean colour.

The intensity and angular distribution of light scattered by particles is strongly influenced by the size, shape, and internal composition and structure of the particle. All of these properties can differ remarkably among the particles commonly found within the marine environment. The size range of optically-significant particles within the ocean encompasses a broad size range spanning particles of diameter smaller than the wavelength of visible light (e.g., colloidal material of order 10^{-9} m) to particles significantly larger than the wavelength (e.g., colonies or aggregates of order 10^{-3} m). These particles also exhibit a wide diversity in composition (terrigenous or biogenous minerals, organic planktonic cells) and internal structure which influences the refractive index. Finally, any body of natural seawater has continually varying proportions of these different particles, which cannot be quantified easily. This complexity, along with limitations on modelling the backscattering of a given particle, limits a quantitative theoretical treatment of backscattering by particles in the ocean (Stramski et al. 2004), and a thorough understanding of which particles represent the principal sources to backscattering is lacking.

Are there any reasons to hypothesize that the light scattering properties of polar waters differ from lower latitude oceans? This question can be considered from the perspective of potential differences between the "typical" oceanic particle assemblage and those that might be encountered in polar seas. Sea ice and glaciers are known to incorporate and concentrate terrigenous material during the freezing process, which, when released through melting, will inject highly-refractive mineral particles into the oceanic environment (e.g., Dierssen et al. 2002). Such "dirty" sea ice has been recognized as a major mechanism of transporting sedimentary material within polar seas (Darby et al. 2011). In the Arctic, river transport of particles into coastal waters and resuspension processes on the broad continental shelves are seasonally important (Macdonald et al. 1998). With regards to the planktonic community, polar regions are known for intense, seasonal blooms in which large phytoplankton cells, often forming chains or colonies, predominate the assemblage. Such conditions imply that much of the chlorophyll-a is contained within large particles that are generally considered to contribute only a small proportion to the total backscattering, which has implications for understanding any relationship (or lack of) between Chla and b_b.

Experimental assessments of backscattering and its natural environmental variability have been hindered by the lack of widely-available instrumentation for measuring $b_b(\lambda)$ in the ocean. Only recently has instrumentation for *in situ* estimates of b_b become commercially available (Maffione and Dana 1997; Sullivan et al. 2013), and there are only a few published measurements available in the polar regions.

Stramski et al. (1999) reported the first measurements of b_b in the Southern Ocean, and demonstrated that particle backscattering was strongly correlated with the concentration of particulate organic carbon in surface waters of the Ross Sea and the APFZ. A significant difference in the relation between b_{bp} and POC for these two regions was noted, however. These observations were extended by Reynolds et al. (2001), who developed and used a semi-analytical reflectance model to demonstrate that the different backscattering properties of these waters was the primary cause of regional differentiation in the behaviour of ocean colour models for estimation of Chla. For a given chlorophyll-a concentration, particle backscattering

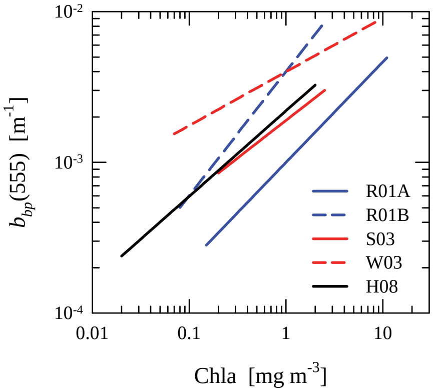

Figure 4.9 Relationships between the particle backscattering coefficient at 555 nm, $b_{\mathrm{bp}}(555)$, and Chla. Observations from within the Ross Sea (R01A) and Antarctic Polar Front Zone (R01B) were reported in Reynolds et al. (2001), the north polar Atlantic (S03) by Stramska et al. (2003), and the Beaufort and Chukchi Seas (W03) by Wang and Cota (2003). For comparison, a relationship developed from measurements in low latitude eastern South Pacific waters (H08; Huot et al. 2008) and reparameterized to 555 nm, is also depicted.

was about four times greater in the APFZ as compared to the Ross Sea (Figure 4.9). Based on measurements of the particle size distribution, they hypothesized that these differences arose from changes in the relative proportion of small and large particles in these waters, perhaps accompanied by changes in the distribution of Chla among size classes and the relative amounts of detrital particles containing little to no Chlorophyll-a.

Two studies have reported relationships between b_{bp} and Chla in high latitude northern waters; Stramska et al. (2003) for the north polar Atlantic, and Wang and co-workers (Wang and Cota 2003; Wang et al. 2005b) in the Chukchi and western Beaufort Seas (Figure 4.9). The relationship for northern Atlantic waters was intermediate between the results of Reynolds et al. (2001), while that for the Chukchi and Beaufort Seas was generally higher at low Chla (<1 mg m^{-3}) but lower at higher Chla than that observed in the APFZ.

For comparison, a relationship reported by Huot et al. (2008) from measurements of b_{bp} and Chla in low latitude waters of the Southern Pacific is also illustrated in Figure 4.9. These results are generally consistent with those reported from higher latitude oceanic environments such as the APFZ and north polar Atlantic. The relationship in the Ross Sea exhibits much lower backscattering per Chla, consistent with the observed dominance of a large colonial species of phytoplankton (*Phaeocystis*). In contrast, the Chukchi/Beaufort Sea measurements suggest much higher b_{bp} per Chla than the other regions for low Chla waters, which would suggest an increased contribution by non-pigmented particles such as mineral or detrital particles. The regional dependency relationships suggest that Chla-specific backscattering can vary more than fivefold for any given value of Chla. Furthermore, the statistical models in Figure 4.9 fail to illustrate the considerable scatter associated with each relationship. This is not surprising, as scattering arises from all particles (not just pigmented ones) and thus there is no *a priori* reason to expect strong correlations between b_{bp} and Chla. There is a clear need for continued research on the magnitude and spectral variability of the backscattering coefficient within polar seas, and their relationship to characteristics of the suspended particle assemblage.

4.4 Sensitivity Analyses to Observed Variability of IOPs

4.4.1 Influence of IOPs on empirical band ratio algorithms

In this section, a semi-analytical radiance model relating ocean colour to the inherent optical properties of seawater is utilized in a sensitivity analysis to examine how variability in the relationships between Chla and spectral coefficients for absorption and backscattering potentially influence the performance of multi-band ocean colour algorithms. The objectives of this exercise are to determine if the observed differentiation in empirical polar Chla algorithms with respect to each other, and to lower latitude models (Figure 4.2), are generally consistent with *in situ* observations of inherent optical properties, and to assess the potential sensitivity of these relationships to the spectral absorption and backscattering coefficients of individual constituents.

The model adopted for this analysis is based on the classical relationship of Gordon et al. (1988b) and similar in form to Equation 4.1. The spectral remote-sensing reflectance, $R_{rs}(\lambda)$, was computed as

$$R_{rs}(\lambda) = C \sum_{i=1}^{2} l_i \left(\frac{b_{bw}(\lambda) + b_{bp}(\lambda)}{a_w(\lambda) + a_g(\lambda) + a_d(\lambda) + a_{ph}(\lambda) + b_{bw}(\lambda) + b_{bp}(\lambda)} \right)^i, \qquad (4.4)$$

where the proportionality factors $l_1 = 0.0949$ and $l_2 = 0.0794$ were derived by Gordon et al. (1988b) from numerical simulations, and the factor C represents the transmittance of subsurface reflectance to above the sea surface. The factors l_1 and l_2 are dependent upon the exact shape of the volume scattering function and radiance distribution, and C can vary weakly with wavelength, but these approximations are generally accurate for many oceanic situations (IOCCG 2006) and considered sufficient for the present analysis.

To represent the optical properties of water, we assumed constant values for the spectral coefficients of absorption (Pope and Fry 1997) and backscattering (Morel 1974). The remaining inputs to the model are measured values of $a(\lambda)$ and $b_b(\lambda)$ for individual non-water constituents, and include the spectral absorption coefficients of phytoplankton, a_{ph}, non-algal particles, a_d, and coloured dissolved organic matter, a_g, and the spectral backscattering coefficient of particles, b_{bp}. To obtain these values, the compiled dataset of observations from each polar region (Table 4.1) was partitioned into four Chla classes based on the interquartile ranges of the frequency distribution of measured $\log_{10}$(Chla) within the dataset, i.e., the 0–25%, 25–50%, 50–75%, and 75–100% values of $\log_{10}$(Chla). These quartiles correspond to Chla of <0.33, 0.33 – <0.62, 0.62 – <1.0, and ≥1.0 mg m^{-3} for the Southern Ocean dataset, and to <0.13, 0.13 – <0.46, 0.46 – <2.2, and ≥2.2 mg m^{-3} for the Arctic data. Within each Chla quartile, the frequency distributions of individual measured IOPs were also determined.

An initial reference spectrum of R_{rs} associated with each Chla quartile was computed for the situation in which median (50^{th} percentile) values of each IOP within that quartile were used, with subsequent determination of the maximum band ratio of blue-to-green reflectance. A sensitivity analysis was conducted by maintaining median values for all input IOPs, but varying one individual constituent IOP between the lower (10%) and higher (90%) decile values of the observations. These values were chosen to minimize the potential influence of inaccurate measurements or extreme but rare conditions, while still capturing the range of variability observed in the data. By varying the value of individual constituent IOPs, the direction and relative change in the R_{rs} band ratios associated with each can be estimated.

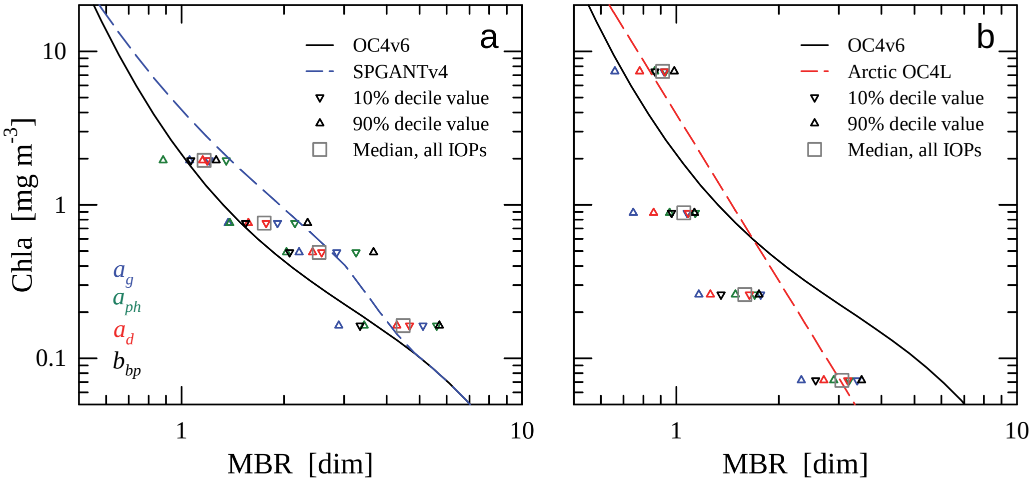

Figure 4.10 Results of a sensitivity analysis examining changes in the maximum band ratio of remote-sensing reflectance, MBR, associated with varying IOPs. Each polar dataset was divided into four discrete ranges of Chla, and the 10, 50, and 90% quantile values determined for each measured IOP within the Chla range. A semi-analytical model was used to compute the MBR for each Chla range from a given set of IOPs. The figures illustrate the values of MBR computed for each Chla when varying an individual IOP (denoted by colour) between the 10 and 90% quantile values while median values were used for all other IOPs. The value calculated by using the median value of all IOPs is also illustrated. Results are depicted for both the (a) Southern Ocean and (b) the Arctic, and include the relationships from the global OC4 algorithm and a regional algorithm for comparison.

As this is a statistical exercise to examine potential sensitivity of the MBR, we do not quantitatively compare computed $R_{rs}(\lambda)$ with measured values. Qualitatively, the model-derived spectra of R_{rs} compare reasonably well in magnitude and spectral shape with measured reflectances within each Chla quartile, suggesting that the model provides an adequate tool for illustrating expected patterns in spectral R_{rs} and the MBR in response to variations in the absorption or backscattering coefficient associated with individual constituents. Figure 4.10 summarizes the results of these model computations for both waters of the Southern Ocean and the Arctic. Overall, the results support the general observations depicted in the MBR vs. Chla relationship (Figure 4.2). At a given concentration range of Chla, the computed MBR varies 1.5 to 2–fold in response to changes in individual constituent IOPs.

For the Southern Ocean, the median value of the computed band ratios for each Chla class is larger than the relationship predicted by the global OC4 algorithm (Figure 4.10a), consistent with the trend observed in Figure 4.2. This is also true for the majority of computed values in which the individual IOP constituents were varied between the lower and upper deciles. The span of these values generally encompass the predicted relationship of the SPGANT regional algorithm, as would be expected for a regionally-parameterized relationship. The constituent exhibiting the lowest impact on changes in the MBR ratio is the absorption coefficient of non-algal particles, which induces only ~10% change in the MBR within its observed range of measurements. The largest ranges computed for the MBR are associated with changes in a_g or b_{bp}; at low to intermediate concentrations of Chla, variability in either of these IOPs leads to a large (>70%) change in the MBR, with smaller (20%) changes at the highest Chla values. Variability in the phytoplankton absorption coefficient has a significant and mostly constant influence (50%) on the range of the computed MBR at all concentrations of Chla.

The situation is much different in high latitude northern waters of the Arctic, but again the results are fully consistent with the *in situ* observations depicted in Figure 4.2. For concentrations of Chla < 1 mg m^{-3}, the MBR calculated from the median values of all constituent IOPs is much smaller than that predicted from the OC4 relationship, but greater relative to OC4 for the quartile associated with the highest Chla values. It is of interest to note that the median MBR and accompanying range of variability is nearly the same for Chla = 1 and Chla = 10 mg m^{-3}, which illustrates the difficulty in obtaining accurate estimates of Chla from simple spectral band ratios in this range. The linearized Arctic OC4L relationship captures well the differences in MBR between the two extreme Chla quartiles, but continues to exhibit bias at the intermediate ranges.

As would be anticipated from Figure 4.8b, variability in the absorption coefficients for CDOM (50% change in MBR) and non-algal particulate matter (20 – 30%) exert the greatest influences on variability in the MBR for Arctic waters for all situations, including the quartile comprising the highest Chla. In contrast to the Southern Ocean, changes in the phytoplankton absorption coefficient have only a small (<15%) impact on computed variability of the MBR. The variability associated with changes in b_{bp} is generally intermediate, inducing a 30% change in the range of the MBR at low concentrations of Chla, decreasing to 15% for the highest Chla quartile.

The direction of change in the maximum band ratio associated with variability in a given constituent IOP is consistent among both polar regions and for all concentrations of Chla. Increasing the absorption coefficient of a given constituent within a Chla quartile leads to reductions in the MBR, whereas increases in b_{bp} lead to an increase in the MBR. The actual magnitude of the change results from the interplay of several factors. As the magnitude of b_b is generally small relative to a for any given wavelength, to a first approximation the direction of change in a reflectance band ratio $R_{rs}(\lambda_1)/R_{rs}(\lambda_2)$ can be interpreted as the product of $[b_b(\lambda_2)a(\lambda_1)]/[b_b(\lambda_1)a(\lambda_2)]$ (e.g., Reynolds et al. 2001). Thus, changes in the R_{rs} spectral band ratios arise from variations in the relative contribution of each constituent (including water molecules) to the total absorption or backscattering coefficients in addition to variability in the spectral shape of each constituent. It is worth noting that, despite the generally lower magnitude of backscattering, as a multiplicative factor the spectral shape of b_b can still exert a significant influence on the R_{rs} band ratio.

A more detailed interpretation of these results would thus need to include quantifying the contribution of each constituent to the summed coefficients for absorption and backscattering, as well as considering changes in the spectral behaviour associated with each constituent. Such an analysis is outside the scope of this report. We simply conclude from this exercise that the observations of the relationship between the maximum band ratio of R_{rs} and Chla concentration reported for both polar regions, and the magnitude and direction of their differentiation from each other and from lower latitude waters, are fully consistent with the available observations and variability associated with measurements of inherent optical properties within each respective region.

4.4.2 Influence of IOPs on the diffuse attenuation coefficient for downwelling irradiance

Surface values of Chla derived from satellite ocean colour provide information on the amount of algal biomass present at a given time and location; however, the rate of photosynthetic carbon assimilation is generally of more direct interest to ecological and biogeochemical studies. Multiple approaches to estimating net rates of primary production (NPP) in polar regions from remotely-sensed measurements have been developed and comprise the subject of Chapter 5 in this report, but nearly all models require a means to vertically propagate incident surface irradiance through the upper water column. A common way to accomplish this employs the spectral (or spectrally-averaged) diffuse attenuation coefficient for downwelling irradiance, $K_d(\lambda)$, which describes the exponential attenuation of irradiance with increasing depth.

Models to estimate K_d range from simple empirical relationships with surface Chla to more sophisticated, radiative-transfer based approaches which relate the vertical distribution of K_d to estimates of water column physical structure and inherent optical properties. Because of its critical importance to NPP estimates, it is of interest to examine how the relationships among IOPs within polar waters influence variability in the spectral behaviour of K_d.

To conduct this analysis, we employed a second semi-analytical model which relates the diffuse attenuation coefficient to the inherent optical properties of seawater. The model was developed by Lee et al. (2005b) from a combination of radiative transfer theory coupled with empirical parameterizations derived from simulations. Specifically, we chose to compute the mean value of the diffuse attenuation coefficient vertically-averaged over the depth interval from the sea surface to the depth at which the level of irradiance is reduced to 10% of the surface value ($E_{10\%}$). Omitting the wavelength arguments for clarity, the value of the attenuation coefficient for this layer can be estimated from (Equation 11 in Lee et al. 2005b):

$$\overline{K}_d(E_{10\%}) = (1 + 0.005\theta_a)a + 4.18(1 - 0.52e^{-10.8a})b_b, \tag{4.5}$$

where θ_a represents the solar zenith angle. For this study, we assumed a constant value of 60° for θ_a, and used input values of individual constituent IOPs determined from the Chla quartiles as defined in the previous section. An implicit assumption of this model is a homogenous vertical distribution of IOPs (and thus optically-significant constituents such as phytoplankton as well) through this depth range, which may be violated in situations where the depth of vertical mixing is much shallower than the depth corresponding to $E_{10\%}$. This is a common occurrence in the Arctic (Hill et al. 2013).

For comparison, we also calculated $K_d(\lambda)$ from a statistical bio-optical model parameterized from measurements in lower latitude oceanic Case 1 waters (Morel and Maritorena 2001; denoted MM01). The median Chla value associated with each quartile range was used as the input. The MM01 model was formulated using average attenuation coefficients derived from measurements within the upper oceanic layer, roughly corresponding to the first attenuation depth, and thus is not strictly representative of the same depth interval as that computed in Equation 4.5.

The results of this analysis are illustrated in Figure 4.11 for both the Southern Ocean and the Arctic. As the Southern Ocean dataset contains a greater percentage of historical data, it thus has a more limited spectral range and resolution than data used in the Arctic simulations. For brevity, within each polar region we do not depict results of the analysis for the quartile corresponding to the lowest values of Chla. Attenuation in these quartiles is strongly determined by the contribution of water molecules and thus approach minimal values. The sensitivity of $\overline{K}_d$ to varying constituent IOPs in these quartiles is similar to that of other quartiles, but the absolute range of values in the attenuation coefficient is small – for example, in this quartile computed $\overline{K}_d$ (443) values span the interval of 0.03 – 0.06 m^{-1} in the Southern Ocean and 0.05 – 0.09 m^{-1} in the Arctic.

The analysis clearly indicates that waters of the Southern Ocean are much less opaque in the blue portion of the visible spectrum than Arctic waters with comparable Chla, with computed values of $\overline{K}_d \leq 0.3\ \mathrm{m}^{-1}$ in this spectral region (Figure 4.11). At longer wavelengths ($\lambda > 550$ nm), the rapidly increasing molecular absorption by water exerts a dominant role and sensitivity to other constituent IOPs is generally reduced.

As can be discerned from Equation 4.5, absorption is the primary determinant of $\overline{K}_d$ and thus the greatest sensitivity to changes in constituent IOPs are observed in the blue spectral region which exhibits a 2 – 2.5 fold range of computed $\overline{K}_d$ values. Within the Southern Ocean, the largest changes within some quartiles reflect variability associated with changes in the phytoplankton absorption coefficient, consistent with the generally strong contribution of a_{ph} to total a in this spectral region (Figure 4.8). A comparable sensitivity is also observed with respect to variability in a_g, which is likely to be even greater in spectral bands less than the 443 nm (the lower limit of our data). The MM01 model generally provides reasonable agreement with the observations for the blue-green spectral bands, with the predictions encompassed within the range of variability associated with changes in constituent IOPs. At longer spectral regions the MM01 model provides consistently lower estimates of $\overline{K}_d$ than the semi-analytical model, a feature that is also seen in the Arctic simulations. This may result from the vertical averaging of $\overline{K}_d$ over a broad depth range in spectral regions of high attenuation, or possibly owing to a failure to include contributions of inelastic scattering processes in the parameterization of the semi-analytical model.

For the quartiles associated with the lowest concentrations of Chla, the values of $\overline{K}_d$

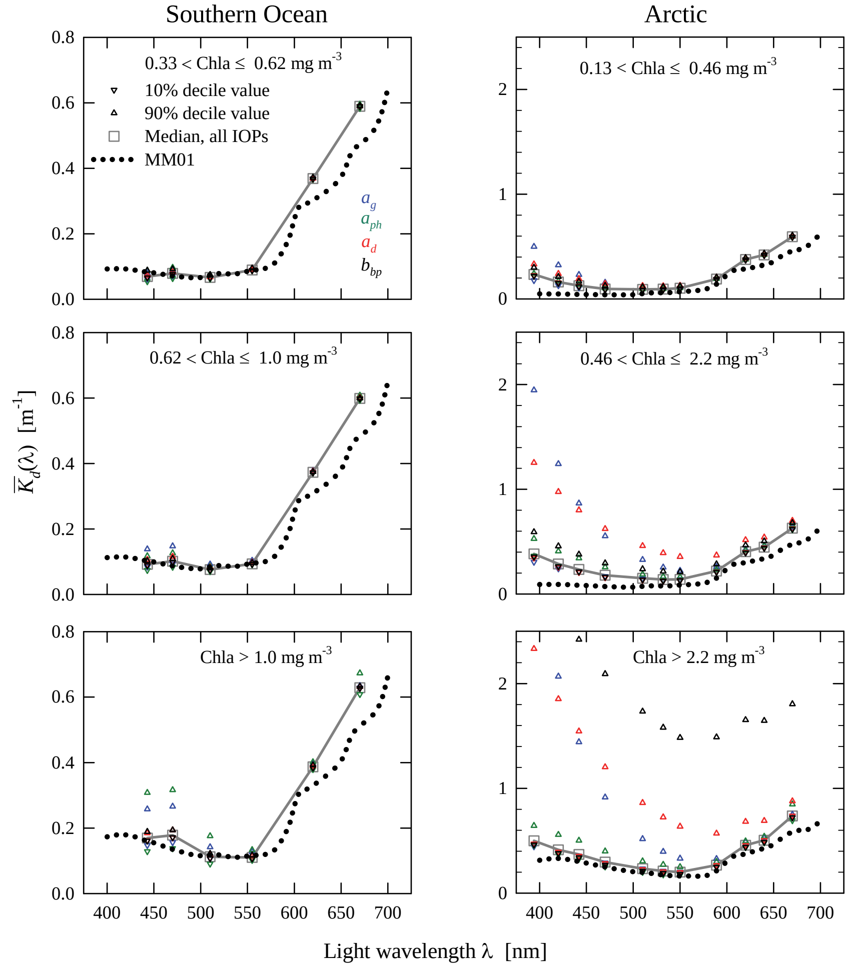

Figure 4.11 Results from a sensitivity analysis examining variability in the spectral diffuse attenuation coefficient of downwelling irradiance averaged over the depth range from the surface to the 10% isolume, $\overline{K}_d(\lambda)$. The polar datasets were partitioned as described in Figure 4.10, and a semi-analytical model used to compute the value of $\overline{K}_d(\lambda)$ associated with the median, 10%, and 90% quantile values of the constituent IOPs. For comparison, the predictions of the Morel and Maritorena (2001) model (MM01) are shown for the median value of Chla within each range. Results from the quartile associated with the lowest values of Chla are not shown. Note that the left (Southern Ocean) and right (Arctic) panels have a different ordinate scale.

computed using median values for all constituent IOPs are generally comparable between the Southern Ocean and the Arctic, with the exception of the 443 nm band where Arctic values are 50% higher (not shown). However, for the remaining quartiles (Chla > ~0.5 mg m^{-3}) the computed values of $\overline{K}_d(\lambda)$ in the Arctic increase much more rapidly than the Southern Ocean in all spectral bands. In addition, values of $\overline{K}_d$ in the blue spectral region are also generally much higher than those computed using the MM01 model. These observations are consistent with an increased relative contribution to absorption by non chlorophyll-containing materials (Figure 4.8), and 5 – 7 fold changes in blue attenuation are associated with variability in a_g

Table 4.6 Calculated ranges of the depth corresponding to the 10% level of surface irradiance, $Z_{10\%}$, for a light wavelength of 443 nm obtained from the sensitivity analysis described in Section 4.4.2. The first value represents the $Z_{10\%}$ obtained using the median value of all constituent IOPs within each Chla quartile, and the values in parentheses refer to the range obtained by varying each individual IOP between the 10% and 90% decile values.

Southern Ocean		**Arctic**	
Chla (mg m^{-3})	$Z_{10\%}$ (m)	Chla (mg m^{-3})	$Z_{10\%}$ (m)
<0.33	58 (38 – 71)	<0.13	37 (25 – 42)
0.33 – <0.62	33 (26 – 42)	0.13 – <0.46	18 (10 – 21)
0.62 – <1.0	25 (17 – 31)	0.46 – <2.2	10 (3 – 11)
≥1.0	14 (7 – 18)	≥2.2	6 (1 – 7)

and a_d in all Chla quartiles. A similar large sensitivity to variability in b_{bp} is also observed to contribute variability in computed $\overline{K}_d$, suggesting that increased scattering from particles can also be significant at times in certain regions. Because variability in the coefficients for a_g, a_d, and b_{bp} is often not correlated with changes in Chla, this highlights the difficulty in using simple pigment-based parameterizations in many regions of the Arctic Ocean.

The depth-averaged values of $K_d(\lambda)$ computed from Equation 4.5 allow calculation of the physical depth corresponding to the 10% isolume of surface irradiance, $Z_{10\%}$, for each spectral band. As the contribution to net primary production from depths greater than this threshold is generally small, this depth can be considered as a proxy for the productive layer of the water column. Table 4.6 lists the range of $Z_{10\%}$ computed from the model within each Chla quartile for the spectral band of 443 nm, which coincides with the Soret band of maximal absorption for Chla *in vivo*. Within the Southern Ocean, the calculated values of $Z_{10\%}$ exhibit an approximate twofold range for a given Chla quartile that is associated with variability in the constituent IOPs. This range of variability is even greater in the Arctic, with the depth of the 10% isolume generally much shallower for a given value of Chla.

4.5 Summary, Conclusions & Recommendations for Future Studies

The IOCCG Polar Seas Working Group's analyses of compiled historical and recently-acquired field data agree with a multitude of previous studies suggesting that both polar regions differ from lower latitude oceans, and from each other, in the empirical relationships observed between surface concentrations of chlorophyll-a and ocean colour. These differences cannot be explained solely by variability associated with the methodology used for pigment determinations, although these methodological issues do complicate and influence the interpretation of such relationships. Unfortunately, most of the historical measurements from polar regions lack the information to correct for such discrepancies, and it is imperative that future studies in these regions utilize current state-of-the-art pigment determinations either exclusively, or minimally on a limited basis to allow reconciliation between the methodologies.

Geography has a major influence on the distinct optical properties of the two polar regions. The Southern Ocean surrounds an ice-covered continent and is bounded to the north by oceanic fronts. As a result, terrestrial influence is limited and waters of the Southern Ocean generally conform to the classical Case 1 paradigm where phytoplankton and co-varying substances are the dominant drivers of optical variability (Morel and Prieur 1977). Phytoplankton often represent the dominant contribution to absorption in the Southern Ocean, and the combination of low light and deep mixing generally favor the presence of large, pigment-laden species which exhibit different optical characteristics from those in the surface waters of lower latitude oceans. In contrast, the Arctic Ocean is a small basin surrounded by land masses with extensive continental shelves, and is the most heavily land-influenced ocean in the world. Strong vertical stratification resulting from freshwater input coupled with the generally dominant contributions of CDOM and non-algal particles from terrigenous sources thus makes it an extremely complex optical environment in which the Case 1 assumptions are often not met.

In this chapter, we have focused primarily on overall trends comparing polar regions with each other, and with lower latitude waters. However, there is considerable evidence that strong regional differences exist within each of the polar regions. The APFZ and the Ross Sea within the Southern Ocean exhibit substantial differences from each other, and even within a season for a given region, depending upon the dominant phytoplankton species (Reynolds et al. 2001; Pabi and Arrigo 2006). The Atlantic and Pacific sectors of the Arctic are also distinct from one another and other northern regions. Such variability is a major challenge for studies targeting global or large regional scale analyses. The use of regionally-parameterized empirical algorithms can improve the predictions obtained from application of standard “global” algorithms, but significant scatter remains that cannot be accounted for easily with empirical algorithms. This is particularly true for the Arctic and surrounding seas, where non-local sources of CDOM and non-algal particles contribute strongly to absorption but exhibit little to no covariance with Chla. Techniques to achieve seamless transitions and the suppression of artificial “lines in the sea” when doing global or regional scale applications of ocean colour are still lacking, although some preliminary approaches have been explored (e.g., Moore et al. 2001; Kahru and Mitchell 2010).

The IOCCG Polar Seas Working Group concluded that the best path forward for improving accuracy of estimating Chla and other biogeochemical parameters from ocean colour remote sensing in polar waters is through the use of semi-analytical models which allow discrimination and quantification of the roles of non-phytoplankton constituents to the optical properties of seawater. Some initial success has been achieved with existing versions of available models, generally with some specific tuning or reparameterization. Because these models have been developed in lower latitude oceans, the assumptions and their parameterizations need to be rigorously assessed before they can be indiscriminately applied to polar waters. To achieve this, there is a strong need for continuing research into the optical properties of the polar oceans and adjacent seas, and the collection of comprehensive sets of optical data (absorption and scattering properties of major constituents) in conjunction with physical and biogeochemical measurements.

The Working Group also encourages research into the use of models for identifying phytoplankton functional types (PFTs), representing dominant taxonomic groups of the phytoplankton community, from ocean colour measurements. Such information can improve estimates of phytoplankton biomass, primary production, and the transfer of carbon to upper trophic layers or the benthos. Several empirical algorithms to detect PFTs from satellite data have been proposed and are the subject of IOCCG (2014); however, most of these are constructed for lower latitude regions and only a few local algorithms within the polar regions have been developed (e.g., Montes-Hugo et al. 2009; Fujiwara et al. 2011). As these algorithms generally require inputs of both Chla and IOPs, their performance will also require accurate determinations of these quantities.

Achieving these types of goals will require optical measurements with higher spectral range and resolution for improved discrimination of spectral shapes associated with individual seawater constituents. Sensors on existing space-borne platforms generally do not meet these requirements, yet we are encouraged that future missions hope to address these limitations (e.g., NASA PACE). In addition, it is anticipated that the increasing use of bio-optical sensors on a variety of autonomous *in situ* platforms (gliders, floats, standard and ice-tethered moorings) will enhance our observational capabilities in the polar regions.

Chapter 5

Estimates of Net Primary Production from Space-based Measurements

Kevin Arrigo, Victoria Hill, Simon Bélanger, B. Greg Mitchell, Toru Hirawake and Marcel Babin

---

5.1 Introduction

Phytoplankton are at the base of most marine food webs and their rates of primary production (defined as the rate of photosynthetic CO_2 incorporation) control the flow of chemical energy to higher trophic levels. As such, primary producers play a fundamental role in controlling the structure and trophodynamics of most oceanic ecosystems. Because of their importance, a great deal of effort has been made to quantify rates of net primary production (NPP) in a wide variety of marine environments. Initially, these measurements were made at sea, usually on board a suitable research vessel, which necessarily limited the amount of data that could be collected due to logistical constraints. Consequently, NPP in most ocean regions was poorly known, particularly over a complete annual cycle.

More recently, our ability to use satellites to remotely assess phytoplankton distributions at high spatial and temporal resolution has made it possible to use this information to quantify rates of marine NPP at spatial scales ranging from local to global, and temporal scales ranging from daily to decadal. This greatly improved our understanding of NPP dynamics across the globe, particularly in areas that had been poorly studied due to their relative inaccessibility, such as the polar regions. However, satellite remote sensing is challenging in places like the Arctic Ocean where solar zenith angles are high, cloud and sea ice cover are often pervasive (Chapter 3), absorption by coloured dissolved organic material (CDOM) is high (Chapter 4), phytoplankton biomass is not distributed uniformly with depth within the water column (Martin et al. 2010; Ardyna et al. 2013), and large phytoplankton blooms can develop beneath the ice where they are invisible to satellites (Arrigo et al. 2012).

The goal of this chapter is to investigate the magnitude of NPP variability in polar waters generated by different productivity algorithms. All of the algorithms used in this study were parameterized specifically for polar waters, taking into account phytoplankton acclimation responses to the generally low irradiance levels and cold temperatures that characterize these high latitude environments. In some respects, this is a more regional version of the exercise performed by Carr et al. (2006) for a large suite of global NPP algorithms, also based on satellite ocean colour data. Note that the fifth primary production algorithm round robin (PPARR5), designed specifically for the Arctic waters, is being performed at the time of writing (Lee et al. in press).

5.2 Primary Production Algorithms

5.2.1 Different types

A variety of approaches have been developed to estimate NPP from remotely-sensed data (Carr et al. 2006), although very few have been used to specifically study polar waters. The broad spectrum of approaches can be categorized according to either their level of sophistication (Behrenfeld and Falkowski 1997a) or by the method they employ to convert static observations into rates of NPP. Levels of sophistication range from simple empirical algorithms that calculate NPP from remotely-sensed surface chlorophyll-a concentration (Chla) (Hill et al. 2013) to complex formulations that use radiative transfer theory to attenuate spectral irradiance with depth throughout the euphotic zone and calculate NPP as a function of phytoplankton physiology, light, and temperature at discrete depths within the water column (Eppley et al. 1985; Platt and Sathyendranath 1988; Morel 1991; Antoine and Morel 1996; Behrenfeld and Falkowski 1997b; Dierssen et al. 2000; Marra et al. 2003; Arrigo et al. 2008a). Two methods are currently being used to convert remotely-sensed Chla and sea surface temperature (SST) into rates of NPP. These include: 1) use of Chla specific photosynthetic parameters (e.g., maximum light-saturated photosynthetic rate and photosynthetic efficiency) obtained from photosynthesis versus irradiance assays coupled with estimates of ambiance irradiance, and 2) the use of the quantum yield of photosynthesis (the amount of carbon fixed per unit of light absorbed) with estimates of light absorption by phytoplankton and estimates of ambient irradiance.

In many of the complex empirical primary production (PP) models parameterized using large data sets of PP measurements, variations in phytoplankton photosynthetic parameters are implicitly accounted for (e.g., Behrenfeld and Falkowski 1997b, and Hill and Zimmerman 2010). One advantage of such models is that they are strongly constrained by actual PP data. Their scope is, however, limited to that of the PP data set used to tune the model. Wavelength- and depth-resolved PP models with an explicit formulation of photosynthesis (so-called semi-analytical), such as those proposed by Platt and Sathyendranath (1988), Morel (1991) or Arrigo et al. (1998), offer unlimited scope because their parameters can be measured, and varied in the model as a function environmental factors or other variables measurable from space, such as Chla. For instance, robust statistical relationships between the chlorophyll-specific phytoplankton absorption coefficient and Chla have been published (e.g., Bricaud et al. 1995), including specifically for the Arctic Ocean (Matsuoka et al. 2014). Behrenfeld et al. (2002) proposed a model that relates variations in the maximum rate of carbon fixation (P^B_{max}) to temperature, irradiance and nutrients. For their PP model for polar waters, Arrigo et al. (1998) used a relationship between the saturation parameter and ambient irradiance at depth. The amount of high latitude data on phytoplankton photosynthetic parameters is, however, still very limited.

Mostly because of the extreme light conditions found there, photosynthetic parameters have average values in polar seas that are quite distinct from those at lower latitudes, including P^B_{max} and E_k which are generally very low (see the recent review of Babin et al. 2015 for the Arctic). For example, Bélanger et al. (2013a) adopted a constant value of 2 mg C mg Chl^{-1} h^{-1} for P^B_{max} based on the values reported for different regions of the Arctic Ocean by Harrison and Platt (1986) and Rey (1991). In their data set collected in the Beaufort Sea during post bloom conditions, Huot et al. (2013) reported an average P^B_{max} of 0.5 mg C mg Chl^{-1} h^{-1}. Palmer et al. (2013) found an average of 1 mg C mg Chl^{-1} h^{-1} and limited variability over a wide range of light and nutrient conditions in the Chukchi and Beaufort Sea during early to late spring and early summer, and much larger values when nitrate was >10 mg m^{-3}. Doubling P^B_{max} in a PP model leads to a 35 to 60% increase in daily PP according to the calculations of Morel et al. (1996). Thus, choosing a given constant value of P^B_{max} or adopting a given statistical relationship to account for its variations, has a significant impact on the resulting PP calculated with a semi-analytical model.

5.2.2 Algorithm input

Regardless of the approach employed, virtually all algorithms that calculate NPP from remotely-sensed data require a similar suite of input data and parameters. These usually include surface Chla (remotely-sensed using ocean colour), SST (remotely-sensed using thermal infrared data), incident light (calculated using radiative transfer codes), and phytoplankton physiological parameters (including physiological responses to temperature and light measured in the laboratory or the field). In polar waters, remotely-sensed sea ice concentration (from passive microwave data) is used to determine the extent of open water suitable for phytoplankton growth. Although polar waters are frequently covered by clouds, preventing Chla retrieval at these locations, no attempt was made to fill gaps in the satellite data by temporal or spatial interpolation. Instead, relatively cloud-free images were chosen from the Arctic and Antarctic, and mean NPP was calculated over each individual scene, ignoring any missing data due to cloud or sea ice cover.

Algorithms that calculate NPP at discrete depths within the water column, and then vertically integrate these values to estimate NPP per unit area, need to make some assumptions about how temperature, Chla, and light are distributed with depth within the euphotic zone (NPP below the euphotic zone is assumed to be zero). The simplest and most common approach is to propagate surface values for Chla and SST throughout the euphotic zone and then calculate light levels using a radiative transfer model that accounts for attenuation by Chla and co-varying optical constituents. This results in uniform distributions of temperature and Chla throughout the euphotic zone and exponentially decreasing light levels. The most common alternative is to use constant values for Chla and temperature within the mixed layer (the depth of which needs to be calculated using a mixed layer model or assigned based on a mixed layer climatology) and vary them in a prescribed way between the base of the mixed layer and the base of the euphotic zone. Another approach is to estimate Chla profiles based on observed relationships between vertical Chla distributions and horizontal Chla gradients, seasonal variability in Chla, and regional Chla variations (Ardyna et al. 2013).

5.2.3 Algorithm output

These algorithms can be used to generate daily maps of NPP at a spatial resolution as high as 1-km, which is dictated by the resolution of the currently available ocean colour sensors. However, while Chla and SST are available at 1-km resolution, light and sea ice concentrations are available at substantially lower resolution (~6 – 25 km depending on sensor and method of data processing). This mismatch in resolution between input variables will increase the uncertainty of the NPP estimate, but because NPP is most strongly dictated by Chla, it is often preferable to accept slightly higher errors to achieve much higher spatial resolution.

5.2.4 Validation

The best way to validate NPP algorithms is to compare algorithm-derived NPP with *in situ* estimates of NPP made at the same time and location. Such an exercise is being performed for Arctic waters, in which algorithms are used to compute NPP using inputs from either satellite or *in situ* (Lee et al, in press). However, because of the small number of cloud-free images that correspond to available *in situ* measurements in polar regions, this approach yields few match-ups. Using this method in the Chukchi Sea, Hill and Zimmerman (2010) determined that strong surface production improves the ability of passive sensors to predict NPP. However, during post-bloom periods, knowledge of the subsurface structure in Chla was necessary to retrieve accurate NPP. A recent Arctic wide analysis of match-ups revealed that summertime subsurface Chla is the biggest limiter to our ability to accurately retrieve integrated PP (Hill et al. 2013). An alternative approach used by Pabi et al. (2008) for the Arctic Ocean was to assume that retrievals of surface Chla by SeaWiFS were reliable (in waters not influenced by river runoff) and then compare regressions of daily NPP against surface Chla produced by their algorithm to a regression generated from *in situ* Arctic data. In essence, this approach seeks to determine if the relationship between Chla and NPP generated by the algorithm is consistent with the relationship between Chla and NPP observed in the field. If it is, any discrepancy between these two relationships can then be attributed to the physiological parameters used in the algorithm rather than to errors in satellite-based estimates of Chla.

In situ measurements of NPP and concurrent surface Chla used in the analysis by Pabi et al. (2008) were obtained from Phase I and II of the Shelf Basin Interaction (SBI) program (`http://www.eol.ucar.edu/projects/sbi/`) conducted in the Chukchi and Beaufort sectors of the Arctic Ocean during 2002 – 2004. Assuming no error in satellite retrieval of Chla, the relationship between surface Chla and daily NPP predicted by their algorithm for the SBI study region agrees well with the *in situ* data, particularly in spring when production is high (Figure 5.1a). In summer, there are clear cases where the algorithm underestimates daily NPP at low surface Chla (Figure 5.1b). These were stations with a particularly strong subsurface Chla maximum (Hill and Cota 2005), which was not detected by the SeaWiFS sensor. Unfortunately, the prevalence of subsurface Chla maxima in the Arctic Ocean was not well known at the time

Pabi et al. (2008) performed their analysis, so the significance of the problem could not be adequately determined.

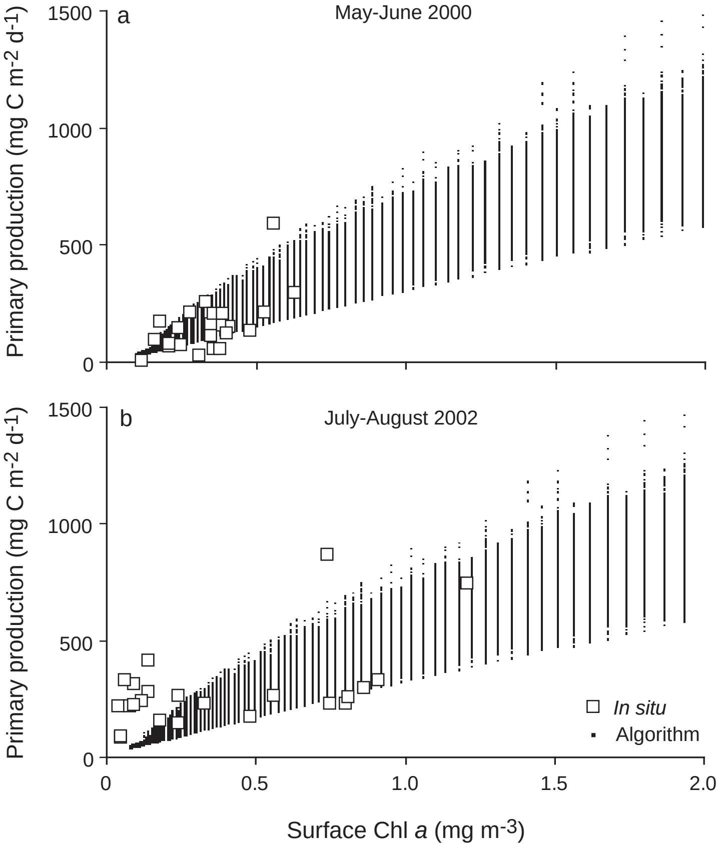

Figure 5.1 Plots of surface Chla versus daily primary production estimated from the NPP algorithm of Pabi et al. (2008) and measured *in situ* at discrete stations from the Chukchi and Beaufort Seas obtained during the Shelf Basin Interaction program during a) May – June 2002 and b) July – August 2002. Algorithm output used in this analysis was restricted to those times and locations for which *in situ* data were available

.

5.2.5 NPP algorithm comparison

A simple comparison of four different polar NPP algorithms was carried out using six arbitrarily chosen Chla images (three Arctic and three Antarctic, Figure 5.2) as algorithm input (the only requirement was that each image have a large number of ice-free pixels). Because the algorithms all differ in either their need for, or their approach in, specifying incident PAR, sea surface temperature, and photosynthetic parameters, the Chla images were the only common inputs to all algorithms. The purpose of this exercise was to obtain a better understanding of the magnitude of the variability between different algorithms when estimating NPP from space-based data for a specific day. Algorithms by Arrigo et al. (2008a) and Hirawake et al. (2011,

2012) were used for both the Arctic and Antarctic images, those by Bélanger et al. (2013b) and Hill et al. (2013) were used for the Arctic only, and the algorithm by Mitchell (unpublished data) was used for the Antarctic only.

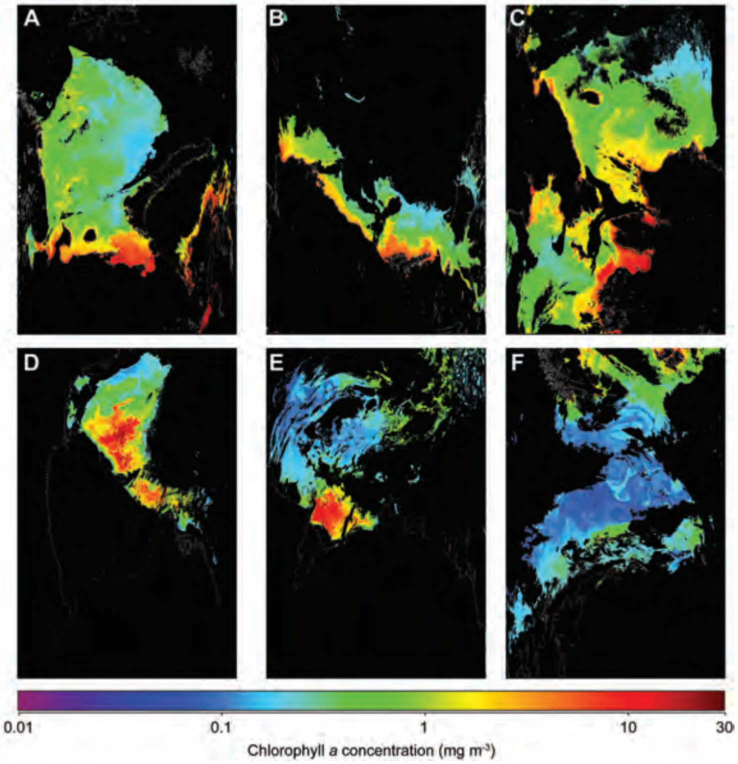

Figure 5.2 Chlorophyll-a concentration images used for the NPP algorithm comparison. Images are from a) Barents Sea (Arctic) on 5 July 2004, b) Beaufort Sea (Arctic) on 18 September 2007, c) Chukchi Sea (Arctic) on 22 August 2008, d) Ross Sea (Antarctic) on 10 December 2010, e) Prydz Bay (Antarctic) on 2 January 2010, and f) the Antarctic Peninsula on 1 November 2003.

The Arrigo et al. (2008a) primary productivity algorithm accounts for variability in sea ice extent, sea surface temperature, sea level winds, downwelling spectral irradiance, and surface Chla. The algorithm was parameterized and validated specifically for use in either the Arctic or the Antarctic and utilizes forcing variables derived either from satellite data or NCEP (National Centers for Environmental Prediction) reanalysis fields. Daily primary productivity (mg C m^{-2} d^{-1}) at each satellite pixel location was computed by integrating over depth and time (24 hours). Below the mixed layer, Chla is assumed to decrease exponentially with depth. In the present study, the mixed layer depth (MLD) is assumed to be 20 m, similar to the value used by Walsh et al. (2005). Primary productivity is calculated each hour and at each depth as a function of the temperature-dependent upper limit to net growth and a light limitation term. The light limitation term is based on the amount of photosynthetically usable radiation (PUR) (*sensu* Morel 1978) and the spectral photoacclimation parameter. Downwelling spectral irradiance at the ocean surface was determined using the radiative transfer model of Gregg and

Carder (1990), corrected for fractional cloud cover (from NCEP Reanalysis data) and specular reflectance. Downwelling spectral irradiance was propagated through the water column using the inherent optical properties typical of the Chukchi Sea and western Beaufort Sea (Wang and Cota 2003; Wang et al. 2005a).

The Hirawake et al. (2011, 2012) algorithm uses the light absorption coefficient of phytoplankton to derive the surface production, which is equivalent to the product of the surface photosynthetic rate and Chla. This value is integrated to the base of the euphotic zone, which is calculated as in Lee et al. (2007b). The absorption coefficient was estimated using the quasi-analytical algorithm (QAA, Lee et al. 2002; Lee et al. 2007b). Extremely high values are induced by higher absorption of noisy pixels, particularly near the sea ice edge, probably due to sub-pixel contamination (Chapter 3). In the case of the Chla product, questionable values were masked and striping noise was reduced. However, correction for the absorption coefficient is still an issue to be resolved when this absorption-based algorithm is applied.

The Hill et al. (2013) algorithm is based on the strong *in situ* Pan-Arctic relationship between Chla and NPP, and uses a vertically-constant Chla based on satellite retrieved values. The model integrates to the shallower of the climatological mixed layer depth (Steele et al. 2001) or the euphotic depth (calculated from satellite K490). In the spring, the mixed layer is deeper than the euphotic zone, biomass within the water column is vertically homogeneous and surface Chla is a good indicator of euphotic integrated Chla. In post-bloom conditions found during the summer, surface Chla is no longer a good indicator of euphotic zone integrated Chla due to high biomass and productivity located at the nutricline. Under these stratified conditions the mixed layer depth is shallower than the euphotic depth and is chosen as the integration limit. The model does not attempt to predict the subsurface PP.

The Bélanger et al. (2013b) algorithm relies on two satellite ocean colour products: Chla and the spectral diffuse attenuation coefficient, $K_d(\lambda)$. The latter is calculated using bulk spectral IOPs (a and b_b) retrieved using the QAA (Lee et al. 2002) at the satellite R_{rs} wavebands and a semi-analytical model relating the IOPs to K_d published and validated by Lee et al. (2005a,b, 2007b). As for the Arrigo et al. (2008a) model, downwelling spectral irradiance was then propagated through the water column according to Beer's law and PUR is calculated using a spectral absorption coefficient derived from Chla using empirical relationships published for the Arctic Ocean (Matsuoka et al. 2011). NPP is calculated using a classical P vs E function with a constant maximum photosynthetic rate at light-saturated Chla-normalized carbon fixation rate (P^B_{max}) set at 2 mg C mg Chla^{-1} h^{-1} (Harrison and Platt 1986), and a photoacclimation parameter (E_k, μmol photons m^{-2} s^{-1}) that varies as a function of PUR following Arrigo et al. (2008a). Another difference with other algorithms resides in the estimation of the incoming downwelling spectral irradiance at the ocean surface, which was determined using the SBDART radiative transfer model of Ricchiazzi et al. (1998), accounting for the cloud optical thickness and corrected for fractional cloud cover (both from ISCCP global radiative flux data, Zhang et al. 2004) and specular reflectance.

The algorithm used by Mitchell (in preparation) is a modification of the global algorithm by Behrenfeld and Falkowski (1997b) with parameters specific for the Southern Ocean. It calculates NPP within the euphotic zone (calculated as a function of K) from P^B_{opt} (which varies as a function of temperature), day length, downwelling spectral irradiance, and surface Chla, which is assumed to be constant over the mixed layer. In this version, algorithm parameters are based on empirical measurements of K and P^B_{opt} made in the Southern Ocean.

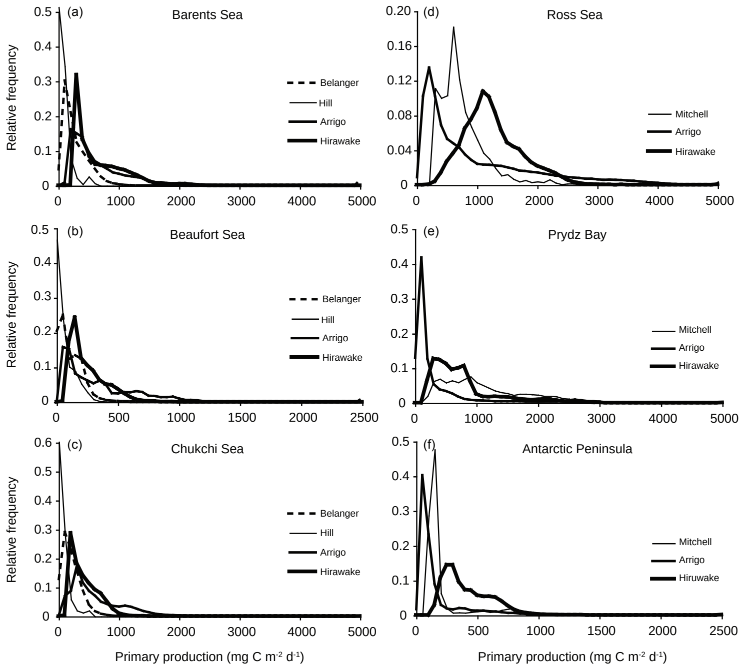

Figure 5.3 Relative frequency of calculated daily net primary production for the (a) Barents Sea (5 July 2004), (b) Beaufort Sea (18 September 2007), and (c) Chukchi Sea (22 August 2008) regions of the Arctic Ocean, and the (d) Ross Sea (10 December 2010), (e) Prydz Bay (2 January 2010), and (f) Antarctic Peninsula (1 November 2003) regions of the Southern Ocean (Antarctic) using different NPP algorithms.

Results for the Arctic (Table 5.1) show that the four algorithms vary by more than a factor of five in both their mean and median estimates of daily NPP for the scenes from the three regions tested (Barents Sea, Beaufort Sea, and Chukchi Sea). Much of this range is due to the values produced by the Hill et al. (2013) algorithm, which were a factor of 3 – 7 lower than the other three, with a frequency distribution that was far more skewed to lower values in the Barents (Figure 5.3a), Beaufort (Figure 5.3b) and Chukchi (Figure 5.3c) seas. The algorithm of Arrigo et al. (2008b) produced the highest NPP values for all of the Arctic images, with a smaller fraction of values below 200 mg C m^{-2} d^{-1} and a greater fraction of values >1,500 mg C m^{-2} d^{-1} than the other algorithms (Figures 5.3a–c). The range in daily mean and median NPP was much smaller amongst the other three algorithms, generally agreeing to within ±25%. Median NPP values for the Arrigo et al. (2008b) and Hirawake et al. (2011, 2012) algorithms were particularly close, varying by 1 – 25% for the three Arctic images. The algorithm of Bélanger et al. (2013b) yields a median NPP that is 16% lower than that of Arrigo et al. (2008b) and Hirawake et al. (2011, 2012), which is likely due to the way downwelling irradiance is propagated through the water column (see below).

Although there are no *in situ* match ups to compare to the models, it is useful at this point

Table 5.1 Daily primary production (mg C m^{-2} d^{-1}) for selected areas of the Arctic (Barents Sea, Beaufort Sea and Chucki Sea) and Antarctic (Ross Sea, Prydz Bay and Antarctic Peninsula) using four different NPP algorithms.

Algorithm	Mitchell	Arrigo	Hirawake	Bélanger	Hill
Barents Sea, 5 July 2004 (N=673,938)					
Minimum	—	34	8	0	5
Maximum	—	7399	4762	29265	604
Mean	—	776	687	515	127
Median	—	542	545	260	97
Beaufort Sea, 18 September 2007 (N=276,802)					
Minimum	—	0	26	0	0
Maximum	—	2917	12192	7227	593
Mean	—	373	278	211	87
Median	—	273	229	116	56
Chukchi Sea, 22 August 2008 (N=846,193)					
Minimum	—	0	154	0	0
Maximum	—	8103	22713	6634	604
Mean	—	805	473	305	115
Median	—	547	418	230	77
Ross Sea, 10 December 2010 (N=314,462)					
Minimum	3	1	9	—	—
Maximum	8087	5562	18617	—	—
Mean	893	1150	1363	—	—
Median	595	777	1290	—	—
Prydz Bay, 2 January 2010 (N=428,873)					
Minimum	2	1	150	—	—
Maximum	14515	4997	68112	—	—
Mean	658	540	867	—	—
Median	230	187	710	—	—
Antarctic Peninsula, 24 February 2003 (N=706,035)					
Minimum	2	1	131	—	—
Maximum	15435	6599	256636	—	—
Mean	355	240	454	—	—
Median	205	112	386	—	—

to compare the model results to representative *in situ* estimates collected in these regions in different years. In mid- to late August, production rates on the Chukchi Shelf and Bering Strait region range from a maximum of 3 g C m^{-2} d^{-1} to a low of 0.08 g C m^{-2} d^{-1}, the highest rates coming from Barrow Canyon and the Bering Strait (Hill and Cota 2005; Lee et al. 2007a). In July, in the Barents Sea, rates have been measured from 0.1 to 1.5 g C m^{-2} d^{-1} (Hodal and Kristiansen 2008). In late summer (September) in the Beaufort Sea rates range between 0.02 and 0.1 g C m^{-2} d^{-1}, with lowest values closest to the coast in the Mackenzie river plume. All of these values are between the higher Arrigo, Hirawake and Bélanger models and the lower Hill estimates.

Only the Arrigo et al. (2008a), Hirawake et al. (2011, 2012), and Mitchell (unpublished data) algorithms were used to estimate NPP in the Antarctic. Interestingly, although the Arrigo et al. (2008a) algorithm produced the highest NPP values in the Arctic, with the least amount of skewness toward low NPP values (Figure 5.3d–f), in the Antarctic, the Hirawake et al. (2011, 2012) algorithm generated the highest mean and median NPP for the three images tested (Table 5.1), with NPP closely approximating a normal frequency distribution. Furthermore, the Arrigo et al. (2008a) algorithm (Figure 5.3d–f) was more skewed toward low NPP values (<500 mg C m^{-2} d^{-1}) than the other two algorithms. In general, estimates of NPP varied by a factor of 2 – 4 between algorithms, with the algorithms by Arrigo et al. (2008a) and Mitchell (unpublished data) showing closer agreement with each other than they did with the algorithm of Hirawake et al. (2011, 2012). This agreement may be due to the fact that these algorithms are conceptually similar, both calculating NPP from surface Chla, while the Hirawake et al. (2011, 2012) algorithm calculates NPP as a function of light absorption using the QAA algorithm.

5.3 Problems with satellite NPP associated with SCM and CDOM

Many areas of the Arctic Ocean are characterized by a well developed subsurface chlorophyll maximum (SCM) that forms at the depth of the nutricline after surface nutrients have been exhausted (Ardyna et al. 2013). SCM can be associated with high NPP in spring and summer (Vedernikov et al. 2001; Hill and Cota 2005; Richardson et al. 2005; Hodal and Kristiansen 2008; Tremblay et al. 2008; Martin et al. 2010) so satellite-derived rates of depth-integrated NPP from surface Chla (e.g., Arrigo and van Dijken 2004; Pabi et al. 2008; Arrigo et al. 2008a) will be underestimated in regions with well-developed SCM.

Most NPP algorithms assume that remotely-sensed surface Chla is representative of the entire upper mixed layer, a problem for space-based Chla algorithms (Morel and Berthon 1989; Sathyendranath and Platt 1989). While this assumption poses little problem when euphotic depths are shallower than the mixed layer depth, the SCM in parts of the Arctic Ocean can have considerable light available for photosynthesis (Martin et al. 2010). Consequently, when a SCM is present, profiles of NPP generated from surface Chla will differ from NPP calculated from *in situ* profiles of Chla.

Furthermore, due to the large riverine fluxes into the Arctic Ocean, concentrations of CDOM in nearshore waters can be very high (Gueguen et al. 2007; Granskog et al. 2007, 2009; Retamal et al. 2008; Osburn et al. 2009; Hessen et al. 2010). CDOM also makes a significant contribution to blue light absorption (>70%) in the Arctic polar mixed layer despite the low concentrations (Pegau 2002; Matsuoka et al. 2007, 2011; Bélanger et al. 2013a). These compounds absorb strongly in the blue wavelengths but much less so in the green, as does the phytoplankton Chl-a molecule. As a result, waters where CDOM is abundant appear from space to have high Chla. Because pigment packaging and high CDOM concentrations render the optical properties of Arctic waters different from the rest of the global ocean (Matsuoka et al. 2007, 2011), the standard OC4v4 algorithm of SeaWiFS (and OC3M of MODIS) overestimates surface Chla, exhibiting a root mean square error (RMSE) of 0.21 mg Chla m^{-3} when compared to *in situ* data (Matsuoka et al. 2007). Errors are largest at low Chla and diminish to near zero at Chla above 0.5 mg m^{-3}. Although the magnitude of this error is likely to be smaller for the more recent OC4v6 SeaWiFS algorithm, which shows improved agreement with *in situ* values in coastal waters (`http://oceancolor.gsfc.nasa.gov/REPROCESSING/R2009/ocv6/`), a recent analysis (Chapter 4) indicates that errors might be even larger. This analysis is based on a larger dataset than that used by Matsuoka et al. (2007) and may be more representative of areas of the Arctic with higher CDOM concentrations. How applicable it is to the entire Arctic will require additional data to determine.

CDOM and non-algal particles also increase light attenuation and must be accounted for in the propagation of spectral downwelling irradiance through the water column. These constituents are poorly correlated to Chla in the Arctic (Matsuoka et al. 2007), introducing potential errors in diffuse attenuation (K_d) estimation from Chla. To assess the approximate magnitude of this error, we compared the median $K_d(488)$ calculated for the three Arctic images shown in Figure 5.2 using the approach by Bélanger et al. (2013b) and by Arrigo et al. (2012). Bélanger et al. (2013b) independently estimated the contribution by CDOM and Chla to $K_d(488)$ while Arrigo et al. (2011) only considered the impact of Chla. However, by not accounting for CDOM absorption, Chla calculated by Arrigo et al. (2011) should be too high, partially compensating for the omission of CDOM in the estimate of $K_d(488)$. Surprisingly, the median $K_d(488)$ calculated for these two independent approaches differed by 2-12%, ranging from 0.68-0.90 m^{-1} and 0.78-0.86 m^{-1}, respectively. The greatest difference in $K_d(488)$ between the two approaches was calculated for the Barents Sea image (Figure 5.2a), yet the resulting difference in the median NPP was <4%. This suggests that while it is desirable to obtain accurate estimates of K_d, when averaged over an entire image, the errors in calculated NPP resulting from oversimplified estimates of K_d are likely to be small.

The absorption-based estimation of primary production (Hirawake et al. 2011, 2012) is one of the ways to reduce the impact of pigment packaging and CDOM. The algorithm calculates the absorption coefficient of phytoplankton (a_{ph}) from remote sensing reflectance (R_{rs}) using the QAA and does not use Chla. It assumes that information of both phytoplankton biomass and photosynthetic rate are included in a_{ph}. Therefore, uncertainty in Chla estimates due to pigment packaging does not need to be taken into account. Furthermore, the QAA may separate the absorption by phytoplankton a_{ph} and by other particles and CDOM (a_{dg}). Although this is different from the separation of the pigment packaging from the CDOM effect, it allows the absorption-based algorithm to estimate primary production without the effect of a_{dg}. Comparisons with Arctic data showed good agreement for a_{ph} at 443 nm (not as good at 412 and 555 nm).

5.3.1 Large-scale analyses of the effect of CDOM and the SCM on NPP

Arrigo et al. (2011) attempted to quantify the magnitude of the error in depth-integrated NPP in the Arctic Ocean estimated using satellite-based NPP algorithms that result from: 1) omission of the SCM from vertical profiles of Chla, and 2) underestimates in surface Chla by the OC4v6 (for SeaWiFS) algorithm due to pigment packaging and overestimates due to CDOM. Differences in the magnitude of this error were quantified for eight different geographic regions within the Arctic Ocean and over monthly, seasonal, and annual timescales.

To assess the potential error associated with satellite-based estimates of depth-integrated

NPP that omit the SCM, Arrigo et al. (2011) quantified the contribution of the SCM to total water column production using *in situ* Chla data from the ARCSS-PP database (`http://accession.nodc.noaa.gov/0063065`, Matrai et al. 2014) as input to the NPP algorithm of Arrigo et al. (2008b) (as modified in Pabi et al. 2008 for Arctic waters). Here we add to the analysis of Arrigo et al. (2011) by also calculating NPP using the algorithm by Hill et al. (2013) to assess the sensitivity of the estimated error associated with the omission the SCM to the NPP algorithm used.

The first step was to calculate mean vertical profiles of *in situ* Chla for each time bin (monthly, seasonal and annual) and geographic sector from the ARCSS-PP database (see below), keeping the SCM intact (Figure 5.4a, solid line). NPP was then calculated (using both the Arrigo et al. 2011 and Hill et al. 2013 algorithms) at each depth for which Chla data were available and these depth-dependent values were integrated vertically (to 100 m) to calculate total water column NPP. Separately, the mean surface Chla concentration from the *in situ* database for a given time bin was applied to the upper water column, essentially removing any SCM that might be present (Figure 5.4b, dashed line). Total water column NPP for each time bin and in each geographic location was then recalculated using the adjusted vertical Chla profiles as input to the NPP algorithm. The difference in vertically integrated NPP between these two approaches reflects the amount of NPP associated with the SCM and provides an estimate of the degree to which NPP algorithms underestimate vertically integrated NPP as a consequence of omission of the SCM.

Arrigo et al. (2011) also quantified the impact that Chla errors by SeaWiFS (resulting primarily from higher pigment packaging and elevated CDOM concentrations in Arctic waters - Matsuoka et al. 2007) would have on calculations of NPP. To do so, they generated new vertical profiles of Chl-a from *in situ* data by increasing the mean surface value in each time bin and geographic location by an amount equivalent to the calculated RMSE of SeaWiFS for Arctic waters (0.21 mg m^{-3}).

It should be noted that the RMSE estimated by Matsuoka et al. (2007) for the Arctic is significantly smaller than that estimated in Chapter 4 of this report. However, the large RMSE in Chapter 4 is the result of a few very large errors at the high end of the Chla range. In fact, inspection of Figure 4.2 from Chapter 4 indicates that the fit of the Arctic data is fairly good for the OC4v6 algorithm at Chla above 1 mg m^{-3} and over the entire data set for OC4L. It is clear that using an RMSE of 2.1 mg Chl-a m^{-3} in this analysis would result in enormous errors in NPP, particularly at low surface Chla. Therefore, we have opted to use the RMSE reported in Matsuoka et al. (2007) until a better error estimate for the Arctic can be generated.

To produce these adjusted profiles, the surface Chla value was held constant throughout the upper water column. These adjusted Chla values impact the estimate of NPP directly due to the higher phytoplankton biomass, and indirectly by increasing light attenuation within the water column. The difference in NPP estimated by their algorithm using the *in situ* Chla profile (Figure 5.4c, solid line) and the adjusted profiles (Figure 5.4c, dashed line) as input provides an estimate of the error in depth-integrated NPP for each time bin and each geographic location resulting from overestimates of satellite-based surface Chla by SeaWiFS.

The results of this analysis showed that for the entire Arctic Ocean, the SCM accounted for only 7.6% or 10.4% of depth-integrated NPP averaged on an annual basis (Table 5.2) respectively,

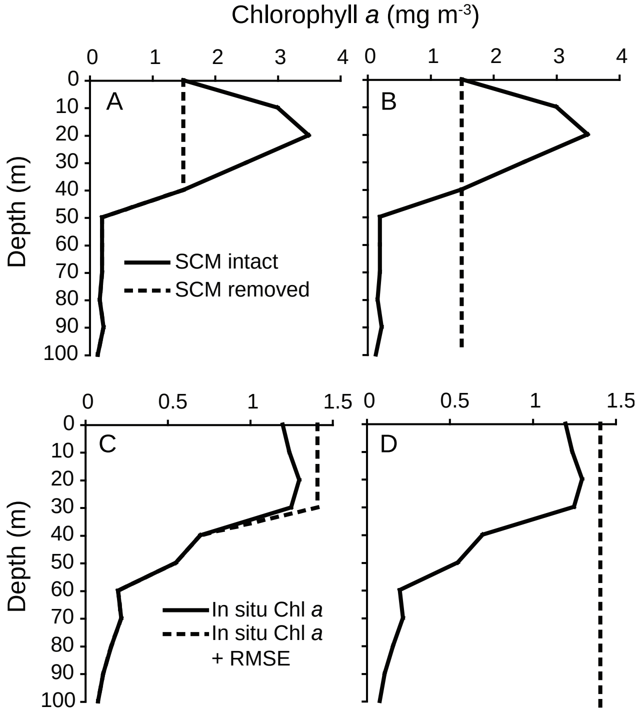

Figure 5.4 Example vertical profiles of Chlorophyll-a illustrating some of the different methods used in the study by Arrigo et al. (2011) to propagate surface Chl-a over depth to: (a-b) remove the SCM, and to (c-d) increase surface Chl-a by 0.21 mg m^{-3}, an amount equivalent to the RMSE of SeaWiFS for Arctic waters (Matsuoka et al. 2007). The solid lines represent the original *in situ* Chl-a profiles from the ARCSS-PP database (Matrai et al. 2014) and the dashed lines are the redistributed Chl-a values used as input to the NPP algorithm.

depending on whether the Arrigo et al. (2011) and Hill et al. (2013) NPP algorithm was used. This value ranged seasonally from 0% in January – March to 8.8% (or 12.4% when using the Hill et al. 2013 NPP algorithm) in April – June. The surprisingly low contribution of the SCM to annual NPP is due, in part, to the fact that of the 61 sector/months for which Chla data were available, 26 (43%) exhibited no SCM (see Table 1 in Arrigo et al. 2011). Thus, contrary to the notion that the SCM is a ubiquitous feature throughout the Arctic Ocean, it appears that its importance to depth-integrated NPP varies as a function of location and time, being most pronounced in summer months. Furthermore, this analysis suggests that the magnitude of the error in satellite-based estimates of NPP, due solely to the inability to resolve the SCM, are <14%, and in many sectors, much less than that (Table 5.2).

Overestimates of NPP resulting from errors in satellite-derived Chla due to CDOM and pigment packaging varied seasonally and by region (Arrigo et al. 2011). At low Chla, the error is large relative to the estimated value, and NPP is dramatically overestimated. At high Chla, the error in depth-integrated NPP is much smaller. During the productive spring-summer period, NPP errors over the entire Arctic were only 3.7 – 9.0% (Arrigo et al. 2011), although specific sectors had errors ranging from 2 – 25%. Errors were even smaller in the seasonal data than

Table 5.2 Percent change in depth-integrated daily net primary production due to removal of the subsurface Chlorophyll-a maximum for different geographic sectors and different time periods. Chlorophyll-a was distributed vertically as shown in Figure 5.4a. Seasonal and annual values in parentheses were calculated using the productivity algorithm of Hill et al. (2013). ND indicates no *in situ* data available.

	January – March	April – June	July – September	October – December	Annual
Chukchi	−19.7 (−25.6)	−12.0 (−18.0)	−6.1 (−9.0)	0.0 (0.0)	−7.6 (−11.2)
Beaufort	−10.7 (−11.2)	0.0 (0.0)	−20.4 (-22.8)	-3.4 (-2.6)	−11.7 (−13.5)
Baffin	−6.6 (−6.2)	−0.2 (−0.2)	−4.1 (−6.5)	−7.5 (−8.2)	−4.1 (−5.9)
Greenland	−20.4 (−24.1)	−2.0 (−1.9)	−6.8 (−6.1)	0.0 (0.0)	−4.5 (−4.1)
Barents	0.0 (0.0)	−2.1 (−2.0)	−2.5 (−2.4)	−4.1 (−4.0)	−1.2 (−1.1)
Kara	ND	0.0 (0.0)	0.0 (0.0)	−1.9 (−2.0)	0.0 (0.0)
Laptev	ND	ND	0.0 (0.0)	ND	0.0 (0.0)
Siberian	ND	ND	−0.5 (−0.5)	ND	−0.5 (−0.5)
All	0.0 (0.0)	−8.8 (−12.4)	−6.8 (−9.1)	−7.4 (−8.7)	−7.6 (−10.4)

in the monthly data because errors in the latter largely offset each other. Annually, for the entire Arctic Ocean, the error in NPP is only about 1% (Arrigo et al. 2011). These small errors can be attributed to the fact that 1) depth-integrated NPP is not linearly related to surface Chla but rather is proportional to the square root of surface Chla (Eppley et al. 1985) and so errors in NPP are smaller than errors in Chla, 2) Chla concentrations in the Arctic are relatively high, especially in the spring and summer, and 3) , errors in depth-integrated NPP associated with satellite-based overestimates in surface Chla are of the opposite sign of errors in NPP associated with ignoring the SCM. As a result, these two errors offset each other.

5.3.2 Consequences for satellite-based estimates of NPP

Arrigo et al. (2011) showed that NPP algorithms that specify a shallow ML depth (e.g., 20 m) will generally underestimate NPP to a greater degree when an SCM is present than algorithms with a deeper ML, although they do better under conditions where low surface Chla values have been underestimated by ocean colour satellites. On an annual basis, however, even the errors when the ML was 20 m were <10% throughout the Arctic.

These results suggest that errors in depth-integrated daily NPP due to omission of the SCM and overestimation of surface Chla due to CDOM are relatively small in algorithms that specify a uniform depth over which remotely-sensed surface Chla is applied. Thus, satellite-based NPP algorithms can perform well in the Arctic Ocean when applied over large spatial and temporal scales, despite its complex bio-optical characteristics and widespread SCM. At regional scale, however, improvements can be achieved by tuning the algorithms with appropriate *in situ* data.

5.4 Acknowledgements

The authors would like to thank Maxime Benoît-Gagné (Takuvik Joint International Laboratory, Université Laval & CNRS) for his contribution to the data analysis of this chapter.

Chapter 6

Recommendations

Despite the limitations and difficulties reviewed in the previous chapters of this report, ocean colour remote sensing remains a highly valuable tool for studying marine ecosystems and biogeochemical fluxes in polar seas. In these remote and virtually inaccessible environments, any source of data is useful. Ocean colour provides a vast amount of information and allows scientists to address important science questions related to the impact of climate change on the marine environment, and more specifically on biogeochemical fluxes and ecosystems. In this last section of the report, we provide a number of recommendations to mitigate limitations and to overcome difficulties in the use of ocean colour remote sensing in polar seas.

- Clouds and fog represent a significant intrinsic limitation of ocean colour remote sensing at high latitudes, especially during late-summer/fall. Multiple polar orbiters may increase the number of successful overpasses for any given location, although the added value of high-frequency observations remains to be quantified in Arctic and Antarctic waters. In any case, methods to fill gaps in the ocean colour products are necessary to derive higher level product such as NPP or phytoplankton phenology.
- The presence of sea ice within, or close to, ocean colour targets is a source of signal contamination that complicates measurements close to the ice edge where the spring bloom takes place, and affects our ability to effectively monitor marine ecosystems. To a large extent, the brief spring bloom fuels the Arctic and Antarctic marine food web. It is possible to flag pixels contaminated by sea ice, but the methods are not yet ready for operational implementation. Further research is required to generalize methodological approaches and explore other strategies to avoid, or correct for, contamination by sea ice.
- Satellite ocean colour data have been used for studying polar sea properties. However, ocean colour products can be further improved with improved atmospheric correction algorithms, in particular, by including Earth curvature effects. Some significant efforts for improving atmospheric correction algorithms in the polar regions (e.g., for cases with large solar-zenith angles) are still required. Although several Arctic and Antarctic coastal sites are equipped with AERONET to monitor aerosol properties, it would be more useful to also have AERONET ocean colour sites in the regions for direct validation and evaluation of satellite ocean colour products. With regards to prevailing low Sun elevation, it might be possible to obtain reliable estimates of nL_w even at SZA larger than 70°, which is the current limit used in the standard L3 processing. The impact of pushing the SZA threshold from 70 to 74° in terms of data coverage for the Arctic

Ocean was also examined. The amount of data available would increase significantly from mid-August to mid-September. Further research is therefore required to extend atmospheric corrections over SZAs larger than 70°.

- Polar seas can be optically complex, therefore standard empirical ocean colour algorithms frequently fail in these waters. The use of regionally-parameterized empirical algorithms can improve predictions obtained from application of standard “global" algorithms, but significant scatter remains. This is particularly true for the Arctic and surrounding seas, where non-local sources of CDOM and non-algal particles contribute strongly to absorption but exhibit little to no covariation with Chla. The best path forward for improving the accuracy of Chla retrieval and other biogeochemical parameters in polar waters is through the use of semi-analytical models that allow discrimination and quantification of the roles of non-phytoplankton constituents. Some initial success has been achieved with existing versions of available models, generally with some specific tuning or re-parameterization. Because these models have been developed for lower latitude oceans, the assumptions and parameterizations need to be rigorously assessed before they can be applied indiscriminately to polar waters. There is thus a strong need for continuing research into the optical properties of the polar oceans and adjacent seas, and the collection of comprehensive sets of bio-optical data (absorption and scattering properties of major constituents) in conjunction with physical and biogeochemical measurements.
- Errors in depth-integrated daily NPP (due to omission of the SCM and overestimation of surface Chla as a result of CDOM) are not seriously compounded in algorithms that specify a uniform depth over which remotely-sensed surface Chla is applied. Although algorithms that specify a deeper mixed layer (or uniform Chla throughout the upper 100 m) perform better, algorithms that employ shallow mixed layers nevertheless exhibit relatively small errors in depth-integrated daily NPP. These results indicate that satellite-based NPP algorithms have the potential to perform quite well in the Arctic Ocean when applied to sufficiently large spatial and temporal scales, despite the complex bio-optical characteristics and widespread SCM in these waters. At regional scales, however, improvements can be achieved by tuning the algorithms with appropriate *in situ* data. Arctic statistical relationships between surface and at-depth chlorophyll concentration have been proposed to overcome this problem. How they actually perform remains to be determined.
- Most ocean colour primary production models currently used for Arctic and Antarctic waters either do not account for variations in phytoplankton photosynthetic parameters, or the applied values are not representative of these environments. A few models use simple relationships between photosynthetic parameters and temperature/light, but these relationships were established using limited data sets from polar waters. Recent Arctic surveys of variations in microalgal photosynthetic parameters (Palmer et al. 2011; Palmer et al. 2013; Huot et al. 2013) show that they vary significantly and are, on average, very different from values found at lower latitudes. There is a clear need to improve the way variations in photosynthetic parameters are accounted for in polar seas PP models,

both through collecting more *in situ* data and analyzing existing data pooled in larger data sets.

- The occurrence of massive under-ice phytoplankton blooms (see Arrigo et al. 2012) is potentially a more serious limitation of ocean colour remote sensing in polar seas. The extent of these blooms is currently unknown and must be determined. If they are common, and occur more frequently because of changes in marine snow and sea-ice dynamics, then new approaches must be designed to estimate their contribution to primary production and to complement measurements achieved using ocean colour in open waters. Possible avenues to be explored include measurements from autonomous platforms (e.g., gliders, profiling floats), the combination of several remote sensing technique to estimate light transmission through snow/sea-ice, and estimating primary production using models not based on biomass measurements.
- The Arctic Ocean is currently experiencing modifications of phytoplankton community composition because of climate change (e.g., Merico et al. 2003; Li et al. 2009). These changes in community structure are expected to have a significant impact on trophic interactions and carbon export to the bottom (Wassmann and Reigstad 2011). Research is therefore encouraged into the use of models for identifying phytoplankton functional types (PFTs) from ocean colour measurements to determine dominant taxonomic groups. Several empirical algorithms to detect PFTs from satellite ocean colour data have been proposed and were the subject of a recent IOCCG Working Group (IOCCG 2014); however, most of these are constructed for lower latitude regions and only a few local algorithms have been developed within the polar regions (e.g., Montes-Hugo et al. 2009; Fujiwara et al. 2011). As these algorithms generally require inputs of both Chla and IOPs, their performance will also require accurate determinations of these quantities. Achieving these types of goals will require optical measurements with a higher spectral range and resolution for improved discrimination of spectral shapes associated with individual seawater constituents. Sensors on existing spaceborne platforms generally do not meet these requirements, but future missions plan to address these limitations (e.g., NASA's PACE mission). Furthermore, it is anticipated that the increasing use of bio-optical sensors on a variety of autonomous *in situ* platforms (gliders, floats, standard and ice-tethered moorings) will enhance our observational capabilities in the polar regions.

Acronyms and Abbreviations

AC	Atmospheric Correction
ACE	Aerosol-Cloud-Ecosystem (NASA)
AERONET	Aerosol Robotic Network
AMSR-E	Advanced Microwave Scanning Radiometer EOS
APFZ	Antarctic Polar Front Zone
AVHRR	Advanced Very High Resolution Radiometer
CALIPSO	Cloud-Aerosol Lidar and Infrared Pathfinder
CDOM	Coloured Dissolved Organic Matter
CZCS	Coastal Zone Color Scanner
DCM	Deep Chlorophyll Maximum
ENVISAT	Environmental Satellite (ESA)
EOS	Earth Observing System
ERS	European Remote-sensing Satellite (ESA)
ESA	European Space Agency
GCOM-W	Global Change Observation Mission – Water (JAXA)
GSM	Garver-Siegel-Maritorena model
HPLC	High Performance Liquid Chromatography
ICESat	Ice, Cloud, and land Elevation Satellite
IFOV	Instantaneous-Field-of-View
IOPs	Inherent Optical Properties
ISCCP	International Satellite Cloud Climatology Project
JAXA	Japan Aerospace Exploration Agency
LAC	Local Area Coverage
LEO	Low Earth Orbit
LUTs	Look-up-Tables
MBR	Maximum Band Ratio
MdR	Median Ratio
MERIS	Medium Resolution Imaging Spectrometer (ESA)
MIZ	Marginal Ice Zones
ML	Mixed Layer
MLD	Mixed Layer Depth
MODIS	Moderate resolution Imaging Spectroradiometer (NASA)
MPCs	Mixed-Phase Clouds
NASA	National Aeronautics and Space Administration (USA)
NCEP	National Centers for Environmental Prediction

NH	Northern Hemisphere
NIR	Near Infrared
NOMAD	NASA bio-Optical Marine Algorithm Data set
NOAA	National Oceanic and Atmospheric Administration (USA)
NOW	North Water Polynya
NPP	Net Primary Production
OC3M	Ocean Chlorophyll 3-band Algorithm (for the NASA MODIS series)
OBPG	Ocean Biology Processing Group (NASA)
OC4	Ocean Chlorophyll 4-band Algorithm (NASA)
OC4E	Ocean Chlorophyll 4-band Algorithm (for ESA MERIS)
PAR	Photosynthetically Active Radiation
PFT	Phytoplankton Functional Type
POM	Particulate Organic Matter
PP	Primary Production
PPA	Plane-Parallel Atmosphere
PSA	Pseudo-Spherical Approximation
PUR	Photosynthetically Usable Radiation
QAA	Quasi-Analytical Algorithm
RGB	Red, Green, Blue
RMSE	Root Mean Square Error
RTE	Radiative Transfer Equation
SAR	Synthetic Aperture Radar
SBDART	Santa Barbara DISORT Atmospheric Radiative Transfer
SBI	Shelf Basin Interaction program
SCM	Subsurface Chlorophyll Maximum
SeaDAS	SeaWiFS Data Analysis System
SeaWiFS	Sea-viewing Wide Field-of-view Sensor (NASA)
SH	Southern Hemisphere
SO	Southern Ocean
SMMR	Scanning Multichannel Microwave Radiometer
SPOT	Satellite Pour l'Observation de la Terre
SSA	Spherical-Shell Atmosphere
SSM/I	Special Scanning Microwave Imager
STD-AC	Standard NASA Atmospheric Correction algorithm
SWIR	Short-Wave Infrared
SZA	Solar Zenith Angles
TOA	Top of Atmosphere
UV	Ultraviolet
VIIRS	Visible Infrared Imaging Radiometer Suite
WMO	World Meteorological Organization

Mathematical Notation

Symbol	**Description**	**Typical Units**
a	Absorption coefficient	$\mathrm{m^{-1}}$
a_d	Absorption coefficient of non-algal particles	$\mathrm{m^{-1}}$
a_g	Absorption coefficient of CDOM (gelbstoff)	$\mathrm{m^{-1}}$
a_{dg}	Absorption coefficient of CDOM plus non-algal particles	$\mathrm{m^{-1}}$
a_p	Absorption coefficient of particles	$\mathrm{m^{-1}}$
a_{ph}	Absorption coefficient of phytoplankton	$\mathrm{m^{-1}}$
a_w	Absorption coefficient of water molecules	$\mathrm{m^{-1}}$
b_b	Backscattering coefficient	$\mathrm{m^{-1}}$
b_{bp}	Backscattering coefficient of particles	$\mathrm{m^{-1}}$
b_{bw}	Backscattering coefficient of water molecules	$\mathrm{m^{-1}}$
Chla	Concentration of Chlorophyll-a	$\mathrm{mg\ m^{-3}}$
C_{ph}	Concentration of phytoplankton carbon	$\mathrm{mg\ m^{-3}}$
E_k	Photoacclimation parameter	$\mu\mathrm{mol\ photons\ m^{-2}\ s^{-1}}$
$E_{10\%}$	Irradiance representing 10% of the surface value	$\mathrm{W\ m^{-2}\mu m^{-1}}$
E_s	Downwelling irradiance at the sea surface	$\mathrm{W\ m^{-2}\mu m^{-1}}$
FChla	Chlorophyll-a concentration determined fluorometrically	$\mathrm{mg\ m^{-3}}$
K_d	Diffuse attenuation coefficient for downwelling irradiance	$\mathrm{m^{-1}}$
λ	Light wavelength in free space	nm
$L_{black-ocn}$	Radiance computed with RTE for a totally absorbing ocean	$\mathrm{W\ m^{-2}\mu m^{-1}\ sr^{-1}}$
L_{ocn}	Radiance of the ocean computed with RTE	$\mathrm{W\ m^{-2}\mu m^{-1}\ sr^{-1}}$
L_w	Water-leaving radiance	$\mathrm{W\ m^{-2}\mu m^{-1}\ sr^{-1}}$
$L_{w,TOA}$	Water-leaving radiance reaching the TOA	$\mathrm{W\ m^{-2}\mu m^{-1}\ sr^{-1}}$
MBR	Maximum Band Ratio of blue-to-green R_{rs}	unitless
nL_w	Normalized water-leaving radiance	$\mathrm{W\ m^{-2}\mu m^{-1}\ sr^{-1}}$
$< \rho >$	Spatially averaged reflectance	unitless
ρ_a	Aerosol reflectance	unitless
ρ_{env}	Environment reflectance	unitless
ρ_{ice}	Sea ice reflectance	unitless
ρ_{path}	Atmospheric path reflectance	unitless
ρ_R	Rayleigh reflectance	unitless
ρ_{Ra}	Coupled Rayleigh-aerosol reflectance	unitless
ρ_{TOA}	TOA reflectance	unitless
ρ_{wc}	White caps reflectance	unitless
ρ_{wN}	Normalized water reflectance	unitless
P^B_{max}	Maximum rate of carbon fixation	$\mathrm{mg\ C\ mg\ Chl^{-1}\ h^{-1}}$
POC	Concentration of particulate organic carbon	$\mathrm{mg\ m^{-3}}$
θ_a	Solar zenith angle	deg
R_{rs}	Remote-sensing reflectance	$\mathrm{sr^{-1}}$

S_a	Atmospheric spherical albedo	unitless
S_d	Spectral slope of a_d	nm^{-1}
S_g	Spectral slope of a_g	nm^{-1}
σ_{ice}	Areal fraction of sea ice within a pixel	%
σ_{wc}	Areal fraction of white caps within a pixel	%
t_d	Atmospheric diffuse transmittance	unitless
T_a	Atmospheric direct transmittance	unitless
TChla	Total Chlorophyll-a concentration determined from HPLC	mg m^{-3}
τ_a	Aerosol optical thickness	unitless
$Z_{10\%}$	Depth corresponding to the value of $E_{10\%}$	m

Bibliography

Ackerman, S. A., C. C. Moeller, K. I. Strabala, H. E. Gerber, L. E. Gumley, W. P. Menzel, and S.-C. Tsay (1998). Retrieval of effective microphysical properties of clouds: A wave cloud case study. *Geophys. Res. Lett.* 25: 1121–1124.

Ackermann, M. et al. (2006). Optical properties of deep glacial ice at the South Pole. *J. Geophys.Res.* 111: D13. DOI: 10.1029/2005JD006687.

Adams, C. N. and G. W. Kattawar (1978). Radiative transfer in spherical shell atmospheres. I. Rayleigh scattering. *Icarus* 35: 139–151.

Ahmad, Z., B. Franz, C. R. McClain, E. J. Kwiatkowska, J. Werdell, E. P. Shettle, and B. N. Holben (2010). New aerosol models for the retrieval of aerosol optical thickness and normalized water-leaving radiances from the SeaWiFS and MODIS sensors over coastal regions and open oceans. *Appl. Opt.* 49: 5545–5560.

Allison, D. B., D. Stramski, and B. G. Mitchell (2010a). Empirical ocean color algorithms for estimating particulate organic carbon in the Southern Ocean. *J. Geophys. Res.* 115: C10. DOI: 10.1029/2009JC006040.

— (2010b). Seasonal and interannual variability of particulate organic carbon within the Southern Ocean from satellite ocean color observations. *J. Geophys. Res.* 115: 1–18.

Allison, I., R. Brandt, and S. Warren (1993). East Antarctic sea ice: Albedo, thickness distribution and snow cover. *J. Geophys. Res.* 98:C7, 12417–12429.

Andreas, E. L. and S. F. Ackley (1982). On the differences in ablation seasons of the Arctic and Antarctic sea ice. *J. Atmos. Sci.* 39: 440–447.

Antoine, D., S. Hooker, S. Bélanger, A. Matsuoka, and M. Babin (2013). Apparent optical properties of the Canadian Beaufort Sea – Part 1: Observational overview and water column relationships. *Biogeosciences* 10: 4493–4509.

Antoine, D. and A. Morel (1996). Oceanic primary production. 1. Adaptation of a spectral light-photosynthesis model in view of application to satellite chlorophyll observations. *Global Biogeochem. Cy.* 10:1, 43–55.

Ardyna, M., M. Babin, M. Gosselin, E. Devred, S. Bélanger, A. Matsuoka, and J.-É. Tremblay (2013). Parameterization of vertical chlorophyll a in the Arctic Ocean: impact of the subsurface chlorophyll maximum on regional, seasonal, and annual primary production estimates. *Biogeosciences* 10:6, 4383–4404. DOI: 10.5194/bg-10-4383-2013.

Ardyna, M., M. Babin, M. Gosselin, E. Devred, L. Rainville, and J.-É. Tremblay (2014). Recent Arctic Ocean sea ice loss triggers novel fall phytoplankton blooms. *Geophys. Res. Lett.* 41:17, 6207–6212.

Arrigo, K. R., P. A. Matrai, and G. L. van Dijken (2011). Primary productivity in the Arctic Ocean: Impacts of complex optical properties and subsurface chlorophyll maxima on large-scale estimates. *J. Geophys. Res.* 116:C11022.

Arrigo, K. R., D. H. Robinson, D. L. Worthen, B. Schieber, and M. P. Lizotte (1998). Bio-optical properties of the southwestern Ross Sea. *J. Geophys. Res.* 103: 21683–21695. DOI: 10.1029/98JC02157.

Arrigo, K. R. and G. L. van Dijken (2004). Annual cycles of sea ice and phytoplankton near Cape Bathurst, southeastern Beaufort Sea, Canadian Arctic. *Geophys. Res. Lett.* 31:L08304.

Arrigo, K. R., G. L. van Dijken, and S. Bushinsky (2008a). Primary production in the Southern Ocean, 1997 – 2006. *J. Geophys. Res.* 113: C8. DOI: 10.1029/2007JC004551.

Arrigo, K. R., G. van Dijken, and S. Pabi (2008b). Impact of a shrinking Arctic ice cover on marine primary production. *Geophys. Res. Lett.* 35:19, L19603.

Arrigo, K. R. et al. (2012). Massive phytoplankton blooms under Arctic Sea ice. *Science* 336: 1408.

Babin, M., D. Stramski, G. M. Ferrari, H. Claustre, A. Bricaud, G. Obolensky, and N. Hoepffner (2003). Variations in the light absorption coefficients of phytoplankton, nonalgal particles, and dissolved organic matter in coastal waters around Europe. *J. Geophys. Res.* 108: 3211. DOI: 10.1029/2001JC000882.

Babin, M. et al. (2015). Estimation of primary production in the Arctic Ocean using ocean colour remote sensing and coupled physical-biological models: strengths, limitations and how they compare. *Prog. Oceanogr.* In press:

Bailey, S. W., B. A. Franz, and P. J. Werdell (2010). Estimation of near-infrared water-leaving reflectance for satellite ocean color data processing. *Opt. Express* 18: 7521–7527.

Baith, K., R. Lindsay, G. Fu, and C. R. McClain (2001). Data analysis system developed for ocean color satellite sensors. *Eos Transactions AGU* 82:18, 202–202.

Balch, W. M., D. T. Drapeau, B. Bowler, and E. S. Booth (2007). Prediction of pelagic calcification rates using satellite measurements. *Deep Sea Res. II* 54: 478–495.

Balch, W. M., D. T. Drapeau, B. Bowler, E. Lyczskowski, E. S. Booth, and D. Alley (2011). The contribution of coccolithophores to the optical and inorganic carbon budgets during the Southern Ocean Gas Exchange Experiment: New evidence in support of the "Great Calcite Belt" hypothesis. *J. Geophys. Res.* 116: 1–14.

Balch, W. M., H. R. Gordon, B. Bowler, D. T. Drapeau, and E. S. Booth (2005). Calcium carbonate measurements in the surface global ocean based on Moderate-Resolution Imaging Spectroradiometer data. *J. Geophys. Res.* 110: C7. DOI: `10.1029/2004JC002560`.

Balzano, S., D. Marie, P. Gourvil, and D. Vaulot (2012). Composition of the summer photosynthetic pico and nanoplankton communities in the Beaufort Sea assessed by T-RFLP and sequences of the 18S rRNA gene from flow cytometry sorted samples. *ISME J.* 6: 1480–1498.

Behrenfeld, M. J. and P. G. Falkowski (1997a). A consumer's guide to phytoplankton primary productivity models. *Limnol. Oceanogr.* 42: 1479–1491.

— (1997b). Photosynthetic rates derived from satellite-based chlorophyll concentration. *Limnol. Oceanogr.* 42: 1–20.

Behrenfeld, M. J., E. Maranon, D. A. Siegel, and S. B. Hooker (2002). Photoacclimation and nutrient-based model of light-saturated photosynthesis for quantifying oceanic primary production. *Mar. Ecol. Prog. Ser.* 228: 103–117. DOI: `10.3354/meps228103`.

Bélanger, S., M. Babin, and J.-É. Tremblay (2013a). Increasing cloudiness in Arctic damps the increase in phytoplankton primary production due to sea ice receding. *Biogeosciences* 10: 4087–4101.

Bélanger, S., S. A. Cizmeli, J. Ehn, A. Matsuoka, D. Doxaran, S. Hooker, and M. Babin (2013b). Light absorption and partitioning in Arctic Ocean surface waters: impact of multiyear ice melting. *Biogeosciences* 10: 6433–6452. DOI: `10.5194/bg-10-6433-2013`.

Bélanger, S., J. Ehn, and M. Babin (2007). Impact of sea ice on the retrieval of water-leaving reflectance, chlorophyll a concentration and inherent optical properties from satellite ocean color data. *Remote Sens. Environ.* 111: 51–68.

Bélanger, S., H. Xie, N. Krotkov, P. Larouche, W. Vincent, and M. Babin (2006). Photomineralization of terrigenous dissolved organic matter in Arctic coastal waters from 1979 to 2003: Interannual variability and implications of climate change. *Global Biogeochem. Cy.* 20: GB4005.

Bélanger, S., M. Babin, and P. Larouche (2008). An empirical ocean color algorithm for estimating the contribution of chromophoric dissolved organic matter to total light absorption in optically complex waters. *J. Geophys. Res.* 113:C4, C04027.

Ben Mustapha, S., S. Bélanger, and P. Larouche (2012). Evaluation of ocean color algorithms in the southeastern Beaufort Sea, Canadian Arctic: New parameterization using SeaWiFS, MODIS, and MERIS spectral bands. *Can. J. Remote Sen.* 38: 535–556.

Bennartz, R. et al. (2013). July 2012 Greenland melt extent enhanced by low-level liquid clouds. *Nature* 496: 83–86.

Bohren, C. F. and D. R. Huffman (1983). *Absorption and Scattering of Light by Small Particles.* Wiley, New York.

Bricaud, A., M. Babin, A. Morel, and M. Claustre (1995). Variability in the chlorophyll-specific absorption-coefficients of natural phytoplankton – analysis and parameterization. *J. Geophys. Res.* 100:C7, 13321–13332. DOI: `10.1029/95JC00463`.

Bricaud, A., A. Morel, M. Babin, K. Allali, and H. Claustre (1998). Variations of light absorption by suspended particles with chlorophyll a concentration in oceanic (case 1) waters: Analysis and implications for bio-optical models. *J. Geophys. Res.* 103: 31033–31044.

Bussmann, I. (1999). Bacterial utilization of humic substances from the Arctic Ocean. *Aquat. Microb. Ecol.* 19: 37–45.

Carlson, C. A. and H. W. Ducklow (1996). Growth of bacterioplankton and consumption of dissolved organic carbon in the Sargasso Sea. *Aquat. Microb. Ecol.* 10:1, 69–85.

Carr, M.-E. et al. (2006). A comparison of global estimates of marine primary production from ocean color. *Deep-Sea Res. II* 53: 741–770.

Cavalieri, D. J. and J. C. Comiso (2000). *Algorithm Theoretical Basis Document for the AMSR-E Sea Ice Algorithm, Revised December 1.* Tech. rep. NASA.

Cavalieri, D. J., P. Gloersen, C. Parkinson, J. Comiso, and H. J. Zwally (1997). Observed hemispheric asymmetry in global sea ice changes. *Science* 278: 1104–1106.

Cavalieri, D. J. and C. L. Parkinson (2012). Arctic sea ice variability and trends. *The Crysphere Discuss.* 6: 957–979.

Chan, M. A. and J. C. Comiso (2013). Arctic cloud cover characteristics as inferred from MODIS, CALIPSO and Cloudsat. *J. Climate.* 26: 3285–3306.

Chen, N., W. Li, T. Tanikawa, M. Hori, T. Aoki, and K. Stamnes (2014). Cloud mask over snow/ice covered areas for the GCOM-C1/SGLI cryosphere mission: Validations over Greenland. *J. Geophys. Res.* DOI: `10.1002/2014JD022017`.

Comiso, J. C. (2002). A rapidly declining Arctic perennial ice cover. *Geophys. Res. Lett.* 29:20, 1956. DOI: `10.1029/2002GL015650`.

— (2006). Impacts of the variability of 2nd year ice types on the decline of the perennial ice cover. *Ann. Glaciol.* 44: 375–382.

— (2010). *Polar Oceans from Space.* Ed. by L. Mysak and K. Haliton. Vol. 41. Atmospheric and Oceanographic Sciences Library. Springer.

Comiso, J. C., R. Kwok, S. Martin, and A. Gordon (2011). Variability and trends in sea ice and ice production in the Ross Sea. *J. Geophys. Res.* 116:C04021. DOI: `1029/2010JC006391`.

Comiso, J. C., N. G. Maynard, W. O. Smith, and C. W. Sullivan (1990). Satellite ocean color studies of Antarctic ice edges in summer and autumn. *J. Geophys. Res.* 95:C6, 9481–9496. DOI: `10.1029/JC095iC06p09481`.

Comiso, J. C., C. McClain, C. Sullivan, J. Ryan, and C. Leonard (1993). Coastal zone color scanner pigment concentrations in the Southern Ocean and relationships to geophysical surface features. *J. Geophys. Res.* 98: 2419–2451.

Comiso, J. C. and F. Nishio (2008). Trends in the sea ice cover using enhanced and compatible AMSR-E, SSM/I, and SMMR data. *J. Geophys. Res.* 113: C02S07.

Comiso, J. C. and C. L. Parkinson (2008). Arctic sea ice parameters from AMSR-E using two techniques, and comparisons with sea ice from SSM/I. *J. Geophys. Res.* 113: C02S05.

Comiso, J. C., C. L. Parkinson, R. Gersten, and L. Stock (2008). Accelerated decline in the Arctic sea ice cover. *Geophys. Res. Lett.* 35: L01703.

Comiso, J. C., J. Yang, H. Susumo, and R. A. Krishfield (2003). Detection change in the Arctic using satellite and in situ data. *J. Geophys. Res.* 108: 3384.

Cota, G. F., W. G. Harrison, T. Platt, S. Sathyendranath, and V. Stuart (2003). Bio-optical properties of the Labrador Sea. *J. Geophys. Res.* 108:

Cota, G. F., J. Wang, and J. C. Comiso (2004). Transformation of global satellite chlorophyll retrievals with a regionally tuned algorithm. *Remote Sens. Environ.* 90: 373–377.

Cullen, J. (1982). The deep Chlorophyll maximum: Comparing vertical profiles of Chlorophyll a. *Can. J. Fish. Aquat. Sci.* 39:5, 791–803.

Curry, J. A. and E. E. Ebert (1992). Annual cycle of radiative fluxes over the arctic ocean: Sensitivity to cloud optical properties. *J. Climate* 5: 1267–1280.

Curry, J., J. Pinto, T. Benner, and M. Tschudi (1997). Evolution of the cloudy boundary layer during the autumnal freezing of the Beaufort Sea. *J. Geophys. Res.* 102: 13851–13860.

Dahlback, A. and K. Stamnes (1991). A new spherical model for computing the radiation field available for photolysis and heating at twilight. *Planet. Space Sci.* 39: 671–683.

Darby, D. A., W. B. Myers, M. Jakobsson, and I. Rigor (2011). Modern dirty sea ice characteristics and sources: The role of anchor ice. *J. Geophys. Res.* 116: 1–18.

De Boer, G., E. Eloranta, and M. Shupe (2009). Arctic mixed-phase stratiform cloud properties from multiple years of surface-based measurements at two high-latitude locations. *J. Atmos. Sci.* 66: 2874–2887.

Dierssen, H. M. and R. C. Smith (2000). Bio-optical properties and remote sensing ocean color algorithms for Antarctic Peninsula waters. *J. Geophys. Res.* 105: 26301–26312.

Dierssen, H. M., R. C. Smith, and M. Vernet (2002). Glacial meltwater dynamics in coastal waters west of the Antarctic peninsula. *Proc. Nat. Acad. Sci. U.S.A.* 99: 1790–1795.

Dierssen, H., M. Vernet, and R. C. Smith (2000). Optimizing models for remotely estimating primary production in Antarctic coastal waters. *Antarct. Sci.* 12: 20–32.

Ding, K. and H. R. Gordon (1994). Atmospheric correction of ocean-color sensors: effects of the Earth's curvature. *Appl. Opt.* 33: 7096–7106.

Doolittle, D., W. K. W. Li, and A. M. Wood (2008). Wintertime abundance of picoplankton in the Atlantic sector of the Southern Ocean. *Nova Hedwigia* 133: 147–160.

Doxaran, D., J. Ehn, S. Bélanger, A. Matsuoka, S. Hooker, and M. Babin (2012). Optical characterisation of suspended particles in the Mackenzie River plume (Canadian Arctic Ocean) and implications for ocean colour remote sensing. *Biogeosciences* 9: 3213–3229.

Edwards, J. M., S. Havemann, J.-C. Thelen, and A. J. Baran (2007). A new parameterization for the radiative properties of ice crystals: comparison with existing schemes and the impact in a GCM. *Atmos. Res.* 83: 19–35.

Eppley, R., E. Steward, M. Abbott, and U. Heyman (1985). Estimating ocean primary production from satellite chlorophyll: Introduction to regional differences and statistics for the Southern California Bight. *J. Plankton Res.* 7: 57–70.

Feldman, G. C. and C. R. McClain (2012). *Ocean Color Web, MODIS-AQUA Reprocessing 2012.0.* NASA Goddard Space Flight Center. URL: `oceancolor.gsfc.nasa.gov`.

Forest, A., S. Bélanger, M. Sampei, H. Sasaki, C. Lalande, and L. Fortier (2010). Three-year assessment of particulate organic carbon fluxes in Amundsen Gulf (Beaufort Sea): Satellite observations and sediment trap measurements. *Deep Sea Res. I* 57: 125–142.

Frey, R., S. Ackerman, Y. Liu, K. I. Strabala, H. Zhang, J. R. Key, and X. Wang (2008). Cloud Detection with MODIS. Part I: Improvements in the MODIS Cloud Mask for Collection 5. *J. Atmos. Oceanic Technol.* 25: 1057–1072.

Frouin, R., M. Schwindling, and P. Y. Deschamps (1996). Spectral reflectance of sea foam in the visible and near-infrared: *In situ* measurements and remote sensing implications. *J. Geophys. Res.* 101: 14361–14371.

Fu, Q. (1996). An accurate parameterization of the solar radiative properties of cirrus clouds for climate models. *J. Climate* 9: 2058–2082.

Fu, Q., P. Yang, and W. B. Sun (1998). An accurate parameterization of the infrared radiative properties of cirrus clouds for climate models. *J. Climate* 11: 2223–2237.

Fujiwara, A., T. Hirawake, K. Suzuki, I. Imai, and S.-I. Saitoh (2014). Timing of sea ice retreat can alter phytoplankton community structure in the western Arctic Ocean. *Biogeosciences* 11: 1705–1716.

Fujiwara, A., T. Hirawake, K. Suzuki, and S.-I. Saitoh (2011). Remote sensing of size structure of phytoplankton communities using optical properties of the Chukchi and Bering Sea shelf region. *Biogeosciences* 8: 3567–3580.

Garcia, C. A. E., V. M. T. Garcia, and C. R. McClain (2005). Evaluation of SeaWiFS chlorophyll algorithms in the Southwestern Atlantic and Southern Oceans. *Remote Sens. Environ.* 95: 125–137.

Garver, S. and D. Siegel (1997). Inherent optical property inversion of ocean color spectra and its biogeochemical interpretation 1. Time series from the Sargasso Sea. *J. Geophys. Res.* 102: 18607–18625.

Giles, K. A., S. W. Laxon, and A. L. Ridout (2008). Circumpolar thinning of Arctic sea ice following the 2007 record ice extent minimum. *Geophys. Res. Lett.* 35: L22402.

Gloersen, P., W. Campbell, D. Cavalieri, J. Comiso, C. Parkinson, and H. Zwally (1992). *Arctic and Antarctic Sea Ice, 1978–1987: Satellite Passive Microwave Observations and Analysis.* Tech. rep. NASA Spec. Publ. 511.

Gordon, H. R. (1997). Atmospheric correction of ocean color imagery in the Earth Observation System era. *J. Geophys. Res.* 102: 17081–17106.

Gordon, H. R., G. C. Boynton, W. M. Balch, S. B. Groom, D. S. Harbour, and T. J. Smyth (2001). Retrieval of coccolithophore calcite concentration from SeaWiFS imagery. *Geophys. Res. Lett.* 28: 1587–1590.

Gordon, H. R., J. W. Brown, and R. H. Evans (1988a). Exact Rayleigh scattering calculations for use with the Nimbus-7 Coastal Zone Color Scanner. *Appl. Opt.* 27: 862–871.

Gordon, H. R., O. B. Brown, R. H. Evans, J. W. Brown, R. C. Smith, K. S. Baker, and D. K. Clark (1988b). A semianalytic radiance model of ocean color. *J. Geophys. Res.* 93: 10909–10924.

Gordon, H. R. and A. Y. Morel (1983). *Remote assessment of ocean color for interpretation of satellite visible imagery: A review.* Springer-Verlag, Berlin.

Gordon, H. R. and M. Wang (1994). Retrieval of water-leaving radiance and aerosol optical thickness over the oceans with SeaWiFS: a preliminary algorithm. *Appl. Opt.* 33: 443–452.

Granskog, M. A., R. W. Macdonald, C. J. Mundy, and D. G. Barber (2007). Distribution, characteristics and potential impacts of chromophoric dissolved organic matter (CDOM) in Hudson Strait and Hudson Bay, Canada. *Cont. Shelf Res.* 27: 2032–2050.

Granskog, M. A. et al. (2009). Coastal conduit in southwestern Hudson Bay (Canada) in summer: Rapid transit of freshwater and significant loss of colored dissolved organic matter. *J. Geophys. Res.* 114:C08012.

Gregg, W. W. and K. L. Carder (1990). A simple spectral solar irradiance model for cloudless maritime atmospheres. *Limnol. Oceanogr.* 35: 1657–1675.

Gregg, W. W. and N. W. Casey (2004). Global and regional evaluation of the SeaWiFS chlorophyll data set. *Remote Sens. Environ.* 93: 463–479.

Grenfell, T. C. (1983). A theoretical model of the optical properties of sea ice in the visible and near infrared. *J. Geophys. Res.* 88: 9723–9735.

Grenfell, T. C. and G. A. Maykut (1977). The optical properties of snow and ice in the Arctic Basin. *J. Glaciol.* 18: 445–463.

Grenfell, T. C. and D. K. Perovich (1981). Radiation absorption coefficients of polycrystalline ice from 400–1400 nm. *J. Geophys. Res.* 86: 7447–7450.

Gross-Colzy, L., S. Colzy, R. Frouin, and P. Henry (2007a). A general Ocean Color Atmospheric correction scheme based on principal component analysis – Part I: Performance on Case 1 and Case 2 waters. In: *Coastal Ocean Remote Sensing.* Proc. of SPIE, 12 pp. DOI: `10.1117/12.738508`.

— (2007b). A general Ocean Color Atmospheric correction scheme based on principal component analysis – Part II: Level 4 merging capabilities. In: *Coastal Ocean Remote Sensing.* Proc. of SPIE, 12 pp. DOI: `10.1117/12.738514`.

Gueguen, C., L. D. Guo, M. Yamamoto-Kawai, and N. Tanaka (2007). Colored dissolved organic matter dynamics across the shelf-basin interface in the western Arctic Ocean. *J. Geophys. Res.* 112:C05038.

Hamre, B., S. Stamnes, K. Stamnes, and J. J. Stamnes (2013). c-disort: A versatile tool for radiative transfer in coupled media like the atmosphere-ocean system. In: *Radiation Processes in the Atmosphere and Ocean (IRS2012), AIP Conf. Proc.* Vol. 1531, 923–926.

Hanesiak, J. and X. L. Wang (2005). Adverse-weather trends in the Canadian Arctic. *J. Climate* 18: 3140–3156.

Harrison, W. G. and T. Platt (1986). Photosynthesis-irradiance relationships in polar and temperate phytoplankton populations. *Polar Biol.* 5: 153–164.

Hessen, D. O., J. Carroll, B. Kjeldstad, A. A. Korosov, L. H. Pettersson, D. Pozdnyakov, and K. Sorensen (2010). Input of organic carbon as determinant of nutrient fluxes, light climate and productivity in the Ob and Yenisey estuaries. *Estuar. Coast. Shelf S.* 88: 53–62.

Hewes, C. D., C. S. Reiss, M. Kahru, B. G. Mitchell, and O. Holm-Hansen (2008). Control of phytoplankton biomass by dilution and mixed layer depth in the western Weddell-Scotia Confluence. *Mar. Ecol. Prog. Ser.* 366: 15–29.

Heymsfield, A. J. and C. M. R. Platt (1984). A parameterization of the particle size spectrum of ice clouds in terms of the ambient temperature and ice water content. *J. Atmos. Sci.* 41: 846–855.

Hill, V. J. (2008). Impacts of chromophoric dissolved organic material on surface ocean heating in the Chukchi Sea. *J. Geophys. Res.* 113:C07024. DOI: `10.1029/2007JC004119`.

Hill, V. J., P. A. Matrai, E. Olson, S. Suttles, M. Steele, L. A. Codispoti, and R. C. Zimmerman (2013). Synthesis of integrated primary production in the Arctic Ocean: II. In situ and remotely sensed estimates. *Prog. Oceanogr.* 110: 107–125. DOI: `10.1016/j.pocean.2012.11.005`.

Hill, V. J. and R. C. Zimmerman (2010). Assessing the accuracy of remotely sensed primary production estimates for the Arctic Ocean, using passive and active sensors. *Deep Sea Res. I* 57: 1243–1254.

Hill, V. and G. Cota (2005). Spatial patterns of primary production on the shelf, slope and basin of the Western Arctic in 2002. *Deep-Sea Res. II* 52: 3344–3354.

Hirawake, T., H. Satoh, T. Ishimaru, Y. Yamaguchi, and M. Kishino (2000). Bio-optical relationship of Case I waters: The difference between the low- and mid-latitude waters and the Southern Ocean. *J. Oceanogr.* 56: 245–260.

Hirawake, T., K. Shinmyo, A. Fujiwara, and S. I. Saitoh (2012). Satellite remote sensing of primary productivity in the Bering and Chukchi Seas using an absorption-based approach. *ICES J. Mar. Science* 69: 1194–1204.

Hirawake, T., S. Takao, N. Horimoto, T. Ishimaru, Y. Yamaguchi, and M. Fukuchi (2011). A phytoplankton absorption-based primary productivity model for remote sensing in the Southern Ocean. *Polar Biol.* 34: 291–302.

Hodal, H. and S. Kristiansen (2008). The importance of small-celled phytoplankton in spring blooms at the marginal ice zone in the northern Barents Sea. *Deep Sea Res. II* 55: 2176–2185.

Holland, M. M., C. M. Bitz, B. Tremblay, and D. A. Bailey (2008). The role of natural versus forced change in future rapid summer Arctic ice loss. In: *Arctic sea ice decline: observations, projections, mechanisms, and implications.* Ed. by E. T. DeWeaver, C. M. Bitz, and L. B. Tremblay. Geophys. Monogr. Ser. 180. AGU, Washington, D. C., 133–150.

Holm-Hansen, O. et al. (2004). Temporal and spatial distribution of chlorophyll-a in surface waters of the Scotia Sea as determined by both shipboard measurements and satellite data. *Deep Sea Res. II* 51: 1323–1331.

Hooker, S. B., W. E. Esaias, G. C. Feldman, W. W. Gregg, and C. R. Mc Clain (1992). An overview of SeaWiFS and ocean colour. In: *SeaWiFS Technical Report Series, NASA Technical Memorandum 104566, 1.* NASA Goddard Space Flight Centre, Greenbelt , Maryland.

Hooker, S. B. et al. (2005). *The Second SeaWiFS HPLC Analysis Round-Robin Experiment (SeaHARRE-2). NASA/TM-2005-212787.* Tech. rep. NASA Goddard Space Flight Center, Greenbelt, Maryland.

Hu, Y.-X. and K. Stamnes (1993). An accurate parameterization of the radiative properties of water clouds suitable for use in climate models. *J. Climate* 6: 728–742.

Huot, Y., M. Babin, and F. Bruyant (2013). Photosynthetic parameters in the Beaufort Sea in relation to the phytoplankton community structure. *Biogeosciences* 10:5. BG, 3445–3454.

Huot, Y., A. Morel, M. S. Twardowski, D. Stramski, and R. A. Reynolds (2008). Particle optical backscattering along a chlorophyll gradient in the upper layer of the eastern South Pacific Ocean. *Biogeosciences* 5:2, 495–507.

Intrieri, J. M., C. Fairall, M. Shupe, P. Persson, E. Andreas, P. Guest, and R. Moritz (2002). Annual cycle of arctic surface cloud forcing at SHEBA. *J. Geophys. Res.* 107: 8039.

IOCCG (1999). *Status and Plans for Satellite Ocean-Colour Missions: Considerations for Complementary Missions.* Ed. by J. A. Yoder. Vol. No. 2. Reports of the International Ocean Colour Coordinating Group. Dartmouth, Canada: IOCCG.

— (2000). *Remote Sensing of Ocean Colour in Coastal, and Other Optically-Complex, Waters.* Ed. by S. Sathyendranath. Vol. No. 3. Reports of the International Ocean Colour Coordinating Group. Dartmouth, Canada: IOCCG.

— (2006). *Remote Sensing of Inherent Optical Properties: Fundamentals, Tests of Algorithms, and Applications.* Ed. by Z.-P. Lee. Vol. No. 5. Reports of the International Ocean Colour Coordinating Group. Dartmouth, Canada: IOCCG.

— (2010). *Atmospheric Correction for Remotely-Sensed Ocean-Colour Products.* Ed. by M. Wang. Vol. No. 10. Reports of the International Ocean Colour Coordinating Group. Dartmouth, Canada: IOCCG.

— (2014). *Phytoplankton Functional Types from Space.* Ed. by S. Sathyendranath. Vol. No. 15. Reports of the International Ocean Colour Coordinating Group. Dartmouth, Canada: IOCCG.

Jacobs, S. and J. Comiso (1993). A recent sea-ice retreat west of the Antarctic Peninsula. *Geophys. Res. Lett.* 20:12, 1171–1174.

Jin, Z. and K. Stamnes (1994). Radiative transfer in nonuniformly refracting media such as the atmosphere/ocean system. *Appl. Opt.* 33: 431–442.

Jonasz, M. and G. Fournier (2007). *Light scattering by particles in water: Theoretical and experimental foundations.* Academic Press: New York.

Kahnert, M., A. D. Sandvik, M. Biryulina, J. J. Stamnes, and K. Stamnes (2008). Impact of ice particle shape on short-wave radiative forcing: A case study for an arctic ice cloud J. *Quant. Spectrosc. Radiat. Transfer* 109: 1196–1218.

Kahru, M., S. Gille, R. Murtugudde, P. Strutton, M. Manzano-Sarabia, H. Wang, and B. Mitchell (2010). Global correlations between winds and ocean chlorophyll. *J. Geophys. Res.* 115:C12.

Kahru, M. and B. G. Mitchell (2010). Blending of ocean colour algorithms applied to the Southern Ocean. *Remote Sens. Lett.* 1: 119–124.

Kattawar, G. W. and C. N. Adams (1978). Radiative transfer in spherical shell atmospheres II, asymmetric phase functions. *Icarus* 35: 436–449.

Kay, J. and A. Gettelman (2009). Cloud influence on and response to seasonal arctic sea ice loss. *J. Geophys. Res.* 114: D18 204:

Key, J. R., P. Yang, B. A. Baum, and S. L. Nasiri (2002). Parameterization of shortwave ice cloud optical properties for various particle habits. *J. Geophys. Res.* 107: D21. DOI: 10.1029/2002JD002061.

Kirchman, D. L., H. Elifantz, A. I. Dittel, R. R. Malmstrom, and M. T. Cottrell (2007). Standing stocks and activity of Archaea and bacteria in the western Arctic Ocean. *Limnol. Oceanogr.* 52: 495–507.

Kirchman, D. L., R. R. Malmstrom, and M. T. Cottrell (2005). Control of bacterial growth by temperature and organic matter in the Western Arctic. *Deep Sea Res. II* 52: 3386–3395.

Kirk, J. T. O. (1994). *Light and Photosynthesis in Aquatic Ecosystems.* Cambridge University Press, Cambridge.

Knobelspiesse, K. D. et al. (2004). Maritime aerosol optical thickness measured by handheld sun photometers. *Remote Sens. Environ.* 93: 87–106.

Korb, R. E., M. J. Whitehouse, and P. Ward (2004). SeaWiFS in the southern ocean: spatial and temporal variability in phytoplankton biomass around South Georgia. *Deep Sea Res. II* 51: 99–116.

Kwok, R. G., G. F. Cunningham, M. Wensnahan, I. Rigor, H. J. Zwally, and D. Yi (2009). Thinning and volume loss of the Arctic Ocean sea ice cover: 2003–2008. *J. Geophys. Res.* 114: DOI: 10.1029/2009JC005312.

Kwok, R. and N. Untersteiner (2011). New high-resolution images of summer sea ice. *Phys. Today* 64: 36–41.

Kwok, R., H. J. Zwally, and D. Yi (2004). ICESat observations of Arctic sea ice: A first look. *Geophys. Res. Lett.* 31: L16401. DOI: 10.1029/2004GL020309.

Langford, V. S., A. J. McKinley, and T. I. Quickenden (2001). Temperature dependence of the visible-near-infrared absorption spectrum of liquid water. *J. Phys. Chem. A* 105: 8916–8921.

Lawson, R. P., B. A. Baker, C. G. Schmitt, and T. L. Jensen (2001). An overview of microphysical properties of arctic clouds observed in May and July 1998 during FIRE ACE. *J. Geophys. Res.* 106: D14. DOI: 10.1029/2000JD900789.

Lawson, R. P., K. Stamnes, J. J. Stamnes, P. Zmarzly, J. Koskuliks, C. Roden, and Q. Mo (2011). Deployment of a tethered balloon system for cloud microphysics and radiative mea- surements at Ny-Ålesund and South Pole. *J. Atmos. Ocean. Tech.* 28: 656–670.

Lawson, R. P. and P. Zuidema (2009). Aircraft microphysical and surface-based radar obser- vations in summertime arctic clouds. *J. Atmos. Sci.* 66: 3505–3529.

Laxon, S. W., N. Peacock, and D. Smith (2003). High interannual variability of sea ice thickness in the Arctic region. *Nature* 425: 947–949.

Lee, S. H., T. E. Whitledge, and S.-H. Kang (2007a). Recent carbon and nitrogen uptake rates of phytoplankton in Bering Strait and the Chukchi Sea. *Cont. Shelf. Res.* 27: 2231–2249.

Lee, Y. et al. (in press). An assessment of phytoplankton primary productivity in the Arctic Ocean from satellite ocean color/ *in situ* chlorophyll-a based models. *J. Geophys. Res.*

Lee, Z. P., M. Darecki, K. L. Carder, C. O. Davis, D. Stramski, and W. J. Rhea (2005a). Diffuse attenuation coefficient of downwelling irradiance: An evaluation of remote sensing methods. *J. Geophys. Res.* 110:C02017.

Lee, Z. P., K. P. Du, and R. Arnone (2005b). A model for the diffuse attenuation coefficient of downwelling Irradiance. *J. Geophys. Res.* 110: C02016. DOI: 10.1029/2004JC002275.

Lee, Z. P. and C. M. Hu (2006). Global distribution of Case-1 waters: An analysis from SeaWiFS measurements. *Remote Sens. Environ.* 101:2, 270–276.

Lee, Z. P., A. Weidemann, J. Kindle, R. Arnone, K. L. Carder, and C. Davis (2007b). Euphotic zone depth: Its derivation and implication to ocean-color remote sensing. *J. Geophys. Res.* 112: C3. DOI: 10.1029/2006JC003802.

Lee, Z.-P., K. L. Carder, and R. A. Arnone (2002). Deriving inherent optical properties from water color : a multiband quasi-analytical algorithm for optically deep waters. *Appl. Opt.* 41: 5755–5772.

Lee, Z. et al. (2011). An assessment of optical properties and primary production derived from remote sensing in the Southern Ocean (SO GasEx). *J. Geophys. Res.* 116:C00F03. DOI: 10.1029/2010JC006747.

Lenoble, J. (1985). *Radiative Transfer in Scattering and Absorbing Atmospheres: Standard Computation Procedures.* Hampton, VA, A. Deepak Publishing.

Li, W., F. McLaughlin, C. Lovejoy, and E. Carmack (2009). Smallest algae thrive as the Arctic Ocean freshens. *Science* 326:

Light, B., T. C. Grenfell, and D. K. Perovich (2008). Transmission and absorption of solar radiation by arctic sea ice during the melt season. *J. Geophys. Res.* 113: C03023.

Light, B., G. A. Maykut, and T. C. Grenfell (2003). Effects of temperature on the microstructure of first-year Arctic sea ice. *J. Geophys. Res.* 108: 3051.

Liu, Y., S. Ackerman, B. C. Maddux, J. R. Key, and R. Frey (2010). Errors in cloud detection over the Arctic using a satellite imager and implications for observing feedback mechanisms. *J. Climate* 23: 1894–1907.

Macdonald, R. W., S. M. Solomon, R. E. Cranston, H. E. Welch, M. B. Yunker, and C. Gobeil (1998). A sediment and organic carbon budget for the Canadian Beaufort Shelf. *Mar. Geol.* 144: 255–273.

Maffione, R. A. and D. R. Dana (1997). Instruments and methods for measuring the backward-scattering coefficient of ocean waters. *Appl. Opt.* 36: 6057–6067.

Maritorena, S., D. A. Siegel, and A. R. Peterson (2002). Optimization of a semianalytical ocean color model for global-scale applications. *Appl. Opt.* 41: 2705–2714.

Marra, J., C. Ho, and C. Trees (2003). *An alternative algorithm for the calculation of primary productivity from remote sensing data.* LDEO Technical Report LDEO-2003-1. Lamont-Doherty Earth Observatory of Columbia University.

Marrari, M., C. Hu, and K. Daly (2006). Validation of SeaWiFS chlorophyll a concentrations in the Southern Ocean: A revisit. *Remote Sens. Environ.* 105: 367–375.

Martin, J. et al. (2010). Prevalence, structure and properties of subsurface chlorophyll maxima in Canadian Arctic waters. *Mar. Ecol. Prog. Ser.* 412: 69–84.

Martin, S., R. S. Drucker, and R. Kwok (2007). The areas and ice production of the western and central Ross Sea polynyas, 1992–2002, and their relation to the B-15 and C-19 iceberg events of 2000 and 2002. *J. Mar. Syst.* 68: 201–214.

Maslanik, J. A., C. Fowler, J. Stroeve, S. Drobot, J. Zwally, D. Yi, and W. Emery (2007). A younger, thinner Arctic ice cover: Increased potential for rapid, extensive sea-ice loss. *Geophys. Res. Lett.* 34: L24501.

Maslanik, J., J. Stroeve, C. Fowler, and W. Emery (2011). Distribution and trends in Arctic sea ice age through spring 2011. *Geophys. Res. Lett* 38: L13502.

Massom, R. A. et al. (2001). Snow on Antarctic sea ice. *Rev. Geophys.* 39:3, 413–445. DOI: `10.1029/2000RG000085`.

Matrai, P. A., E. Olson, S. Suttle, V. Hill, L. A. Codispoti, L. B., and M. Steele (2014). Synthesis of primary production in the Arctic Ocean: I. Surface waters, 1954-2007. *Progr. Oceanogr.* 110: 93–106.

Matsuoka, A. (2008). Bio-optical characteristics of the Arctic Ocean: Application to an Arctic ocean color algorithm. PhD thesis. Hokkaido University.

Matsuoka, A., M. Babin, D. Doxaran, S. B. Hooker, B. G. Mitchell, S. Belanger, and A. Bricaud (2014). A synthesis of light absorption properties of the Arctic Ocean: application to semianalytical estimates of dissolved organic carbon concentrations from space. *Biogeosciences* 11:12, 3131–3147. DOI: `10.5194/bg-11-3131-2014`.

Matsuoka, A., V. Hill, Y. Huot, M. Babin, and A. Bricaud (2011). Seasonal variability in the light absorption properties of western Arctic waters: Parameterization of the individual components of absorption for ocean color applications. *J. Geophys. Res.* 116:C02007.

Matsuoka, A., S. B. Hooker, A. Bricaud, B. Gentili, and M. Babin (2013). Estimating absorption coefficients of colored dissolved organic matter (CDOM) using a semi-analytical algorithm for southern Beaufort Sea waters: application to deriving concentrations of dissolved organic carbon from space. *Biogeosciences*, 917–927.

Matsuoka, A., Y. Huot, K. Shimada, S.-I. Saitoh, and M. Babin (2007). Bio-optical characteristics of the western Arctic Ocean: implications for ocean color algorithms. *Can. J. Remote Sens.* 33: 503–518.

Matsuoka, A. et al. (2012). Tracing the transport of colored dissolved organic matter in water masses of the Southern Beaufort Sea: relationship with hydrographic characteristics. *Biogeosciences* 9: 925–940.

McClain, C. R. (2009). A decade of satellite ocean color observations. *Ann. Rev. Mar. Sci.* 1: 19–42.

Merico, A., T. Tyrrell, C. Brown, S. Groom, and P. Miller (2003). Analysis of satellite imagery for *Emiliania huxleyi* blooms in the Bering Sea before 1997. *Geophys. Res. Lett.* 30:1337. DOI: `10.1029/2002GL016648`.

Mitchell, B. G. (1990). Algorithms for determining the absorption coefficient of aquatic particulates using the Quantitative Filter Technique (QFT). *Proc. SPIE, Ocean Optics X,* 1302: 137–148. DOI: `10.1117/12.21440`.

— (1992). Predictive bio-optical relationships for polar oceans and marginal ice zones. *J. Mar. Sys.* 3: 91–105.

Mitchell, B. G. and O. Holm-Hansen (1991). Bio-optical properties of Antarctic Peninsula waters: differentiation from temperate ocean models. *Deep Sea Res. A* 38: 1009–1028.

Mitchell, B. G. and M. Kahru (2009). Bio-optical algorithms for ADEOS-2 GLI. *J. Remote Sens. Soc. Japan* 29: 80–85.

Mitchell, B. G. and D. A. Kiefer (1988). Chlorophyll a specific absorption and fluorescence excitation spectra for light-limited phytoplankton. *Deep Sea Res. A* 35: 639–663.

Mitchell, B. G. et al. (2000). Determination of spectral absorption coefficients of particles, dissolved material and phytoplankton for discrete water samples. In: *Ocean Optics Protocols For Satellite Ocean Color Sensor Validation, Revision 2. NASA/TM-2000-209966.* Ed. by G. S. Fargion and J. L. Mueller. NASA: Greenbelt, Maryland, 125–153.

Mitchell, D. L., S. K. Chai, Y. Liu, A. J. Heymsfield, and Y. Dong (1996a). Modeling cirrus clouds: Part I. Treatment of bimodal size spectra and case study analysis. *J. Atmos. Sci.* 53: 2952–2966.

Mitchell, D. L., A. Macke, and Y. Liu (1996b). Modeling cirrus clouds Part II: treatment of radiative properties. *J. Atmos. Sci.* 53: 2967–2988.

Mobley, C. D. (1994). *Light and water: Radiative transfer in natural waters.* Academic Press.

Montes-Hugo, M., S. C. Doney, H. W. Ducklow, W. Fraser, D. Martinson, S. E. Stammerjohn, and O. . Schofield (2009). Recent changes in phytoplankton communities associated with rapid regional climate change along the western Antarctic Peninsula. *Science* 323: 1470–1473.

Moore, T. S., J. W. Campbell, and H. Feng (2001). A fuzzy logic classification scheme for selecting and blending satellite ocean color algorithms. *IEEE Trans. Geosci. Remote Sens.* 39:8, 1764–1776. DOI: `10.1109/36.942555`.

Morel, A. (1974). Optical properties of pure water and pure seawater. In: *Optical Aspects of Oceanography*. Ed. by N. G. Jerlov and E. Steeman Nielsen. Academic Press: New York, 1–24.

— (1978). Available, usable, and stored radiant energy in relation to marine photosynthesis. *Deep-Sea Res. II* 25: 673–688.

— (1991). Light and marine photosynthesis – a spectral model with geochemical and climatological implications. *Prog. Oceanogr.* 26:3, 263–306.

Morel, A., D. Antoine, M. Babin, and Y. Dandonneau (1996). Measured and modeled primary production in the northeast Atlantic (EUMELI JGOFS program): The impact of natural variations in photosynthetic parameters on model predictive skill. *Deep-Sea Res. I* 43:8, 1273–1304. DOI: `10.1016/0967-0637(96)00059-3`.

Morel, A. and J. F. Berthon (1989). Surface pigments, algal biomass profiles, and potential production of the euphotic layer - relationships reinvestigated in view of remote-sensing applications. *Limnol. Oceanogr.* 34: 1545–1562.

Morel, A. and A. Bricaud (1981). Theoretical results concerning light absorption in a discrete medium, and application to specific absorption of phytoplankton. *Deep Sea Res. A.* 28: 1375–1393.

Morel, A. and S. Maritorena (2001). Bio-optical properties of oceanic waters: A reappraisal. *J. Geophys. Res.* 106:C4, 7163–7180.

Morel, A. and L. Prieur (1977). Analysis of variations in ocean color. *Limnol. Oceanogr.* 22: 709–722.

Morel, A. and S. Bélanger (2006). Improved detection of turbid waters from ocean color sensors information. *Remote Sens. Environ.* 102: 237–249.

Morrison, H., G. de Boer, G. Feingold, J. Harrington, M. D. Shupe, and K. Sulia (2012). Resilience of persistent arctic mixed-phase clouds. *Nat. Geosci.* 5: 11–17.

Mueller, J. L. et al. (2003). *Ocean Optics Protocols For Satellite Ocean Color Sensor Validation, Revision 5, Volume V: Biogeochemical and Bio-Optical Measurements and Data Analysis Protocols.* Tech. rep. NASA: Greenbelt, Maryland.

Mundy, C. J. et al. (2009). Contribution of under-ice primary production to an ice-edge upwelling phytoplankton bloom in the Canadian Beaufort Sea. *Geophys. Res. Lett.* 36: 17. DOI: `10.1029/2009GL038837`.

Naik, P., E. J. D’Sa, J. I. Goes, and H. R. Gomes (2010). Assessment of particulate absorption properties in the southeastern Bering Sea from in-situ and remote sensing data. *J. Appl. Remote Sens.* 4:1, 043561. DOI: `10.1117/1.3525572`.

Nelson, J. R. and S. Guarda (1995). Particulate and dissolved spectral absorption on the continental shelf of the southeastern United States. *J. Geophys. Res.* 100: 8715–8732.

Neveux, J. et al. (1990). Comparison of chlorophyll and phaeopigment determinations by spectrophotometric, fluorometric, spectrofluorometric and HPLC methods. *Marine Microb. Food Webs* 4: 217–238.

O’Reilly, J. E. et al. (2000). Volume 11, SeaWiFS Postlaunch Calibration and Validation Analyses, Part 3 Part 3. In: *NASA Tech. Memo. 2000–206892*. Ed. by E. R. Hooker S. B.and Firestone. NASA Goddard Space Flight Centre, Greenbelt , Maryland.

O’Reilly, J. et al. (1998). Ocean color chlorophyll algorithms for SeaWiFS. *J. Geophys. Res.* 103: 24937–24953.

Osburn, C. L., L. Retamal, and W. F. Vincent (2009). Photoreactivity of chromophoric dissolved organic matter transported by the Mackenzie River to the Beaufort Sea. *Mar. Chem.* 115: 10–20.

Pabi, S. and K. R. Arrigo (2006). Satellite estimation of marine particulate organic carbon in waters dominated by different phytoplankton taxa. *J. Geophys. Res.* 111: 1–8.

Pabi, S., G. L. van Dijken, and K. R. Arrigo (2008). Primary production in the Arctic Ocean, 1998-2006. *J. Geophys. Res.* 113: C8. DOI: `10.1029/2007JC004578`.

Palmer, M. A., G. L. van Dijken, B. G. Mitchell, B. J. Seegers, K. E. Lowry, M. M. Mills, and K. R. Arrigo (2013). Light and nutrient control of photosynthesis in natural phytoplankton populations from the Chukchi and Beaufort Seas, Arctic Ocean. *Limnol. Oceanogr.* 58: 2185–2205.

Palmer, M. D., D. J. McNeall, and N. J. Dunstone (2011). Importance of the deep ocean for estimating decadal changes in Earth’s radiation balance. *Geophys. Res. Lett.* 38:13, L13707.

Parkinson, C. L. and D. J. Cavalieri (2012). Antarctic sea ice variability and trends. *The Crysphere Discuss.* 6: 871–880.

Parkinson, C. L. and J. C. Comiso (2008). Antarctic sea ice from AMSR-E from two algorithms and comparisons with sea ice from SSM/I. *J. Geophys. Res.* 113: C02S06.

— (2013). On the 2012 record low Arctic sea ice cover: Combined impact of preconditioning and an August storm. *Geophys. Res. Lett.* 40: 1–6. DOI: `10.1002/grl.50349`.

Pegau, W. S. (2002). Inherent optical properties of the central Arctic surface waters. *J. Geophys. Res.* 107:C10, 8035. DOI: `10.1029/2000JC000382`.

Pegau, W. S., D. J. Gray, and J. R. V. Zaneveld (1997). Absorption and attenuation of visible and near-infrared light in water: dependence on temperature and salinity. *Appl. Opt.* 36:24, 6035–6046.

Perovich, D. K. (1996). *The optical properties of sea ice.* Monogr. 96-1, 25 pp., Cold Reg. Res. and Eng. Lab., Hanover, N. H.

Perovich, D. K. and J. W. Govoni (1991). Absorption coefficients of ice from 250 to 400 nm. *Geophys. Res. Lett.* 18: 1233–1235.

Perovich, D. K., T. C. Grenfell, B. Light, and P. V. Hobbs (2002). Seasonal evolution of the albedo of multiyear Arctic sea ice. *J. Geophys. Res.* 197: 8044.

Perovich, D. K., S. V. Nghiem, T. Markus, and A. Schweiger (2007). Seasonal evolution and interannual variability of the local solar energy absorbed by the Arctic sea ice-ocean system. *J. Geophys. Res.* 112: C03005.

Perovich, D. K. and J. A. Richter-Menge (1994). Surface characteristics of lead ice. *J. Geophys. Res.* 99: 16341–16350.

Perovich, D. K., J. A. Richter-Menge, K. F. Jones, and B. Light (2008). Sunlight, water and ice: Extreme Arctic sea ice melt during the summer of 2007. *Geophys. Res. Lett.* 35:L11501. DOI: `10.1029/2008GL034007`.

Perovich, D. (2007). Light reflection and transmission by a temperate snow cover. *J. Glaciol.* 53:181, 201–210.

Perrette, M., A. Yool, G. D. Quartly, and E. E. Popova (2011). Near-ubiquity of ice-edge blooms in the Arctic. *Biogeosciences* 8: 515–524.

Platt, T. and S. Sathyendranath (1988). Oceanic primary production: estimation by remote sensing at local and regional scales. *Science* 241: 1613–1620.

Polashenski, C., D. Perovich, and Z. Courville (2012). The mechanisms of sea ice melt pond formation and evolution. *J. Geophys. Res.* 117: C01001.

Pope, R. M. and E. S. Fry (1997). Absorption spectrum (380-700 nm) of pure water. 2. Integrating cavity measurements. *Appl. Opt.* 36: 8710–8723.

Popova, E. E., A. Yool, A. C. Coward, Y. K. Aksenov, S. G. Alderson, B. A. de Cuevas, and T. R. Anderson (2010). Control of primary production in the Arctic by nutrients and light: insights from a high resolution ocean general circulation model. *Biogeosciences* 7:11, 3569–3591. DOI: `10.5194/bg-7-3569-2010`.

Quinn, P. K., T. L. Miller, T. S. Bates, and G. E. Shaw (2002). A 3-year record of simultaneously measured aerosol chemical and optical properties at Barrow , Alaska. *J. Geophys. Res.* 107: 1–15.

Quinn, P. K., G. Shaw, E. Andrews, E. G. Dutton, T. Ruoho-Airola, and S. L. Gong (2007). Arctic haze: current trends and knowledge gaps. *Tellus B* 59: 99–114.

Rangno, A. and P. Hobbs (2001). Ice particles in stratiform clouds in the arctic and possible mechanisms for the production of high ice concentrations. *J. Geophys. Res.* 106: 15065–15075.

Retamal, L., S. Bonilla, and W. F. Vincent (2008). Optical gradients and phytoplankton production in the Mackenzie River and the coastal Beaufort Sea. *Polar Biol.* 31: 363–379.

Rey, F. (1991). Photosynthesis-irradiance relationships in natural phytoplankton populations of the Barents Sea. *Polar Res.* 10:1, 105–116.

Reynolds, R. A., D. Stramski, and B. G. Mitchell (2001). A chlorophyll-dependent semianalytical reflectance model derived from field measurements of absorption and backscattering coefficients within the Southern Ocean. *J. Geophys. Res.* 106: 7125–7138.

Ricchiazzi, P., S. R. Yang, C. Gautier, and D. Sowle (1998). SBDART: A Research and Teaching Software Tool for Plane-parallel Radiative Transfer in the Earth's Atmosphere. *B. Am. Meteorol. Soc.* 79: 2101–2114.

Richardson, K., S. Markager, E. Buch, M. F. Lassen, and A. S. Kristensen (2005). Seasonal distribution of primary production, phytoplankton biomass and size distribution in the Greenland Sea. *Deep-Sea Res. I* 52: 979–999.

Riggs, G. A., D. K. Hall, S. A. Ackerman, and S. Lawrence (1999). Sea ice extent and classification mapping with the Moderate Resolution Imaging Spectroradiometer Airborne Simulator. *Remote Sens. Environ.* 4257: 152–163.

Riggs, G. A., D. K. Hall, and V. V. Salomonson (2006). *MODIS Snow Products User Guide to Collection 5*. URL: `http://nsidc.org/data/docs/daac/modis_v5/dorothy_snow_doc.pdf`.

Robinson, W. D., B. A. Franz, F. S. Patt, S. W. Bailey, and P. J. Werdell (2003). Masks and flags updates. In: *SeaWiFS Postlaunch Technical Report Series*. Ed. by S. Hooker and E. Firestone. Vol. 22. NASA Tech. Memo. 2003-206892. NASA Goddard Space Flight Center, Greenbelt, Maryland, 34–40.

Rossow, W. B. and R. A. Schiffer (1991). ISCCP Cloud Data Products. *Bull. Am. Meteorol. Soc.* 72: 2–20.

Rothrock, D. A., Y. Yu, and G. A. Maykut (1999). Thinning of the Arctic sea-ice cover. *Geophys. Res. Lett.* 26:23, 3469–3472.

Röttgers, R., D. McKee, and C. Utschig (2014). Temperature and salinity correction coefficients for light absorption by water in the visible to infrared spectral region. *Opt. Express* 22:21, 25093. DOI: `10.1364/OE.22.025093`.

Ruddick, K. G., F. Ovidio, and M. Rijkeboer (2000). Atmospheric correction of SeaWiFS imagery for turbid coastal and inland waters. *Appl. Opt.* 39: 897–912.

Sandvik, A., M. Biryulina, N. G. Kvamstø, J. J. Stamnes, and K. Stamnes (2007). Observed and simulated microphysical composition of arctic clouds – data properties and model validation. *J. Geophys. Res.* 112:D05205. DOI: `10.1029/2006JD007351`.

Santer, R. and C. Schmechtig (2000). Adjency effects on water surfaces: primary scattering approximation and sensitivity study. *Appl. Opt.* 39:3, 361–375.

Sassen, K. et al. (1995). The 5–6 December 1991 fire IFO-II jet stream cirrus case study: possible influences of volcanic aerosols. *J. Atmos. Sci.* 52: 97–123.

Sathyendranath, S., G. F. Cota, V. Stuart, H. Maass, and T. Platt (2001). Remote sensing of phytoplankton pigments: A comparison of empirical and theoretical approaches. *Int. J. Remote Sens.* 22: 249–273.

Sathyendranath, S. and T. Platt (1989). Remote-sensing of ocean chlorophyll — consequence of nonuniform pigment profile. *Appl. Opt.* 28: 490–495.

Schutz, B. E., H. J. Zwally, C. Shuman, D. Hancock, and J. P. DiMarzio (2005). Overview of the ICESat Mission. *Geophys. Res. Lett.* 32: L21S01.

Schweiger, A. and J. R. Key (1994). Arctic ocean radiative fluxes and cloud forcing estimates from the ISCCP C2 cloud dataset. *J. Appl. Meteor.* 33: 948–963.

Serreze, M. C., M. M. Holland, and J. Stroeve (2007). Perspectives on the Arctic's Shrinking Sea-Ice Cover. *Science* 315: 1533–1536. DOI: `10.1126/science.1139426`.

Shi, W. and M. Wang (2012a). Sea ice properties in the Bohai Sea measured by MODIS-Aqua: 1. Satellite algorithm development. *J. Mar. Sys.* 95: 32–40.

— (2012b). Sea ice properties in the Bohai Sea measured by MODIS-Aqua: 2. Study of sea ice seasonal and interannual variability. *J. Mar. Sys.* 95: 41–49.

Shiklomanov, I. (1993). World fresh water resources. In: *Water in Crisis: A Guide to the World's Fresh Water Resources.* Ed. by P. Gleick. Oxford University Press., 13–24.

Shupe, M. (2011). Clouds at arctic atmospheric observatories. part 2: Thermodynamic phase characteristics. *J. Appl. Meteorol.* 50: 645–661.

Shupe, M., S. Matrosov, and T. Uttal (2006). Arctic mixed-phase cloud properties derived from surfacebased sensors at SHEBA. *J. Atmos. Sci.* 63: 697–711.

Siegel, D. A., M. Wang, S. Maritorena, and W. Robinson (2000). Atmospheric correction of satellite ocean color imagery: The black pixel assumption. *Appl. Opt.* 39: 3582–3591.

Sikand, M., J. Koskulics, K. Stamnes, B. Hamre, J. J. Stamnes, and R. P. Lawson (2010). Optical properties of mixed phase boundary layer clouds observed from a tethered balloon platform in the arctic. *J. Quant. Spectrosc. Radiat. Transfer* 111: 1921–1930.

Simpson, J. and R. Keller (1995). An improved fuzzy logic segmentation of sea ice, clouds, and ocean in remotely sensed Arctic imagery. *Remote Sens. Environ.* 54: 290–312.

Slusser, J. et al. (1996). Comparison of air mass computations. *J. Geophys. Res.* 101: 9315–9321.

Smirnov, A. et al. (2002). Optical properties of atmospheric aerosol in maritime environments. *J. Atmos. Sci.* 59: 501–523.

Smirnov, A. et al. (2011). Maritime aerosol network as a component of AERONET – first results and comparison with global aerosol models and satellite retrievals. *Atmos. Meas. Tech.* 4:3, 583–597. DOI: `10.5194/amt-4-583-2011`.

Smith, R. C. and K. S. Baker (1981). Optical properties of the clearest natural waters. *Appl. Opt.* 20: 177–184.

Smith, R. et al. (1995). The Palmer LTER: A long-term ecological research program at Palmer Station, Antarctic. *Oceanography* 8:3, 77–86.

Smyth, T. J., T. Tyrrell, and B. Tarrant (2004). Time series of coccolithophore activity in the Barents Sea, from twenty years of satellite imagery. *Geophys. Res. Lett.* 31:11, L11302. DOI: `10.1029/2004GL019735`.

Sobolev, V. (1975). *Light Scattering in Planetary Atmospheres.* Pergamon Press, New York.

Sogandares, F. M. and E. S. Fry (1997). Absorption spectrum (340-640 nm) of pure water. I. Photothermal measurements. *Appl. Opt.* 36: 8699–8709.

Sosik, H. M. and B. G. Mitchell (1991). Absorption, fluorescence, and quantum yield for growth in nitrogen-limited *Dunaliella tertiolecta. Limnol. Oceanogr.* 36: 910–921.

— (1995). Light absorption by phytoplankton, photosynthetic pigments and detritus in the California Current System. *Deep Sea Res. I* 42: 1717–1748.

Spurr, R., K. Stamnes, H. Eide, W. Li, K. Zhang, and J. Stamnes (2007). Simultaneous retrieval of aerosol and ocean color: A classic inverse modeling approach: I. Analytic Jacobians from the linearized CAO-DISORT model. *J. Quant. Spectrosc. Radiat. Transfer* 104: 428–449.

Stamnes, K., R. G. Ellingson, J. A. Curry, J. E. Walsh, and B. D. Zak (1999). Review of science issues and deployment strategies for the North Slope of Alaska/Adjacent Arctic Ocean (NSA/AAO) ARM site. *J. Climate* 12: 46–63.

Steele, M., R. Morley, and W. Ermold (2001). PHC: A Global Ocean Hydrography with a High-Quality Arctic Ocean. *J. Climate* 14: 2079–2087.

Steinmetz, F., P. Y. Deschamps, and D. Ramon (2011). Atmospheric correction in presence of sun glint: application to MERIS, *Opt. Express* 19: 9783–9800.

Stramska, M. (2010). The diffusive component of particulate organic carbon export in the North Atlantic estimated from SeaWiFS ocean color. *Deep Sea Res. I* 57: 284–296.

Stramska, M. and D. Stramski (2005). Variability of particulate organic carbon concentration in the north polar Atlantic based on ocean color observations with Sea-viewing Wide Field-of-view Sensor (SeaWiFS). *J. Geophys. Res.* 110: 1–16.

Stramska, M., D. Stramski, R. Hapter, S. Kaczmarek, and J. Ston (2003). Bio-optical relationships and ocean color algorithms for the north polar region of the Atlantic. *J. Geophys. Res.* 108:C5, 3143. DOI: 10.1029/2001JC001195.

Stramski, D., E. S. Boss, D. J. Bogucki, and K. J. Voss (2004). The role of seawater constituents in light backscattering in the ocean. *Prog. Oceanogr.* 61: 27–56.

Stramski, D., R. A. Reynolds, M. Kahru, and B. G. Mitchell (1999). Estimation of particulate organic carbon in the ocean from satellite remote sensing. *Science* 285:5425, 239–242. DOI: 10.1126/science.285.5425.239.

Stroeve, J., M. M. Holland, W. Meier, T. Scambois, and M. Serreze (2007). Arctic sea ice decline: Faster than forecast. *Geophys. Res. Lett.* 34:L09501, DOI: 10.1029/2007/GL029703.

Stroeve, J. C., V. Kattsov, A. Barrett, M. Serreze, T. Pavlova, M. Holland, and W. N. Meier (2012). Trends in Arctic sea ice extent from CMIP5, CMIP3 and observations. *Geophys. Res. Lett* 39:16, L16502.

Stumpf, R. P., R. A. Arnone, R. W. Gould, P. M. Martinolich, and V. Ransibrahmanakul (2003). A partially coupled ocean-atmosphere model for retrieval of water-leaving radiance from SeaWiFS in coastal waters. In: *SeaWiFS Postlaunch Technical Report Series.* Ed. by S. B. Hooker and E. R. Firestone. Vol. 22. NASA Tech. Memo. 2003-206892. NASA Goddard Space Flight Center, Greenbelt, MD., 51–59.

Sturm, M., J. Holmgren, and D. Perovich (2002). The winter snow cover on the sea ice of the Arctic Ocean at SHEBA: Temporal evolution and spatial variability. *J. Geophys. Res.* 107: C10. DOI: 10.1029/2000JC000400.

Sullivan, C., K. Arrigo, C. McClain, J. Comiso, and J. Firestone (1993). Distributions of phytoplankton blooms in the Southern Ocean. *Science* 262: 1832–1837.

Sullivan, J. M., M. S. Twardowski, J. Ronald, J. R. V. Zaneveld, and C. C. Moore (2013). Measuring optical backscattering in water. In: *Light Scattering Reviews 7.* Ed. by A. Kokhanovsky. Springer, 189–224.

Takao, S., T. Hirawake, S. W. Wright, and K. Suzuki (2012). Variations of net primary productivity and phytoplankton community composition in the Indian sector of the Southern Ocean as estimated from ocean color remote sensing data. *Biogeosciences* 9: 3875–3890.

Tanré, D., M. Herman, and P. Y. Deschamps (1981). Influence of the background contribution upon space measurements of ground reflectance. *Appl. Opt.* 20:20, 3676–3684.

Tanré, D., M. Herman, P. Y. Deschamps, and A. de Leffe (1979). Atmospheric modeling for space measurements of ground reflectances, including bidirectional properties. *Appl. Opt.* 18:21, 3587–3594.

Thomas, G. and K. Stamnes (1999). *Radiative transfer in the atmosphere and oceans.* Cambridge University Press, Cambridge.

Throndsen, J. and S. Kristiansen (1991). *Micromonas pusilla* (Prasinophyceae) as part of pico-and nanoplankton communities of the Barents Sea. *Polar Res.* 10: 201–208.

Tomasi, C. et al. (2012). An update on polar aerosol optical properties using POLAR-AOD and other measurements performed during the International Polar Year. *Atmos. Environ.* 52: Physical, chemical, optical and radiative properties of polar aerosols – IPY 2007 — 2008, 29–47. ISSN: 1352-2310. DOI: http://dx.doi.org/10.1016/j.atmosenv.2012.02.055.

Tooma, S. G., R. A. Mennella, J. P. Hollinger, and R. D. Ketchum (1975). Comparison of sea-ice type identification between airborne dual-frequency passive microwave radiometry and standard laser/infrared techniques. *J. Glaciol.* 15: 225–239.

Trabjerg, I. and N. K. Højerslev (1996). Temperature influence on light absorption by fresh water and seawater in the visible and near-infrared spectrum. *Appl. Opt.* 35: 2653–2658.

Trees, C. C., R. R. Bidigare, and J. M. Brooks (1986). Distribution of chiorophylls and phaeopigments in the Northwestern Atlantic Ocean. *J. Plankton Res.* 8: 447–458.

Tremblay, J.-E., K. Simpson, J. Martin, L. Miller, Y. Gratton, D. Barber, and N. M. Price (2008). Vertical stability and the annual dynamics of nutrients and chlorophyll fluorescence in the coastal, southeast Beaufort Sea. *J. Geophys. Res.* 113:C07S90.

Tsay, S. C., K. Stamnes, and K. Jayaweera (1989). Radiative energy budget in the cloudy and hazy arctic. *J. Atmos. Sci.* 46: 1002–1018.

Tucker, W. B., D. K. Perovich, A. J. Gow, W. F. Weeks, and M. R. Drinkwater (1992). Physical properties of sea ice relevant to remote sensing. In: *Microwave Remote Sensing of Sea Ice.* American Geophysical Union, 9–28. DOI: `10.1029/GM068p0009`.

Turner, J. et al. (2009). Non-annular atmospheric circulation change induced by stratospheric ozone depletion and its role in the recent increase of Antarctic sea ice extent. *Geophys. Res. Lett.* 36:L08502. DOI: `10.1029/2009GL037524`.

Vant, M., R. Ramseier, and V. Makios (1978). The complex-dielectric constant of sea ice at frequencies in the range 0.1–40 GHz. *J. Appl. Phys.* 49:3, 1234–1280.

Vedernikov, V., V. I. Gagarin, and V. I. Burenkov (2001). Features of distribution of primary production and chlorophyll in the Pechora Sea in August-September 1998. *Oceanology* 41: 64–74.

Verlinde, J., J. Y. Harrington, G. M. Mcfarquhar, V. T. Yannuzzi, A. Avramov, and S. E. Greenberg (2007). The mixed phase arctic cloud experiment. *Am. Meteorol. Soc.* 106: 14989–15014.

Vodacek, A., N. V. Blough, M. D. DeGrandpre, E. T. Peltzer, and R. K. Nelson (1997). Seasonal variation of CDOM and DOC in the middle Atlantic Bight: Terrestrial inputs and photooxidation. *Limnol. Oceanogr.* 42: 674–686.

Voigt, S., J. Orphal, K. Bogumil, and J. P. Burrows (2001). The temperature dependence (203– 293 K) of the absorption cross section of O_3 in the 230 – 850 nm region measured by Fourier-transform spectroscopy. *J. Photochem. Photobiol. A* 143: 1–9.

Wadhams, P. (2006). Arctic sea ice thickness – A review of current techniques and future possibilities. In: *Arctic sea ice Thickness: Past, present and future.* Ed. by P. Wadhams and G. Amanatidis. European Commission, Belgium, 12–21.

Wadhams, P. and N. R. Davis (2000). Evidence of thinning of the Arctic ice cover north of Greenland. *Nature* 345: 795–797.

Walsh, J. J. et al. (2005). A numerical model of seasonal primary production within the Chukchi/Beaufort seas. *Deep-Sea Res. II* 52: 3541–3576.

Walsh, J. and W. L. Chapman (1998). Arctic cloud-radiation-temperature associations in observational data and atmospheric re-analyses. *J. Climate* 11: 3030–3045.

Wang, J. and G. F. Cota (2003). Remote-sensing reflectance in the Beaufort and Chukchi seas: observations and models. *Appl. Opt.* 42: 2754–2765.

Wang, J., G. Cota, and D. A. Ruble (2005a). Absorption and backscattering in the Beaufort and Chukchi Seas. *J. Geophys. Res.* 110: C04014.

Wang, M. (2002). The Rayleigh lookup tables for the SeaWiFS data processing: Accounting for the effects of ocean surface roughness. *Int. J. Remote Sens.* 23: 2693–2702.

— (2003). Light Scattering from Spherical-Shell Atmosphere: Earth curvature effects measured by SeaWiFS. *Eos Trans. AGU* 84: 529. DOI: `http://dx.doi.org/10.1029/2003eo480003`.

— (2005). A refinement for the Rayleigh radiance computation with variation of the atmospheric pressure International. *J. Remote Sens.* 26: 5651–5663.

— (2007). Remote sensing of the ocean contributions from ultraviolet to near-infrared using the shortwave infrared bands: simulations. *Appl. Opt.* 46: 1535–1547.

Wang, M., K. D. Knobelspiesse, and C. R. Mcclain (2005b). Study of the Sea-Viewing Wide Field-of-View Sensor (SeaWiFS) aerosol optical property data over ocean in combination with the ocean color products. *J. Geophys. Res.* 110:D10S06.

Wang, M. and J. Overland (2012). A sea ice free summer Arctic within 30 years: An update from CMIP5 models. *Geophys. Res. Lett* 38:18. DOI: `10.1029/2012GL052868`.

Wang, M. and W. Shi (2006). Cloud masking for ocean color data processing in the coastal regions. *IEEE Trans. Geosci. Rem. Sens.* 44: 3196–3205.

— (2007). The NIR-SWIR combined atmospheric correction approach for MODIS ocean color data processing. *IEEE Trans. Geosci. Rem. Sens.* 15: 15722–15733.

— (2009). Detection of ice and mixed ice – Water pixels for MODIS ocean color data processing. *IEEE Trans. Geosci. Rem. Sens.* 47: 2510–2518.

Wang, X. and J. R. Key (2005). Arctic surface, cloud, and radiation properties based on the AVHRR Polar Pathfinder dataset. Part I: Spatial and temporal characteristics. *J. Climate* 18: 2558–2574.

Warren, S. G. (1982). Optical properties of snow. *Rev. Geophys. Space Phys.* 20: 67–89.

Warren, S. G. and R. E. Brandt (2008). Optical constants of ice from the ultraviolet to the microwave: A revised compilation. *J. Geophys. Res.* 113: D14220.

Warren, S. G., C. J. Hahn, J. London, R. M. Chervin, and R. L. Jenne (1988). *Global distribution of total cloud cover and cloud type amounts over ocean.* Tech. rep. NCAR Technical Note NCAR/TN-317+STR, National Center for Atmospheric Research, Boulder, CO, USA,

Wassmann, P. and M. Reigstad (2011). Future arctic ocean seasonal ice zones and implications for pelagic-benthic coupling. *Oceanography* 24: 220–231.

Weeks, W. F. and S. F. Ackley (1982). *The growth, structure, and properties of sea ice.* Tech. rep. CRREL Monograph 82-1, 130 pp, Cold Reg. Res. and Eng. Lab., Hanover.

Werdell, P. J. and S. W. Bailey (2005). An improved in-situ bio-optical data set for ocean color algorithm development and satellite data product validation. *Remote Sens. Environ.* 98: 122–140.

White, W. B. and R. G. Peterson (1996). An Antarctic circumpolar wave in surface pressure, wind, temperature and sea ice extent. *Nature* 380: 699–702.

Worden, A. Z. et al. (2009). Green evolution and dynamic adaptations revealed by genomes of the marine picoeukaryotes Micromonas. *Science* 324: 268–272.

Yamonouchi, T., K. Suzuki, and S. Kauragouchi (1987). Detection of clouds in Antarctica from infrared multispectral data of AVHRR. *J. Meteor. Soc. Japan* 65: 949–961.

Yan, B. and K. Stamnes (2003). Fast yet accurate computation of the complete radiance distribution in the coupled atmosphere–ocean system. *J. Quant. Spectrosc. Radiat. Transfer* 76: 207–223.

Yang, H. and H. Gordon (1997). Remote sensing of ocean color: assessment of water-leaving radiance bidirectional effects on atmospheric diffuse transmittance. *Appl. Opt.* 36: 7887–7897.

Zhang, T., S. A. Bowling, and K. Stamnes (1997). Impact of the atmosphere on surface radiative fluxes and snow melt in the Arctic and Subarctic. *J. Geophys. Res.* 102: 4287–4302.

Zhang, X. and L. Hu (2009). Estimating scattering of pure water from densityfluctuation of the refractive index. *Opt. Express* 17: 1671–1678.

Zhang, X., L. Hu, and M.-X. He (2009). Scattering by pure seawater: Effect of salinity. *Opt. Express* 17: 5698–5710.

Zhang, Y. C., W. B. Rossow, A. A. Lacis, V. Oinas, and M. I. Mishchenko (2004). Calculation of radiativefluxes from the surface to top of atmosphere based on ISCCP and other global data sets: Refinements of the radiative transfer model and the input data. *J. Geophys. Res.* 109:D19105.

Zheng, G., D. Stramski, and R. Reynolds (2014). Evaluation of the Quasi-Analytical Algorithm for estimating the inherent optical properties of seawater from ocean color: Comparison of Arctic and lower-latitude waters. *Remote Sens. Environ.* 155: 194–209.

Zuidema, P. et al. (2004). An arctic springtime mixed-phase cloudy boundary layer observed during SHEBA. *J. Atmos. Sci.* 62: 160–176.